Development of Optically Interrogated Diagnostic Systems within Materials Ageing Experiments

Thomas Charles Dyer

Submitted for the degree of
Doctor of Engineering in Applied Photonics

Heriot-Watt University
School of Engineering and Physical Sciences
Edinburgh, UK

AWE
Materials and Analytical Science
Aldermaston, UK

June 2019

Abstract

This research project aimed to develop diagnostic options for *in situ* use within future materials ageing experiments in complex engineering environments. The techniques developed were required to be suitable for multi-decade deployment and have minimal impact upon the experimental chemical ageing evolution.

Optical fibre based diagnostic options for measuring temperature, barometric pressure, and gaseous concentrations were reviewed. The long-term suitability of fibre Bragg grating (FBG) temperature sensors, fibre Fabry-Pérot (FFP) pressure sensors, O_2-sensing fluorescence probes, and optical fibre switches were assessed experimentally in experiments that lasted up to 1 year. A bespoke fibre-coupled multi-pass spectroscopic gas cell was developed for the detection of H_2O with a path-length of (6.47 ± 0.05) m, along with novel techniques to package FBG and FFP sensors, hermetically pass optical fibres into the experimental volume, and route optical fibres. Custom optical fibre connectors for use both inside and outside the experiment were designed and evaluated. To support the diagnostics investigated, a bespoke interrogation system was created, with a design focus on modularity, redundancy, and long-term support.

The research was evaluated against the project requirements, and together formed a potential concept for future materials ageing experiments requiring comprehensive and enhanced embedded diagnostic capabilities. The developed technologies were assessed as ranging in technology readiness level (TRL) from 2 to 6. For use in an experiment, further work would be required to mature the techniques up to TRL 9, and potential maturation routes are presented.

Acknowledgements

In the creation of this thesis I have been assisted by a great many, to whom I would like to express my thanks.

First, I thank my wife, Beccy, for her unwavering support; keeping me calm and sane throughout (and for some years before too)! I also thank my parents and sister for all their ongoing moral support throughout my life.

My two supervisors, Dr Simon Brooks and Dr Bill MacPherson, have been fantastic to work with; always offering prompt and *often* useful advice when requested. I couldn't have asked for more of their time or to show me more enthusiasm towards my work.

I have also been assisted by many colleagues at AWE. I would like to thank all those who helped me along the way, including: Dr Dave Knox, Dr Alexander Thomson, Dr Matthew Kingston, Miss Amy Bruce, Mr Alex Clark, Mr Tony Attoe, Dr Adrian King, Dr Joe Marshal-Reed, and Dr Phil Keenan. The technical support and good humour was greatly appreciated!

Finally, I gratefully acknowledge support for this research from AWE and the UK Engineering and Physical Sciences Research Council, under Grant number EP/L01596X/1.

"*And now all the others are saying, 'What about Us?' So perhaps the best thing to do is to stop writing Introductions and get on with the book.*"

– A.A. Milne, 1926 [1]

ACADEMIC REGISTRY

Research Thesis Submission

Please note this form should be bound into the submitted thesis.

Name*:*	**Thomas Dyer**		
School:	**Engineering & Physical Sciences**		
Version: *(i.e. First, Resubmission, Final)*	**Final**	Degree Sought:	**Doctor of Engineering (EngD)**

Declaration

In accordance with the appropriate regulations I hereby submit my thesis and I declare that:

1. The thesis embodies the results of my own work and has been composed by myself
2. Where appropriate, I have made acknowledgement of the work of others
3. Where the thesis contains published outputs under Regulation 6 (9.1.2) these are accompanied by a critical review which accurately describes my contribution to the research and, for multi-author outputs, a signed declaration indicating the contribution of each author
4. The thesis is the correct version for submission and is the same version as any electronic versions submitted*.
5. My thesis for the award referred to, deposited in the Heriot-Watt University Library, should be made available for loan or photocopying and be available via the Institutional Repository, subject to such conditions as the Librarian may require
6. I understand that as a student of the University I am required to abide by the Regulations of the University and to conform to its discipline.
7. Inclusion of published outputs under Regulation 6 (9.1.2) shall not constitute plagiarism.
8. I confirm that the thesis has been verified against plagiarism via an approved plagiarism detection application e.g. Turnitin.

* *Please note that it is the responsibility of the candidate to ensure that the correct version of the thesis is submitted.*

Signature of Candidate*:*		Date:	

Submission

Submitted By *(name in capitals):*	
Signature of Individual Submitting:	
Date Submitted:	

For Completion in the Student Service Centre (SSC)

Received in the SSC by *(name in capitals):*			
Method of Submission *(Handed in to SSC; posted through internal/external mail):*			
*E-thesis Submitted (**mandatory for final theses**)*			
Signature:		Date:	

Contents

List of Tables

List of Figures

List of Acronyms and Nomenclature

A_M	Molar absorptivity	
α	Absorbance	
α_Λ	Coefficient of thermal expansion	$= \frac{1}{\Lambda}\frac{\partial \Lambda}{\partial T}$
α_n	Thermo-optic coefficient	$= \frac{1}{n}\frac{\partial n}{\partial T}$
AC	Alternating current	
ADC	Analogue to digital converter	
ASE	Amplified spontaneous emission	
AWE	The Atomic Weapons Establishment	
BJT	Bipolar junction transistor	
BOM	Bill of materials	
χ	Mole fraction	
C	Computer programming language	
C	Capacitance	
$\mathbf{C}$	Cell round trip transformation matrix	
c (c_0)	Speed of light (in vacuum)	$(= 299\,792\,458\,\mathrm{m\,s^{-1}}$ [2])
CC	Constant current	
CC1	Control card 1	
CC2	Control card 2	
CH_4	Methane	
CMR	Circular multi-reflection	
CO_2	Carbon dioxide	
COTS	Commercial off-the-shelf	
CRD	Cavity ring-down	
CTE	Coefficient of thermal expansion	

DAQ	Data acquisition	
DBR	Distributed Bragg reflector	
DFB	Distributed feedback	
DFG	Difference-frequency generation	
DIP	Dual in-line package	
DL	Detection limit	$\equiv \frac{\text{Resolution}}{\text{Sensitivity}}$
DOAS	Differential optical absorption spectroscopy	
η	Efficiency	
E	Photon energy	$= \frac{hc}{\lambda}$
E_a	Arrhenius activation energy	
EDX	Energy-dispersive X-ray	
EMF	Electromotive force (voltage)	
EOM	Electro-optic modulator	
eV	Electron Volt	$\approx 1.6022 \times 10^{-19}$ J [2]
f	Modulation frequency	
$\mathcal{F}$	Finesse	
FBG	Fibre Bragg grating	
FFP	Fibre Fabry-Pérot	
FFT	Fast Fourier transform	
FPGA	Field-programmable gate array	
FSR	Free spectral range	
FTIR	Fourier-transform infrared	
FWHM	Full-width half-maximum	
GRIN	Graded refractive index	
h	Planck's constant	$\approx 6.6261 \times 10^{-34}$ J s [2] $\approx 4.1357 \times 10^{-15}$ eV s [2]
H_2O	Water	
HDL	Hardware descriptive language	
HITRAN	High-resolution transmission molecular absorption database	

I	Electrical current	
I	Signal or measured intensity	
I_0	Initial or input intensity	
IB1	Interface buffer 1	
IC	Integrated circuit	
I^2C	Inter-integrated circuit protocol	
InGaAs	Indium gallium arsenide	
IoT	Internet of things	
IP	Intellectual property	
IV	Current (I) against Voltage (V)	
j	Gas transition	
JTAG	Joint test action group	
k	Gas-specific function	$= \sum S\ n\chi\psi$
k	Light coupling efficiency experimental constant	
k_B	Boltzmann constant	$\approx 1.3806 \times 10^{-23}\,\mathrm{J\,K^{-1}}$ [2]
k_q	Biomolecular quenching rate constant	
$\mathcal{k}$	Reaction rate (chemical)	
λ	Interrogation wavelength	
$\delta\lambda$	Optical bandwidth	
λ_B	Bragg wavelength	
$\Delta\lambda_B$	Bragg wavelength shift	
Λ	Spatial period	
L	Cavity length	
L	Optical path length	
L	Grating length	
LDO	Low drop-out	
M	Ray matrix	
MB1	Module buffer 1	
MEMS	Micro-electro-mechanical system	
MFC	Mass flow controller	

MIR	Mid-infrared	
MM	Multi-mode	
MOD	Ministry of Defence	
MOSFET	Metal-oxide-semiconductor field-effect transistor	
MPPT	Maximum power-point tracking	
MPO/MTP	Multiple-fibre push-on-pull-off/mechanical transfer polished	
Mux	Multiplexor	
ν	Frequency	
n	Refractive index	$\equiv \frac{c_0}{v}$
$\bar{n}$	Average refractive index	
n	Number density	
N_A	Avogadro constant	$\approx 6.022\,14 \times 10^{23}\,\text{mol}^{-1}$ [2]
NA	Numerical aperture	$\equiv n \sin\theta$
NDIR	Non-dispersive infrared	
NEA	Noise equivalent absorption	
NIR	Near infrared	
NTC	Negative temperature coefficient	
Ω	Electrical resistance	$= \frac{V}{I}$
Ω	Optical fibre constant for core propagation confinement	
ω	Frequency (angular)	
O_2	Oxygen	
OFDR	Optically frequency-domain reflectometry	
OIES	Optically isolated electronic sensors	
OR	Optic and routing	
Op-amp	Operational amplifier	
OPO	Optical parametric oscillator	
OSA	Optical spectrum analyser	
OTDR	Optical time-domain reflectometry	

π	Pi	$\approx 3.141\,59$ [2]
Φ	Quantum yield	
ϕ	Phase	
$\varnothing$	Diameter	
ψ	Lineshape function	
P	Electrical power	
P_w	Water vapour pressure (mbar)	
P_{ws}	Saturation water vapour pressure (mbar)	
PCB	Printed circuit board	
PD	Photodiode	
PFM	Pulse frequency modulation	
PID	Proportional, integral, differential	
PRT	Platinum resistance thermometer	
PSU	Power supply unit	
PTAT	Proportional to absolute temperature	
PTC	Positive temperature coefficient	
PV	Photovoltaic	
$\|Q\|$	Quencher chemical concentration	
q_e	Charge of an electron	$\approx 1.6022 \times 10^{-19}$ C [2]
R	Reflectivity	
R	Electrical resistance	
$\bar{R}$	Mean reflectivity	
$\mathbf{R}$	Spherical mirror transformation matrix	
RC	Resistor-capacitor	
RF	Radio frequency	
RMS	Root mean square	
RMSE	Root mean square error	
RP	Rapid prototype	
RTC	Real time clock	
S	Linestrength	
SEM	Scanning electron microscope	

SCC	Short-circuit current
SD	Secure Digital
SLED	Superluminescent light emitting diode
SM	Single mode
SNR	Signal-to-noise ratio
SOA	Semiconductor optical amplifier
SSE	Sum of squared errors
τ	Emission lifetime
τ_0	Quencher-free emission lifetime
θ	Angle
T	Absolute temperature
$\mathbf{T}$	Translation transformation matrix
TDLAS	Tunable diode-laser absorption spectroscopy
TEC	Thermo-electric cooler
TRL	Technology readiness level
UART	Universal asynchronous receiver-transmitter
USB	Universal serial bus
UV	Ultraviolet
V	Interferogram visibility
V	Electrical voltage
V_T	Temperature dependant voltage
V_{BG}	Bandgap voltage
VCSEL	Vertical cavity surface-emitting laser
VI	Virtual instrument, created in NI LabVIEW
WDM	Wavelength-division multiplexing
WMS	Wavelength modulation spectroscopy
X	Electrical reactance

List of Publications by the Candidate

Below contains a list of selected research publications and outputs by the candidate in reverse chronological order, separated into output type.

Patent Applications

T. Dyer, W. MacPherson, S. Brooks, *"Miniaturised optical fibre integrated spectroscopic gas cell,"* [Application in draft with MOD].

T. Dyer, W. MacPherson, S. Brooks, *"Optical Fibre Connector,"* [3] [Application filed; GB1820122.8].

Conference Proceedings

T. Dyer, W. N. MacPherson, S. J. Brooks, S. McCulloch, *"Accelerated Through-Life Performance Evaluation of Fibre Fabry-Pérot Pressure Sensors,"* proceedings of the 26th International Conference on Optical Fibre Sensors (OFS-26), 2018 [4].

Conference Presentations

T. Dyer, W. N. MacPherson, S. J. Brooks, S. McCulloch, *"Accelerated Through-Life Performance Evaluation of Fibre Fabry-Pérot Pressure Sensors,"* poster presentation at the 26th International Conference on Optical Fibre Sensors (OFS-26), Lausanne, Switzerland, 24-28 Sep. 2018.

T. Dyer, W. N. MacPherson, S. J. Brooks, *"Using Electronic Sensors in an Optical Sensor Research Project,"* oral presentation at the CDTAP Annual Conference, St. Andrews University, Scotland, 15 Jun. 2018.

T. Dyer, W. N. MacPherson, S. J. Brooks, *"Evaluation Performance for Long-Term*

Optical Diagnostics," poster presentation at the CDTAP Annual Conference, Heriot-Watt University, Scotland, 23 Jun. 2017.

T. Dyer, W. N. MacPherson, S. J. Brooks, *"Development & Integration of Optically Interrogated Diagnostics within Materials Ageing Experiments,"* poster presentation at the Photonic Systems for Sensing and Metrology Summer School, St-Andrews, Scotland, 25 Jun. – 1 Jul. 2016.

T. Dyer, N. Stevenson, M. Reilly, *"Optical Interrogation of a MEMS-based Spectroscopic Gas Cell,"* poster presentation at the CDTAP Annual Conference, St-Andrews, Scotland, 24 Jun. 2016.

Part I

Introductions

Chapter 1: Introduction

This research project aimed to produce functional technology concepts towards an optically-interrogated diagnostic system suitable for long-term experiments. The scope included the development of *in situ* diagnostic sensors, optoelectronic interrogation hardware, and the optical fibre infrastructure to enable integration within an experiment. The concepts produced would be used by the Atomic Weapons Establishment (AWE) to inform further development towards potential deployment of optical diagnostics supporting long-term materials ageing experiments. *In situ* optical sensors could provide real-time measurement of material ageing parameters without perturbing the experiment.

As a nuclear weapon state, the United Kingdom maintains a credible nuclear deterrent, but since ratifying the comprehensive nuclear test ban treaty in 1998 has committed itself to underwriting the weapon stockpile's credibility through scientific research, rather than through nuclear testing [5]. As materials age, it is appreciated that their chemical composition and physical properties are likely to change. The ability to predict these changes forms an important part of underwriting a nuclear weapon stockpile [6]. A long-term materials ageing experiment is one approach for collecting data to support such material change predictions [7].

This work was based at AWE, and aimed to develop concept demonstrator hardware covering the full diagnostic system design, including: optical diagnostics, interrogation hardware, and fibre integration. The focus on optically interrogated techniques was due to their potential for small size, chemical compatibility, remote sensing capabilities, and ability to provide electrical isolation [7]. The project was conducted following a review of objectives and technical requirements, and a review of literature and commercial products. Laboratory experiments and evaluations were performed to assess both commercial and bespoke optical sensing techniques. Engineering design of electronic circuits, printed circuit boards (PCBs), mechanical enclosures, sensor assemblies, and optical systems was performed; supported by mathematical simulations, where appropriate.

The practical aspects of the work described in this project commenced in May 2016,

following commencement of the EngD in September the previous year and completion of academic modules at St. Andrews, Strathclyde, and Glasgow Universities. The following account of the project is not presented in chronological order, opting instead to arrange the work by topic. Given the broad scope of the work, there were typically multiple streams of work performed in parallel.

1.1 Materials Ageing Experiment Motivation

The diagnostics developed within this project were intended for use within a future long-term materials ageing experiment. Such an experiment would typically impose restrictions; the experiment may be hermetically sealed, temperature cycled, electrically isolated, and operated over multiple decades. *In situ* sensing of materials ageing phenomena, such as chemical and physical parameters, was considered advantageous [7]. However, any additions to the experiment would need to cause minimal impact, ensuring experiments with diagnostics evolve comparably to those without. Therefore the diagnostics located within the experimental volume were required to be chemically compatible, meaning they would not cause chemical reactions, desorption, adsorption, absorption, or ion exchanges, so that the chemical species and concentrations present were not effected. The hardware was also required to fit within the geometry of the experiment, therefore physically small techniques were more likely to be compatible with a wider range of experiments. The hermetic seal of the experimental volume would need to be maintained. An example of a conceptual configuration is shown in figure 1.1.

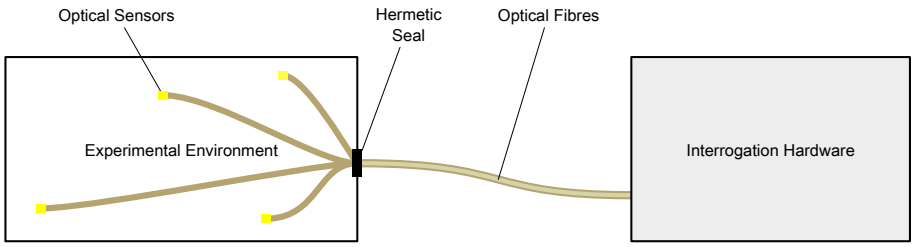

Figure 1.1: Example of a long-term experimental configuration containing optically interrogated sensors, optical fibres, and interrogation hardware.

For the duration of the experiment the internal environment may not be perturbed, meaning that access to the *in situ* diagnostics would not be possible until the experiment was concluded. Equally, the interrogation hardware would be required to monitor the sensors throughout the multi-decade duration; potentially up to 30 years [7]. Designing a system to provide high quality data over such a time-frame, with no access for periodic

sensor calibration, was one example of the challenges explored in this thesis.

1.2 Project Aim and Objectives

The aim of this research project was the conceptual design of a diagnostic system with the ability, following further maturation and development, to support a future materials ageing experiment. Production of hardware was considered advantageous by enabling the experimental evaluation of the techniques, and to provide concept demonstration for review and inform any potential further developments.

To deliver the project, three objectives were created which covered separate parts of the diagnostic system. The three objectives were to:

1. Investigate sensor interrogation hardware solutions.

2. Develop optical diagnostic techniques.

3. Develop optical fibre integration technologies.

The sensor interrogation hardware investigation would ensure deployed optical diagnostics could be consistently monitored throughout the experimental duration. Optical sensor technique development for temperature, barometric pressure, and gas detection, was to provide confidence in the long-term performance of the sensors and diagnostics, and thereby ensure high quality data from the experiment. Optical fibre integration technologies were considered vital to ensuring optical diagnostics could be successfully included within a future long-term experiment.

1.3 Project Technical Requirements

The techniques and technologies investigated within the project were required to satisfy technical requirements to ensure the outcome of the work would meet the needs of AWE. Throughout the project, the requirements were used to enable technique evaluation. Specific requirements are discussed as appropriate within this work, but below is a general overview of the project requirements, separated into the three objective topics. The concepts produced should provide:

1. Interrogation hardware

    (a) An integrated interrogation hardware solution capable of measuring optical

diagnostics supporting periodic (approximately hourly) measurements of each sensor deployed.

(b) A strategy to maintain the system for approximately 30 years, with minimal downtime.

(c) Hardware solutions to enable fibre Bragg grating (FBG) measurement by two techniques.

(d) FBG wavelength detection sensitivity of ± 5 pm in the region of 1550 nm with a bandwidth of 100 nm (equivalent to a wavelength resolution of 200 pm).

(e) A hardware solution to enable optically isolated electronic sensors (OIES) interrogation.

(f) A hardware framework considered able to support tunable diode-laser absorption spectroscopy (TDLAS) with a minimum detectable absorption of 1×10^{-3} $\mathrm{Hz}^{-1/2}$ (absorbance range of 0.01 to 3).

(g) A modular approach that supports hot-swapping of modules.

(h) Inclusion of system-monitoring sensors within the module designs.

(i) System-monitoring of temperature from -10 °C to 40 °C with an accuracy of ± 1 °C (1 K).

(j) System-monitoring of humidity from 10 %RH to 90 %RH with an accuracy of ± 5 %RH (from -25 °C to 25 °C dew point with an accuracy of ± 2 °C dew point).

(k) System-monitoring of barometric pressure from 900 mbar to 1100 mbar with an accuracy of ± 5 mbar.

2. Optical diagnostics

(a) Concepts that are based on mature technologies to reduce long-term deployment risks.

(b) Concepts that are chemically compatible with materials ageing experiments.

(c) General chemical compatibility within this thesis focuses on minimal inclusion of organics and metals which may interact with oxygen and water (e.g. copper).

(d) Concepts with the potential to be long-term stable over multiple decades.

(e) Concepts that are interrogated from a distance (remote sensing) via optical fibres.

(f) Concepts that are physically small and robust. Threshold longest dimension < 160 mm; objective longest dimension < 20 mm.

(g) A technique to measure the *in situ* temperature at defined points within a system using FBG sensors.

(h) Temperature measurement capability from -20 °C to 70 °C wih an accuracy of ± 1 °C (1 K).

(i) A technique to measure the *in situ* barometric pressure.

(j) Barometric pressure measurement capability from 0 mbar to 1200 mbar wih an accuracy of ± 2 mbar to support both vacuum and atmospheric experiments.

(k) A technique to measure water vapour (H_2O) concentration compatible with the direct TDLAS interrogation method.

(l) H_2O detection capability from 40 ppm (by volume) to $100\,000$ ppm with a resolution of 40 ppm (from -54 °C to 44 °C dew point with an accuracy of ± 0.5 °C dew point, and from 0.1 %RH to 100 %RH with an accuracy of ± 1 %RH).

(m) A technique to measure gaseous oxygen (O_2) concentration.

(n) O_2 detection capability from 0 % to 25 % with a resolution of 0.1 %.

(o) A technique for supporting electronic diagnostic sensors remotely via optical fibres (OIES) that provide both power and data comunications.

(p) The OIES system should be compatible with near infrared (NIR) optical fibres (SMF-28 preferred).

(q) The OIES system should not pose a significant laser safety hazard (Class 2M or lower).

3. Fibre integration

(a) Concepts that are chemically compatible with materials ageing experiments.

(b) General chemical compatibility within this thesis focuses on minimal inclusion of organics and metals which may interact with oxygen and water (e.g. copper).

(c) Concepts with the potential to be long-term stable over multiple decades.

(d) Concepts that are physically small and robust. Threshold longest dimension $< 160\,\text{mm}$; objective longest dimension $< 20\,\text{mm}$.

(e) A technique to provide hermetic sealing around optical fibres entering an experimental system with a helium leak rate below $1 \times 10^{-9}\,\text{mbar}\,\text{l}\,\text{min}^{-1}$.

(f) A technique to enable optical fibre connections both outside and inside the experimental system.

(g) A technique to enable fibres to enter the sealed system.

(h) A technique to package the sensor technologies.

(i) A technique to encapsulate the optical fibres within an experimental volume.

(j) Components outside the experimental environment should be simple for a user to use and provide environmental sealing capabilities.

1.4 Thesis Structure

The work is presented over ten chapters that, after the introductions and an initial literature review (Chapter 2), separates the project into the three objective topics: interrogation, diagnostics, and integration. A conclusions chapter and two appendices complete the work. The content within these chapters is summarised below.

Interrogation hardware

Chapter 3 discusses the process of designing bespoke modular interrogation hardware for interrogating diagnostic sensors over optical fibres with a focus on redundancy and long-term maintenance. The design represents a novel solution for enabling multiple sensor technique interrogation within a modular enclosure, integrating optical fibre routing, and enabling stand-alone operation.

Chapter 4 provides an evaluation of miniature digital electronic sensors which were integrated into each of the interrogation modules. The sensors were intended to provide real-time condition monitoring data to assist in assessments of hardware health and maintenance requirements. An experimental evaluation was conducted to compare the sensor performance with the project requirements for temperature, barometric pressure, and humidity measurements.

Optical Diagnostics

Chapter 5 investigates optical temperature sensing techniques and selects FBGs for evaluation. The sensors are rapidly tested over the period of a year in a novel systematic study to provide confidence in their long-term performance.

Chapter 6 investigates optical barometric pressure sensors, selecting fibre Fabry-Pérot (FFP) based sensors for evaluation. These sensors are also rapidly tested over the period of a year within a novel experiment to provide confidence in their long-term performance.

Chapter 7 details gaseous chemical detection and quantification. TDLAS in the NIR was chosen for development and a bespoke multi-pass spectroscopic cell was designed and built for evaluation. The spectroscopic cell achieved a higher level of integration for optical fibre coupling and long-term stability than previously reported. A commercial off-the-shelf (COTS) oxygen chemical detection probe was also evaluated for long-term stability.

Chapter 8 discusses a technique developed for remotely powering and communicating with electronic sensors down a single optical fibre. The system was built and evaluated and then further developed into a higher-efficiency system. A second system was also constructed for evaluation. Both systems were created using COTS components and operated using single mode (SM) NIR optical fibres.

Fibre integration and conclusions

Chapter 9 provides details on techniques developed to enable integration of the optically interrogated diagnostics into an experiment. The techniques included investigation of hermetic optical fibre feed-throughs, optical fibre routing and ruggedisation, sensor housing, and multi-fibre umbilical connectors. Information regarding the assembly of a complex experimental configuration is also provided, using the techniques investigated.

Chapter 10 discusses the work conducted within the project and draws conclusions and suggestions for areas of further development, many of which are in progress at the time of writing.

Appendix A provides a reference guide for the technology readiness level (TRL) system, which is used in an assessment of an individual technologies *readiness* for deployment.

Appendix B provides simulated gas absorption spectra which were generated using the high resolution transmission (HITRAN) database. The specra were used as a reference

for designing NIR gas absorption configurations.

Chapter 2: Literature Survey

A literature survey was conducted of commercial products and scientifically proven techniques that may satisfy the project requirements for this thesis. As per the project objectives and specification, detailed in Chapter 1, the review included optical diagnostic techniques for temperature, pressure gaseous chemical detection, interrogation hardware, electronic sensor technologies, optically powered electronic systems, and optical fibre infrastructure components. Some technologies were pre-selected for this work by the Atomic Weapons Establishment (AWE), as noted in Chapter 1. The review was conducted to provide confidence an alternative technique did not exist with significant advantages.

2.1 Temperature Sensing

The project required, as discussed in Chapter 1, a technique for temperature sensing within a materials ageing experiment. The technique was required to be optical fibre based, chemically compatible with the experiment, suitable for long-term use, and enable temperature measurement from $-20\,^{\circ}\text{C}$ to $70\,^{\circ}\text{C}$ with an accuracy of $\pm 1\,^{\circ}\text{C}$.

Temperature measurement is commonly achieved in industry using thermocouples, which are electronic sensors constructed from a bi-metallic junction, utilising the Seebeck effect [8]. Other electronic techniques are also widely used, as discussed further in Chapter 4, but optical techniques are typically reserved for more specialist applications likely due to the typically higher cost. Optical temperature sensing has been demonstrated using reflection, interference, fluorescence, scattering, absorption spectroscopy, and thermally generated radiation techniques [9, 10]. Techniques based on reflection, interference, fluorescence, and scattering were reviewed for their suitability to this thesis.

Absorption spectroscopy has been demonstrated to provide temperature information from the gas being measured through analysis of the absorption peak profile [10–12], but this technique was discounted from the survey. The techniques accuracy is dependant on the gaseous species and concentration being measured, but since the exact chemicals

present within an experiment will vary depending on the exact configuration, a more general technique was desired. Thermally generated radiation techniques are based on measuring the black-body emission from a sensor probe. They were not reviewed since they are inherently limited in their low-temperature use and typically cannot measure temperatures below $100\,°C$ [9].

Fibre Bragg grating (FBG)

The fibre Bragg grating (FBG) is a common and commercially available optical component that uses an optical reflection, from a Bragg grating formed within an optical fibre, to relay information about the sensor's environment [13]. A temperature sensor can be formed by isolating the sensor from other sources of measurement, such as mechanical strain, resulting in a sensor that will reflect light at a temperature-varying wavelength [14]. Previous work at AWE using FBG sensors meant they were preferred as the optical temperature sensor for this work [15].

The FBG is formed from a length of periodic refractive index variation, within the fibre core, which reflects light at the Bragg wavelength, λ_B [16]. The FBG structure and optical characteristics are discussed further in Chapter 5. FBGs are sensitive to mechanical strain, as well as temperature. This cross-sensitivity usually requires FBG temperature sensors to be housed in strain-isolating enclosures, ensuring the only external influence on the sensor is temperature. A number of enclosure designs have been reported [7, 14, 17] and are also available from commercial suppliers [18], but these enclosures result in sensors physically larger than desired in this thesis ($> 30\,$mm length).

Commercial FBGs are available from a number of manufacturers, such as Micron Optics (USA), FBGS (Belgium), Advanced Optical Solutions (Germany), Technica Optical Components (USA), and FemtoFiberTec (Germany). FBG temperature sensors are often specified with accuracies in the range of $\pm 1\,°C$ [19], but the interrogation system has a significant impact on the measurement uncertainty achieved. Commercial interrogators with wavelength accuracies in the range of $\pm 1\,$pm to $\pm 5\,$pm are available [20, 21]. Using typical sensor responsitivities in the range of $10\,\text{pm}\,°C^{-1}$ to $29\,\text{pm}\,°C^{-1}$ [19, 22], suggests interrogation accuracies between $\pm 0.03\,°C$ to $\pm 0.5\,°C$ would be possible. It has been shown however that the response is not linear and could deviate by $20\,$pm over the range $-30\,°C$ to $80\,°C$ [23], so sensor characterisation is typically required. FBG sensing has been widely demonstrated in literature [7, 13, 14,

17, 23–52], over multiple decades, suggesting it is a well matured technique.

FBGs have been demonstrated to operate over the required temperature range, and likely to perform within the accuracy requirements. They were considered a mature and well understood technique, but studies of long-term drift or failure mode characteristics were not found. Since the sensor is formed within fused-silica optical fibres, the chemical compatibility will depend of the fibre coatings and strain-isolation enclosure used.

Fibre Fabry-Pérot (FFP)

An alternative temperature sensing technique, utilising optical interferometry, has been demonstrated. A Fabry-Pérot cavity can be created within, or at the end of, an optical fibre [53], defined by a pair of partially reflecting surfaces. The interferometer is characterised by an approximately sinusoidal transfer function [54]; of the form:

$$I = I_0 \bar{R} \left(1 + V \cos \phi\right), \tag{2.1}$$

where I is the output signal intensity, I_0 is the input signal intensity, $\bar{R}$ is the mean mirror reflectivity, and V is the interferometer visibility [55]. The interferometer phase, ϕ, can be expressed as:

$$\phi = \frac{4\pi n}{\lambda} L, \tag{2.2}$$

where n is the refractive index within the cavity, λ is the interrogation wavelength and L is the cavity length [54, 56]. Changes in temperature can change the cavity length and/or the refractive index, and thus the phase to wavelength relationship of the sensor [57–62]. This relationship is typically measured as a change in free spectral range (FSR), the spacing between adjacent interference peaks in the measured spectrum.

Commercially available sensors utilising this technique are available from FISO (Canada) [63], and OpSens (Canada) [64]. The sensors are specified for use between $-40\,$°C and $225\,$°C with an accuracy of $\pm 1\,$°C, and $-40\,$°C and $250\,$°C with an accuracy of $\pm 1\,$°C respectively. The specified performance of the sensors met the requirements for this project, and the sensors were coupled to multi-mode (MM) optical fibres. However, the maximum fibre lengths specified are $15\,$m [63] and $5\,$m [64], likely due to inter-modal and coherence length effects, which would significantly restrict the separation distance between the interrogation hardware and experiment. Further investigation would

be required to assess the use of such sensors over longer distances, to ensure flexibility within the the ageing experiment design.

Wang *et al.* [59] demonstrate an air-gap fibre Fabry-Pérot (FFP) temperature sensor where the end of the optical fibre is held within a capillary tube, spaced apart from another section of optical fibre, as shown in figure 2.1. The reflections from the cleaved

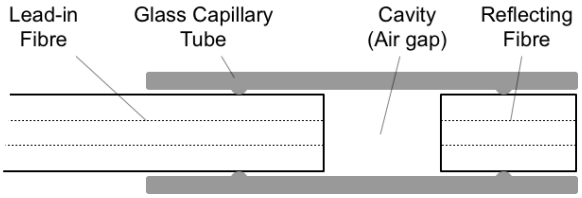

Figure 2.1: Air-gap FFP temperature sensor formed using a short section of optical fibre as a reflector, as demonstrated by Wang *et al.* [59].

surfaces and refractive-index contrast creates the low-finesse FFP. This same sensor is also reported to have a significant pressure response, so the temperature sensor is encased in an isolation tube to remove cross-sensitivity. Temperatures up to $200\,^{\circ}\mathrm{C}$ are demonstrated with a resolution of $0.02\,^{\circ}\mathrm{C}$. The temperature range and resolution would satisfy the requirements for this project, but tube-based design and need for isolation could make this sensor physically large, limiting its deployment within an assembly. Kilpatrick *et al.* [57] demonstrate a dual FFP temperature sensor which uses a zinc selenide (ZnSe) layer between two mirror coatings fixed to the end of a single-mode optical fibre. ZnSe is utilised because its thermo-optic coefficient is an order of magnitude greater than fused-silica's thereby increasing the sensitivity of the device. The sensor was demonstrated over a measurement range of 20 to $180\,^{\circ}\mathrm{C}$ with a measurement accuracy of approximately $0.1\,^{\circ}\mathrm{C}$, which would also satisfy the requirements of this project. The combination of multiple materials used to form the Fabry-Pérot cavity might need to be evaluated for material compatibility and sensor lifetime requirements. Schneller *et al.* [60] demonstrate an FFP temperature sensor utilising a Chromium layer as a partial reflector, fusion spliced within the sensor head. This technique reports a sensor with resulting high tensile strength, small size and an maximum operating temperature of $1000\,^{\circ}\mathrm{C}$, but their implementation has a lower resolution, $< 10\,^{\circ}\mathrm{C}$, meaning further work would be required if such a sensor were to meet this project's requirements. A multi-day high temperature study of similarly constructed sensors has been demonstrated by Polyzos *et al.* [62], which reports no drift once the sensor has been annealed. Bae *et al.* [61] demonstrate a dual FFP sensor for pressure and temperature measurements. A polymer cavity is attached to a silica fibre for the temperature measurement, which utilises the large

coefficient of thermal expansion (CTE) of the polymer to provide temperature sensitivity. The technique was evaluated from $26\,°C$ to $50\,°C$ and was demonstrated to achieve a measurement uncertainty of $0.03\,°C$ [61]. The temperature range demonstrated was not sufficient to meet the requirements, but the measurement uncertainty was sufficiently low. The long-term stability of the polymer material, and its chemical compatibility, mean this approach is unacceptable for this thesis.

Temperature FFP sensors are commercially available and have also been demonstrated, achieving measurement accuracies suitable for use within this project. The specified sensing range of the commercial sensors satisfied the project requirement, but the devices presented in the literature were evaluated from $60\,°C$ to $200\,°C$ [59], $20\,°C$ to $180\,°C$ [57], $25\,°C$ to $1000\,°C$ [60], and $26\,°C$ to $50\,°C$ [61], not the required range of $-20\,°C$ to $70\,°C$ for this project. The multiple materials typically used within the sensor design were not ideal, meaning the sensors would require material compatibility studies, as well as long-term assessments, before being considered.

Luminescence

Luminescent probes have been demonstrated as temperature sensors, and are reviewed extensively by Wang *et al.* [65]. A broad range of photoluminescent chemicals have been demonstrated as being suitable for measuring temperature, and typically operate by illuminating the material and measuring the longer-wavelength emission properties. Further details of measurement techniques is included in Chapter 7, in a discussion on fluorescence sensing. When fluorescent materials absorb photons, lower energy photons can be emitted through multiple electron de-excitation routes [66, 67]. Measurement and analysis of the emitted light can be used as an indication of material properties, such as temperature.

Typically a photoluminescent chemical is located at the end of an optical fibre. Both the illuminating and emitted light are contained within the optical fibre, which is connected to an interrogator. Some chemicals, such as the florescent $Yb_2Ti_2O_7$ [68] and $Eu(TTA)_3^a$ in PMMA [69] have been shown to meet the project requirement for temperature measurement range and accuracy, with resolutions reported of $0.08\,°C$ [69]. Chromium(III)-doped yttrium aluminium borate (Cr3+:YAB), is demonstrated by Venturini *et al.* [70] to operate over the range: $0\,°C$ to $200\,°C$ achieving a resolution of $0.1\,°C$. This technique is reported to have a fast response and high stability when

compared to alternative phosphors. It is also reported to have no cross-sensitivity with oxygen which is a common cross-sensitivity for luminescent sensors [70].

(Photo)luminescent temperature sensors have been demonstrated with the potential to satisfy the sensing range and accuracy requirements. For use within this project, the chemical compatibility and potential decomposition of the analyte, especially if organic-based, would need to be assessed.

Distributed sensing

Distributed optical fibre sensing, typically refers to scattering based sensing, which is often demonstrated to measure temperature and strain [51,71–82]. The technique provides values at all points along a fibre, thus the term *distributed*, and is often performed in unmodified fused silica fibres or high-scatter speciality fibres. The most common techniques measure the backscatter signal, which returns down the fibre to the light source. The most common scattering sensing techniques, Rayleigh, Raman, and Brillouin, have been demonstrated measuring temperature, strain, pressure, radiation dose, radiation flux, light, electro-magnetic fields, and vibration [81–84].

Koyamada *et al.* [75] demonstrate Rayleigh-based temperature sensing using a coherent optical time-domain reflectometry (OTDR) technique to record the measurements. The technique is evaluated over an $8\,\text{km}$ length of sensing fibre, constructed from unmodified single-mode fibre, with a temperature resolution of $0.01\,^{\circ}\text{C}$ and spatial resolution of $1\,\text{m}$. The temperature range evaluated ($24.9\,^{\circ}\text{C}$ to $25.0\,^{\circ}\text{C}$) was significantly smaller than the required sensing range, but the low spatial resolution would require potentially bulky coils of fibre to be included within an experimental configuration to provide point-localised temperature measurements; likely not meeting the requirement for small size.

Commercial distributed temperature sensing systems are available, such as the ODiSI 6000 Series from Luna (USA) [85] which specifies a measurement range of $-40\,^{\circ}\text{C}$ to $200\,^{\circ}\text{C}$ with a resolution of $0.1\,^{\circ}\text{C}$. The system measures the Rayleigh backscatter using an optically frequency-domain reflectometry (OFDR) [34,72] and achieves a spatial resolution of $1.3\,\text{mm}$ in a fibre up to $50\,\text{m}$ long. The specification for sensing range and resolution, suggest the system could satisfy the project sensing requirements.

Distributed sensing based on Rayleigh scattering was suggested likely to satisfy the project sensing requirements, based on the provided measurement range and resolution

values. The technique can utilise unmodified fused-silica optical fibres, resulting in chemical compatibility being dependant on the fibre coating. The long-term stability of the system was suggested to be high [85], since the fibre contained no sensor structure as such, but a long-term evaluation was not identified.

Conclusions

The review of optical temperature sensors investigated FBG, FFP, luminescent, and distributed (backscatter) techniques. A summary of the assessed likelihood of each technique to satisfy the project requirements is shown in table 2.1.

Sensor technology	Measurement range	Measurement accuracy	Chemical compatibility	Long-term stability
FBG	✓	✓	✓	?
FFP	✓	✓	?	?
Luminescent	✓	✓	?	?
Distributed	✓	✓	✓	?

Table 2.1: Summary of the assessed optical temperature sensing techniques against the project requirements.

FBG sensors and distributed (Rayleigh) sensing were assessed as most likely to be suitable for use within a future long-term materials ageing experiment. The long-term stability of each technique was unknown, but the distributed technique was potentially more stable, since there was no grating structure to change over time. However, FBG sensors were considered to be a more mature technology, and supported by greater availability, and lower technical complexity, of commercial interrogators. The recommended optical temperature sensing technique for development was therefore FBG based. If, after assessment, it was deemed unsuitable for use, future work was recommended to investigate the potential of the distributed techniques. Controlled long-term analysis of FBG sensors was not identified within the literature, so a novel study of the stability of FBG temperature sensors was recommended, and detailed in Chapter 5.

FBG sensors are commercially available for measuring many parameters such as temperature and strain from a number of manufacturers [19, 22, 86]. Studies, applications, and novel sensing configurations utilising FBGs have been widely reported in literature [13,14,23–52], demonstrating it to be a reliable, versatile, and well researched technique.

Some of the published work has discussed the use of such sensors over long time-frames and some application studies report on multi-year deployments of FBG

sensors [42, 62]. However, no controlled study has been published which evaluates the sensor performance for long-term deployments.

2.2 Barometric Pressure Sensing

In addition to a technique for temperature sensing, the project required, as discussed in Chapter 1, a technique suitable for pressure sensing within a materials ageing experiment. Barometric (atmospheric) pressure was required over the range 0 mbar to 1200 mbar with an accuracy of ± 2 mbar. As with the temperature sensors, the pressure sensors were required to be optically fibre based, chemically compatible, and long-term stable.

Industrial barometric pressure measurements are typically achieved using electronic resistance or capacitance transducers, as discussed later in this chapter. This survey concentrated on optical techniques and both FBG and FFP based sensors are demonstrated for use as pressure sensors [87], and are reviewed here. Use of absorption spectroscopy to measure gas pressure has been previously demonstrated [88, 89], using a similar method as with absorption gas sensing, but the technique was not reviewed in this work since a gaseous chemical independent technique was considered preferable.

Fibre Fabry-Pérot (FFP)

FFP pressure sensors are typically constructed with an extrinsic cavity mounted on the end of a fibre. A thin diaphragm typically acts as one of the cavity mirrors, and deflects as the pressure difference between the cavity and environment varies, changing the cavity length. This length change can be detected as a change in interferometer FSR, previously described. FFP devices are commercially available from companies such as FISO Technologies (Canada) and OpSens Solutions (Canada). FISO devices are available with stated operating ranges from 0 mbar to 340 mbar, with an accuracy of ± 2 mbar (also available with higher pressure ranges, but with lower accuracies) [90]. OpSens devices are available with operating ranges from 0 mbar to 1720 mbar, with an accuracy of ± 9 mbar [91]. These commercial options suggest the technique has the potential to perform within the required measurement range, but the accuracy requirement may not be satisfied. Following the commercial product search, a study of published literature was performed, and a range of work has been reported [55, 56, 92–96], and are discussed below:

Watson *et al.* [92] report a sensor that measures up to 8 bar with resolutions down to

3 mbar. This work focused on a short response time rather than high sensitivity, achieving a rise time $< 4\,\mu s$. Wang *et al.* [93] demonstrate a high pressure sensor capable of operating up to 550 bar with an accuracy of ± 24 bar. Chavko *et al.* [94] demonstrate a FFP sensor response from vacuum to 520 mbar that is highly linear. MacPherson *et al.* [56] present a FFP sensor constructed with an extrinsic copper diaphragm attached with adhesive. The sensor is demonstrated from vacuum to 4 bar and reports a sensitivity of 5 mbar. The measurement range demonstrated would satisfy the project requirement, but the accuracy achieved was not stated. The use of an adhesive to secure the diaphragm would need to be evaluated for long-term reliability and chemical compatibility. Cibula *et al.* [96] report an all glass FFP pressure sensor which is tested from vacuum up to 70 bar, with a cavity length response of $1100\,\text{nm bar}^{-1}$. This was predicted to provide a phase sensitivity of $8.9\,\text{rad bar}^{-1}$, which, with a 10 mrad resolution interrogation system, would equate to a pressure resolution of 1.1 mbar. This sensor design, constructed entirely from fused-silica, could enable a chemically compatible pressure sensing technique. The measurement range demonstrated would satisfy the range required, and if a suitable interrogator was used would potentially satisfy the accuracy requirement.

FFP pressure sensors were reviewed and both commercial and literature sources were identified. The technique appeared moderately mature, and had been demonstrated multiple times up to higher pressures than required in this project. Temperature cross-sensitivity of the presented FFP sensors were not reported, but due to the dependency on physical distance a cross-sensitivity was considered likely. In an experimental configuration it would therefore likely be required to co-locate an optical temperature sensor alongside a FFP to provide temperature compensation. The measurement range and accuracy were not demonstrated to satisfy the project requirement simultaneously, and neither was the long-term stability of the technique known.

Fibre Bragg grating (FBG)

FBG sensors have been demonstrated to measure physical strains [44, 46, 97], but in a novel study Maier *et al.* [98] demonstrate a barometric pressure sensor utilising two orthogonally arranged FBG strain sensors. A mechanical arrangement forms a bellows-based barometer that transfers and amplifies a strain to one of the FBG sensors in response to pressure changes. The second FBG sensor is included to enable temperature compensation due to the inherent temperature cross-sensitivity when using FBGs. The

reported technique had an operation range from 800 mbar to 1100 mbar with an accuracy of ± 1.5 mbar.

The accuracy demonstrated would satisfy the requirement for this project, but the measurement range was too small. It could be conceivable to increase the measurement range by altering the physical configuration of the system, but the use of mechanical bellows would likely introduce a fundamental limit on the minimum pressure measurable. The moving mechanical parts, including a compression spring, would be a cause of concern to meet the desired life-time for use within this research project. Due to the mechanical design, the technique was also physically large, with a length of 70 mm, which was not ideal for in situ measurements. The chemical compatibility of the technique would also require review, given the number of components used and the potential for lubricants to be required.

Conclusions

The review of optical pressure sensors investigated FFP and FBG techniques. A summary of the assessed likelihood of each technique to satisfy the project requirements is shown in table 2.2.

Sensor technology	Measurement range	Measurement accuracy	Chemical compatibility	Long-term stability
FFP	✓	?	(✓)	?
FBG	×	✓	?	×

Table 2.2: Summary of the assessed optical pressure sensing techniques against the project requirements.

Of the two optical techniques discussed, the FFP method was considered the more mature and most likely to satisfy the project requirements. Experimental evaluation was recommended to confirm the long-term performance of the technique.

Figure 2.2 shows a schematic of the type of sensor construction used in this work [4, 56, 90]. This sensor is attached to the end of a length of optical fibre and is composed of a low-finesse Fabry-Pérot interferometer, with the cavity formed between the fibre end and the diaphragm. The cavity length changes as the diaphragm moves in response to the barometric pressure in the sensor environment, relative to the vacuum within the cavity.

Optical fibre based sensors have previously been evaluated for long-term use [62] including real-time deployments [42], but these previous studies were using significantly different configurations of optical fibre sensors than the one used in this work. Polyzos *et*

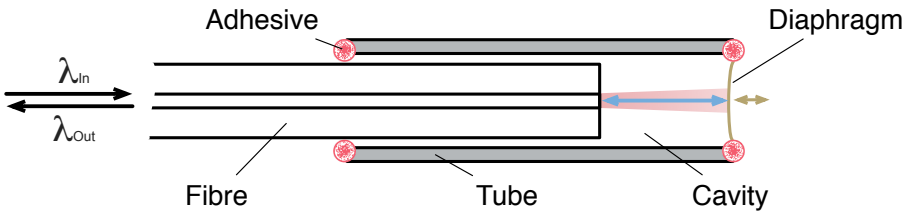

Figure 2.2: Schematic of a fibre Fabry-Pérot barometric pressure sensor, not to scale. The fibre has a diameter of 125 µm and the cavity length is typically 16 µm to 18 µm.

al. evaluate Fabry-Pérot temperature sensors, with a solid silica glass cavity, and Chan *et al.* evaluate FBG sensors deployed in-situ on a suspension bridge. The lack of a study of the long-term performance of Fabry-Pérot pressure sensors motivated this experimental evaluation. This study and results were presented at the 26th international conference on optical fibre sensors (OFS-26), Lausanne, by the author [4].

2.3 Gaseous Chemical Detection

The project required a technique to measure H_2O and O_2 concentration within the internal environment of a materials ageing experiment, as discussed in Chapter 1. The techniques were required to support the use of optical fibres between the interrogation hardware and the experiment, be long-term stable, and chemically compatible with the chemistry within the experiment. Detection of H_2O was required from 40 ppm to 100 000 ppm with a resolution of 40 ppm. O_2 detection was required from 0 % to 25 % with a resolution of 0.1 %. These resolutions were also stated as a being satisfied by an interrogation system with a minimum detectable absorption of 1×10^{-3} $Hz^{-1/2}$.

The optical detection of gaseous chemicals can be achieved in multiple ways, but one of the most common is absorption spectroscopy [99]. Absorption spectroscopy does not chemically alter, consume, or adsorb the gas during measurement, which is ideal for a long-term *in situ* technique. Over a multi-decade experiment, even low levels of gas consumption or reaction from a sensor could contribute to a significant perturbation in the resulting environment. This survey focuses on the techniques for performing absorption spectroscopy in order to recommend the most likely technique to satisfy the project requirements.

Absorption spectroscopy is an optical technique which can be used to both identify and measure the concentration of chemicals. The measurement of gas absorption lines has been demonstrated in the ultraviolet (UV), visible, near infrared (NIR) and mid-infrared (MIR) [99]. Optical arrangements for the UV are more complex than those for

the visible and NIR since typical silica glasses are absorbent in the UV. MIR optical fibre components, while available, are again more specialist, less mature, and more costly when compared to those in the NIR. For use within this project, a technique operating over NIR was investigated, in order to enable integration within the materials ageing experiment and compatibility with the interrogation hardware (Chapter 3).

Techniques suitable for performing absorption spectroscopy in the NIR were surveyed and two of the most common, tunable diode-laser absorption spectroscopy (TDLAS) and cavity ring-down (CRD) spectroscopy [99], were reviewed. The direct absorption variant of TDLAS was preferred by AWE over the wavelength modulation spectroscopy (WMS) variant, due to the significantly simplier analysis techniques, but at the cost of additional required path-length within the experimental configuration [100].

Each technique was summarised, and the requirements for deployment within materials ageing experiments were discussed, to enable an assessment for suitability in satisfying the project requirements.

Tunable diode-laser absorption spectroscopy (TDLAS)

TDLAS is a technique for recording the optical transmission spectrum, through a gas of interest, over a narrow wavelength range, typically less than 1 nm. The wavelength is chosen specifically to coincide with absorption lines of the gas to be measured, and typically one or more are resolved. As a spectrum is recorded, the absorption line-shape can be assessed, as well as peak height and area; which can prove useful during result analysis [15].

Demonstrated wavelengths and chemicals detected with the technique were discussed earlier within this chapter, in table 2.4, alongside a description of typical interrogation techniques. Gas was measured using a direct path from source to detector (or between a launch and collection lens) [10, 101–103], or using a multi-pass cell [104–107]. The use of a multi-pass cell enables an optical gas interaction path length longer than the length of the cell [99], in some cases just two passes are used [104, 107], and in others many more [106]. For a given interrogation configuration, the longer the path length, the greater the measurement sensitivity that is achievable, which is especially advantageous when detecting trace concentrations. Satisfying the project requirements for chemical measurement ranges and resolutions would depend on the path length used, and the technique has been demonstrated with path lengths from cm to km [99]. The impact

of path length on the gas concentration measurement including saturation, and multi-pass cell designs, are discussed further in Chapter 7.

The use of NIR optical fibres within the interrogation hardware of the TDLAS configurations has been demonstrated with detection limits reported down to $2.82 \times 10^{-3}\,\mathrm{Hz}^{-1/2}$ [10, 102, 105], suggesting the technique was likely to satisfy the fibre compatibility and $1 \times 10^{-3}\,\mathrm{Hz}^{-1/2}$ detection limit requirements, following further development.

Cavity ring-down (CRD) spectroscopy

CRD spectroscopy detects the presence of gas by measuring the optical decay time of a resonant high-finesse cavity (cell). Optical loss, or absorption, within the cavity reduces the decay time, and is detected. The technique was demonstrated in 1988 [108] and has been subsequently developed, incorporating a number of detection techniques, including continuous wave, pulsed, and phase-shift [99, 109–113].

The technique is demonstrated with mirror separations from cm to m, but due to the high-finesse design, the equivalent path length can be many km. The detection of oxygen [108] and water vapour [112, 113] is presented. Optical fibre based techniques have presented utilising evanescent wave cavity ring down spectroscopy [114,115], where a ring-cavity is formed using the optical fibre, with an input and output coupler and a tapered region of fibre. In the tapered region the evanescent wave of the propagating light can interact with the surrounding gas, providing the sensing element [114].

CRD spectroscopy may not be well suited to use within a long-term experiment and within a sealed system, since particulate contamination, either to mirrors or tapered fibre surfaces, could be envisioned. During the experiment such an effect could reduce the cavity finesse, which would result in a reduction in cavity decay time and could be incorrectly interpreted as an increase in gas concentration, or decrease the evanescent field interaction with the environment resulting in interpretation as a decrease in gas concentration. Reductions in finesse could also be caused by a change in optical alignment, or reduction in mirror reflectivity [99].

Conclusions

A survey of optical gas sensing techniques was conducted and TDLAS and CRD spectroscopy were reviewed. Based on work demonstrated in the literature, TDLAS was

likely to satisfy the requirements for NIR optical fibre compatibility, and measurement ranges and resolutions. The measurement range and resolution of the technique was largely dependant on path length, but the technique has been demonstrated using lengths spanning four orders of magnitude, suggesting a suitable length could be selected. The ability of the technique to resolve the absorption line-shape was considered advantageous for long-term use, since it could provide additional measurement parameters, and therefore confidence in the results. CRD spectroscopy was reviewed and has been demonstrated to enable measurement of both O_2 and H_2O. The use of a high-finesse optical cell was considered disadvantageous for use within this project, since variations in optical alignment and mirror reflectivity could be anticipated within an experiment lasting multiple decades.

Based on this review, TDLAS was recommended for further development since it was considered likely to satisfy the project requirements and yield high confidence results. The technique has been demonstrated incorporating optical fibres, but this thesis required a higher level of integration than previously presented, as detailed in Chapter 7.

2.4 Interrogation Hardware

The search for interrogation hardware and measurement techniques was separated into three parts: an integrated hardware system, FBG measurement, and TDLAS interrogation. The optically isolated electronic sensors (OIES) system review is included later within this chapter.

Integrated hardware system

The project required a sensor interrogation solution which would enable the measurement of FBGs, OIESs, and the ability to support TDLAS, within a single device, with confidence it could remain operational over the multi-decade duration with minimal down-time.

A search was conducted for commercial diagnostic systems designed to measure multiple types of sensor, intended for use in material ageing experiments, or for long-term *in situ* chemical analysis. No systems were found, since the preference among manufacturers appeared to be delivering specialised solutions. The most modular system that was found was the PRO8 platform from Thorlabs (USA) [116], which is a modular system able to support distributed feedback (DFB) lasers, optical fibre switches, and

the electronics to control constant current (CC) lasers with thermo-electric coolers (TECs) and amplify photodiode currents. As a modular system it offered flexibility in configuration, and a clear maintenance strategy; substitute replacement modules into the system to maintain uptime. However, the limited range of available modules would not enable FBG or OIES interrogation, and supply of replacement modules over the required experimental duration was unknown. The PRO8 system would also require additional electronic components, such as signal generators, and fibre routing, to create an experimental system, resulting in a non-integrated system and complex maintenance.

It was accepted that no commercial solution would enable OIES interrogation, due to its bespoke design, but the lack of a suitable system for FBG and TDLAS resulted in the recommendation to develop an in-house interrogation hardware solution. The use of modules was considered an advantageous feature of the PRO8 design, and it was noted that internal fibre routing would be beneficial.

Fibre Bragg grating (FBG) interrogation

Interrogators for FBG sensors are available from a number of commercial manufacturers, and a range of devices is shown in table 2.3. To satisfy the project temperature sensing accuracy requirement of $\pm 1\,°C$, an interrogator accuracy of approximately $\pm 10\,pm$ is required [19]. The values are based on the available product specifications, and the

Manufacturer	Model	Wavelength	Resolution	Accuracy
Ibsen Photonics	I-MON 256 [117]	1525 - 1570 nm	0.5 pm	±5 pm
Prime Photonics	VectorLight 300 [118]	1510 - 1590 nm	0.5 pm	±1 pm
Micron Optics	SM125 [21]			
Smart Fibres	W4 [119]			
Micron Optics	SI155 [120]	1510 - 1590 nm	2 pm	±1 pm
Smart Fibres	SmartScan [20]	1528 - 1568 nm	0.4 pm	±1 pm
Smart Fibres	SmartScope [121]	1528 - 1568 nm	0.2 pm	±2 pm

Table 2.3: Typical performance of commercially available FBG sensor interrogation systems, specifying their wavelength scan range and FBG measurement resolution and accuracy.

interrogators are intended for FBG sensors in the region of $1550\,nm$ which was the preferred operating range for AWE based on previous work [15].

The Ibsen Photonics (Denmark) I-MON 256 [117] is an optical spectrum analyser (OSA) intended for use in one of the two most common interrogation methods, which consists of: a broadband source, such as a superluminescent light emitting diode (SLED), which is used to illuminate the fibre containing the FBG under interrogation. The reflected

light returns down the optical fibre and is diverted to a OSA for analysis using an optical fibre circulator or directional coupler. The I-MON 256 is a dispersive spectrometer which features a 256-pixel indium gallium arsenide (InGaAs) line-camera and a diffraction grating. This interrogation method is resolution limited by the OSA system used, and wavelength range limited by the SLED source. The Micron Optics (USA) SM125, also sold under a few other names [21,118,119], uses the second method: a swept laser is used to illuminate the FBG, constructed from a tunable Fabry-Pérot filter and a semiconductor optical amplifier (SOA) [122]. The reflected light is again diverted but measured using a photodiode. The resolution of this technique is limited by the control electronics and Fabry-Pérot filter, and the tuning range is limited by the bandwidth of the SOA. When using either technique peak fitting techniques can be applied to increase the measurement resolution achievable. For instance, the I-MON 256 [117] has a detector pixel spacing corresponding to approximately $180\,\text{pm}$, yet its stated resolution is $\pm 0.5\,\text{pm}$ suggesting use of an internal peak fitting algorithm using intensity values from a number of pixels.

A wide wavelength range enables multiple FBGs to be measured on a single optical fibre, via wavelength-division multiplexing (WDM). This can reduce the number of optical fibres required, and reduces the need to use optical fibre switches. Alternative multiplexing techniques have been demonstrated, such as those utilising time and phase demodulating detection systems [36, 123]. These techniques are improvements to the two common interrogation schemes, and such improvements can produce higher accuracy measurements. The accuracies specified by the commercial equipment were considered within the project requirements, as discussed later in this chapter. Therefore it was recommended to investigate development of FBG interrogation based on the two most-common techniques.

Tunable diode-laser absorption spectroscopy (TDLAS)

TDLAS is a technique often used for gaseous chemical detection in the NIR [99, 124] and based on previous work at AWE was the selected gas measurement technique [15]. The technique uses a tunable diode laser in conjuction with a photodiode to measure one or more molecule-specific absorption lines, to provide chemical speciation (identification) and concentration measurements. More details on absorption spectroscopy is included in Chapter 7.

Commercial products utilising the TDLAS technique are available [125], and details

on the typical hardware configurations are readily available in the literature [10, 101–106]. The most common configuration uses a DFB laser whose light is passed through the environment of interest. The light is then collected and measured with a photodiode for analysis. The laser wavelength is chosen to align with absorption line(s) targeted for the gas of interest, typically requiring a laser for each gas of interest, but dual-gas measurements have been demonstrated [106]. The laser wavelength is modulated to tune over an absorption line, typically by varying the drive current to the DFB using a sawtooth, or more complex, waveform. Techniques have been demonstrated where additional higher-frequency modulation, typically sinusoidal, is superimposed on the sawtooth. WMS enables a reduction in measurement system noise, and therefore higher sensitivity measurements [101–103]. The disadvantage of the technique is increased complexity in the driving of the DFB and in the demodulation of the photodiode signal, which is typically achieved using a lock-in amplifier [102]. The use of WMS was not considered desirable within this thesis due to the increased demodulation and analysis complexity. For repeated gas measurements in an industrial setting, the verification of the analysis software is an important but time-consuming task. As a result, it was chosen to focus on demonstrating direct TDLAS before potentially investigating the WMS variant in the future [100], even though longer optical path-lengths would subsequently be required in the experimental system for the same measurement sensitivity.

A summary of presented TDLAS systems, which were performed using DFB lasers, is shown in table 2.4 detailing typical gasses and wavelengths used with this technique.

Ref	Gas	Wavelength
Seidel *et al.* [104]	H_2O	1370 nm
Zhang *et al.* [10]	H_2O	1395 nm
Knox *et al.* [105]	H_2O, CH_4	1358 nm, 2004 nm
Pogàny *et al.* [106]	H_2O, CO_2	2700 nm
Sur *et al.* [101]	H_2O, CO_2, CH_4, CO	1350 nm, 2020 nm, 2290 nm, 2330 nm
Chighine *et al.* [102]	CO_2	1997.2 nm
Li *et al.* [103]	CH_4	1654 nm

Table 2.4: Gases and wavelengths where TDLAS is demonstrated in the reviewed literature.

Seidel *et al.* [104] demonstrate a TDLAS configuration using a 1.98 meter path-length, a 1370 nm DFB laser tuned across an H_2O absorption line at 5039.8 Hz. Zhang *et al.* [10] present H_2O measurement using a 1395.6 nm DFB laser, tuned across two absorption lines at 1 Hz and an optical path-length up to 0.6 meter. Knox *et al.* [105] demonstrate both H_2O and CH_4 detection at 1358 nm and 2004 nm respectively. A path-length of

0.69 m was used to achieve a minimum detectable absorption of 2.82×10^{-3} $Hz^{-1/2}$. Pogàny *et al.* [106] present H_2O and CO_2 detection using a 76 m path-length achieving a minimum detectable absorption of 2.82×10^{-3} $Hz^{-1/2}$ operating at 2700 nm. Sur *et al.* [101] demonstrate the detection of H_2O, CO_2, CH_4, and CO using DFBs at 1350 nm, 2020 nm, 2290 nm, and 2330 nm. The WMS variant of TDLAS was utilised using an 0.08 m path-length. No minimum absorption was stated, but the short path-length was likely achievable due to the use of WMS. Chighine *et al.* [102] presents a WMS technique utilising an field-programmable gate array (FPGA) demodulation scheme for CO_2 detection using a 1997.2 nm DFB laser. A 5 Hz ramp modulation signal with superimposed 50 kHz sine wave is used with a 0.055 m path-length. No minimum absorption was reported. Li *et al.* [103] report a technique for CH_4 detection using a 1654 nm DFB and a path length of 0.4 m to achieve a detection limit of 29.52 ppm.

The reported use of TDLAS for the detection of multiple gaseous species at wavelengths compatible with NIR optical fibres, supporting such detection within this work. H_2O detection was demonstrated using FBG lasers at 1350 nm [101], 1358 nm [105], 1370 nm [104], 1395 nm [10], and 2700 nm [106].

Alternative tunable laser sources have been demonstrated, such as distributed Bragg reflectors (DBRs), vertical cavity surface-emitting lasers (VCSELs) and external cavity lasers (ECLs) [126]. For example, Chen *et al.* [107] demonstrate O_2 WMS using a VCSEL operating at 763 nm. However, DFB laser diodes are commercially available covering a wide range of the NIR, and operation in the NIR is advantageous since telecommunications technology can be leveraged, such as optical fibres, detectors, lasers, and optical switches. TDLAS has been demonstrated in systems using optical fibres and components such as optical switches and couplers [10, 101, 105].

From this review, a TDLAS system would require the interrogation hardware to support a tunable laser, such as a DFB, which can be modulated using either a sawtooth wave, or a more complex waveform to achieve WMS. A photodiode is required to measure the return signal, potentially coupled to the hardware to support WMS demodulation. Both the laser and the photodiode could be optical fibre coupled, to enable the use of optical switches and couplers within an interrogation system.

Conclusions

A search for commercial integrated interrogation systems was conducted, along with a review of FBG and TDLAS interrogation techniques. The development of a bespoke interrogation solution was considered the most effective method of achieving the project requirements whilst reducing system complexity, and a modular based design was recommended. Two techniques for FBG interrogation were identified for development, and were considered likely to satisfy the project requirements, based on their common use within commercial systems. Developing two techniques, one utilising a swept-laser source and photodiode detector, and the other a broadband SLED source and OSA detector, would provide redundancy and increase the diversity of techniques investigated. The required components and infrastructure to perform TDLAS were identified to inform the development of the interrogation hardware. An integrated modular interrogation system, designed for the measurement of multiple sensing parameters, was not identified as being available from commercial companies nor as being presented in the scientific literature.

2.5 Electronic Sensor Technologies

A survey was conducted to review common commercially available electronic sensor techniques for measuring temperature, humidity, and barometric pressure. The techniques were evaluated for suitability for integration into the interrogation hardware modules and OIES sensor node, focussing on minimising additional components and measurement complexity, while delivering the project requirements.

Temperature

Electrical techniques for measuring temperature commonly rely on measuring a resistance or voltage, but techniques utilising changing capacitance or piezoelectric oscillation frequency are also available [9]. The more common commercially available techniques were chosen for review, which included: thermistors, platinum resistance thermometers, thermocouples, and semiconductor junction sensors. Each technique is briefly summarised and reviewed for its suitability against the requirements.

A change in temperature can vary the resistance of some conductive materials, and therefore be used as the basis of a temperature sensor. Both thermistors and platinum resistance thermometers (PRTs) utilise this method and are interrogated by measuring

their resistance. The resistance is commonly measured using 2-wire, 3-wire, or 4-wire techniques [9], which all pass current through the device while monitoring the voltage drop. The additional complexity of the 4-wire technique over the other two typically results in higher accuracy measurements since it negates the resistance of the leads connecting to the sensor [127]; an example of a 4-wire configuration is shown in figure 2.3.

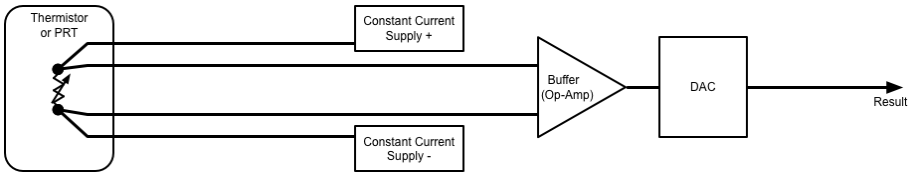

Figure 2.3: Schematic of a typical thermistor or PRT 4-wire measurement configuration.

Temperature dependant resistors are generically referred to as thermistors, and are available in either positive temperature coefficient (PTC) or negative temperature coefficient (NTC) types depending on whether resistance increases or decreases with a rise in temperature. The resistance response is typically non-linear with respect to temperature. Thermistors are available in many shapes, sizes, nominal resistances, operating ranges and tolerances. Due to the vast array of types and configurations, thermistors typically require individual characterisation before use, but commercial off-the-shelf (COTS) devices with a nominal resistance of $10\,\mathrm{k}\Omega$ are available [128] which offer device to device consistency within $\pm 0.1\,^{\circ}\mathrm{C}$. Such devices are specified for operation over the required temperature range with an accuracy of $\pm 1.4\,^{\circ}\mathrm{C}$ [128]. This accuracy exceeded the project requirements, suggesting thermistors were not suitable for use within this project.

PRTs are similar to thermistors, but are standardised to use a thin wire or coating of platinum as the variable-resistance material [9]. As a result they are typically more consistent between components than thermistors, thus not requiring individual calibration [127]. The conversion from PRT resistance to temperature is typically achieved using the Callendar-Van Dusen equation [127, 129]. Industrial class PRTs are available with specified accuracies down to $\pm\ 0.03\,^{\circ}\mathrm{C}$ [130]. Commercial equipment such as the Isotech (UK) TTI-22 and the National Instruments (USA) NI-9216 are intended for PRT measurement. Their stated measurement uncertainties were $\pm\ 1\,\mathrm{m}^{\circ}\mathrm{C}$ and $\pm\ 0.4\,^{\circ}\mathrm{C}$ respectively, in 4-wire configuration [131, 132]. The TTI-22 unit was not specified to operate over the ambient temperature range required, which may in part account for the difference in uncertainties, since the NI-9216 was specified to operate

within the required range [132]. The NI-9216 uncertainty dominated compared to the PRT sensor uncertainty, but the combined measurement uncertainty would still be within the project requirements. A PRT was therefore considered able to meet the project requirements for temperature sensing range and accuracy, but would require a number of additional components to integrate onto an interrogation module. The large differences in uncertainties between commercial equipment suggests the design considerations required to achieve low uncertainty results would be considerable. From interrogation modules (Chapter 3) which incorporated 4-wire measurement circuits, for thermistors built into optoelectronic device packages containing TECs, it was known the measurement circuit would require approximately seven additional components to be added to each module. This was not a great number of components, and on modules driving TECs they would already be included in the bill of materials (BOM), but it was still considered a specialist arrangement to add to modules as a secondary feature.

The review continued to thermocouples, which are likely the most used temperature sensing technique in industry, due to the range of temperatures they can measure [9]. Thermocouples measure the small induced electromotive force (EMF) (voltage) known as the Seebeck effect, which is present between two dissimilar metals. The voltage induced varies with temperature, therefore enabling the use as a sensor [9, 133]. The voltages are very small, in the mV range, so they are amplified before measurement which typically requires additional electrical components. Since the induced voltage is present between all dissimilar metals, care is also required in the cabling and interrogation of the sensor not to create unintended additional bi-metal junctions, and compensate for the unavoidable junction at the measurement electronics termination point. The compensation typically requires a local temperature sensor at the termination point. A typical measurement scheme for thermocouples is shown in figure 2.4. The key attractions of using

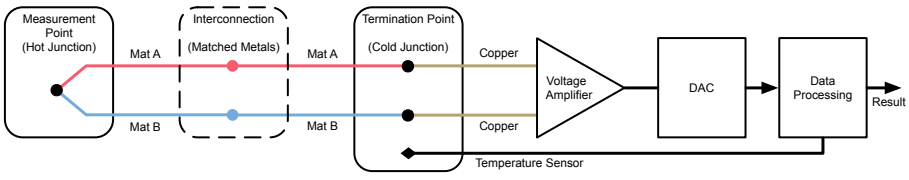

Figure 2.4: Schematic of a typical thermocouple measurement configuration.

thermocouples to measure temperature is their low cost, large temperature measurement ranges, and the well characterised conversion from EMF to temperature; usually achieved using the ITS-90 scale [134]. Thermocouples are commercially available in a number of types, where each type is constructed from a different combination of junction materials.

A summary of thermocouple types, measurement ranges, tolerance bands, and usage notes are shown in table 2.5. The only thermocouple type that met both the required temperature

Type	Junction			Range, °C	Class 1, °C	Class 2, °C	Notes
A	$W+Re_{0.05}$	/	$W+Re_{0.2}$	1000 to 2500	-	$\pm$ 10	†, ⋄, ♡
B	$Pt+Re_{0.3}$	/	$Pt+Re_{0.06}$	600 to 1700	-	$\pm$ 6	†, ⋄, ♠
C	$W+Re_{0.05}$	/	$Pt+Re_{0.26}$	426 to 2315	-	$\pm$ 5	†, ⋄, ♡
E	Ni+Cr	/	Cu+Ni	-40 to 800	$\pm$ 1.5	$\pm$ 2.5	⋄
J	Fe	/	Cu+Ni	-40 to 750	$\pm$ 1.5	$\pm$ 2.5	⋄, ⋈
K	Ni+Cr	/	Ni+Al	-40 to 1000	$\pm$ 1.5	$\pm$ 2.5	⋄, ♠
N	Ni+Cr+Si	/	Ni+Si	-40 to 1000	$\pm$ 1.5	$\pm$ 2.5	⋄
R	$Pt+Re_{0.13}$	/	Pt	0 to 1600	$\pm$ 1	$\pm$ 1.5	†, ♠
S	$Pt+Re_{0.1}$	/	Pt	0 to 1600	$\pm$1	$\pm$ 1.5	†, ♠
T	Cu	/	Cu+Ni	-40 to 350	$\pm$ 0.5	$\pm$ 1	

Table 2.5: Comparison of thermocouple types, ranges and tolerances [134]. Thermocouples are available in 10 common types, and most types are available in three classes. Tolerance bands for class 1 and class 2 devices are shown. Notes: †, range not suitable for requirements, ⋄, uncertainty band not suitable for requirements, ⋈, not recommended for use below 0 °C, ♠, not recommended for use in vacuum, ♡, only recommended for use in vacuum.

range (-10 °C to 40 °C) and accuracy requirements ($\pm$ 1 °C), from Table 2.5, was the T-Type. Commercial thermocouple reading equipment, such as the Fluke (USA) 50 series or Omega (USA) HH912T, each have a specified $\pm$ 0.3 °C measurement uncertainty. National Instrument's best performing thermocouple compactDAQ module, NI-9214, has a stated measurement uncertainty in excess of $\pm$ 1 °C [135]. The low-cost National Instruments USB-TC01 has a measurement uncertainty in excess of $\pm$ 2 °C [136]. This suggests complex electronic systems are required to achieve the lowest uncertainties, and that measuring a T-Type: Class 1 thermocouple could result in a measurement uncertainty of between $\pm$ 0.6 °C and $\pm$ 2.1 °C, depending on the system used. The calculation error associated with converting from EMF to ITS-90 temperature is small: for the T-Type thermocouple it is given as $\pm$ 0.025 °C for temperatures above 0 °C, and as $+$ 0.038 °C/ $-$ 0.017 °C for temperatures below 0 °C. Thermocouples were not considered for further study and integration into the interrogation modules due to their large measurement uncertainties and integration complexities. Only one type of thermocouple was compatible with the requirement of $\pm$ 1 °C. The electronic integration of thermocouples would require careful consideration of interconnection and termination materials, cold-junction temperature compensation (likely requiring another temperature sensing method), high-gain amplification, and an analogue to digital converter (ADC). It was also considered such a configuration would require careful layout on the printed circuit board (PCB) and considerable board space.

The second voltage-based temperature sensing technique reviewed was based on semiconductor junction measurements. The typical configuration utilises the relationship between the base-emitter voltage, V_{BE}, and collector current, I_C of a bipolar junction transistor (BJT):

$$V_{BE} = T \cdot \frac{k_B}{q_e} \cdot \ln\left(\frac{I_C}{I_S}\right), \tag{2.3}$$

where T is the temperature in Kelvin, k_B is Boltzmann's constant, q_e is the charge of an electron, and I_S is a device-specific internal current [137]. The relationship suggests the voltage V_{BE} would vary linearly with temperature while I_C and I_S are constant. However, both I_C and I_S are temperature dependant, meaning a more complex arrangement, incorporating more than one transistor, is typically used for accurate results. A configuration called the proportional to absolute temperature (PTAT) circuit is able to eliminate contributions from both I_C and I_S and provide a voltage output proportional to absolute temperature, and also a voltage output which is stable with voltage [137, 138]. A simplified diagram of a PTAT circuit is shown in figure 2.5 [137].

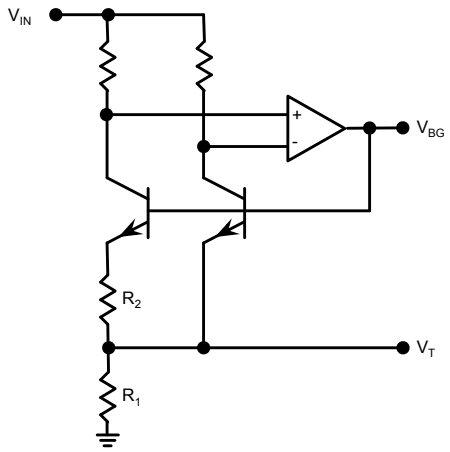

Figure 2.5: Proportional to absolute temperature simplified schematic for providing a linear voltage with absolute temperature, V_T, and a temperature-stable voltage output, $V_{BG} + V_T$.

The temperature dependant voltage output, V_T, relationship for the PTAT circuit shown is:

$$V_T = T \cdot \frac{k_B \ln(2)}{q_e} \cdot \frac{2R_1}{R_2}, \tag{2.4}$$

where R_1 and R_2 are as defined in figure 2.5 [137]. The bandgap voltage, V_{BG}, is complementary to absolute temperature, so summing with V_T can provide a temperature-stable reference voltage [137]. Increasing the number of transistors in parallel increases

the constant within the natural logarithm, $\ln(n)$, and hence the sensitivity. Likewise, the ratio between R_1 and R_2 can be varied within the design to affect the sensitivity. A key advantage of the semiconductor sensing technique is that all the required components can be integrated onto a single silicon wafer. Therefore the size, cost, and integration complexity of such devices is potentially low [9]. Commercial devices, such as the Texas Instruments LMT70 [139], are specified to operate over the required temperature range with an accuracy of $\pm 0.2\,°C$ and a maximum deviation of $0.1\,°C$ between devices. The sensor physically measures less than $1\,mm$ by $1\,mm$, and the output voltage is suitable for direct measurement by an ADC. Semiconductor junction sensors were considered suitable for meeting the project requirements. They were specified for operation over the required temperature range and their stated accuracy was within the required $\pm 1\,°C$. The only required components, in addition to the sensor, was an ADC, but where a micro-controller was present on a module it could be possible to utilise internal ADC hardware where available. Semiconductor sensors were therefore preferable to PRTs due to the reduction in additional components. To ensure maximum compatibility with all interrogation modules, semiconductor devices with internal ADCs and providing a digital serial interface were considered. Devices such as the STS21 from Sensirion [140] feature a semiconductor junction sensor, ADC, and inter-integrated circuit protocol (I^2C) digital interface. Therefore the only component required to be added to the module would be the sensor, and they would be compatible with both micro-controllers and FPGAs.

Electronic sensing techniques were reviewed including thermistors, PRTs, thermocouples, and semiconductor junction sensors. Each technique was reviewed for its operation over the required measurement range and ability to meet the measurement accuracy requirement. A key consideration was also the additional complexity of integrating the technique onto the interrogation modules, with the ideal solution requiring minimal additional components. The use of semiconductor junction temperature sensors were recommended for further study, specifically those with internal ADCs and a digital communication interface, thereby only requiring firmware changes to incorporate the measurement.

Humidity

The most common electronic techniques for measuring humidity typically rely on measuring changes in capacitance or resistance, but some sensors also utilise: temperature

differences between a known *dry* thermometer and one located in the measurement environment, reflectivity of a chilled mirror, or changes in piezoelectric oscillator frequency [141–143]. Sensing materials for both capacitative or resistance systems have been demonstrated based on electrolytes, porous ceramics, semiconductors, and polymer films, which provide measurable changes due to their adsorption and desorption of water molecules [143].

Resistive sensors could be interrogated using the 2-wire, 3-wire, or 4-wire techniques discussed during the temperature sensor review. Capacitative sensors are typically measured using either frequency measurement, where the capacitance value of the sensor varies the frequency of an oscillating signal [144], or using a capacitance bridge arrangement [145], such as the Schering bridge which is similar in arrangement to resistance measurements, but driven with alternating current (AC) [146]. This review focused on capacitive sensing methods based on porous ceramics and polymer films, due to their high maturity and commercial availability. Each technique is briefly summarised and reviewed for its suitability against the requirements.

One of the most common sensing materials used in ceramic based systems is Al_2O_3, as used in the Michell Instruments (UK) Easidew system [147]. The Easidew is specified to have an accuracy of $\pm 2\,^{\circ}\mathrm{C}$ dew point, which matched the required measurement accuracy. An Al_2O_3 system is typically physically large to maximise sensing area, so was considered unlikely to satisfy the project limitations on physical size and integration complexity. The Easidew sensor head is, for example, $132\,\mathrm{mm}$ long with a diameter of $27\,\mathrm{mm}$ [147].

Commercially available polymer film based humidity sensors are available, such as the SHT21 from Sensirion (Germany) [148]. The device utilises a capacitance-based measurement of the film to monitor the quantity of absorbed water [149, 150], and also features an internal ADC and I^2C digital interface. Similar devices are also available from Bosch Sensortec (Germany), such as the BME280 [151], which senses humidity in a similar manner [152]. Both sensors were specified to operate over the measurement range and within the accuracy required, and physically would occupy approximately $3\,\mathrm{mm}$ by $3\,\mathrm{mm}$ of PCB space. The highly integrated construction of these sensors shared the benefits noted in the temperature sensor section of reducing the required parts count down to the sensor itself, while remaining compatible with micro-controllers and FPGAs. The SHT21 is also marketed as a temperature sensor [148], with similar specifications to the STS21 [140] highlighted in the temperature sensor review, which could result in the

SHT21 being capable of measuring two of the required parameters within one device.

Within the scope this work's application, relevant electronic sensing techniques were reviewed including capacitive methods based on sensing materials constructed from porous ceramics and polymer films. Each technique was reviewed for its potential to operate over the required measurement range and within the required accuracy. The use of polymer film capacitive sensors with integrated ADCs and digital interface were recommended for further study.

Pressure

Electronic barometric pressure sensors typically rely on measuring the movement of a flexible diaphragm. Typically the diaphragm deflection is measured via a resistive [153] or capacitance [154] technique, depending on the design of the sensor. As well as macro-sized devices [153, 154], miniaturised micro-electro-mechanical system (MEMS) based devices are commercially available, these commonly utilise piezoresistive membranes for the diaphragm [152]. Alternative techniques, such as temperature-gradient, Pirani, and Penning gauges, were not reviewed due to their typical applicability to very low pressure sensing[1] and physically large size.

Many commercial devices were available with the potential to satisfy the project sensing requirements [153, 155], but the review focused on MEMS-based devices. From the reviews conducted for temperature and humidity sensors, devices which were physically small and incorporated internal ADCs and digital interface were likely to be the best match to the project. Many such devices were found, such as the TE Measurement Specialties (USA) MS5611-01BA03 [155], and the Bosch Sensortec (Germany) BMP280 [156], both of which were specified to meet the sensing range and accuracy requirements, while requiring no external components due to their integrated digital interfaces (I^2C). Both devices required PCB space less than $5\,\text{mm}$ by $3\,\text{mm}$. The BME280 [151] device, highlighted in the humidity sensor review, was also specified to measure pressure with specifications matching the BMP280.

Electronic sensing techniques were reviewed, but based on the previous reviews, the search focused on miniature devices. Small MEMS sensors with integrated membranes, ADCs, and digital interface were investigated and their specifications suggested they could satisfy the project requirements. Further study into such devices was recommended and experimental evaluation is reported in Chapter 4 to assess their suitability within this

[1] Typically suited to measurements in the sub-microbar to low millibar range

thesis.

2.6 Optically Powered Electronic Sensor Systems

Commercial uses of optical powering techniques are not common, but some do exist. A few products utilise optical powering of electronics within their design, such as the electrically isolated oscilloscope probe from Tektronix (UK) [157–160], which uses the measured signal to modulate the intensity of light returned, to provide isolated floating measurements. Other companies provide components intended for the optically powered market, such as photovoltaic (PV) converters from Broadcom (USA) [161], or sub-system assemblies from MH GoPower Company (Taiwan) [162]. The availability of these components together with the evidence of products practically deploying the technique suggest the technique is mature and readily deployable. Patents on the topic date back to 1989 [163, 164], yet academic work is still being conducted to refine the technique and enable its mainstream viability. The Broadcom photovoltaic converters have only become available since August 2018, with similar previously manufactured devices by JDSU (USA) [165, 166] having limited availability for some time [167], especially since 2015 when JDSU split into Viavi Solutions (USA) and Lumentum Holdings (USA) (Lumentum was since purchased by Broadcom). The converters were typically only available in the 800 nm wavelength range [167], but reportedly a 1500 nm range version was developed [166, 168]. At the time this work was conducted in 2017, no PV array converters were found to be commercially available for purchase.

A survey of optically-powered systems reported in open literature was conducted. The survey was limited to optical fibre based systems, and a summary is presented in table 2.6. Typically the highest conversion efficiency systems used PV arrays, such as the devices made by JDSU [165, 166]. For this project, it was considered ideal if the system operated at 1310 nm or 1550 nm to enable compatibility with SMF-28, and potentially enable higher optical powers while remaining within the laser classes desired (1 mW limit at 800 nm compared to 10 mW at 1550 nm, and 500 mW at 1310 nm [179]).

The systems reviewed which operated in the NIR region of interest were those demonstrated by Takahashi *et al.* [173], Tanaka *et al.* [174, 178] and Rosolem *et al.* [168]. In 2008 Rosolem [168] demonstrated a system which used an indium phosphide PV array, which was indicated to have been sourced from JDSU. The system was successfully demonstrated to be stable over a wide temperature range, but the low conversion efficiency

Ref	Optical Source	Optical Receiver	λ	Optical Power	O to E Eff. (η_{OE})	
Heinzelmann *et al.* [169]		PV Array	800 nm	6 mW	45 %	
Beaumont *et al.* [170]		PV Array	810 nm	22.8 mW	43 %	
Werthen *et al.* [171]	LED	PV Array	800 nm	100 mW	40 %	
Peña *et al.* [172]	LED	PV Array	809 nm	700 mW	29 %	
Takahashi *et al.* [173]	Laser	(PV Array)	1500 nm	1.5 mW	25 %	✓
Tanaka *et al.* [174]	Laser	PV Array	1570 nm	1.8 mW	20 %	✓
Budelmann *et al.* [175]	LED	Photodiode		6 mW	17 %	
Böttger *et al.* [176]	Laser	PV Array	810 nm	1 W	13 %	
Röger *et al.* [177]	Laser	PV Array	808 nm	22 mW	< 12 %	
Tanaka *et al.* [178]	Laser		1550 nm	1.7 mW	7 %	✓
Budelmann [167]	LED	Photodiode	650 nm	1.25 mW	2 %	
Rosolem *et al.* [168]	Laser	PV Array	1480 nm	110 mW	0.2 %	

Table 2.6: Summary of optically powered literature systems. Values are those presented in the literature, or estimates from the data provided. Not all values were provided or could be estimated and are indicated by blanks in the table. λ denotes the wavelength used for the light which was converted, and η_{OE} is the optical to electrical conversion efficiency. Systems demonstrated with the potential to satisfy the project laser class requirement are shown with a ✓.

and use of a scarce PV converter meant this system could not be easily developed within this project. The system demonstrated in 2009 by Tanaka [174] used a PV array composed of nine series InGaAs photovoltaic segments for power conversion, and a liquid-crystal optical modulator for data transmission. No details are provided for the source of the PV array or optical modulator, so this system was also not chosen for further development. The 2009 work by Takahashi [173] used a PV converter, but from the data provided it was most likely a single InGaAs photodiode. The converted voltage was boosted by a custom DC:DC converter for use in their design. They also describe evaluating eight series InGaAs junctions, but their final system used a single junction and a DC:DC boost circuit. A MEMS optical modulator was used for data transmission. This system provided a tractable basis for further development due to the topology requirements of InGaAs photodiodes and DC:DC converters, which are both readily available. In 2012 Tanaka [178] presented a system similar to the one previously described [173], but with a focus on the operation of the MEMS optical modulator which was of bespoke design, rather than the optical to electrical conversion.

Based on the lack of commercial availability for PV converters, at the time of the research, and the reported success using single photodiodes, the system to be developed was chosen to operate at the SMF-28 design wavelengths (1310 nm or 1550 nm) and use readily available InGaAs photodiodes for optical to electrical power conversion. The electrical output voltage would then need boosting using a DC:DC converter. It

was outside the scope of this project to implement a bespoke boost topology, so a commercially available device would be required.

A search was conducted for commercial DC:DC converters with an input voltage range suitable for single photodiode connection and an output suitable for micro-controllers and sensors. Table 2.7 details a summary of the search. The devices found

Device	V_{IN}, **Input Voltage**	V_{OUT}, **Output Voltage**	η_P, **Pk Eff.**	**Notes**
LTC3108 [180]	0.01 V to 2 V	2.2 V to 5.25 V	80 %	$V_{STORE} = 5.25$ V
LTC3525D-3.3 [181]	0.85 V to 6 V	3.3 V fixed	95 %	No storage
BQ25504 [182]	0.33 V to 3 V	2.5 V to 5.25 V	90 %	$V_{STORE} = V_{OUT}$
BQ25570 [183]	0.33 V to 5.1 V	2 V to 5.5 V	95 %	$V_{STORE} \leq 5.5$ V

Table 2.7: Low input-voltage DC:DC converter device search summary.

were designed for energy harvesting applications and the internet of things (IoT) market, or for single-cell battery boosting. The Linear Technology (USA) LTC3108 features the lowest input voltage capability and uses a dual DC:DC topology; a transformer resonant step-up DC:DC converter followed by a *charge-pump* converter. The boost voltage was limited by a shunt regulator to 5.25 V [180]. The input voltage range is configurable by selection of the transformer used, but the use of the resonant converter reduces the converter efficiency. The Linear Technology LTC325D-3.3 is a burst-mode synchronous *boost* converter with a fixed output operation of 3.3 V [181]. The device topology should achieve higher efficiencies than a *charge-pump* converter, but its fixed burst-mode operation may not be suitable for an energy harvesting application where the significant limitation is on the input power available. The Texas Instruments (USA) BQ25504 is a *boost* converter which features a startup voltage of 330 mV and once started an operating minimum voltage of 80 mV. The device also features maximum power-point tracking (MPPT) capability and is designed to charge a battery or capacitor, and provide that stored energy to the load system. The converter regulates using pulse frequency modulation (PFM) and actively transitions between a cold-start mode and PFM (with MPPT) [182]. The Texas Instruments BQ25570 is similar in topology to the BQ25504, but has the addition of a DC:DC *buck* converter. This enables the device to store energy in capacitors or a battery at a higher voltage, and then reduce it using the *buck* converter for use at the circuit voltage [183]. A higher storage voltage results in increased energy within the same value storage capacitors.

The open circuit voltage for a single InGaAs photodiode was predicted to be in the

region of 0.45 V, but under load this would reduce. To account for the photodiode voltage dropping below 0.33 V, the LTC3108 was chosen for use within the developed system.

In the literature systems reviewed, data transfer was typically achieved using a laser diode or an optical modulator at the remote end. The optical modulator route required significantly less power to be converted in the node [157, 169, 173, 174, 178], but those reported were typically custom made [174, 178]. As a result a commercially available electro-optic modulator (EOM) was chosen for integration in the developed system.

2.7 Optical Fibre Infrastructure Components

Commercial products and published literature were reviewed for their suitability on the six technique topics of interest: optical fibre hermetic seals, fibre connector for use inside an experiment, optical fibre feed-throughs, rugged sensor packaging, optical fibre encapsulation, and optical fibre umbilical connector. Due to similarities in features, the hermetic seals and feed-throughs were considered together, as were the internal connector and umbilical connector.

Hermetic fibre seals and fibre feed-throughs

Optical fibre hermetic seals are commercially available. Most are based on an epoxy resin seal between the silica optical fibre and the housing, such as those sold by SEDI-ATI (France), SQS Vláknová optika (Czech Republic), Douglas Electrical Components (USA), and the Pave Technology (USA) [184]. The use of epoxy was not considered suitable due to its organic nature. Over time it could degrade, affecting the experimental chemistry and/or the seal integrity. Some manufacturers provide glass to metal seals suitable for optical fibre use. For example, Sinclair Manufacturing (USA), provides the capability to seal optical fibres using gold/tin solders [185]. Use of a metal based seal was considered advantageous in providing a long-term stable and robust seal.

Patents related to hermetic fibre seals are numerous and typically aimed at the telecommunications industry. Some use epoxy resin arrangements [186, 187] and others, which are of more interest, use solder [188–191], such as silver/tin. Publications reviewing the use of solder as a hermetic seal for optical fibres [192–194] added support to the potential the technique.

The commercial solder-seal options found would have required manufacturing of the seal at the commercial company. If the seal was made directly in the experimental vessel

wall this would result in a large and delicate item for shipping.

Typically seals are made in smaller components which form a feed-through that can later be assembled into the vessel of choice. Commercial feed-throughs typically seal onto the vessel using o-rings [184], made from organic materials such as Viton^{TM}. Again, the use of an organic o-ring is not suitable for use within this project, since it may degrade over the experimental duration. Commercial seals are also available that utilise nickel, stainless steel, or copper [195], and following a material compatibility assessment could be suitable for sealing a pre-assembled fibre seal onto an experimental system. Soldering, brazing, or welding of the feed-through to the vessel is not often an option due to the fragile nature of the fibres and the seal.

This project aimed to investigate creation of solder seals in-house at AWE that could enable the seal to be created directly through the vessel wall without requiring shipping to a manufacturer. Approaches for integrating a solder-sealed feed-through with the vessel during assembly, without the use of o-rings, were also investigated.

Sensor Packaging

The integration of sensors within an experiment requires care to ensure the sensor responds as expected. For optical techniques such as temperature sensors based on FBGs, the sensors are typically packaged to isolate mechanical strain [19, 22]. If they were not strain-isolated the single measurement would contain a superposition of both temperature and strain data. Another reason to house sensors is to increase their mechanical robustness, to ensure they operate as expected throughout the experiment [44].

Commercial housings are typically large [19, 22] due to their industrially robust design. This work investigated a bespoke, physically small, and robust sensor package suitable for use within a materials ageing experiment.

Optical fibre encapsulation

Encapsulation of optical fibres was of interest due to its potential to isolate the fibres from the experimental environment while increasing their physical robustness and ease of handling. Some commercial options exist, such as using metal coated fibres [196], optical fibre in metal tubes [197], and flexible stainless steel tubing [198].

Metal coatings on fibres are often used as the basis for the solder seals discussed above, and while they assist in isolating the silica fibre from the environment they don't

generally produce a more robust fibre [199]. Fibres in metal tubes is a technique promoted for use in the petrochemical industry where an optical fibre is contained within a thin-walled stainless steel tube [197]. The technique would satisfy the isolation and robustness requirements of the project, but the addition of gel within the tube, which acts as a hydrogen getter [200], is not ideal. If the tube was damaged in assembly or during the experiment, the presence of the gel could negatively impact the experimental chemistry. Flexible stainless steel tubing is available to add mechanical protection to optical fibres, and make them easier to handle. Unfortunately the tubing's interlocking helix design results in a lack of sealing, so the fibres would not be isolated from the environment. A combination of metal coated fibres and flexible tubing could provide a viable solution, but the manufacture of such a fibre assembly could be complex. Coating the fibres in metal may provide a technique for chemical isolation but results in additional work during fibre termination, compared to an acrylate coated fibre. Placing the fibres within flexible metal tubing should provide mechanical robustness and make them easy to handle, but would significantly increase the dimensions of the fibre (increasing it from $\varnothing 0.25$ mm to up to $\varnothing 2.3$ mm [198]). Therefore the need to both isolate the optical fibre, and provide mechanical protection, may not be possible using a single technique.

It was recommended that alternative encapsulation techniques were explored with the aim to find an option that would satisfy the project requirements, but was easier to assemble and physically smaller than the commercial options reviewed.

Optical fibre connectors

Two optical fibre connectors were required for the project, one to enable connections to occur within the experimental volume, and the other to connect a large number of fibres between the interrogation equipment and the experimental system. A significant number of optical fibre connectors exist, but most are based around either 1.25 mm or 2.5 mm diameter ferrules. Housings are then formed around these ferrules to create industry standard connectors, such as SC, LC, ST, and FC [201]. Multi-fibre ferrules are also available, such as the multiple-fibre push-on-pull-off/mechanical transfer polished (MPO/MTP) ferrule [202], which also has corresponding housings available [201, 203].

These standard optical fibre connectors were reviewed and in general were considered to be physically too large for use as an internal connector. There was also concern about concealed volumes created when connectors were mated, and the use of plastic housings.

These features could impact the experimental chemistry in unpredictable ways through decomposition, virtual leaks, or micro-environments.

Multi-fibre connectors suitable for use as an umbilical were typically formed by placing a large number of single ferrules within a connector shell [204]. Termination of such an assembly was considered a time consuming job, and in many cases the connectors were only available for purchase as complete assemblies [205]. This restriction would have limited the ability to vary the fibre types used during the system development. A multi-ferrule connector design from Molex (USA), uses MPO/MTP ferrules [206] which would have the potential to reduce the assembly time. Upon enquiry it was revealed the connector was not planned for production, and if it was ever available, it would only be provided as completed assemblies, not component parts [207], limiting its flexibility.

For both the internal connector and the umbilical connector is was decided to explore bespoke solutions. The key aim of the internal connector was to produce a physically compact solution. The key aim for the umbilical connector was to enable a large fibre count with high flexibility, without requiring excessive assembly time.

2.8 Conclusions

A survey was conducted to assess technologies that were likely to satisfy the project requirements. The recommendations from the survey were used to inform the development activities within this project.

Following the review of commercial interrogation systems it was recommended to pursue a bespoke interrogation solution, in order to provide multiple measurement schemes within a single unit, and confidence of long-term support. Investigating FBG interrogation techniques resulted in multiple techniques being suitable and two techniques were recommended for development. TDLAS interrogation requirements were discussed, to ensure the developed system could support TDLAS measurements in the future.

The review of optical temperature sensing techniques concluded that FBG sensing was a mature optical technique, with the potential to satisfy the project requirements. The review of barometric pressure sensing techniques recommended investigation of FFP pressure sensors, which were commercially available. The review of gas sensing techniques concluded that TDLAS had the potential to satisfy the project requirements.

Part II

Interrogation Hardware

Chapter 3: Modular Interrogation System

This chapter details the development of a bespoke conceptual interrogation system which aims to support optical diagnostics within a future long-term materials ageing experiment. The design focused on modularity and long-term serviceability, in order to provide constant and robust data over the multi-decade time frame of the experiment. The system was required to be self-contained, and intended to interrogate all the diagnostics within an experiment from a single unit. This chapter details the system concept and the demonstration hardware which was designed, manufactured, and evaluated within this project.

The decision to develop a bespoke modular interrogation system was based on the lack of suitable and complete commercial options, as discussed in Chapter 2, and the need for long-term support. A number of commercial systems were available that could individually measure the required sensors, but they typically were not user-serviceable and access to spare parts were reliant on commercial support, which may not be available over the anticipated experimental duration. For example, an extended warranty from Micron Optics (USA) only provides three years of cover [21]. To ensure an experiment could be maintained for multiple decades, full intellectual property (IP) ownership was considered worthwhile to manage the risk of obsolescence, as discussed within this chapter.

The interrogation hardware discussed in this work was required to measure FBGs and the optically isolated electronic sensors (OIES) remote node, discussed in Chapter 8. To interrogate these sensors, relatively specialist optoelectronic components were required, which presented an obsolescence risk that like-for-like replacement parts could be unavailable decades after deployment of the interrogation system. A further requirement of the interrogation system was the need for it to remain operational throughout the experimental duration, with minimal downtime for maintenance and repair.

This work describes an approach to design a serviceable and maintainable system suitable for multi-decade use. It accepts components will need replacement during the

lifetime of the system and acknowledges that direct replacement components may not be available. A system capable of interrogating FBGs (by two methods) and electrical sensors over an optical fibre was entirely designed, manufactured and demonstrated within this project. The system was also designed for flexibility and to support additional interrogation capabilities as required in the future, such as TDLAS gaseous chemical measurements and/or fluorescence spectroscopy.

Requirements

The interrogation system was required to demonstrate the ability to obtain measurements from optical fibre based sensors using bespoke modular hardware. The requirements were separated by module type: interrogation infrastructure requirements, control module requirements, interrogation module requirements, and optical routing module requirements. These requirements are discussed as relevant throughout the chapter.

The interrogation infrastructure was required to interface the control modules, interrogation modules, and optical routing modules, as well as provide a user interface. The user interface was to enable system operation and status to be evaluated in a user-friendly manner, and to allow collection of local data storage media. The system was required to support connection and disconnection of modules, without requiring power-down; i.e. to support module replacement during operation. While the sensors could not be periodically calibrated during an experiment, due to their location, the interrogation system could, through the use of external reference devices. It was required to include connections to support calibration of the interrogation modules while they were located within the system.

The control modules were required to provide sequencing commands to the interrogation and routing modules, collect data from all modules as required, store the measured data, and update the user interface.

Interrogation modules were required to interface with the system infrastructure using a common connection scheme. Modules were required to enable FBG sensor interrogation by two methods, to demonstrate technique diversity and module redundancy. Also a module was required to interrogate the OIES node, discussed in Chapter 8.

The optical routing modules were required to interface via the same common connections as the interrogation modules. Modules suitable for routing optical fibres from optical sources, to detectors, and to/from multi-fibre umbilical connectors were required.

Modules suitable for supporting optical fibre components, such as directional couplers and/or circulators, were also required.

3.1 Obsolescence Awareness

Obsolescence management in the context of this work was considered to be a compromise between risk and cost. The risk that the interrogation system could become unable to provide data from the experiment was considered to be separable into short-term *system uptime* considerations, and long-term *IP ownership* concerns. *System uptime* could be maximised by including built-in redundancy and/or a supply of readily available spare parts and modules. *IP ownership* provides full knowledge of the system design and would increase confidence in replacement part availability, since their production would be within the user's control. Reducing risk in either of these areas would potentially increase cost at both the procurement and support phases of the system life-cycle.

Full IP ownership, down to component level, such as laser diodes, microprocessors, and op-amps, would provide the maximum level of spare parts control. However, such an endeavour would be highly costly and would rely on maintaining many diverse competencies to reproduce the parts for decades. This work chose to investigate a strategy for using commercially available components, but retain a high level of confidence in integrating replacement parts as required.

Figure 3.1 details four example strategies for component replacement following a component failure. The number of tasks on each route approximately represents the length

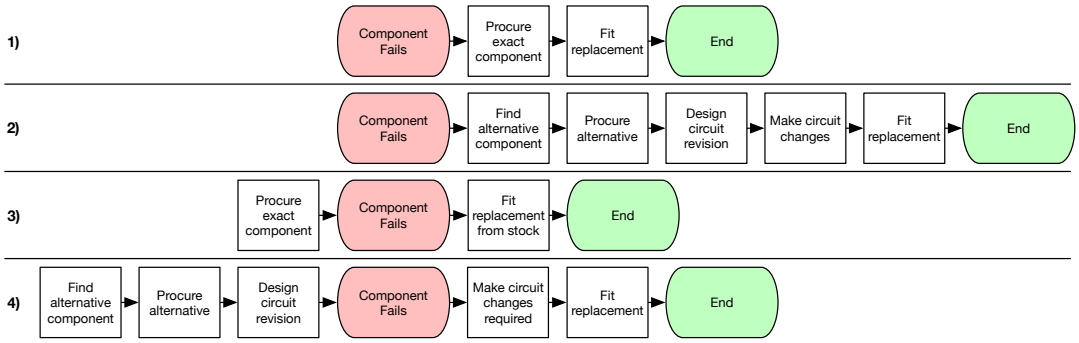

Figure 3.1: Four component replacement workflows in the context of component obsolescence. Each route, 1-4, demonstrates an example strategy for system maintenance prior to and following component failure.

of down-time for the interrogation system or module. Strategy (1) represents the case where direct replacement of the failed component is available. Strategy (2) represents the case where no direct replacement is available and describes a more complex task

including searching for alternatives and designing circuit modifications. Strategies (3) and (4) represent the same scenarios respectively, but where the need for component replacement was planned for. These two strategies could also represent a proactive maintenance scenario where vital components are routinely replaced to a schedule before they fail.

For vital system components the availability of replacements throughout the experiment would need to be monitored to enable the proactive strategy (4). This means that if a component becomes obsolete, a plan for sourcing an alternative and integration into the system with minimal modification can be created without impacting the system uptime.

It was recommended to pursue development of an interrogation system which integrated COTS components, such as laser diodes, microprocessors, and op-amps, to a module level. The module IP would be owned by AWE, thereby providing the necessary knowledge to re-produce or re-engineer the modules as required throughout the system lifetime. A redesigned module would interface with the interrogation system in the original way, but could support alternative components to achieve comparable functionality. It was also recommended to enact a proactive maintenance process, before using such a system in a long-term experiment.

3.2 Modular System Concept and Overview

The system was designed, from its initial concept, to be highly modular, which was considered to provide the benefits of flexibility, redundancy, and the potential to manage system uptime and obsolescence risk. System uptime would rely on a ready supply of replacement modules, but component level failures are also de-risked, as previously discussed. The modular system design concept is shown in figure 3.2.

This system design separated the routing, interrogation, and control modules. Each source and detector was contained on its own module and could be routed to the required optical sensor via the routing modules. Most measurement schemes required one of the optics modules, and co-ordination between source and detector interrogation modules.

This design architecture potentially allowed for a small number of source and detector modules to interrogate a large number of sensors by having provision for multiple routing modules. This architecture relied on periodic sensor interrogation to allow for optical multiplexing, where not all sensors are connected to sources and detectors at all times.

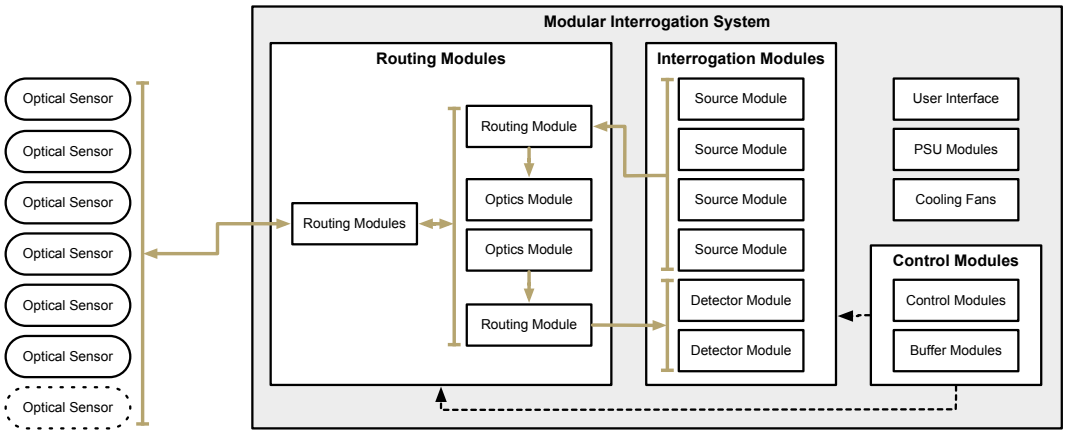

Figure 3.2: Diagram of interrogation system design overview. Each solid box represents a module or integrated PCB. Solid yellow connections show optical fibre connections, dashed black connections show electrical control signals.

In a materials ageing experiment the environment was predicted to vary slowly, and was therefore well suited to periodic interrogation.

The system design featured a module chassis system fitted with custom PCB backplanes, a user interface, and external optical fibre connectors for connection into the experiment. The system infrastructure incorporated air cooling, power distribution, and fibre routing to support the modules.

The system was designed to locally record the acquired data onto solid-state secure digital (SD) card media, and to run fully autonomously, requiring no computer connection. This design decision was taken so that the scope of the obsolescence management plan was not required to extend to computer hardware and operating systems. Instead, the scope is reduced to managing the ability to read the solid-state media, revise the module designs, and update micro-controller firmware and FPGA hardware descriptive language (HDL) code.

For modules vital to the system operation, incorporating redundancy was considered a worthwhile investment, so provisions were included for dual power supplies and dual controller modules. Redundant optoelectronic (source, detector and routing) modules could also be supported, but the cost benefits would depend on the exact experimental configuration.

Each interrogation and routing module was fitted with a common electrical connector and a dual multiple-fiber push-on/pull-off (MPO/MTP) connector system. Both connectors were fitted to the rear of the module and interface with the backplane on module insertion. Electrically, each module featured opto-coupler and/or radio-frequency isolators and local power supply regulation. Optically, each MTP ferrule was assembled

with a loop-back fibre enabling connector loss to be monitored once the module was installed. This arrangement enabled module hot-swapping while the system was powered and operational, enabling serviceability at the module level with minimal impact on the interrogation tasks. The electrical signal isolation also ensured that a component failure on one module would be unlikely to damage components on other modules or the infrastructure.

User Interface Design

The user interface of the modular interrogation system was designed to be generic, enabling reconfiguration of modules without having to update the interface. It was primarily for use in routine checks to evaluate the status of the system, and to support module-level fault finding.

Figure 3.3 shows an image of the front panel of the interrogation system. The panel was separated into four prominent bands, from top to bottom. The upper band featured eight user control buttons and a touch screen; the upper-middle band contained the global and module status indicators; the lower-middle band contained a control mode key-switch, SD card slots, and remote data and servicing connections; the lowest band featured up to six multi-fibre umbilical connectors.

With the control mode key set to auto-acquire, a user was only permitted to activate the display and view measurement values. All other buttons were inactive, but their illumination state represented their current status as appropriate, e.g. a green power supply button indicated the supply was active. The display presented the latest measurement values and could be navigated by the user through on-screen buttons.

Provision was included for up to six umbilical connectors with could enable the interrogation of multiple long-term experiments from one system. The umbilical connector used was of bespoke design, discussed in Chapter 9.

Figure 3.3: Front panel photograph of the interrogation system, featuring 8 primary dual-colour illuminated push-buttons, 10 secondary dual-colour illuminated push buttons, a full colour touch screen, four primary status dual-LED indicators, 128 module-status LED indicators, a three-position key-switch, two SD card slots, three electrical connectors, and optical fibre umbilical connectors.

3.3 Interrogation Configurations

The modular interrogation system was designed to measure a range of optical fibre based sensors. It was required for the system to support FBG sensing by two methods, and the OIES system discussed in Chapter 8, but provision in the design was also included for TDLAS gas detection.

A description of the modules and their interconnections required to enable the system to perform FBG sensing, OIES interrogation, and TDLAS are provided.

Optical fibre Bragg grating detection

There are a number of methods for detecting the Bragg reflection wavelength [49], but two are most common [21, 119, 208]. The first uses a swept laser to scan over a range of

wavelengths while monitoring the reflection intensity with a photodiode. The wavelength of the FBG is determined through analysis of the photodiode signal and correlation with the laser wavelength. The second technique uses a broadband source, such as a SLED, and an optical spectrum analyser (OSA). Analysis of the OSA signal reveals the Bragg wavelength. Both schemes were designed to be supported by the interrogation system.

Figure 3.4 details how the first technique could be achieved using the modular interrogation system. A dedicated swept laser module would tune the output wavelength

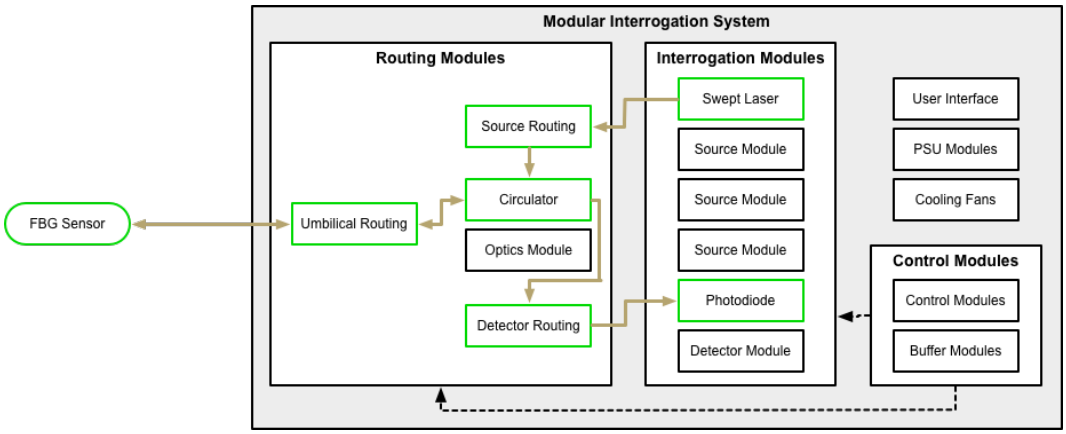

Figure 3.4: Diagram of FBG detection technique using a swept laser, circulator, and photodiode module. Green boxes denote the active modules and features.

over the range where the FBG reflection was expected. The light would be routed through an optical circulator, which would direct reflected light to a photodiode detector, through a second routing module. From the circulator the light would be routed out of the system from an umbilical connector and to the sensor of interest (located within the experiment).

The second technique is shown in figure 3.5. The broadband light from an SLED is routed through the circulator and to the FBG sensor, in the same way as the swept laser, but the reflected light is routed to an OSA module.

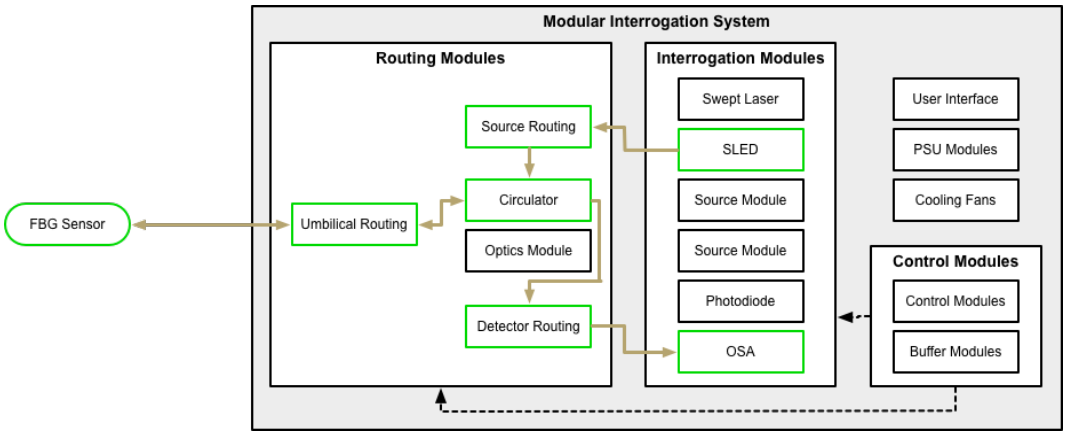

Figure 3.5: Diagram of FBG detection technique using a SLED, circulator, and OSA module. Green boxes denote the active modules and features.

The inclusion of both techniques within the design meant a fault with a source or detection module would not render FBG sensing unavailable. It also increased the number of techniques and modules investigated, providing more concepts for future down-selection and maturation. In each technique two interrogation modules were required, with the swept laser and OSA modules being the most technically complex. The commercial interrogators based on the swept laser technique specify a higher accuracy than the OSA based interrogators (table 2.3).

Optically isolated electrical sensor interrogation

The module created to provide the optical power and receive data from the electrical sensor system detailed in Chapter 8 was self-contained. As a result, it required a single fibre to be routed through to the umbilical which was used for bi-directional signals, as shown in figure 3.6.

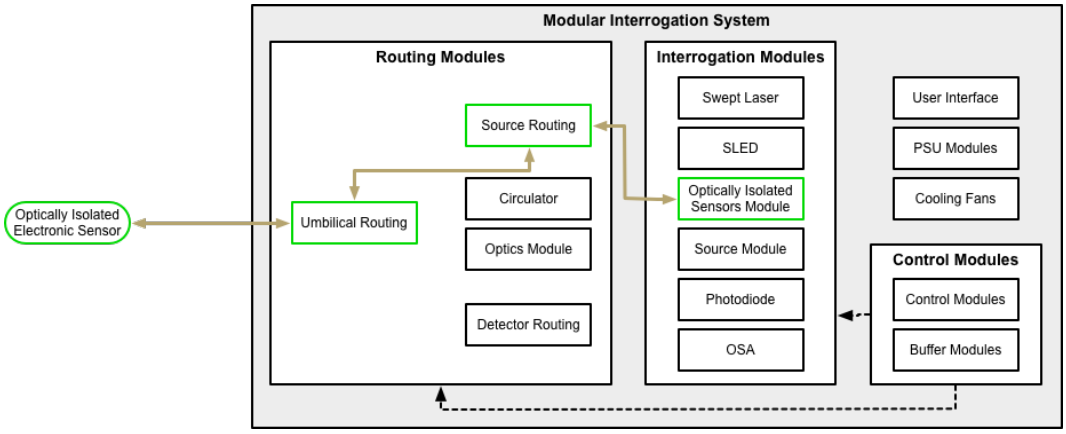

Figure 3.6: Diagram of optically isolated electronic sensor routing using the self-contained interrogator. Green boxes denote the active modules and features.

TDLAS gas detection

The provision to perform TDLAS was included, but would require a DFB laser module to be created, and one installed in the system for each gas to be measured. For instance, a module based at $1358\,\text{nm}$ could be used for H_2O detection, and additional modules such at ones at $2004\,\text{nm}$ for CO_2, and/or one at $1654\,\text{nm}$ for measuring CH_4 could be installed.

The light from the DFB module would be routed through the umbilical to the input of a gas cell (Chapter 7). The output from the cell would then be routed to the photodiode module, as shown in figure 3.7.

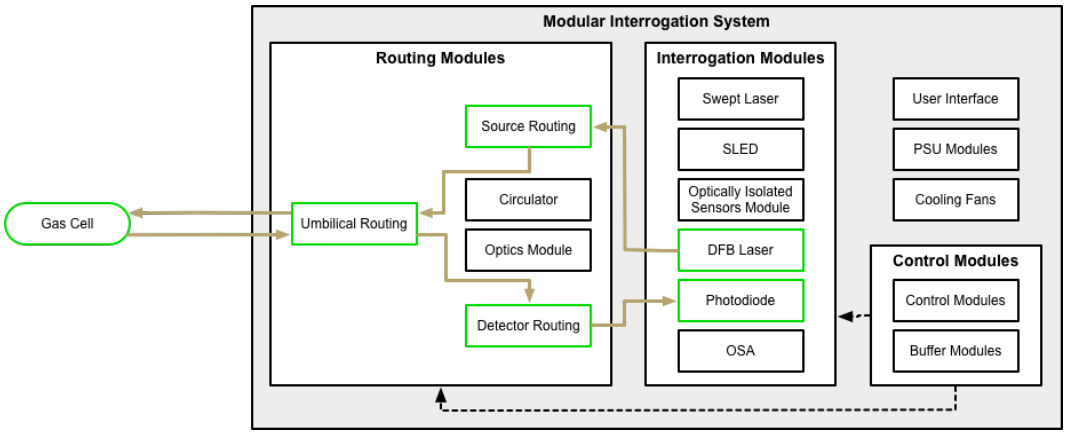

Figure 3.7: Diagram of the TDLAS detection technique using a DFB and photodiode module. Green boxes denote the active modules and features.

System modules required

Based on the interrogation system concept and the above interrogation schemes, a list of required modules could be formed. The system infrastructure was assembled from a number of non-modular PCBs, plus a loopback monitoring module, two fan modules, and up to two power supply unit (PSU) modules. The control modules consisted of two system control cards (control card 1 (CC1) and control card 2 (CC2)), and two buffer modules (module buffer 1 (MB1) and interface buffer 1 (IB1)). The interrogation and optical routing modules were selected based on the interrogation schemes for FBG detection, OIES interrogation, and TDLAS, summarised in table 3.1.

Due to the system architecture, the modules could be used for multiple techniques, which resulted in a final list of required interrogation and optical routing modules, as detailed in table 3.2.

Technique	Module Type	Description
FBG1	Interrogation	Swept Laser
	Interrogation	Photodiode
	Optic	Circulator
	Routing	Source routing
	Routing	Umbilical routing
	Routing	Detector routing
FBG2	Interrogation	SLED
	Interrogation	OSA
	Optic	Circulator
	Routing	Source routing
	Routing	Umbilical routing
	Routing	Detector routing
OIES	Interrogation	OIES integrated interrogator
	Routing	Source routing
	Routing	Umbilical routing
TDLAS	Interrogation	DFB (per gas)
	Interrogation	Photodiode
	Routing	Source routing
	Routing	Umbilical routing
	Routing	Detector routing

Table 3.1: Summary of interrogation and optical routing modules by technique. TDLAS was included in this design, but was not required to be developed to completion.

Module	Block Type	Sensing Scheme
Swept Laser	Interrogation	FBG1
SLED	Interrogation	FBG2
OIES integrated interrogator	Interrogation	OIES
†DFB (per gas)	Interrogation	TDLAS
Photodiode	Interrogation	FBG1, TDLAS
OSA	Interrogation	FBG2
Circulator	Optic	FBG1, FBG2
Source routing	Routing	FBG1, FBG2, OIES, TDLAS
Umbilical routing	Routing	FBG1, FBG2, OIES, TDLAS
Detector routing	Routing	FBG1, FBG2, TDLAS

Table 3.2: List of interrogation and optical routing modules required. †DFB module was provisioned in the architecture, but not required within the scope of this thesis.

Combining the list of infrastructure, control, interrogation, and optical routing modules, provided a complete list of modules required for system operation. The list of modules and a summary of their primary functions are detailed below. Modules marked, †, were provisioned within the infrastructure design since their future inclusion was considered beneficial, but were outside the scope and requirements of this project.

Fan
Primary cooling method for the system; two required

PSU
Power supply unit module to deliver $12\,\mathrm{V}$, $-12\,\mathrm{V}$, and standby $3.3\,\mathrm{V}$ rails; up to two required

†Loopback Monitoring
Monitoring module actively measuring the backplane MTP losses of each module on insertion to assess the optical connection

†Control Card 1 (CC1)
Primary control of the system, sets module modes and collates data

Control Card 2 (CC2)
Monitor control card 1, secondary control of the system (if CC1 is not present or malfunctioned), PSU monitoring, environmental monitoring

Module Buffer (MB1)
Buffer the module signals to/from the control cards

Interface Buffer (IB1)
Buffer the user interface signals to/from the control cards

Swept Laser Source
Optical source module for FBG measurement

SLED Source
Optical source module for FBG measurement

†DFB Source(s)
Optical source(s) for TDLAS, one required per gas to be detected

Circulator Optic
Optical component for use in FBG measurements

†Coupler Optic
Optical component for use with multimode sensing techniques

Photodiode Detector
Optical detector for FBG and TDLAS measurements

OSA Detector
Optical spectrum analyser detector for FBG measurements

OIES Interrogator Module
Integrated module for OIES interrogation, discussed further in this chapter and in Chapter 8

Source Route SM
Single-mode fibre routing of the source modules

†**Source Route MM**
Multimode fibre routing of the source modules

Detector Route SM
Single-mode fibre routing to the detector modules

†**Detector Route MM**
Multimode fibre routing to the detector modules

†**Umbilical Routing**
Optical fibre routing to the umbilical connector(s); up to six required

Red Laser Module
Visible laser fibre fault-detection module for system development use

The 21 modules listed above could result in up to 30 modules within the interrogation system, since multiples of some modules could be required. These modules could be created from 15 individual circuit designs, since the optical component modules and fibre routing modules (with exception of the umbilical routing module), could be achieved using a single PCB design.

This list of modules only detailed part of the interrogation system, but the supporting infrastructure was also required. This consisted of the two control and interrogation backplanes, to which the modules connect, the internal fibre and electrical cable routing, user interface, data storage, and mechanical structure of the system.

3.4 Summary of Module Designs

15 different module designs were required to provide the interrogation system concept with full functionality. Within this research project not all the modules were designed, since the project scope was limited and the requirements were evolving to meet the capabilities of the diagnostics and fibre accessories under concurrent development. Focus was placed on the system infrastructure and modules required to demonstrate FBG measurement and OIES interrogation in operation. These were designed and manufactured within this project, including electronic circuit design, optical system design, PCB layout, generation of manufacturing files, and module assembly.

For the control, buffer, SLED, and photodiode modules, a summary of their key operations and a top level block diagram is presented in this section, detailing some of the key design decisions taken. More detailed descriptions of the routing, OSA, swept laser,

and OIES modules are included later in the chapter. In general, all modules featured local voltage regulation, optically-isolating (opto-isolators) signal buffers, radio-frequency isolating signal buffers, and/or other circuit protection, on all backplane connections. This was to enable module connection and disconnection during system operation. Each module could also be powered individually when external from the interrogation system for module programming, testing, and debugging. Each module also featured LED indicators which were visible on the rear of the interrogation system and mirrored the front panel module status block, to aid in operation confirmation and fault-finding.

The interrogation and optical routing modules all shared a common backplane interface which featured a 48-pin electrical connection and a twin MPO/MTP connector. The electrical connector contained connections for: $12\,\mathrm{V}$, $-12\,\mathrm{V}$, and $3.3\,\mathrm{V}$ opto-isolator supplies, module status indication, module identification, system fault mode, module operation mode, data to/from the MB1 module, common multi-drop data, dedicated module to module synchronisation, and global serial data communications. The MPO/MTP connections were also standardised and included defined single mode (SM) and MM , input, output, and loopback fibre positions.

Control Module Designs

CC2 was developed to provide the interrogation system with the capabilities for autonomous operation. The module was responsible for controlling the system PSUs, maintaining the system time, triggering the fan modules to boost their airflow, and provide $3.3\,\mathrm{V}$ to the system backplanes for opto-isolator driving. The secondary roles for the module included the ability to control the diagnostic modules (via the MB1 module), and store measurement data. These roles were included to enable the system to operate without CC1.

During development of the alternative interrogation system chassis, CC2 was revised to CC2B, enabling communication with diagnostic modules directly, without requiring the MB1 module. The revised module retained all functionality required for operation in the full interrogation chassis, therefore superseding the initial design in all uses. A block diagram for the module is shown in figure 3.8.

CC1 was intended to be the primary system controller and would have been FPGA-based. The module was not developed within this project, since CC2 was able to control the system sufficiently to enable system demonstration and evaluation. CC1 would be

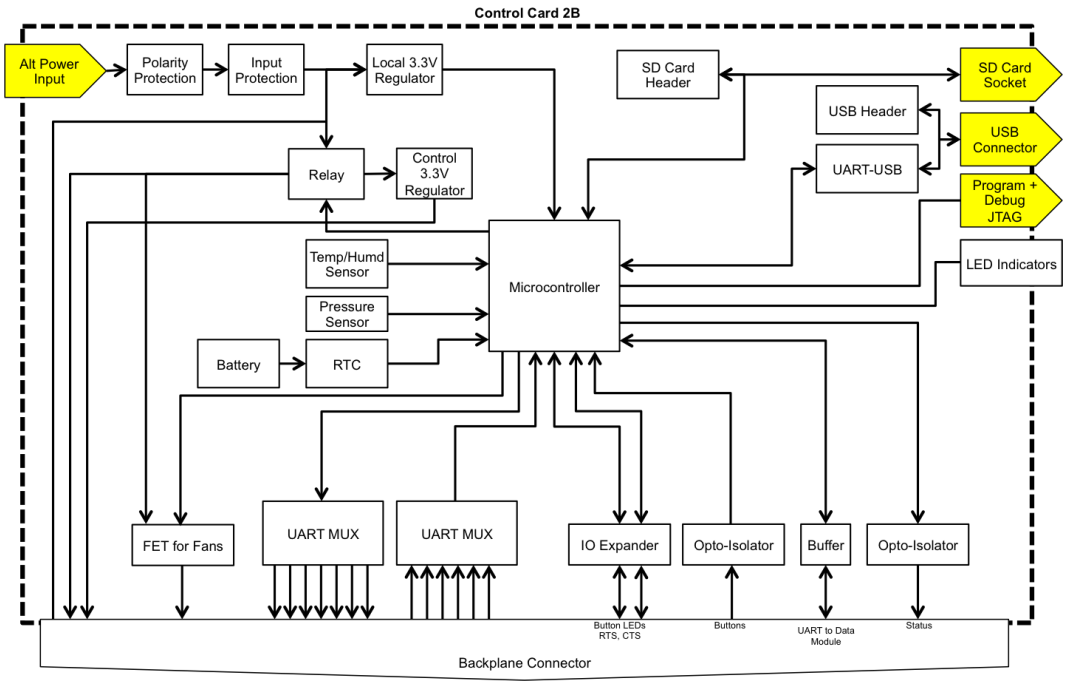

Figure 3.8: Block diagram of the control card 2B module design.

required in the future to provide control redundancy, and to enable high-speed data transfer from the diagnostic modules.

Buffer Module Designs

The interrogation system design placed buffer modules between the control cards (CC1 and CC2) and the diagnostic modules and the user interface. The primary purpose of the modules was to provide an additional layer of electrical isolation between the system control and the modules, to limit the potential impact on system operation of a module malfunction.

The MB1 module provided the link between the control cards and all the interrogation and optical routing modules. A block diagram of its functions is shown in figure 3.9. An additional purpose of the module was to expand the number of connections available from the control cards to the number required for each module, via serial data links from the control cards. This approach was effective in reducing the number of input and output connections required on each control card.

The IB1 module provided a link between the user interface, buttons and display, and the control cards. A block diagram of the module is shown in figure 3.10.

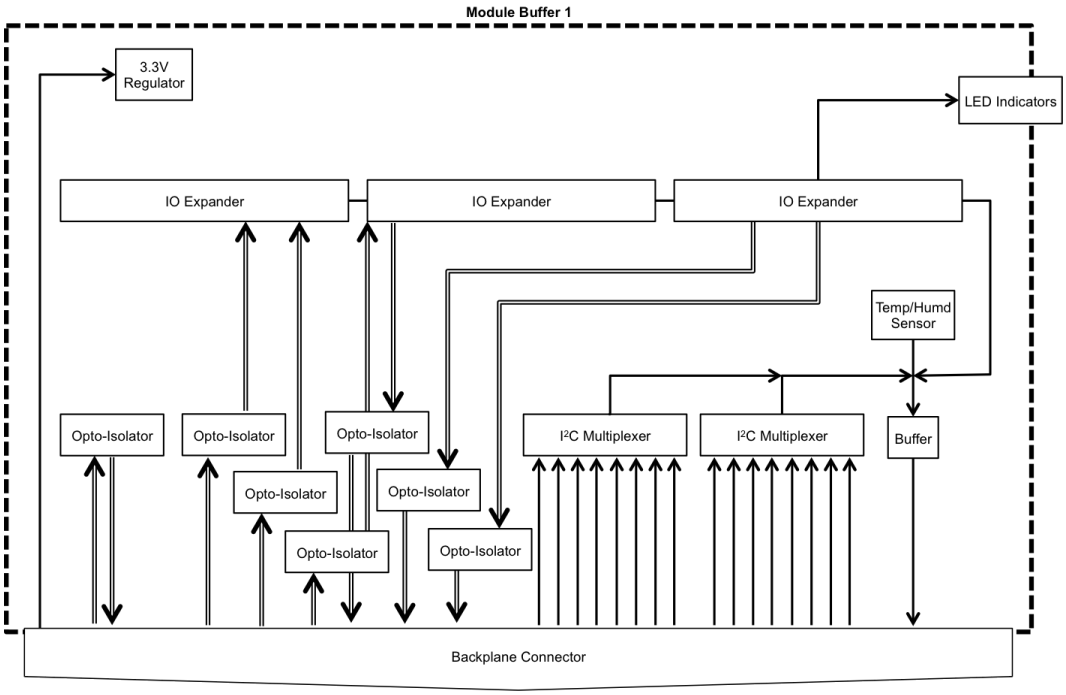

Figure 3.9: Block diagram of the module buffer 1 module design.

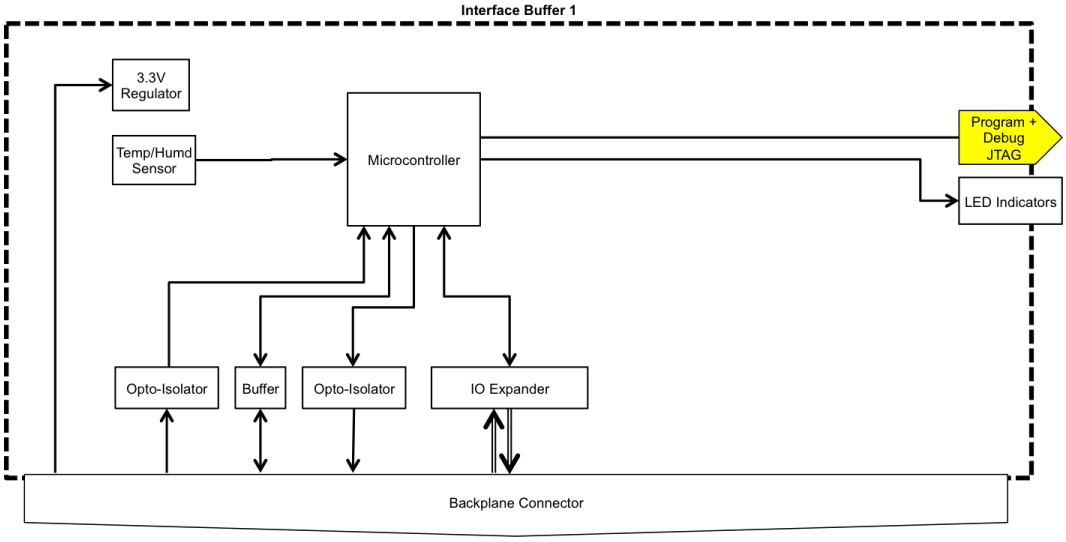

Figure 3.10: Block diagram of the interface buffer 1 module design.

The module was able to provide an interactive user experience by handling the illuminated button and display update functions autonomously, and providing consolidated user intent instructions to the control cards. Similarly, updated data and operation modes were relayed from the control cards to the system front panel via the IB1 module.

Both modules were designed and manufactured. They operated as required, providing key links between CC2 and the interrogation system.

SLED Module Design

The SLED module was intended to enable driving of optical sources requiring a CC source and, optionally, a TEC controller, such as SLEDs and static-wavelength laser diodes. The block diagram of the module is shown in figure 3.11. The module was designed,

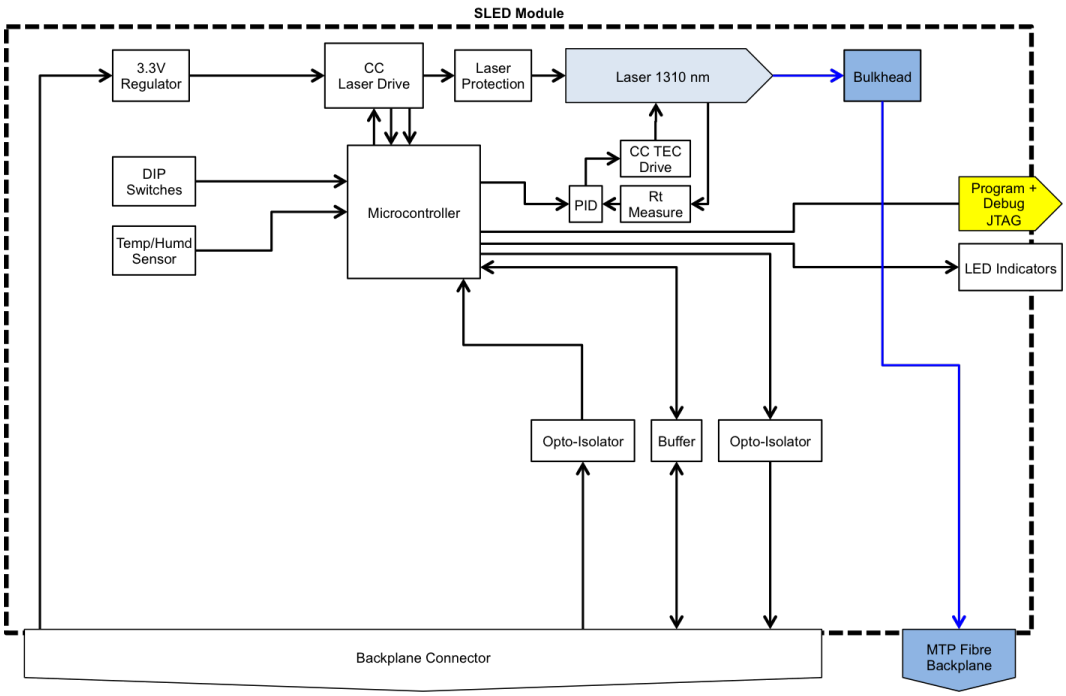

Figure 3.11: Block diagram of the SLED module design.

manufactured, and assembled with a 1550 nm SLED. The current limit for both the SLED drive and the TEC circuit were set by physically choosing resistor values on the PCB; this was done by hand after board production. In operation, the current and target TEC resistance were controllable from the micro-controller, up to the resistor-set limits. The resistors ensured there was a hardware limit for the drive currents, protecting the SLED to over-current faults. Due to the variability in commercial SLED drive currents it was necessary to match the resistors to an individual device at the time of assembly.

The SLED module operated as expected and was programmed to enable SLED on/off control from the system control cards (CC1 or CC2, via the IB1 module). The SLED was operated at a constant current of (530 ± 2) mA and produced a stable (3.0 ± 0.2) mW of optical output power, measured using a Thorlabs (USA) PM20C power meter.

In addition to the 1550 nm SLED module, the same design was used to create a module containing a red laser diode emitting at 639 nm, which was used to confirm fibre routing and sensor sequencing during development, since the light exiting the fibre could be visually seen.

Photodiode Module Design

The photodiode (PD) module provided the system with the ability to measure optical intensity for FBG and TDLAS measurements. The block diagram for the module is shown in figure 3.12. The module could also be used for verifying optical switch operation, and

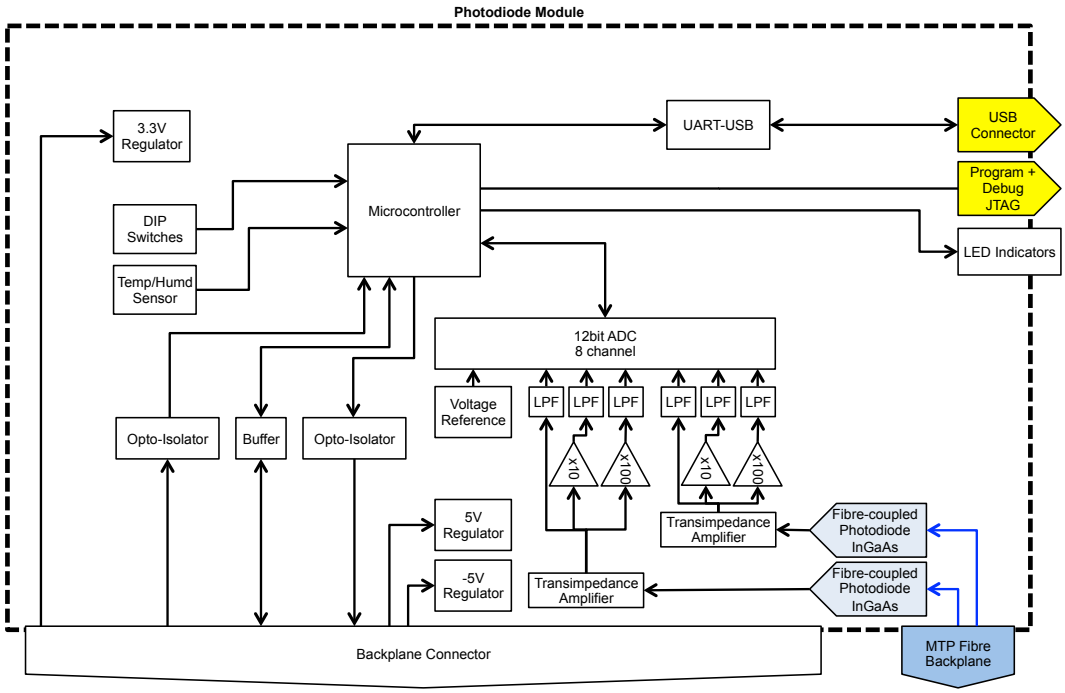

Figure 3.12: Block diagram of the photodiode (PD) module design.

checking the optical source modules.

One version of the module was designed, manufactured, and evaluated. The module was designed to support two InGaAs photodiodes, one intended to be coupled to SM fibre and the other MM. The assembled module only had one photodiode fitted which was coupled to SM fibre.

The use of a multi-channel ADC and discrete signal amplification enabled the simultaneous measurement of the signal at multiple gains. The photodiode was coupled

to a transimpedance amplifier, providing a conversion from current to voltage, while also providing an adjustable output signal level. The circuit was designed to provide negative-voltage biasing to the photodiode annode, but in the evaluated configuration the annode was connected to the circuit ground, since it was evaluated to perform as required.

The optical detection was tested for an optical signal at 1310 nm and at 1550 nm, with optical powers between (0.80 ± 0.03) mW and (3.0 ± 0.2) mW respectively. In both cases the photodiode module measured the intensity with a signal noise equivalent to the least significant bit of the ADC (± 0.7 mV).

3.5 Detailed Design: Routing Module

The optic and routing (OR) module was designed to support either an optical fibre component, such as a circulator, or an optical fibre switch for optical signal routing. When used with an optical component, the module would incorporate a 2×2 switch to enable the selectable insertion of the optic, as shown in figure 3.13, where the input fibre would

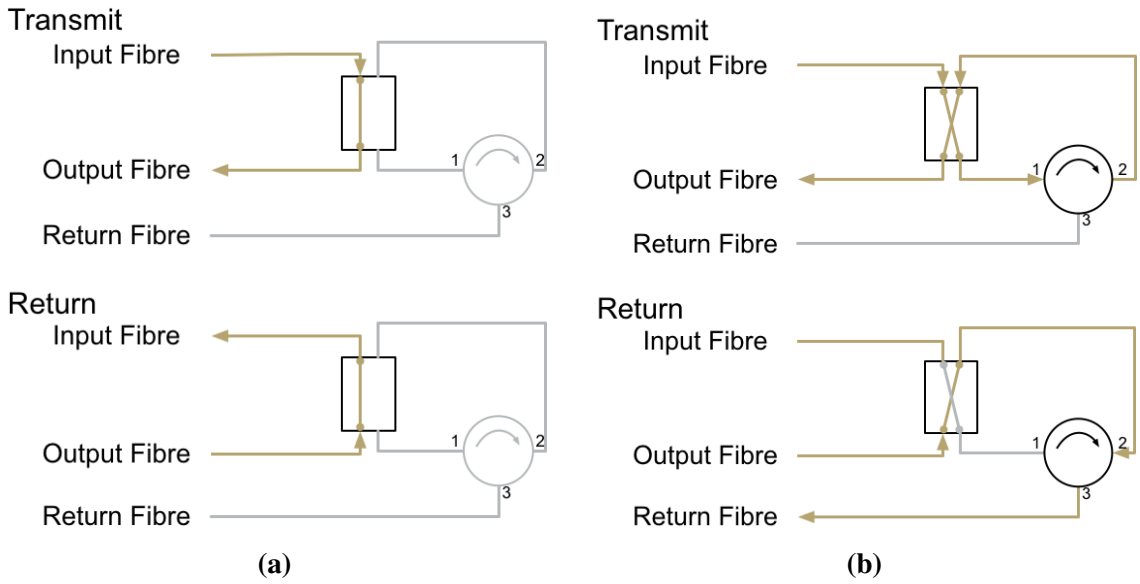

Figure 3.13: OR module 2×2 optical fibre switching arrangement for an optical component, (a) shows the switch in the *bar* state where the circulator is not required, (b) shows the switch in the *cross* state where the circulator controls the flow of optical signals depending on their direction. The circulator directs light entering port 1 to port 2, and light entering port 2 to port 3. Yellow lines denote active optical fibres, with arrows indicating the direction of light propagation. Grey lines denote in-active optical fibres.

be from the optical source module, the output fibre would connect to the sensor, and the return fibre would connect to an optical detector module, as required.

For optical routing, the module was designed to support either 1×4 or 1×8 optical switches using either SM or MM fibre. A block diagram of the module is shown

in figure 3.14, which did not require a micro-processor or FPGA. Instead the binary

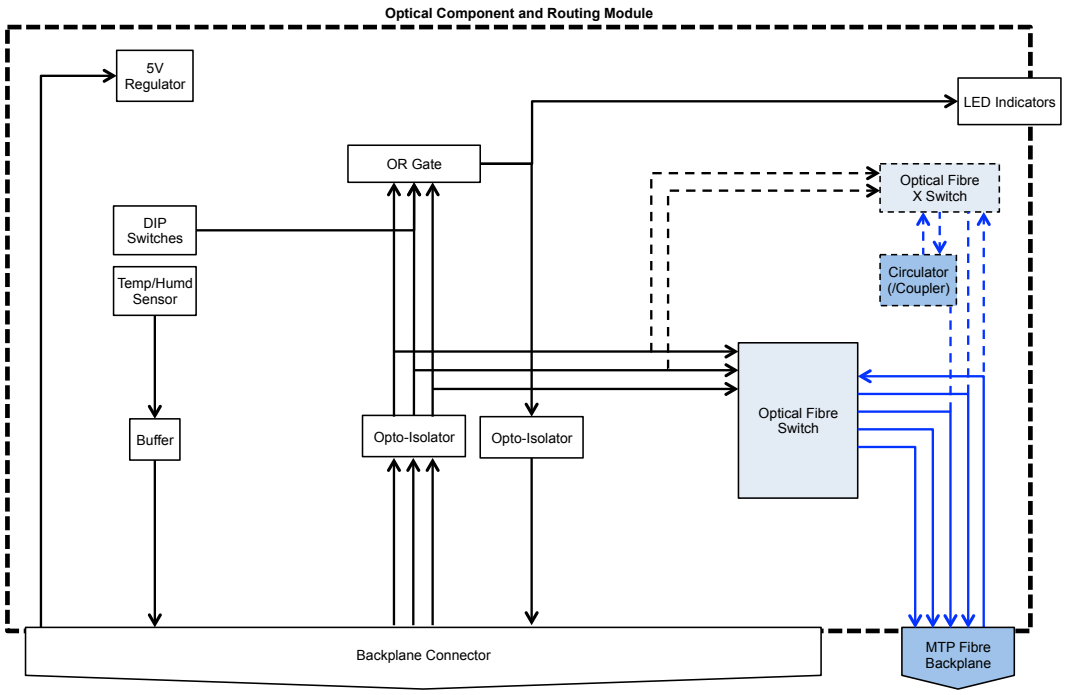

Figure 3.14: Block diagram of the OR module design.

digital mode signals from MB1 module were sufficient to enable selection of the module functions.

A logic OR gate was included to enable an LED indication for when the module was in an activated state, which was considered useful for system-level fault finding. The use of a logic gate was selected due to the lack of a micro-controller or FPGA on the module.

The module was required to utilise the standardised backplane connections, and enable control of 2×2, 1×4, and 1×8 optical fibre switches. Local power regulation and electrical signal buffering was required, along with a local environmental sensor. The dual in-line package (DIP) switch identified to the control card what optical switch or other optical component was installed.

Switch Technologies

The module was designed to support three models of optical switch: the Oplink OFMS22MID1021H1 from Molex (USA), and the 1×4 and 1×8 models from Laser Components (UK). The Oplink switch was based on an opto-mechanical technique [209] whereas the Laser Components devices were based on a piezoelectric technique [210]. Alternative switch technologies exist, including those based on the electro-optic effect, acousto-optic effect, thermo-optic effect, liquid-crystals, MEMS, and SOAs [211]. The

choice of device was based on previous work at AWE [15], COTS switch availability, and cost.

Module evaluation

Multiple modules were assembled, one with a 1×4 optical switch is shown in figure 3.15, and another with an optical circulator is shown in figure 3.16. Both configurations were

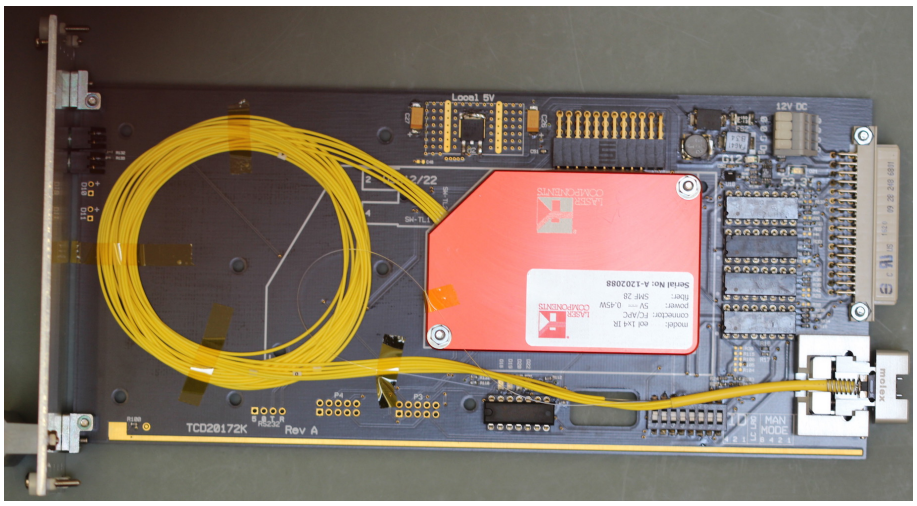

Figure 3.15: Photograph of assembled 1×4 detector routing module. The module is dominated by the optical switch (red) and fibre routing (yellow).

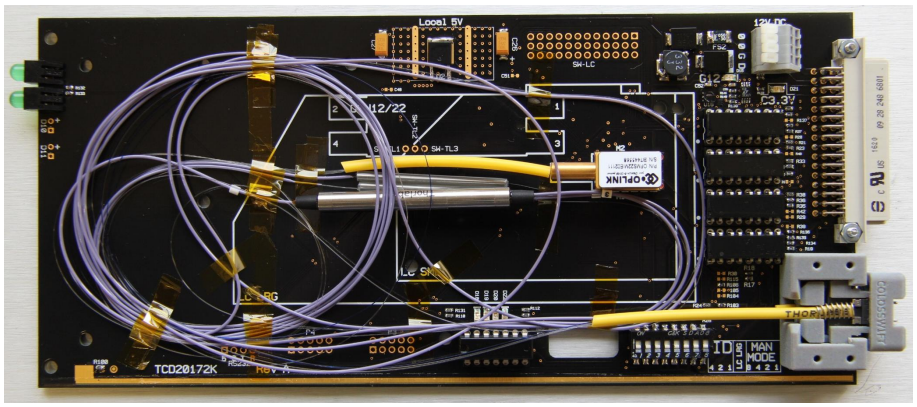

Figure 3.16: Photograph of assembled circulator module, without the module front-panel fitted. Circulator and 2×2 optical switch visible (center).

tested and the optical switches were found to be controllable from the CC2 module via MB1. The temperature and humidity at the module were also measurable via I^2C.

Optical Switch Reliability Tests

In the interrogation system topology, the optical fibre routing was a critical part, enabling connection from the small number of interrogation modules to a large number of optical

sensors. As such, the reliability of the switches was of interest. If a switch were to fail, a replacement module would need to be fitted causing downtime and cost. It was therefore desired that modules would operate for at least 2 years before replacement was required.

An experiment was performed to repetitively switch one of the 1×4 piezoelectric optical switches and evaluate the optical transmission repeatability. The experiment was constructed using a 1550 nm SLED as the optical source, and switching the optical switch from a National Instruments (USA) DAQ controlled from a PC, as shown in figure 3.17. A

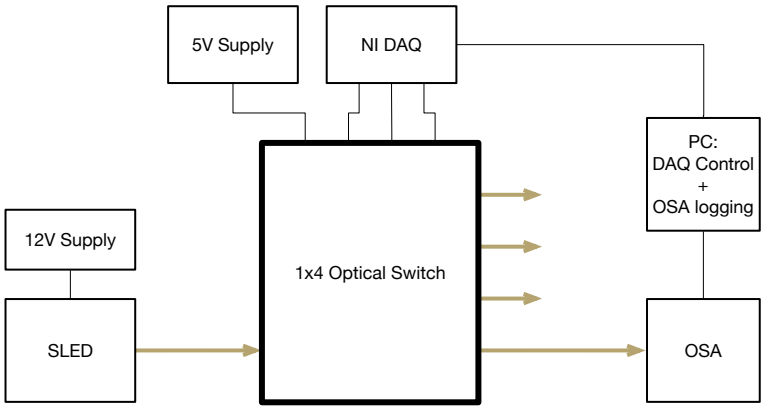

Figure 3.17: Optical switch repeated switch evaluation, experimental configuration. Light from an SLED optical source is routed into the optical switch. One output from the switch is routed into an OSA. Gold lines denote optical fibres, black lines denote electrical connections.

Thorlabs OSA, OSA203, was used to measure the channel 0 output of the switch, logging the data to the PC. The switch was cycled repeatedly, as per the pattern in table 3.3, with a switch every 5 seconds. Every time the switch was on Ch 0, an OSA spectrum

Step	Output Setting
1	Ch 0
2	Ch 1
3	Ch 0
4	Ch 2
5	Ch 0
6	Ch 3
7	Ch 0
8	Ch 4

Table 3.3: Cycle pattern used for the 1×4 piezoelectric optical switch evaluation experiment.

was recorded. Each spectrum was divided into four wavelength bands for integration. Therefore, every 10 seconds four integrated intensity values were collected from the experiment. An example of the SLED recorded spectrum, with integration bands overlaid, is shown in figure 3.18. Integrating in bands enabled wavelength-dependant switching effects to be monitored, as well as the total transmitted intensity, while reducing the

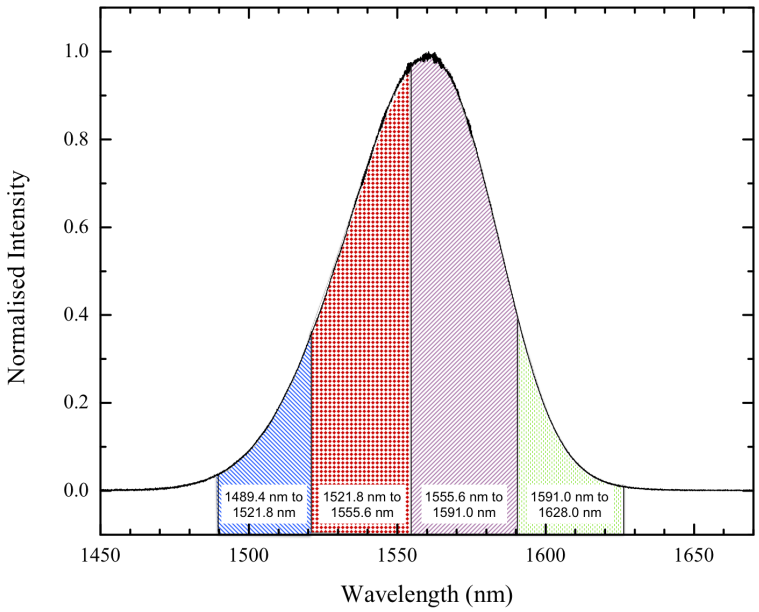

Figure 3.18: Plot of SLED profile, as measured using the OSA through the optical switch. Overlaid are the four bands that were used for integrating the signal.

amount of data to store and analyse.

The experiment was conducted over a period of one week, in two measurement blocks with approximately two days of down-time between. In total over $40\,000$ measurements were captured, which required over $80\,000$ switches, which was estimated in the order of switching cycles required for 20 years of system operation. A time-line of the recorded data is shown in figure 3.19, with a clear discontinuity during system down-time which was attributed to laboratory temperature variations. The integration intensities were each normalised, and deviations are visible from the data shown. Over the measured period the total intensity transmitted through the switch was not observed to decrease, suggesting the switch was still in good operating order at the end of the experiment. Large intensity deviations were rare, but were captured by the experiment, as shown in figure 3.20, which plots the intensities as histograms. It suggests that the measured data was within $\pm 4\,\%$ of the average intensity, but approximately $0.25\,\%$ of the time the optical switch introduced significant optical attenuation. Inspection of a reduced intensity spectrum revealed no discernible wavelength-dependent effects, but a general reduction in transmission through the optical switch was observed.

None of the techniques intended for operation within the interrogation system, FBG measurements, OIES interrogation, or TDLAS, are sensitive to absolute intensity, so variations within $\pm 4\,\%$ was not considered to be problematic. In cases where a poor connection was made, it should be possible to detect automatically and initiate a re-switch

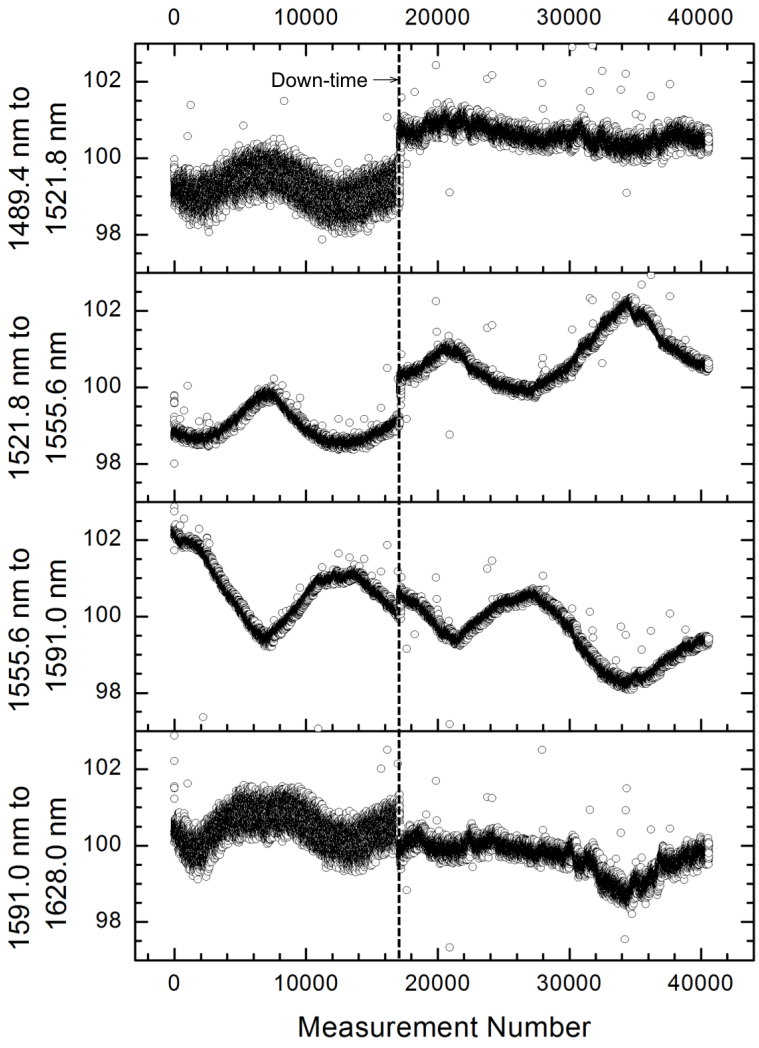

Figure 3.19: Plot of switch intensity measurements time series. Over 40 000 measurements were captured within the duration of the experiment.

sequence. This control routine was recommended for inclusion with the system control card programming.

The intensity variations seen in figure 3.19 suggested sensitivity to laboratory temperature variations and also correlation between the integration bands. During the experimental down-time the building heating system was activated, which was attributed to the discontinuity visible in the data. The variations were considered to either be caused by temperature effecting the SLED peak emission wavelength, or temperature effects causing wavelength-specific losses within the switch. Figure 3.21 shows the correlation in intensity variations between the lower central band (1555.6 nm to 1591.0 nm), and the other three.

Strong negative correlation is visible between the lower central band, and the (red) upper central band, but correlation is less clear for the other two bands. This suggested the peak of the SLED was varying in wavelength, but the overall emission shape was more

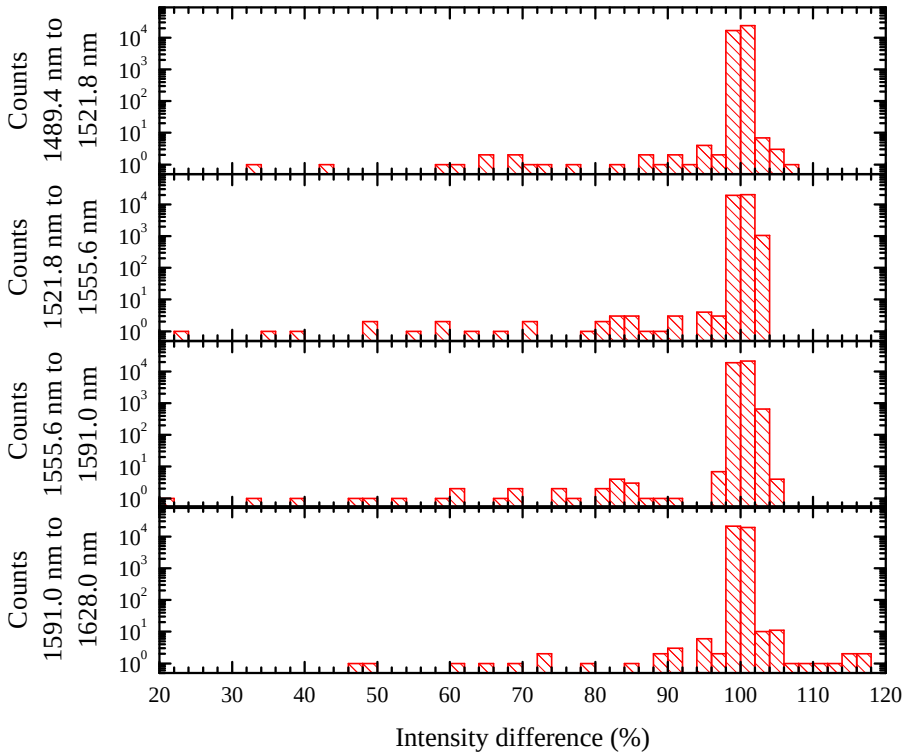

Figure 3.20: Plot of switch performance histograms. The average intensity within each integration band was normalised to 100 %. The vertical scales are logarithmic.

consistent. It was thought unlikely the optical switch would cause such a wavelength specific effect, which has caused a strong negative correlation between two neighbouring bands.

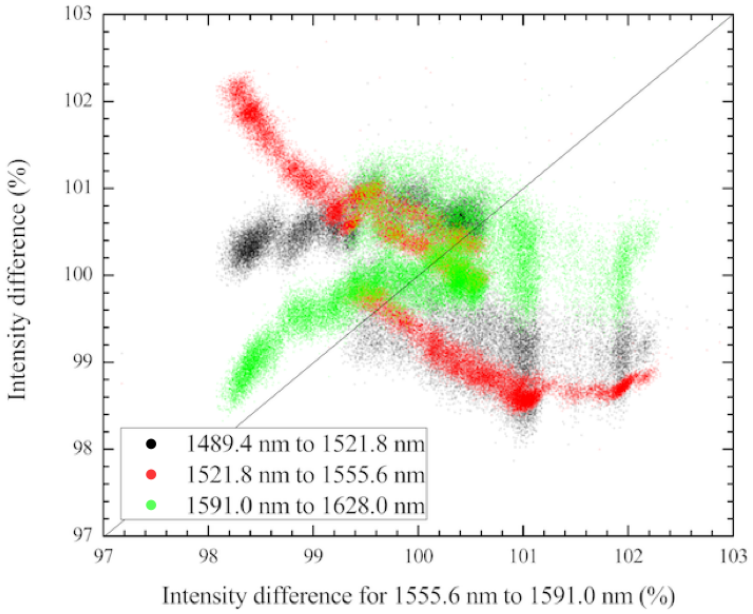

Figure 3.21: Plot of switch intensity measurement correlation between the 1555.6 nm to 1559.0 nm integration band and the other three. Trends of data points with positive or negative gradient denote positive and negative correlation respectively. Ideally no trends would be visible, suggesting a no-correlation result.

Conclusions

The OR module was designed to support optical components and optical fibre switches. Modules were manufactured and assembled for evaluation and were found to function in both roles. The stability of repeatedly using an optical fibre switch, based on piezoelectric technology, was assessed, and deemed suitable for multi-year use within the interrogation system. Further evaluations conducted in a similar way would benefit from temperature-stabilising the SLED, either by using a device with integrated TEC or by placing it within a temperature-stable chamber.

3.6 Detailed Design: Spectrometer Module

The OSA module was intended to provide an option for the measurement of FBG sensors, when coupled with an SLED (on the SLED module), and routed through a circulator (on an OR module). A secondary use of the module could be to verify the wavelength stability of optical sources within the interrogation system, to provide added measurement confidence between system calibration schedules.

Recording a spectrum is the process of measuring the signal intensity as a function of frequency. In the case of an optical spectrum analyser, or spectrometer, it can be achieved in a number of ways. One of the most popular is to use a dispersive optical element, such

as a diffraction grating, to separate frequencies of light onto different spatial positions; a camera can then measure the intensity in each position to record the spectrum [212].

The technique chosen in this work was to use a tunable filter to sweep over the wavelength range of interest, while a photodiode recorded the signal intensity. The block diagram of the module is shown in figure 3.22, showing a micro-controller based

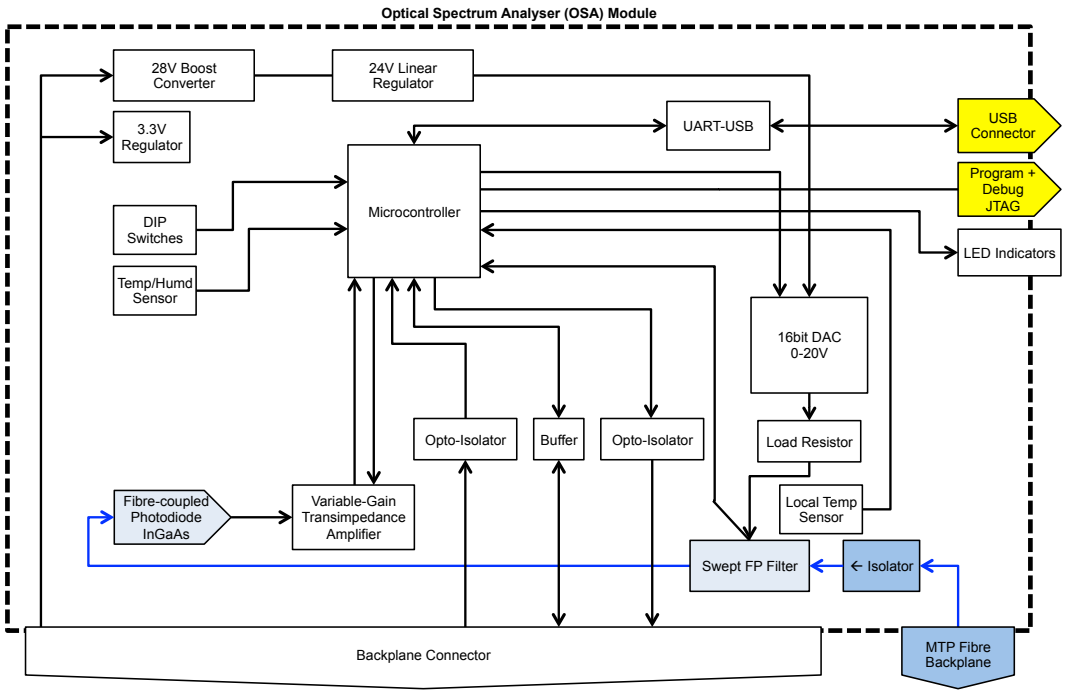

Figure 3.22: Simplified block diagram of the OSA module featuring a swept Fabry-Pérot filter and photodiode. Blue lines denote optical fibre connections, dark blue fill denotes optical components and light blue fill denotes electro-optic components. Yellow fill denotes connections and components only used during programming and testing.

system which was able to drive a swept Fabry-Pérot filter between $0\,\mathrm{V}$ and $20\,\mathrm{V}$ with a $0.3\,\mathrm{mV}$ resolution. A temperature sensor is located close to the filter to enable temperature compensation of the filter response. An optical isolator is included to prevent reflections from the filter travelling back into the interrogation system.

The OSA module was required to interface with the interrogation system using the standardised backplane connections, and to function in the region of the SLED module (centre on $1550\,\mathrm{nm}$), with a bandwidth of $100\,\mathrm{nm}$, and resolution of $200\,\mathrm{pm}$. These specifications were to enable the OSA to be used for FBG interrogation with a peak tracking resolution of $\pm 5\,\mathrm{pm}$.

Spectrometer filter selection

The key component to this spectrometer design was the tunable filter. This was also the most financially costly component of the module, so care in the correct product

selection was required. Commercially available filter specifications were reviewed, and mathematical simulations using Mathworks (USA) Matlab were conducted to assist in the filter selection.

A Fabry-Pérot filter was selected due to their reported use for this function [49, 213–216], ability to posses narrow bandwidths, large FSRs, and low electronic control voltages.

Tunable Fabry-Pérot filters were available in varying finesse ($\mathcal{F}$) [217]. By first approximation, the higher the $\mathcal{F}$, the better the wavelength resolution of the spectrometer, but budgetary constraints limit the selection since the cost is directly proportional to the $\mathcal{F}$. To assist in the cost/value assessment, mathematical modelling using MathWorks (USA) MATLAB was conducted. This spectrometer was primarily designed for measuring FBG reflection peak wavelength values, so a typical FBG reflection spectrum is first modelled.

The model for a FBG within an optical fibre with a refractive index of ≈ 1.47, a grating length of $10\,\text{mm}$, and a refractive index difference between layers of 5×10^{-5}, was written using the transfer matrix method, which is a technique commonly used for optical systems [45,46,218–224], and is discussed further in Chapter 7. Figure 3.23 shows the FBG spectra from the simulation. White noise was added to three of the spectra to aid

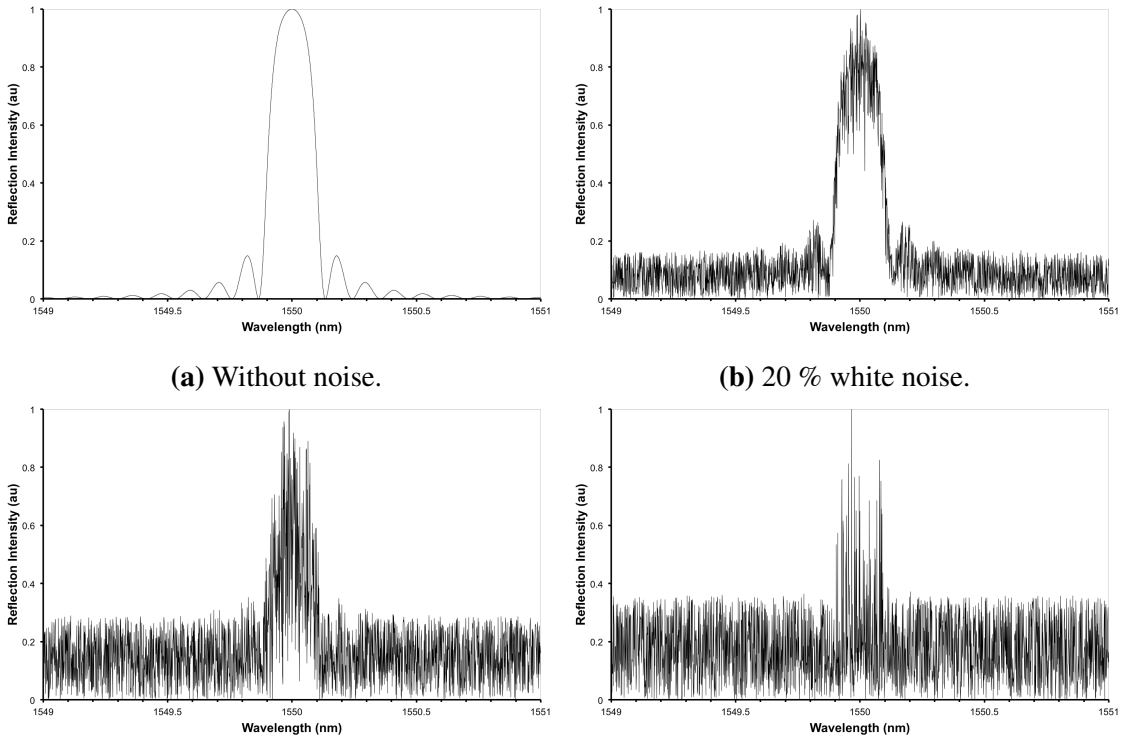

(a) Without noise.

(b) 20 % white noise.

(c) 50 % white noise.

(d) 80 % white noise.

Figure 3.23: Simulation of the transfer matrix modelled fibre Bragg grating profile with and without noise.

in the evaluation of each filter $\mathcal{F}$. It was thought unlikely for measured signals to contain more than the simulated $20\,\%$ white noise.

COTS filters are available with a $\mathcal{F}$ of 500, 1000, 2000 and 10000 [217]. Each of these filters was modelled for a single fringe centred at $1550\,\text{nm}$, as shown in figure 3.24.

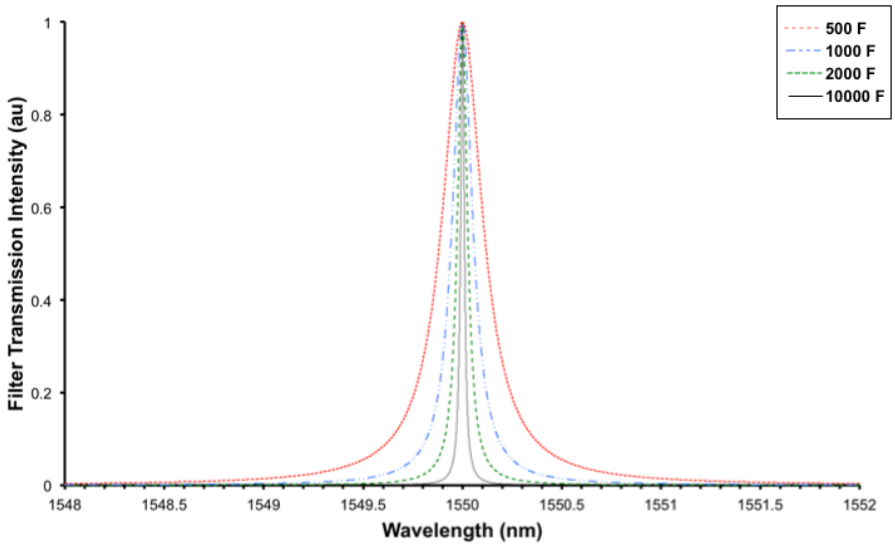

Figure 3.24: Simulation of Fabry-Pérot filters. Red dotted line represents the $500\mathcal{F}$ filter, blue long-dashed represents $1000\mathcal{F}$, green short-dashed $2000\mathcal{F}$, and black solid line the $10000\mathcal{F}$ filter.

The key parameters of each filter are listed in table 3.4.

Finesse, $\mathcal{F}$	**FSR**	**FWHM**	**Insertion Loss**
500	120 nm	240 pm	2.5 dB
1000	120 nm	120 pm	3 dB
2000	120 nm	60 pm	3 dB
10000	240 nm	22 pm	4 dB

Table 3.4: Summary of commercially available swept Fabry-Pérot filters.

Each filter simulation was mathematically convolved with the simulated FBG reflection peak at each simulated noise level, to simulate an OSA result. The results are shown in figure 3.25, and the calculated peak characteristics shown in table 3.5.

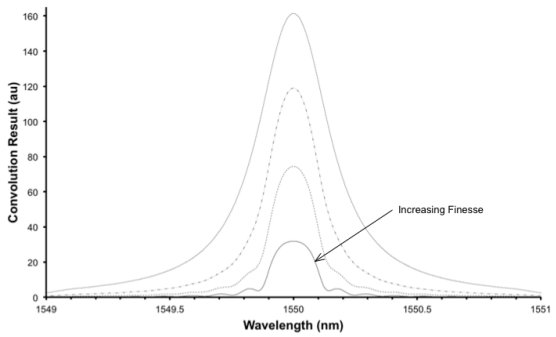

(a) Without noise.

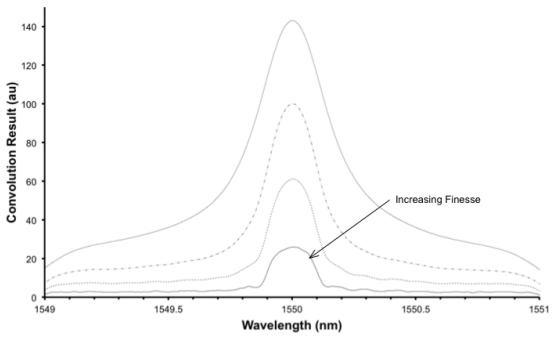

(b) 20 % white noise.

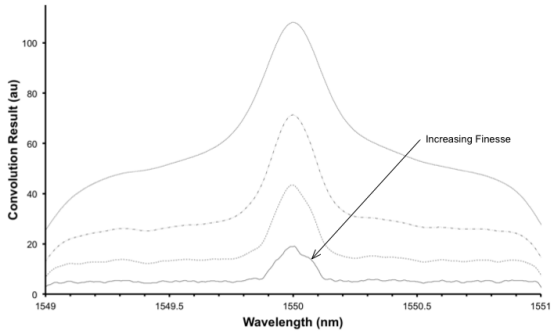

(c) 50 % white noise.

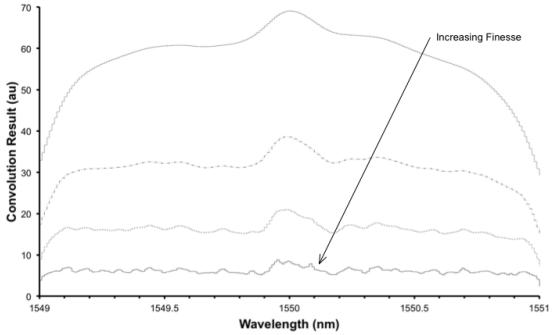

(d) 80 % white noise.

Figure 3.25: Convolution simulation of simulated Fabry-Pérot filter with a simulated FBG reflection, with and without simulated noise on the FBG spectrum. Dotted line represents the $500\mathcal{F}$ filter, long-dashed represents $1000\mathcal{F}$, short-dashed $2000\mathcal{F}$, and solid line the $10000\mathcal{F}$ filter.

FBG Noise	Filter $\mathcal{F}$	Peak Deviation	FWHM	SNR
Raw FBG	-	1550.000 nm	192 pm	-
None	500	**0 pm**	340 pm	-
	1000	**0 pm**	240 pm	-
	2000	**0 pm**	206 pm	-
	10000	**0 pm**	194 pm	-
20 %	500	**2 pm**	341 pm	5.8
	1000	**2 pm**	237 pm	7.1
	2000	4 pm	200 pm	7.0
	10000	4 pm	192 pm	8.7
50 %	500	**0 pm**	313 pm	2.2
	1000	−1 pm	212 pm	2.7
	2000	−3 pm	179 pm	3.2
	10000	5 pm	165 pm	3.8
80 %	500	**0 pm**	248 pm	1.1
	1000	−10 pm	175 pm	1.2
	2000	−10 pm	166 pm	1.3
	10000	−50 pm	125 pm	1.4

Table 3.5: Summary of simulated Fabry-Pérot filter performance at measuring a simulated FBG reflection peak with and without noise. Values in bold font show the preferred filter at that noise level. Preference selects narrowest variance uncertainty that encompasses the correct value.

The deviation in the peak wavelength, identified with the filters, was larger for the higher finesse filters, likely due to their ability to resolve the noise to a higher degree than the lower finesse filters. At lower finesse the noise was effectively averaged and therefore had a smaller influence, but at the expense of full-width half-maximum (FWHM) and signal-to-noise ratio (SNR). As previously noted, the simulated noise levels exceeded those predicted to be experimentally observed, but the simulations show likely responses of this module if the noise levels were to increase during the experiment lifetime.

From the analysis of the simulated convolutions, the filter selected for use within this OSA module was the $2000\mathcal{F}$ version. This filter was considered to be the balance between small FWHM values, small peak deviations, and cost.

Module performance evaluation

The OSA module was designed, manufactured, and assembled for evaluation. A photograph of the partially-assembled module can be seen in figure 3.26. The Micron

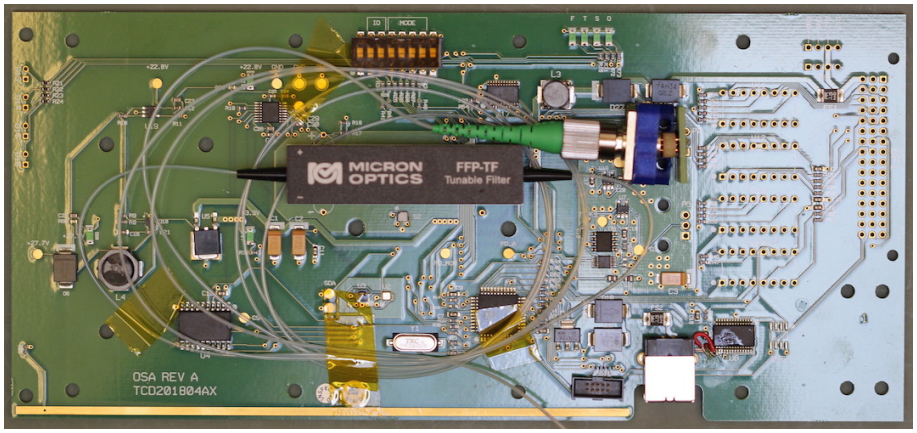

Figure 3.26: Photograph of partially assembled OSA module. Connectors and electrical buffers on the right hand side of the image have not been populated in this photograph.

Optics (USA) tunable Fabry-Pérot filter is clearly visible dominating the centre of the PCB.

The module was fully assembled and its electrical operation was verified successfully. Initially a test program was written which varied the filter voltage, and therefore wavelength, while transmitting the measured photodiode signal to a PC over the module's USB connection. This program enabled the OSA module optical performance to be evaluated.

An evaluation experiment was assembled as shown in figure 3.27. An SOA was used to provide an amplified spontaneous emission (ASE) broadband source for the evaluation. The light was passed through a low finesse ($10\mathcal{F}$ [217]) Fabry-Pérot etalon to provide

a regular fringe pattern. The output from the etalon was split using an optical fibre directional coupler, with one half feeding the OSA module, and the other entering a fibre coupled reference OSA, a Thorlabs (USA) OSA203 [225]. The regularity of the Fabry-Pérot peaks in frequency was used to linearise the tunable filter response and enable a conversion from filter voltage to wavelength to be created, based on a 2nd order polynomial.

The two resulting spectra from the experiment are shown overlaid in figure 3.28.

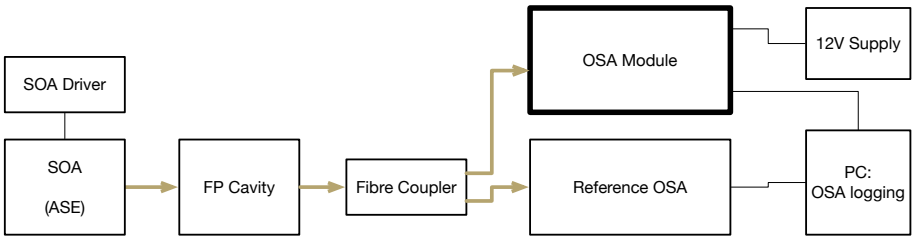

Figure 3.27: OSA module experimental evaluation configuration, containing a SOA operating as an ASE source, a low-finesse Fabry-Pérot etalon, a directional optical coupler, and a reference spectrometer.

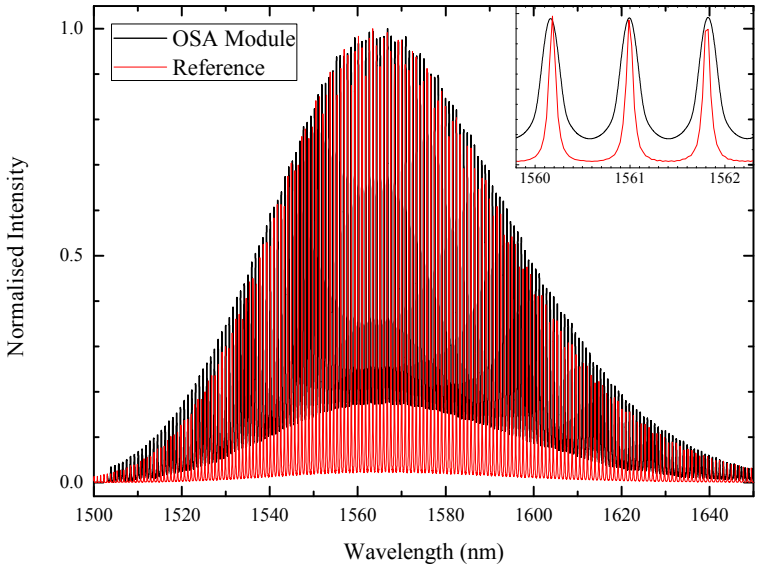

Figure 3.28: Plot of OSA module measurements compared to reference OSA results of a Fabry-Pérot etalon.

Phasing between the two sets of peaks can be observed, suggesting the voltage to wavelength fitting for the OSA module was not exact. Based on the analysis of the resolved peaks (figure inset), the OSA module was estimated to have a resolution of (140 ± 10) pm. For reference, the OSA203 had a resolution of 60 pm at 1550 nm [225]. It was noted the OSA module was able to measure over a 150 nm bandwidth without FSR or control voltage (0 V to 20 V range) limitations.

Conclusions

The OSA module was designed, manufactured, assembled, and evaluated. Theoretical simulations were used to support the selection of the Fabry-Pérot filter finesse used as the basis of the spectrometer.

The module was evaluated to function as expected, and to operate in the region of 1550 nm with a bandwidth over 150 nm. The resolution of the spectrometer was evaluated as being (140 ± 10) pm. These values satisfied the requirements for the module and the resolution was smaller than the typical FWHM for a FBG, 250 pm [19].

Further development of the module could apply corrections to improve the voltage to wavelength fit, and characterise the filter sufficiently to enable reverse-convolution analysis of the captured data, which could significantly improve the module resolution.

3.7 Detailed Design: Swept Laser Module

The swept laser module was designed to provide an option for the measurement of FBG sensors, when coupled with a photodiode (on the PD module), and routed through a circulator (on an OR module). This method was an alternative to using the SLED and OSA modules.

The module block diagram, including the laser optical arrangement, is shown in figure 3.29.

The swept laser was constructed from optical fibre coupled components, with the optical gain being provided from an SOA. A Fabry-Pérot tunable filter, of the same type used in the OSA module, was used to select the lasing wavelength. Two optical fibre Faraday-rotation isolators were used to block the back-reflected light from the filter from entering the SOA, and to ensure the cavity operated in the correct direction. A 50:50 optical fibre directional coupler was used as the laser output coupler. The laser was designed to operate with an output intensity of up to 10 mW. Similar arrangements of laser cavities have been previously demonstrated [122].

The module featured a CC drive circuit for the SOA along with a TEC driving circuit, both similar to those on the SLED module. The tunable filter was driven in the same way as on the OSA module. A *pico*Wave® from Micron Optics (USA) [226] was included in the design, which contained a temperature stabilised low finesse Fabry-Pérot etalon and FBG. These were included to enable the module to monitor its wavelength scan during operation, enabling an internal self-calibration. A TEC driving circuit was included

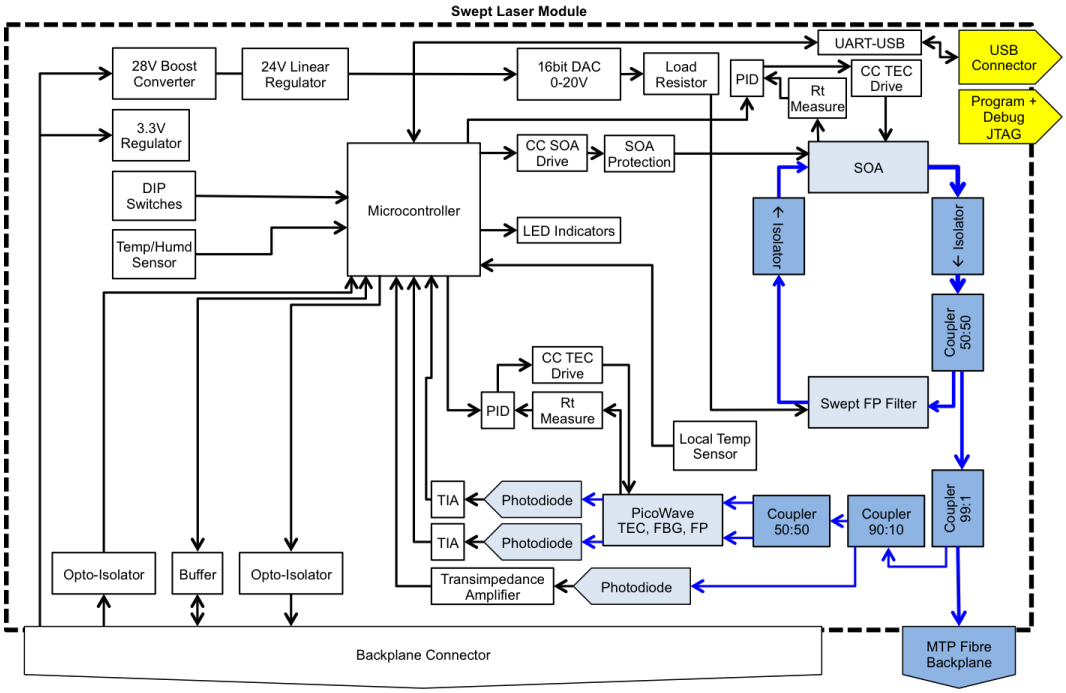

Figure 3.29: Block diagram of the Swept laser module design. Blue fill denote optical and optoelectronic components, blue lines denote optical fibre connections.

to stabilise the *pico*Wave®, along with two monitoring photodiodes. An additional monitoring photodiode was included to enable the module to monitor the laser optical output power.

The swept laser module was required to interface with the interrogation system using the standardised backplane connections, and to emit light tunable around 1550 nm. A sweep range of 80 nm was required with a laser line-width of 150 pm (18.7 GHz). The output optical power was to be below 10 mW to result in the laser being classified as a Class 1M laser in the wavelength range 1400 nm to 4000 nm [179]. The module was also required to be capable of measuring a COTS FBG temperature sensor.

Breadboard laser evaluation

The laser design was initially tested on optical breadboard using a commercial laser driver to control the SOA and a signal generator to control the filter. A photograph of the breadboard layout is shown in figure 3.30.

The configuration shown differed from the one chosen for final operation, since the tunable filter was located before the output coupler, but in figure 3.29 it is located after. The move to after the coupler was made to reduce the optical power passing through the filter; the filter had the lowest optical power damage threshold of the components used. The move potentially enabled the laser to operate at twice the optical power, since the

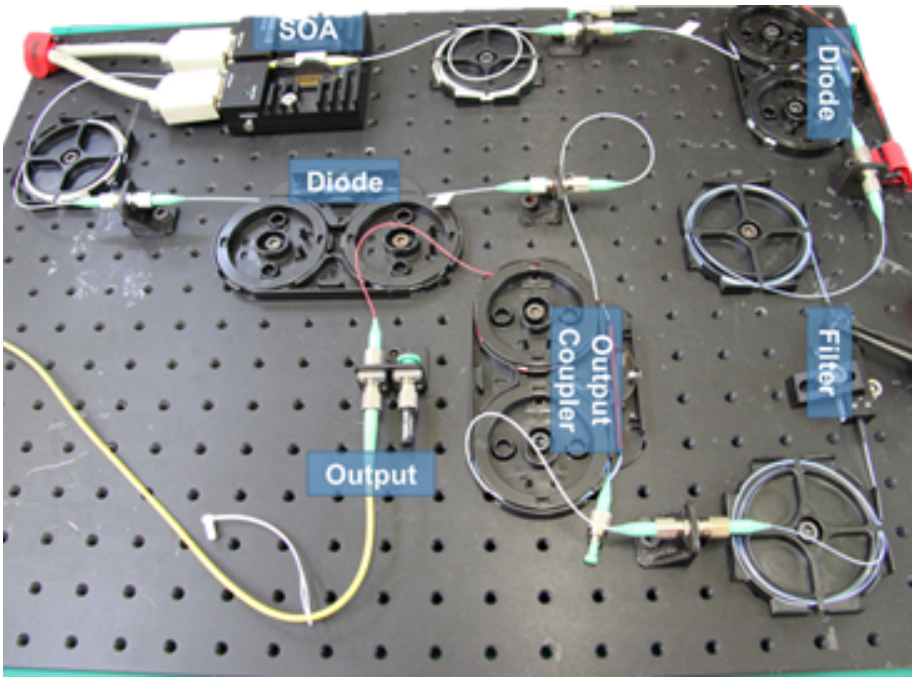

Figure 3.30: Photograph of breadboarded swept laser testing, with labels marking the position of the SOA, optical diodes (isolators), Fabry-Pérot filter, output coupler, and output fibre.

output coupler chosen was $50\,\%$. The potential disadvantage of the move was that on laser start-up and during wavelength changes, wavelengths other than those selected by the filter could potentially be emitted by the laser.

The laser was confirmed to function as expected and was measured to have a peak output power of $(9.6 \pm 0.1)\,\mathrm{mW}$ when the SOA was operated at a constant current of $300\,\mathrm{mA}$ at $25\,^{\circ}\mathrm{C}$. The wavelength sweep range was not evaluated, but it was confirmed using an OSA that a change in output wavelength was occurring. The laser line-width was also not evaluated, since the development continued to the design and manufacture of a module-based swept laser. The completed module was evaluated for output power, sweep range, and line-width.

Module evaluation

Based on the promising breadboard laser evaluation results, the design was completed, and the module was manufactured, and assembled. A photograph of the assembled module is shown in figure 3.31. The module was constructed from two PCBs, with the upper board only containing the SOA in a *butterfly* package and the lower board containing all the remaining components and circuitry. The upper board was required to enable efficient heat-sinking to the SOA package, which was necessary due to its internal TEC, and assisted by the large white heatsink visible in the figure. During assembly, the

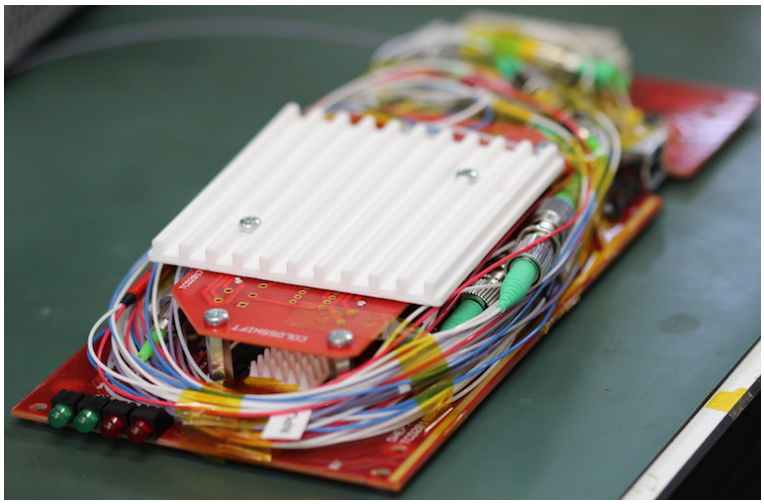

Figure 3.31: Photograph of assembled swept laser module, without module front panel fitted.

optical fibres were not shortened and fusion spliced, as intended, since it was considered preferable to first confirm correct module operation. As a result the length of optical fibre and number of connectors exceeded the space allocated on the module. The *pico*Wave® device was also not fitted, along with its corresponding coupler and two photodiodes. The module was electrically tested and all the functions were found to operate as intended.

The laser wavelength sweep range was measured by passing its output through a Fabry-Pérot etalon and into an OSA, as were used to evaluate the OSA module. The resulting data as shown in figure 3.32; the OSA measurement saturated so the on-module intensity monitor data is also shown to indicate laser output intensity. The laser output was evaluated to sweep from $1501\,\text{nm}$ to $1646\,\text{nm}$.

An output power considered sufficient for sensing applications, $> 0.5\,\text{mW}$, was

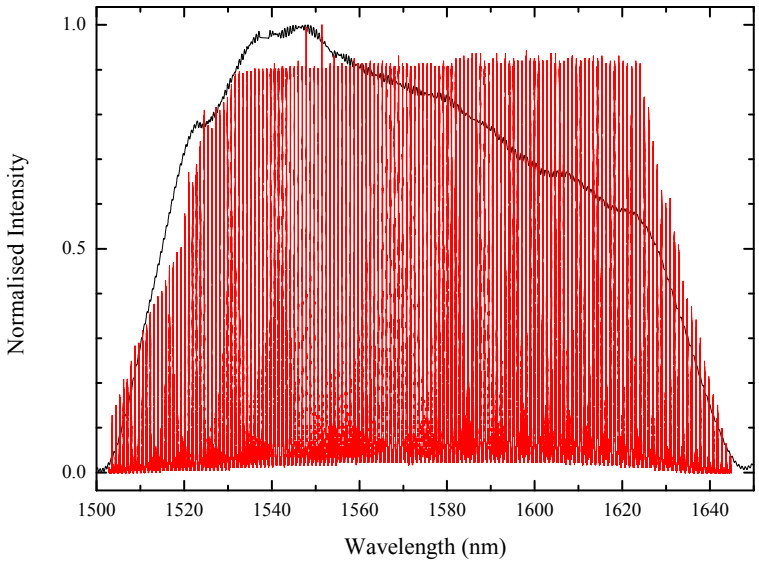

Figure 3.32: Swept laser module wavelength sweep range measurement. Red line shows the data from the OSA and a Fabry-Perot etalon. Black line shows the on-module intensity monitor output.

measured from (1503.0 ± 0.7) nm to (1644.0 ± 0.7) nm, suggesting a sweep range of (141 ± 1) nm. This measured sweep range exceeded the requirement for a sweep of 80 nm, and satisfied the requirement for operation around 1550 nm.

The laser line-width was evaluated by analysing the Fabry-Pèrot etalon result during a laser sweep. The etalon peak at 1560.6 nm was measured to have a FWHM of (140 ± 1) pm (17.2 GHz), and is shown in figure 3.33. The etalon contained peaks of

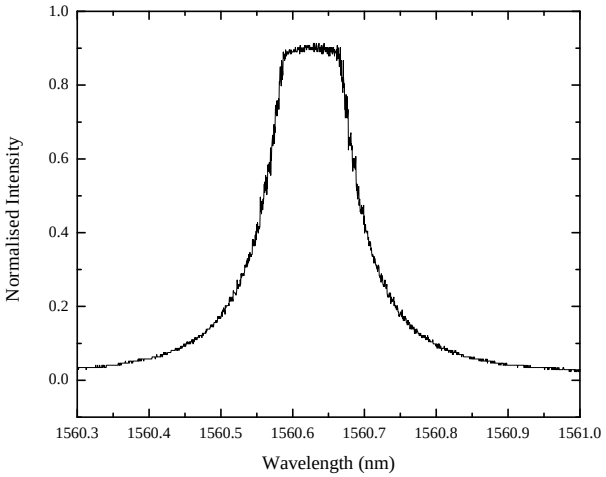

Figure 3.33: Measured Fabry-Pérot etalon peak for the swept laser module, recorded on the OSA.

width less than 10 GHz, therefore contributing minimally to the measurement. The OSA measurement of the etalon peak saturated and failed to provide the full shape, instead clipping the highest intensity signals. Measuring the width of a saturated peak was conducted by first masking all data points from the top of the profile with normalised intensities over 0.8, then peak fitting to the data. The fitted peak was then used to conclude the measured value satisfied the module requirement for a line-width below 150 pm.

The peak optical power was measured using a calibrated fibre-coupled power meter to be (9.8 ± 0.1) mW, which satisfied the laser optical power requirement.

The swept laser module was used to measure a Micron Optics (USA) os4100 FBG temperature sensor [22], as shown in figure 3.34. The measurement resolved the FBG with a high signal to noise ratio, and upon inspection (figure inset), the peak was considered well resolved and of the expected shape. There were 68 data-points over the peak, suggesting a peak fitting algorithm would produce a high probability estimation of the FBG peak wavelength. The module was considered to have demonstrated the ability to measure a FBG sensor, satisfying the module requirement.

It was speculated the swept laser could also prove useful in measuring low finesse Fabry-Pérot interferometers, such as those present in FFP barometric pressure sensors

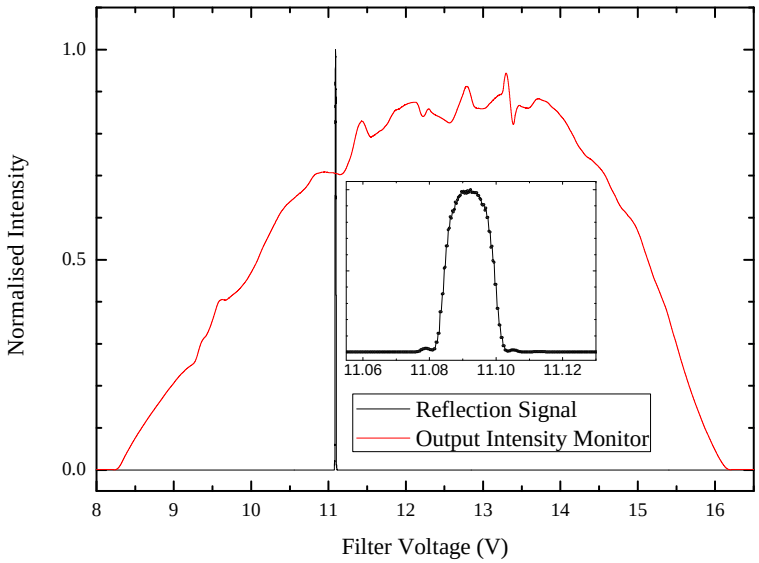

Figure 3.34: Plot of swept laser module interrogating an FBG temperature sensor. The black line denotes the reflection intensity, as measured by a photodiode. The red line shows the on-module intensity monitor output. Insert shows the measured reflection peak with a zoomed in filter voltage range.

(Chapter 6), or those demonstrated for measuring material movement [227, 228]. To evaluate the laser for this function, an air-cavity interferometer was formed at the end of a short section of multi-mode optical fibre by spacing two parallel-polished fibres apart by $150\,\mu m$. The reflection signal and on-module laser intensity monitor measurements are shown in figure 3.35.

Periodic intensity variations, which could have been interferometric fringes, were visible in the reflection signal, but the visibility was not considered high, likely due to the use of multi-mode optical fibre and the low-reflectivity of the glass fibre surfaces. A fast Fourier transform (FFT) of the measured data was performed and the resulting data is shown in figure 3.36.

A dominant peak was visible in the FFT data, which corresponded to the gap between the two fibres, which was evaluated to be $(145 \pm 5)\,\mu m$. The measurement using the laser module and FFT technique was confirmed using a commercial swept-laser FBG interrogator [21, 119] with a resulting value of $(142 \pm 20)\,\mu m$, showing agreement. The swept laser module had a wider wavelength sweep range than the commercial unit, and a higher wavelength resolution, resulting in the reduction in measurement uncertainty.

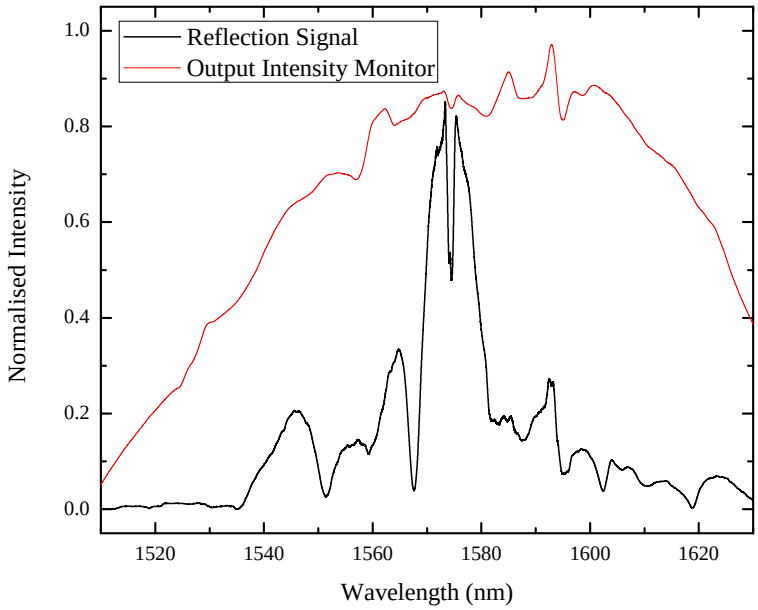

Figure 3.35: Plot of swept laser module interrogating a Fabry-Pérot interferometer formed by a gap between two fibres. The black line denotes the reflection intensity, as measured by a photodiode. The red line shows the on-module intensity monitor output.

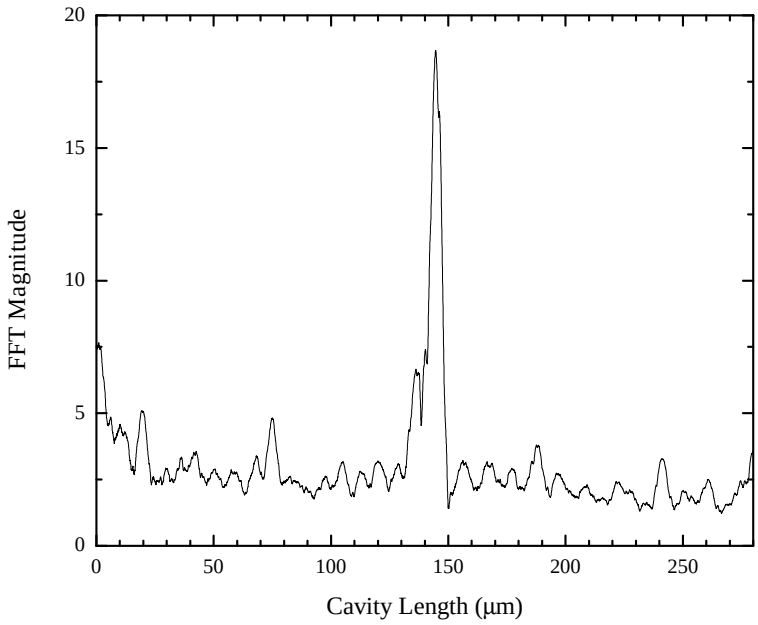

Figure 3.36: FFT of swept laser module measurement while interrogating a Fabry-Perot cavity formed by a fibre gap.

Conclusions

A swept laser module was designed, tested, manufactured, and evaluated. The module was intended to perform FBG measurements, and was demonstrated as capable to achieve that requirement. The laser module satisfied its requirements and was evaluated to sweep over (141 ± 1) nm in the 1550 nm range. The laser line-width was evaluated to be (140 ± 1) pm, and the peak output power of the module was (9.8 ± 0.1) mW. The electronic design of the module was evaluated and found to operate as expected. The module was also demonstrated measuring low finesse Fabry-Pérot interferometers with a mirror separation in the 150 µm range.

Future work on the module design would evaluate the use of the *pico*Wave® device and required programming to enable on-module continuous wavelength calibration. Incorporating into the programming the ability to peak fit the FBG wavelength, and perform an FFT for FFP sensing, could reduce the amount of data which would need to be stored and later analysed.

3.8 Detailed Design: OIES Module

The OIES integrated interrogation module was required to provide optical power to a remote, optically powered, sensor node, and subsequently receive the optical return data from the module. The OIES optically powering technique is discussed in detail within Chapter 8.

The interrogation module was required to interface with the interrogation system using the standardised backplane connectors, and to support a 1310 nm diode laser with an optical power output of 50 mW which was used to provide power to the remote OIES node. An optical circulator and photodiode were also required to measure the modulated optical data return signal from the remote sensor node.

A block diagram of the module is shown in figure 3.37, detailing the key features, such as a laser diode and associated constant current supply, two photodiodes, a micro-controller, and local sensors.

The micro-controller was programmed to operate as described in the flowchart shown in figure 3.38. The module would activate and run a self-test initialisation routine, which if passed would then initiate local readings of temperature, pressure, humidity, laser drive current, laser drive circuit temperature, and photodiode intensity levels. These values were checked against expected values and if deviations were small the operation

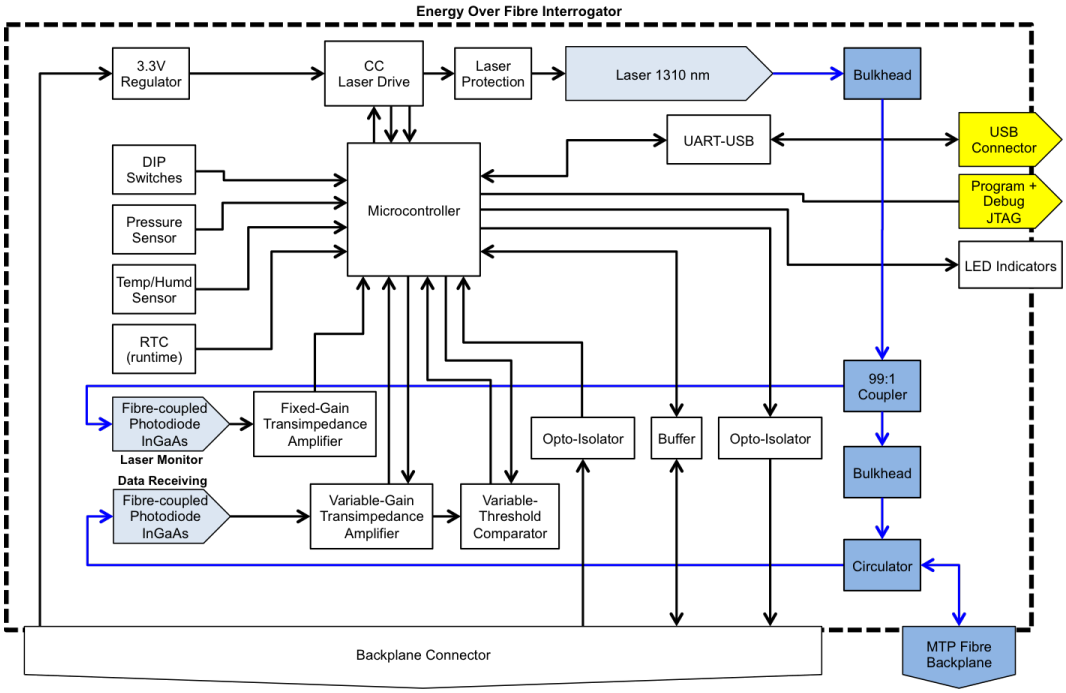

Figure 3.37: Block diagram of the OIES integrated interrogation module design.

continued. If the module mode value, as set by CC1 or CC2 via MB1, enabled the module's *automatic mode* the program would continue, else the module would wait until instructed. Once in the correct mode, the laser was activated by enabling the CC laser drive circuit. A short time after activation, local readings were taken to ensure the laser was operating as expected; if not, the laser was deactivated. Once the laser was on, the module would wait for data to be detected from the remote sensor node. If the received data was successfully parsed as complete and valid, it was transmitted to the control card(s) via MB1. The module would periodically run self-check readings to ensure it was operating as expected, and update a life-time runtime counter to aid in fault prediction. The periodicity of these checks was controlled by the on-board real time clock (RTC) via an interrupt flag.

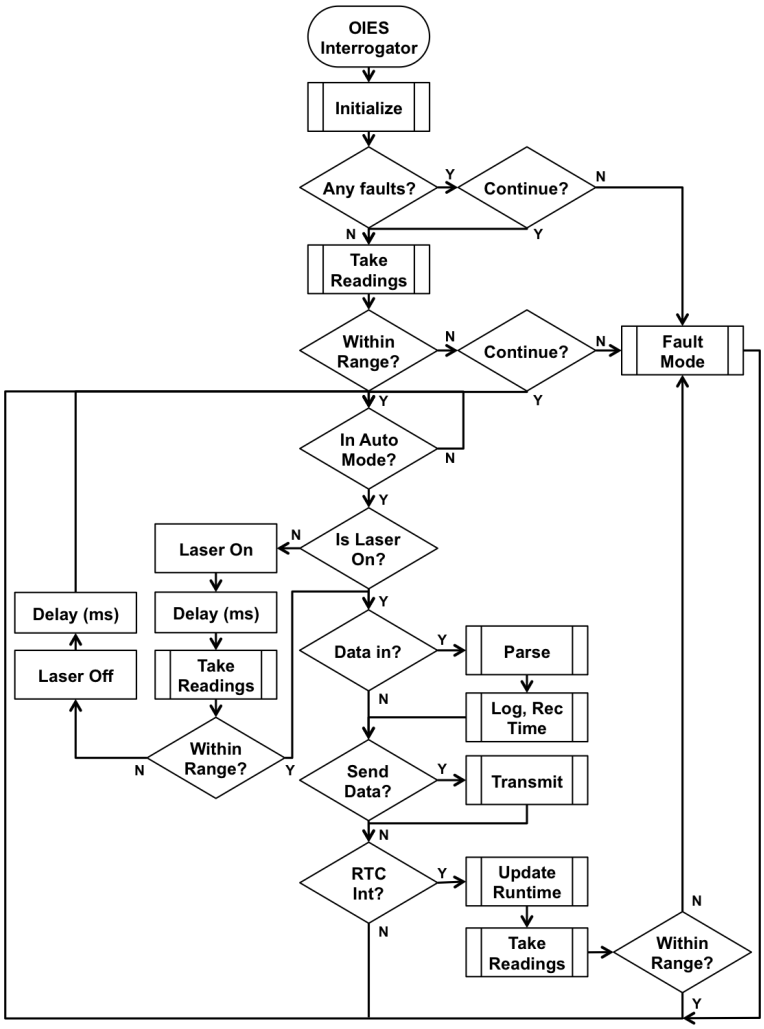

Figure 3.38: OIES interrogation module program flow diagram.

Module evaluation

The module was assembled and tested along with the optically isolated electronic sensor remote node, discussed in Chapter 8. A photograph of the assembled module is shown in figure 3.39.

Experimental evaluation of the module confirmed it performed the expected functions, successfully received data from the remote node, and provided the data to the interrogator control card (CC2). All functions were tested and found to operate correctly.

It was found the return signal intensity could vary, and monitoring of the intensity level to provide corrective adjustment of the signal photodiode gain and comparator threshold was required. This was achieved through a simple control loop within the programming (not shown in figure 3.38). The control loop ensured the module data burst was consistently interpreted correctly, by tracking the previous data peak intensity. The data peak intensity was measured using the micro-controller ADC. The transimpedance

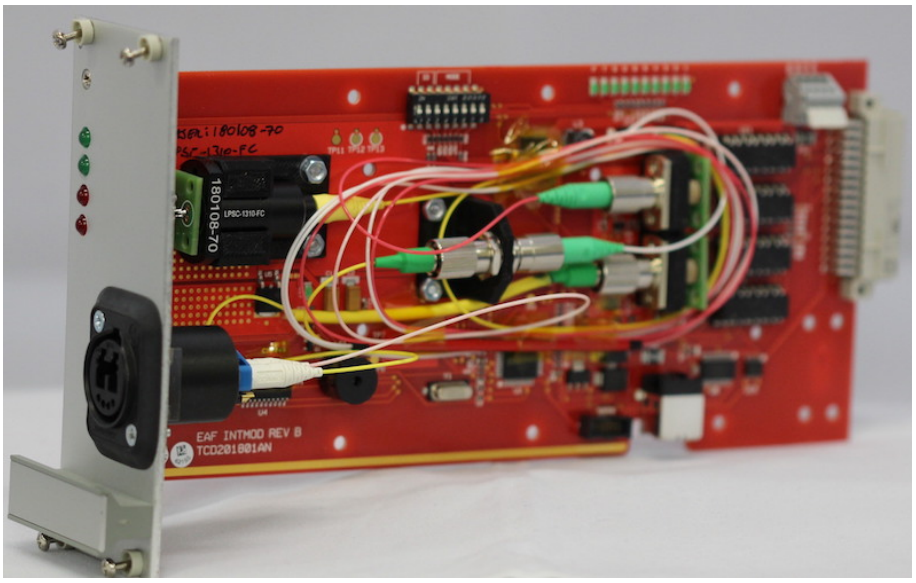

Figure 3.39: Photograph of assembled OIES interrogation module. A front-panel optical connector was fitted for developmental use.

amplifier gain was then varied based on the ADC value. This process was repeated every time data was received from the remote node, and enabled all data bursts to be correctly received during evaluation.

Conclusions

An integrated interrogation module for the optically isolated electronic sensor remote node, discussed in Chapter 8, was designed, assembled, and evaluated. It was found to function correctly and a number of duplicate modules were later assembled. It was also found possible to utilise the module to drive a 200 mW laser diode at 1310 nm, which was used in the later revision of the OIES technique.

3.9 Alternative Module Configurations

During the development of the interrogation system and modules, it was realised that useful smaller diagnostic configurations could be constructed from the modules, and potentially be used to support smaller short-term experiments. To enable the use of single or a few modules together, a smaller chassis needed to be designed.

Two small-chassis solutions were developed and demonstrated, which could support two or six modules respectively. Each chassis design required new mechanical frames, backplanes, front panels, and touch screens. The same control cards and modules could be used interchangeably between the three systems, following a revision of CC2 to CC2B.

The small chassis were intended for short time-scale experiments, which would not

require the redundancy and serviceability included within the large interrogation system. As a result a considerable reduction is size was achieved. Figure 3.40 shows the smallest, two module, chassis. The two module configuration was considered useful for measuring

Figure 3.40: Photograph of smallest interrogation system design which could support two diagnostic modules and one control card.

FBGs, using the OIES modules, or even performing TDLAS type measurements in the future.

The six module chassis is shown in figure 3.41. This chassis was considered useful for medium sized experiments which may require many temperature and/or pressure sensors to be deployed, or multiple gaseous chemical species to be measured, but only over an experimental time lasting a few months. Longer experimental times would be better served by the full interrogation system due to the additional signal buffering and control redundancy.

Both chassis systems were constructed and evaluated. They were considered a useful addition to the overall interrogation suite, with many of the modules being subsequently demonstrated within the two-module chassis. Use of the smallest chassis system proved a fast development route due to the reduced time required for buffer and control card programming.

Figure 3.41: Photograph of medium-sized interrogation system that could support six diagnostic modules, one control card, and one PSU.

3.10 Modular Interrogation System Conclusions

An interrogation system was designed and assembled based around a modular architecture. The system infrastructure contained a user interface, module connection backplanes, electrical routing, optical fibre routing, PSUs, and air cooling fans. Modules consisted of control modules, interrogation modules, and optical routing modules.

A summary of the modules which were planned and their final status are detailed in table 3.6. Each of the assembled modules were tested and evaluated. A number of the out-of-scope modules were marked as designed, as noted in the table, due to the ability to re-use module PCB designs, such as the OR design.

In addition to these modules, the interrogation system infrastructure required a number of PCBs to be designed and assembled. The main interrogator infrastructure comprised nine PCB designs: a front panel, display interface support, module indicator, interrogator indicator, button interface, service connectors interface, environmental sensors, control backplane, and module backplane. The medium and small sized interrogator each required a further two PCB designs: a front panel, and a backplane.

This work accepted that components would be likely to fail within the duration of a multi-decade experiment and therefore a strategy to manage their replacement was required. A modular interrogation system was developed providing redundancy, serviceability, and a management strategy for component obsolescence. Redundancy was achieved through installation of additional modules above the number required for general operation. Serviceability was achieved by including the ability to remove individual modules for service and calibration, without halting the operation of the

Module	Design	Assembly
Fan	✓	✓
PSU	✓	✓
†Loopback Monitoring	–	–
†Control Card 1 (CC1)	–	–
Control Card 2 (CC2)	✓	✓
Module Buffer (MB1)	✓	✓
Interface Buffer (IB1)	✓	✓
Swept Laser Source	✓	✓
SLED Source	✓	✓
†DFB Source(s)	–	–
Circulator Optic	✓	✓
†Coupler Optic	✓	–
Photodiode Detector	✓	✓
OSA Detector	✓	✓
OIES Module	✓	✓
Source Route SM	✓	✓
†Source Route MM	✓	–
Detector Route SM	✓	✓
†Detector Route MM	✓	–
†Umbilical Routing	–	–
Red Laser Module	✓	✓

Table 3.6: Summary of interrogation module design and production status, detailing 17 designs and 14 modules assembled. †These modules were not within the scope of this project, but provisioned within the modular design work.

entire interrogation system. Obsolescence planning was achieved by incorporating interchangeable modules enabling alternative modules to be inserted at any time. Module and system IP was owned by AWE, enabling redesign and modification of modules throughout the experiment duration.

Further work could investigate developing additional module count configurations, further supporting small and medium-scale experiments. Additional sensing modules could also be designed, to expand the interrogation system beyond FBG and OIES systems, to include techniques such as TDLAS and/or fluorescence sensing.

Chapter 4: Electronic Sensor Integration and Evaluation

This thesis focuses on optical interrogation methods, but electronic sensors were also considered for ageing experiment use, as discussed in Chapter 8. Also the interrogation system discussed in the previous chapter (Chapter 3) incorporated electronic sensors on each interrogation module. This chapter details the review, experimental evaluation, and selection of the sensors which were incorporated into the OIES system (Chapter 8) and modular interrogation system (Chapter 3).

The OIES sensors were required to satisfy the same requirements as the optical diagnostics, as they would be utilised within the experimental environment.

The interrogation system sensors were intended to provide data which could support the maintenance of the interrogation hardware throughout the experimental duration of ≈ 30 years. By monitoring the local environment of each module, the history of conditions each module experiences would be captured and could potentially assist in predicting module failure, planned maintenance schedules, and future design improvements. In this chapter, the monitoring sensors were down-selected, assembled into a bespoke test-bed system, and their performance was evaluated. The sensors recommended for integration within this chapter were incorporated into the Chapter 3 and Chapter 8 hardware designs.

Since the interrogation hardware was primarily electronic in design, it was deemed advantageous to utilise electronic sensor techniques, rather than the optical sensor techniques which are the primary topic of this thesis. Electronic sensors typically require fewer additional components than optical techniques, due to extensive development, simplifying their integration into the system. Evaluating electronic sensors also had the benefit of increasing the range of technologies which were explored within this project and which may be useful to AWE in the future, as demonstrated in Chapter 8: *optically isolated electronic sensors*.

The local environment-monitoring sensors would be a secondary measurement for the interrogation modules since their primary function would be supporting the optical

sensor measurements. As such, the monitoring sensors should require minimal demands on module resources, and present no interference with the primary module functions. Sensor techniques which required minimal host power and processing time were therefore preferred. As a secondary feature of the modules, the component cost and design cost of adding the sensors needed to be suitability low, so simpler techniques were preferred. The long-term performance of the the electronic sensors was not assessed, since their location within the interrogation hardware would enable periodic calibration during the experiment. Further work would be required to evaluate the long-term performance for use within an experimental environment if integrated within an OIES sensor node.

Requirements

The required measurement parameters within the modular interrogation system were those considered to impact the operational lifetime of optical, electrical, and optoelectronic hardware; which included: temperature, barometric pressure, and humidity [229]. Temperature was required to be measured from $-10\,°\text{C}$ to $40\,°\text{C}$ with an accuracy of $\pm 1\,°\text{C}$, barometric pressure from $900\,\text{mbar}$ to $1100\,\text{mbar}$ with an accuracy of $\pm 5\,\text{mbar}$, and humidity from $10\,\%\text{RH}$ to $90\,\%\text{RH}$ with an accuracy of $\pm 5\,\%\text{RH}$. The sensors were to be integrated into a range of interrogation modules, therefore small physical size ($< 5\,\text{mm}$), a low number of additional components, and low integration complexity (cost and time), were required. The requirement in terms of %RH were also stated in terms of dew point, and required a measurement range of $-25\,°\text{C}$ to $25\,°\text{C}$ with an accuracy of $\pm 2\,°\text{C}$, to assist in the comparison of sensor values. Satisfying either the %RH or dew point specification was considered as satisfying the project requirements.

The required measurement parameters for use within a OIES sensor node were temperature, humidity, and barometric pressure, to the same specification as the optical techniques. Temperature sensing was required from $-20\,°\text{C}$ to $70\,°\text{C}$ with an accuracy of $\pm 1\,°\text{C}$. Humidity sensing was required from $40\,\text{ppm}$ to $100\,000\,\text{ppm}$ with a resolution of $40\,\text{ppm}$ (equivalent to $0.1\,\%\text{RH}$ to $100\,\%\text{RH}$ with an accuracy of $\pm 1\,\%\text{RH}$ or $-54\,°\text{C}$ to $44\,°\text{C}$ dew point with an accuracy of $\pm 0.5\,°\text{C}$ dew point). Barometric pressure sensing was required from $0\,\text{mbar}$ to $1200\,\text{mbar}$ with an accuracy of $\pm 2\,\text{mbar}$.

4.1 System Integration of Commercially Available Sensors

The electronic sensors required experimental evaluation to support down-selection of the sensor options for integration into the modular interrogation system (Chapter 3) and OIES sensor node (Chapter 8). To enable sensor evaluation, an electronic sensor test-bed system was developed which could support the digital sensors reviewed. The system was designed, manufactured, and assembled; photographs of the six-PCB structure and assembled system within its enclosure can be seen in figure 4.1. A block diagram of the

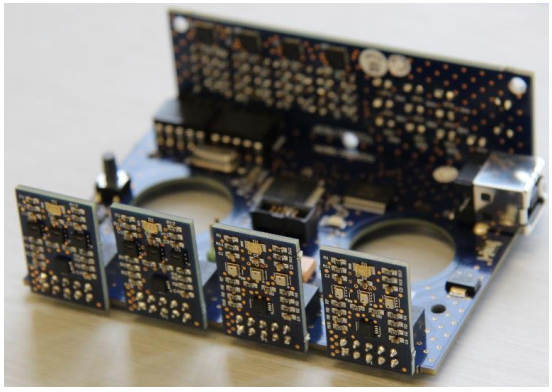

(a) Photograph of integration test-bed PCB assembly. From back to front, the rear of the display board, the main board, and the four sensor boards; each sensor board contains three sensors.

(b) Photograph of integration test-bed assembled within a translucent acrylic rapid-prototyped enclosure. The numerical display provides a live sensor reading, coupled with the LED matrix to the right which identifies the displayed sensor and measurement. A button enables cycling through the measurements.

Figure 4.1: Electronic integration test-bed system.

test-bed system is shown in figure 4.2. The system contained four sensor modules, each

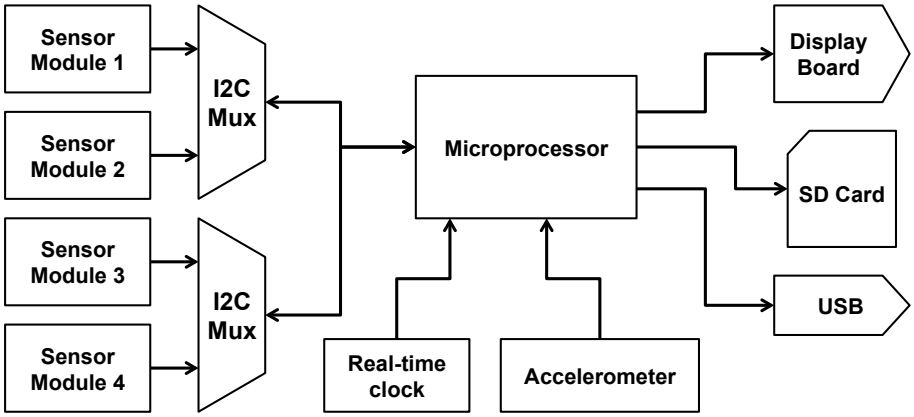

Figure 4.2: Electronic integration test-bed block diagram.

containing three sensors, communicating via I^2C. Two multiplexors (muxs) were required to interface the sensors to the micro-controller's single hardware I^2C peripheral. This

technique was chosen in preference to using multiple software-generated I^2C interfaces on the micro-controller, since it afforded more programming flexibility for display updates, data storage, and USB data streaming, and thus simplified the software development. I^2C typically supports multiple devices in parallel on a single bus, but this configuration was not used for the sensor connections due to I^2C address conflicts (identical addresses) present when testing multiple identical devices at once.

The module was capable of recording the measured data to an SD card or stream the data over USB to a custom-written LabVIEW virtual instrument (VI). The display board contained the complete user interface, consisting of multiplexed LEDs and a menu select button. A real-time clock was incorporated to enable time and date information to be stored along with the sensor data. The accelerometer was intended to enable automatic display rotation if the module was inverted during use, to simplify reading the display, but this feature was not written into the software since the evaluation primarily utilised the USB data link.

The sensors integrated onto the four sensor modules were the Sensirion (Germany) STS21, the Sensirion SHT21, the Bosch Sensortec (Germany) BMP280, and the Bosch Sensortec BME280; each module contained three duplicates of the sensor. The measurement parameters, ranges and accuracies are detailed in table 4.1. All four sensors

Manufacturer	Sensor	Measurement	Range	Accuracy
Sensirion	STS21 [140]	Temperature	$-40\,°C$ to $125\,°C$	$\pm\,0.2\,°C$
Sensirion	SHT21 [148]	Humidity	$0\,\%$ RH to $100\,\%$ RH	$\pm\,2\,\%$ RH
		Temperature	$-40\,°C$ to $125\,°C$	$\pm\,0.3\,°C$
Bosch Sensortec	BMP280 [156]	Pressure	$300\,mbar$ to $1100\,mbar$	$\pm\,1\,mbar$
		Temperature†	$-40\,°C$ to $85\,°C$	$\pm\,1\,°C$
Bosch Sensortec	BME280 [151]	Humidity	$0\,\%$ RH to $100\,\%$ RH	$\pm\,3\,\%$ RH
		Pressure	$300\,mbar$ to $1100\,mbar$	$\pm\,1\,mbar$
		Temperature†	$-40\,°C$ to $85\,°C$	$\pm\,1\,°C$

Table 4.1: Electronic sensor details for test-bed integration. Notes: †, temperature compensation sensor, not intended for ambient measurement.

featured digital I^2C communication interfaces, operating from $3.3\,V$, with all analogue measurement, signal processing, and digitisation occurring within the sensor package itself. The temperature sensors were of semiconductor junction design, and both the humidity and pressure sensors operated using capacitive techniques. Use of sensors with such a high level of integration significantly reduced the number of components and circuit complexity required to add environmental sensing to the interrogation system modules.

The external shape and dimensions of the enclosure used for the test-bed system were provided by AWE for use within this project, and the six PCBs were designed to fit inside. The enclosure was designed and manufactured in-house at AWE from an aluminium alloy, which incorporated internal PCB mounts and cut-outs for the display board, USB connector, SD card, and sensors. Manufacture of the enclosure enabled the test-bed system to be evaluated within varying temperature, pressure, and humidity environments, without suffering mechanical damage. The assembled PCBs were conformally coated (excluding the sensor packages) to mitigate the risk of condensation damage during temperature and/or humidity performance evaluation experiments.

The test-bed system was designed and manufactured with the ability to measure temperature, barometric pressure, and humidity. The system incorporated 12 COTS electronic sensors of four different types for evaluation towards integration into the modular interrogation system (Chapter 3) and OIES sensor node (Chapter 8). The assembled system was demonstrated and experimentally evaluated in order to assess the performance of the sensors.

4.2 Performance Review of Integrated Sensors

The electronic sensors were integrated into the test-bed system and they were demonstrated to operate within an electronic data logging system, similar in design to the modular interrogation system. The sensors were designed to measure temperature, humidity, and barometric pressure. Experiments were conducted to investigate the sensor performance against the project requirements.

Temperature Evaluation

The temperature sensors integrated into the sensor test-bed were the Sensirion (Germany) SHT21 and STS21. The test-bed also included the Bosch Sensortec (Germany) BME280 and BMP280 sensors, which also measured temperature. These temperature measurements were primarily intended for barometric pressure sensor compensation, as opposed to environmental monitoring. The SHT21 is specified to have a typical accuracy of $\pm 0.3\,^{\circ}\mathrm{C}$ (maximum of $\pm 0.7\,^{\circ}\mathrm{C}$ within evaluated range) [148], the STS21 is specified to have a typical accuracy of $\pm 0.2\,^{\circ}\mathrm{C}$ (maximum of $\pm 0.6\,^{\circ}\mathrm{C}$ within evaluated range) [140]. The BME280 and BMP280 sensors had a specified accuracy of $\pm 1\,^{\circ}\mathrm{C}$ [151, 156].

The temperature evaluation experiment was conducted within an environmental

chamber manufactured by TAS, whose configuration is discussed in Chapter 5. The sensors were evaluated from $-10\,°C$ to $40\,°C$ in $10\,°C$ increments. The chamber was temperature regulated by a proportional, integral, differential (PID) control system and had been evaluated to have a temperature stability of $\pm 0.9\,°C$. A minimum of 350 measurements were taken at each temperature, once the chamber had reached temperature regulation. The sensor measurements were initiated using the test-bed system and the data was sent via USB to a PC running a custom LabVIEW VI.

This experimental configuration was intended to evaluate if the sensors had the potential to meet the project requirements, not to perform sensor calibration or confirmation of the specified sensor accuracy. An example of the experimental measurements for sensor 1 (an SHT21 sensor) are shown in figure 4.3. The experiment consisted of 8850 measurements equating to approximately $12\,h$ of data. The experiment was conducted over the course of two working days. The temperature response for

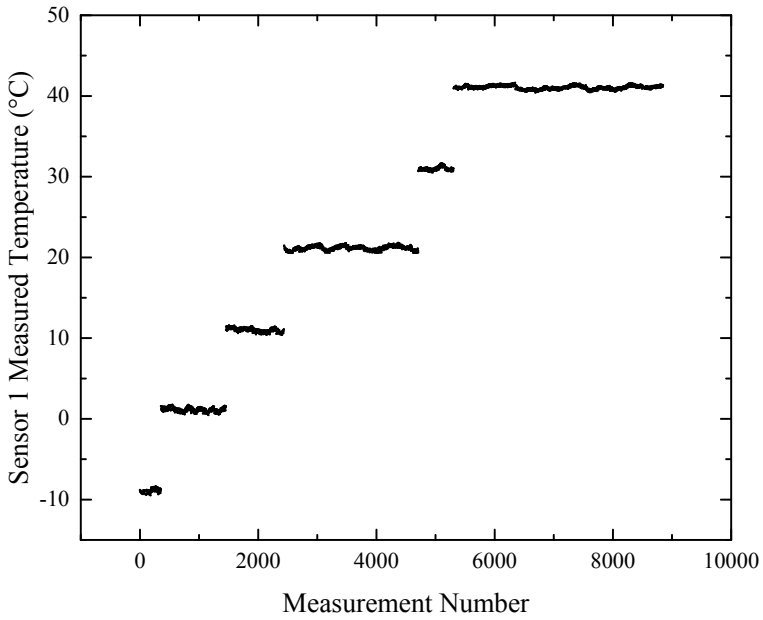

Figure 4.3: Electrical sensor temperature profile sensor 1 (a Sensirion SHT21 sensor) sensors.

each sensor was plotted against chamber set-point temperature in order to enable linear regression analysis. The measured temperature response for sensor 4 (an STS21 sensor) is shown in figure 4.4. The linear regression was fitted to the data points, taking the x-axis uncertainty into account ($\pm 0.9\,°C$), using OriginPro 9.2, made by OriginLab (USA). Residual analysis from the linear regression revealed a histogram, shown in figure 4.5.

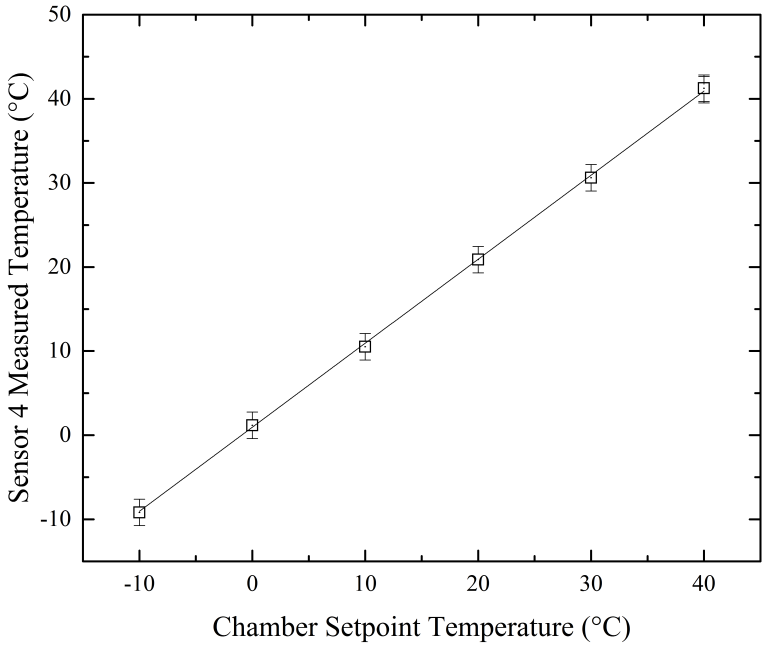

Figure 4.4: Electrical sensor temperature response for sensor 4 (a Sensirion STS21 sensor) with linear regression fitted.

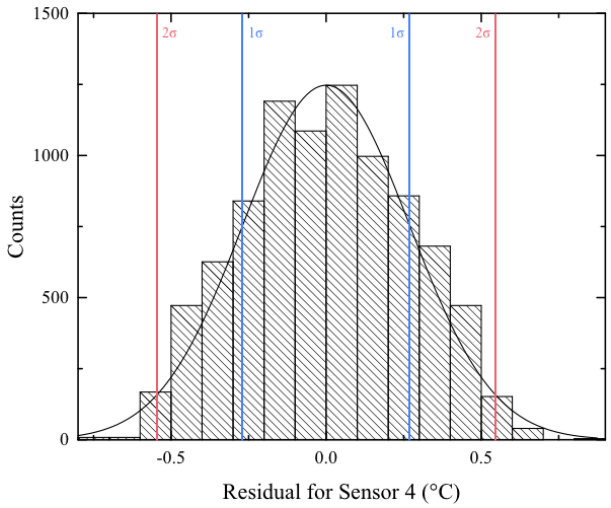

Figure 4.5: Electronic sensor histogram of residuals for the analysis of sensor 4, a Sensirion STS21.

The analysis enabled the sensor responsivity, measurement offset, and measurement deviations, to be assessed. This analysis was performed on all 12 sensors within the test-bed system. The linear regression parameters and standard deviation, root mean square error (RMSE), are shown in table 4.2. The gradients calculated for each sensor are within ± 0.003 for the SHT and STS sensor types, and within ± 0.058 for the BME and BMP compensation sensors. These deviations were considered small, and over the evaluated range the SHT and STS sensors would remain within the specified $\pm 1\,^{\circ}\text{C}$ requirement. The fit offsets calculated were all positive, where it was expected for a distribution around $0\,^{\circ}\text{C}$. This asymmetry suggested the chamber temperature was, on average, higher than the set-point temperature. This could have been due to the PID settings used and a difference in heating and cooling power of the chamber. The long-term experiment discussed in Chapter 5 was conducted using the same chamber, and measured the chamber to be most often $0.2\,^{\circ}\text{C}$ to $0.4\,^{\circ}\text{C}$ above the set-point temperature, but with a broad distribution within the $\pm 0.9\,^{\circ}\text{C}$ chamber uncertainty. The offset values had a maximum of $1.10\,^{\circ}\text{C}$, which was within the experimental margin (for a sensor performing at $\pm 1\,^{\circ}\text{C}$ and a chamber stability of $\pm 0.9\,^{\circ}\text{C}$) of $\pm 1.34\,^{\circ}\text{C}$. The standard deviations (RMSEs) of all 12 sensors suggested they were all operating within the required accuracy of $\pm 1\,^{\circ}\text{C}$ over the temperature range of $-10\,^{\circ}\text{C}$ to $40\,^{\circ}\text{C}$.

	Sensor	Fit Gradient	Fit Offset, °C	RMSE, °C
1:	SHT21	0.999	1.09	0.27
2:	SHT21	1.002	1.10	0.27
3:	SHT21	1.000	1.08	0.28
4:	STS21	1.000	0.94	0.27
5:	STS21	1.003	1.00	0.27
6:	STS21	1.000	0.98	0.28
7:	BME280	1.018	0.53	0.30
8:	BME280	1.002	1.03	0.29
9:	BME280	1.011	0.77	0.31
10:	BMP280	1.056	0.06	0.35
11:	BMP280	1.056	0.31	0.33
12:	BMP280	1.058	0.17	0.33

Table 4.2: Temperature evaluation results for the electronic sensor integration test-beds. Results are calculated using a linear regression for each sensor's measured response.

Humidity Evaluation

The humidity sensors integrated into the test-bed system were the Sensirion (Germany) SHT21, and the Bosch Sensortec (Germany) BME280. The range and stated accuracy of each sensor type were 0 to (100 ± 2) %RH and 0 to (100 ± 3) %RH respectively [148, 151]. Both sensors used their integrated temperature sensors to perform humidity measurement *compensation*.

To generate a range of known humidities, a humidity generator was used which had been previously assembled at AWE. The humidity generator was of split-flow design, similar to that reported by Chen and Chen [230], but with the mass flow controllers (MFCs) located after the bubble vessel. The system was fed with dry nitrogen from a gas cylinder, through an arrangement of pipework, pressure regulators, and valves. Once within the generator, the gas flow was split in two, with one feed being passed through an MFC which set the flow rate of dry nitrogen into the system. The second feed passed through a water bubble vessel which provided water-saturated nitrogen to a second MFC, which set the flow rate of saturated nitrogen into the system. By varying the levels of the two MFCs, it was possible to vary the humidity from approximately $-40\,$°C to $25\,$°C dew point. The dew point was measured using a calibrated chilled mirror which was placed in the flow of gas in line with the sensor test-bed. The humidity generator was specified to have an uncertainty of $\pm 0.5\,$°C dew point which incorporated the contributions from the nitrogen cylinder, MFCs, bubbler temperature, and the chilled mirror [231]. The sensor measurements were captured using the test-bed system and sent to a PC via USB and stored using a second VI.

The humidity environment for the sensors was varied from $-38\,$°C to $24\,$°C dew point in six levels. Between each level the humidity generator was left to stabilise, a process that required up to two hours. A minimum of 500 measurements were taken at each humidity level. The sensor output data was provided in %RH, but for evaluation it was converted to dew point, T_{dp}, using the temperature sensor within the SHT21 and BME280 sensors on a measurement-by-measurement basis. The conversion was performed to minimise errors due to temperature differences between the chilled mirror and electronic sensors, and account for ambient temperature variations throughout the duration of the experiment. The conversion from measured %RH to T_{dp} was achieved using work by Wagner and Pruß [232–234]. The limited ambient temperature range ($-20\,$°C to $50\,$°C) equations were

used, which have a maximum calculation error of $0.083\,\%$ of value:

$$T_{dp} = \frac{T_n}{\frac{m}{\log_{10}\left[\frac{\%RH}{100}\cdot 10^{\left(\frac{m\cdot T}{T_n+T}\right)}\right]} - 1}, \tag{4.1}$$

where the two empirical conversion constants T_n and m equal $240.7263\,°\text{C}$ and $7.591\,386$ respectively, and T is the ambient temperature in °C [233]. This conversion equation was used in preference to any other, such as the Sonntag (Magnus) formula found in BS1339-1 [235], since Sensirion (Germany) recommended the above for conversion when using their sensors [234].

The sensor response was plotted for each sensor and a linear regression performed. The linear response for sensor 1 (an SHT21 sensor) is shown in figure 4.6. Uncertainties are included within the linear fit calculation which originate from the sensor

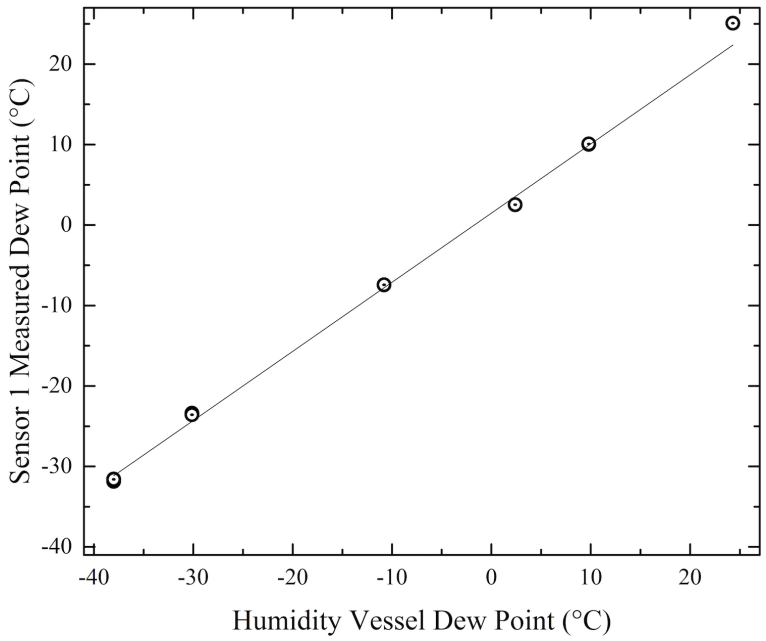

Figure 4.6: Electrical sensor humidity response for one of the Sensirion SHT21 sensors with linear regression fitted. The measurement uncertainties are represented by the data-point diameter.

measurements, the conversion from %RH to dew point, and the uncertainty in the dew point generator used ($\pm 0.5\,°\text{C}$).

From the linear regression, the fit parameters: gradient and offset, were calculated along with the measured sensor RMSEs. The results from all six sensors are shown in table 4.3. The RMSE in units of %RH was calculated from converting the data from dew point to relative humidity and a performing linear regression.

Table 4.3 indicates significant responsivity variations between the sensors evaluated, based on the fitted line gradients; over the required measurement range such sensor

	Sensor	Fit Gradient	Fit Offset, °C	RSME, °C	RSME, %RH
1:	SHT21	0.859	1.48	0.81	0.70
2:	SHT21	0.853	1.57	0.80	0.74
3:	SHT21	0.839	1.67	0.85	0.70
7:	BME280	0.968	−0.70	0.49	0.93
8:	BME280	0.960	−0.51	0.51	1.00
9:	BME280	0.836	0.91	0.80	0.95

Table 4.3: Humidity evaluation results for the electronic sensor integration test-beds. Results are calculated against a linear regression performed for each sensor.

response variation would result in sensor deviations greater than 2 °C dew point between sensors. The variations in responsitivies suggest that individual sensors would require calibration before use in a deployed system. The fit offsets calculated were large compared to the humidity generator stability of ±0.5 °C dew point, but were within the project accuracy requirements; sensor characterisation would account for the variations in offset. The standard deviations in °C dew point suggested the sensors were performing to the accuracy required by the interrogation system within this project of ±2 °C dew point. The standard deviations in %RH suggested the sensors were operating within their stated accuracies of ±2 % and ±3 % for the SHT21 and BME280 models respectively [148,151]. The sensors were not considered to satisfy the OIES sensor node accuracy requirement of ±0.5 %.

The six humidity sensors were evaluated to be performing as specified by their manufacturers, and within the project requirements. However, individual sensor characterisation would be recommended before deployment.

Barometric Pressure Evaluation

The barometric pressure sensors integrated into the sensor test-bed were the Bosch Sensortec BME280 and BMP280. Both models were specified for operation between 300 mbar and 1100 mbar with an accuracy of ±1 mbar [151, 156]. The project required pressure sensing from 900 mbar to 1000 mbar with an accuracy of 5 mbar for interrogation system monitoring, and from 0 mbar to 1200 mbar with an accuracy of 2 mbar for material ageing sensing.

The pressure evaluation experiment was conducted within a PID controlled vessel assembled for long-term evaluation of optical sensors, discussed in Chapter 6. The sensors were evaluated over the range ≈ 0 mbar to 1000 mbar in 200 mbar increments. The evaluation range extended to lower pressures than the sensor specified operating

pressures, but this use was of interest to AWE. The vessel was evaluated to operate with a pressure stability of ± 4 mbar (Chapter 6).

The experiment was conducted over the period of 40 h, capturing approximately $17\,000$ measurements per sensor. The test pressure sequence can be seen in the sensor 7 (a BME280 sensor) results, shown in figure 4.7. Plotting the vessel pressure (measured using

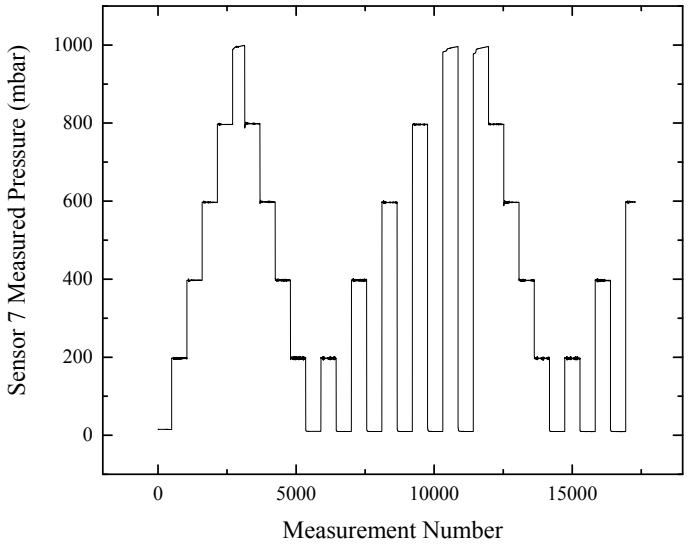

Figure 4.7: Electrical sensor pressure profile for one of the Bosch Sensortec BME280 sensors, sensor 7. Data was recorded over a 40 hour period, with approximately one our per pressure step.

a calibrated pressure transducer with a resolution of 0.03 mbar and accuracy of ± 2 mbar) against the sensor measurement provides a linear response, as shown in figure 4.8. The

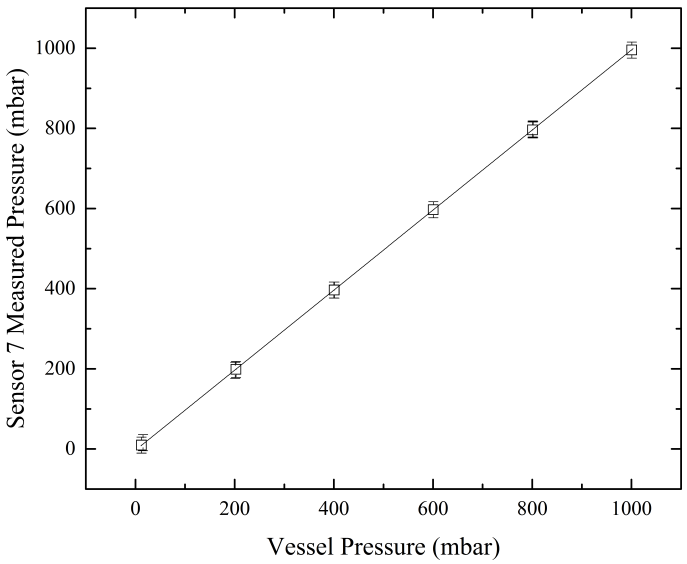

Figure 4.8: Electrical sensor pressure response for one of the Bosch Sensortec BME280 sensors with linear regression fitted.

response was well characterised with a linear regression, even for measurements below the stated sensor minimum pressure of 300 mbar, suggesting operation at low pressures

would be possible. However, longer-term studies would be required to confirm operation outside of the manufacturer's intended range.

Analysis of the residuals from the linear fit reveals information on the sensor performance. A histogram of the residuals for sensor 7 is shown in figure 4.9. The

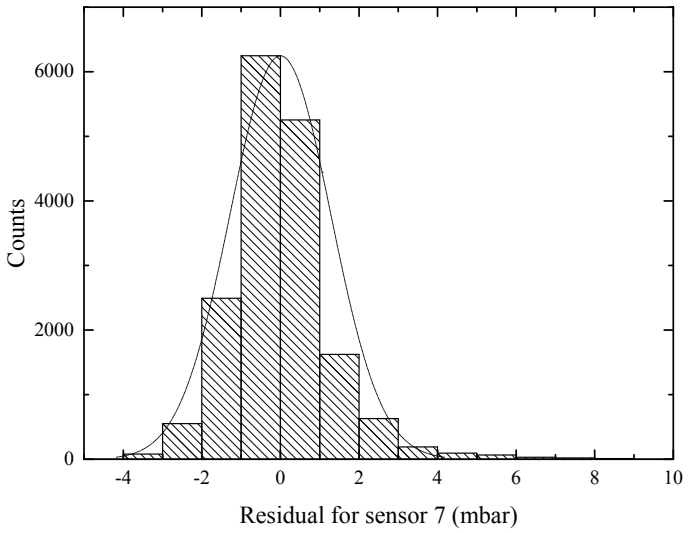

Figure 4.9: Electronic sensor regression analysis for sensor 7, a Bosch Sensortec BME280.

same analysis was conducted for all six pressure sensors within the test-bed, and the linear fit parameters and RMSE for each are included in table 4.4. The linear fit gradients

	Sensor	Fit Gradient	Fit Offset, mbar	RSME, mbar
7	BME280	0.999	−3.03	1.28
8	BME280	0.999	−3.48	1.28
9	BME280	0.998	−3.25	1.28
10	BMP280	0.998	−1.57	1.38
11	BMP280	0.998	−1.26	1.39
12	BMP280	0.998	−1.33	1.38

Table 4.4: Barometric pressure evaluation results for the electronic sensor integration test-beds. Results are calculated against a linear regression for each sensor.

suggested the sensors were operating very close to the expected unity responsivity. The fit offsets were all negative, suggesting some asymmetry in the experiment configuration caused the vessel, on average, to be below the set-point pressure. A difference in response time between the reference transducer and sensors under test could result in the systematic negative offset observed. The largest sensor offset of $3.48\,\text{mbar}$ was within the project accuracy requirement of $5\,\text{mbar}$. The difference in offsets between the BME280 and BMP280 sensors suggested a systematic variation between models, which could be removed by individual sensor characterisation prior to use. The standard

deviations, RMSEs, suggested all six sensors were operating within the interrogation system requirement of ± 5 mbar, but not the material ageing requirement of ± 2 mbar.

The six barometric pressure sensors were evaluated experimentally in a controlled vessel to assess their performance. All six sensors were found to operate within their specified accuracies, based on the standard deviation of their response residuals. Measurement offsets were identified suggesting individual sensor characterisation would be advisable before deployment.

4.3 Conclusions

Electronic sensors were required for integration into the modular interrogation system detailed in Chapter 3 and the OIES sensor node detailed in Chapter 8. The sensors were required to measure temperature, humidity, and barometric pressure, in order to support experiment diagnostic measurements, and interrogation system condition monitoring and predictive maintenance processes during experimental operation.

A review of electronic sensing technologies was conducted and highly-integrated COTS sensing techniques which featured digital communications were selected. This type of sensor provided a physically compact solution which required minimal additional components and design consideration when added as a secondary feature to an interrogation module.

Four models of electronic sensors were selected for review and a sensor test-bed system was designed and built. The test-bed could measure three of each sensor type in a compact and rugged enclosure. The sensors were experimentally evaluated for temperature, humidity, and pressure measurement performance, against the project requirements. All the sensors tested functioned within the project requirements, but in multiple cases it was noted that variations in sensor performance would necessitate individual sensor characterisation prior to deployment.

For measuring temperature, the best-performance was measured from the Sensirion (Germany) SHT21 sensor, but very similar results were measured for the Sensirion STS21 sensor. For humidity measurement, the SHT21 sensor performed with a lower RMSE than the Bosch Sensortec (Germany) BME280. For measuring pressure, the Bosch Sensortec BMP280 performed similarly to the BME280. With all sensors performing within the project requirements, a combination of SHT21 sensors and BME280 sensors was recommended to achieve the best performance, based on the assessments conducted.

The two sensors recommended were incorporated into the designs for the interrogation system modules. Each module included a single SHT21 sensor to provide localised temperature and humidity measurements. The barometric pressure was considered unlikely to vary throughout the system, so the BME280 was only included on the CC2B module. Additionally, three SHT21 sensors were located at the front-panel of the interrogation system with vents to enable the external environment temperature and humidity to be evaluated. Additional sensors were included on some interrogation modules to support their primary functions, such as TEC monitoring thermistors, but they were in addition to the SHT21.

Future work would investigate the long-term performance of the sensors, to further support their potential for deployment into an experimental system design. Since this work was performed, newer models of similar sensors are now available, which could also be evaluated. The modular design of the test-bed system could potentially enable the evaluation of these additional sensor models with minimal design effort, if it was required. Based on the maturity level of the interrogation system, no further evaluation of the condition monitoring sensors was considered necessary within this project.

Part III

Optical Diagnostics

Chapter 5: Temperature Sensing

Chemical processes and reaction rates are temperature dependant [236], therefore within a materials ageing experiment the measurement of temperature is of high importance. Absorption spectroscopy may be used within a materials ageing experiment for gas sensing [124, 237]. In this case, temperature has an effect on the measured absorption linestrengths and lineshapes [88, 238, 239], further necessitating the requirement for temperature sensing.

Optical fibre temperature sensing has been most often demonstrated using the FBG technique [14, 26, 42, 48–52]. Many commercial companies offer FBGs at user selected wavelengths, reflectivities, and bandwidths, with or without sensor housings. Housings can provide supports for attaching the sensors onto structures in addition to making them more rugged. Previous work at AWE investigated temperature sensors manufactured by Micron Optics (USA), based on FBGs [19, 22], and they were found to be capable of operating within the required temperature range and accuracy of this project [237]. However, their use in a long-term experimental configuration was not evaluated.

This work aimed to evaluate the long-term stability of FBG based temperature sensors to support an assessment of their suitability for use within a materials ageing experiment. The sensors were repeatedly temperature cycled to simulate long duration experimental use. Analysis of sensor failure modes would be used to support a prediction of sensor lifetime within an experiment.

Temperature sensing capabilities from $-20\,^{\circ}\mathrm{C}$ to $70\,^{\circ}\mathrm{C}$ with an accuracy of $\pm 1\,^{\circ}\mathrm{C}$ were required, including suitability for use throughout the multi-decade experimental duration.

5.1 Theory and Predicted Failure Modes

An FBG is constructed from a regular periodic change of refractive index within the core of an optical fibre. If the core of the fibre has a refractive index, n_1, the grating may oscillate between refractive indices n_2 and n_3. The grating structure causes a reflection

peak at the Bragg wavelength, λ_B. To a first order approximation, the Bragg wavelength is defined as [35]:

$$\lambda_B = 2\bar{n}\Lambda, \tag{5.1}$$

where $\bar{n}$ is the average effective refractive index of the fibre core, $(n_2 + n_3)/2$, and Λ is the grating period.

The reflectivity of the grating is primarily dependant on the variation in refractive index ($\Delta n = n_3 - n_2$), and the length of the grating, as shown by [13, 240]:

$$R = \tanh^2\left[\pi\bar{n}\frac{\Delta n}{\bar{n}}\frac{L}{\lambda_B}\Omega\right], \tag{5.2}$$

where R is the grating reflectivity, L is the grating length, and Ω is a fibre constant for the propagation confinement to the core. The bandwidth of the reflection peak, $\delta\lambda$, can be roughly related to the parameters described [13]:

$$\delta\lambda = \lambda_B\sqrt{\left(\frac{\Delta n}{2\bar{n}}\right)^2 + \left(\frac{\Lambda}{L}\right)^2}. \tag{5.3}$$

These two equations suggest that if Δn were to increase, the grating reflectivity would increase as would the bandwidth of the peak.

A change in temperature can cause a change in the Bragg wavelength via two mechanisms: the thermal expansion of the fibre, which causes a change in Λ; and by a change in refractive index via the thermo-optic coefficient, which causes a change in $\bar{n}$. Therefore temperature is related to the the Bragg wavelength change by the relation [13]:

$$\Delta\lambda_B = \lambda_B\left(\alpha_\Lambda + \alpha_n\right)\Delta T, \tag{5.4}$$

where α_Λ is the coefficient of thermal expansion, α_n is the thermo-optic coefficient, and ΔT is the change in temperature. The thermo-optic coefficient for fused silica fibres is typically an order of magnitude larger than the coefficient of thermal expansion. As a result the thermal expansion term is sometimes neglected [13].

Over a protracted time-frame, changes in the structure of the FBG could occur. These were considered to include changes to the refractive index profile of the grating, changes to the material thermal expansion coefficient, and changes to the material thermo-optic coefficient. A change in these parameters was considered unlikely, especially in the

temperature range of interest to this thesis, but due to the lack of a published study and currently identified requirement for operational duration, the evaluation was considered beneficial. Published work demonstrates the ability for dopants within optical fibres to migrate at high temperatures [241], which could cause variations in these parameters, but such migrations are observed above $900\,°C$, which is significantly higher than the maximum required temperature of $70\,°C$ for this thesis.

A change in refractive index profile could reduce the contrast between the varying refractive indices, n_2 and n_3. This would have the effect of reducing the intensity of the reflected light, and the bandwidth of the peak. In extreme cases this change could result in peaks which would be undetectable by the interrogation hardware. A change in either refractive index would cause a corresponding variation in $\bar{n}$, and therefore a shift in λ_B. This would cause an offset shift to the measurement, introducing a systematic error that would ultimately reduce the accuracy of the measurement, if it were undetected.

A change in thermal expansion coefficient would cause a variation in the sensor responsivity, but the effect would be small compared to a change in the thermo-optic coefficient that is approximatly an order of magnitude larger, which could result in large variations in FBG responsivity. Changes in coefficients is considered unlikely, but could be caused by dopant migration within the optical fibres [241].

5.2 Long-Term Evaluation

An experiment was conducted to temperature cycle FBG sensors repeatedly in order to assess their performance and potential suitability for long-term diagnostic use.

Experimental Design

Three FBG temperature sensors from Micron Optics (USA): two os4100 [22] and one os4200 [19], were attached to a common stainless steel flange, as shown in figure 5.1. Both the os4100 and os4200 sensor types incorporated strain-isolation within their design [19, 22], ensuring they operated as temperature sensors. Any failure in stain-isolation was considered detectable within the experimental design as a change in responsivity. The flange provided a near-isothermal structure to enable comparison between the sensor results. The two os3100 strain sensors also visible in the image were not used in this experiment. The sensors, on their flange, were placed within a calibrated TAS (Temperature Applied Sciences, UK), 750LT [242] thermal chamber

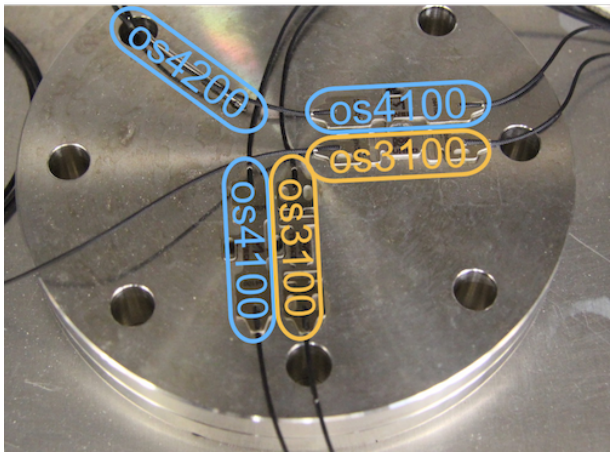

Figure 5.1: FBG testing experimental configuration showing three temperature sensors and two strain FBG sensors attached to a stainless steel flange.

and were temperature cycled following a 24 h pattern, which was repeated througout the experiment (1 year), detailed in table 5.1. The sequence was operated such that the four

Step	Duration	Temperature
1	2 h	0 °C
2	4 h	20 °C
3	2 h	60 °C
4	4 h	100 °C
5	2 h	60 °C
6	2 h	20 °C
7	2 h	−20 °C
8	4 h	−40 °C
9	2 h	−20 °C

Table 5.1: Temperature FBG sensor test pattern which was repeated every 24 hours.

hour step at 20 °C occurred during the working day, to allow for periodic visual inspection when the chamber was at a safe temperature to access. Inspection was required to ensure water did not build up internally due to condensation when at low temperatures.

The experiment was configured as shown in figure 5.2. The thermal chamber featured an integrated PID controller which could be controlled from a PC via the Modbus protocol. A custom VI within LabVIEW was written to send temperature set-points to the controller and measure the current chamber temperature every 10 s, using its internal calibrated PT100 probe. The three FBG temperature sensors were connected in series and measured by a Smart Fibres (UK), swept-laser based SmartScan Interrogator [20]. An example of the measured spectra is shown in figure 5.3. The interrogator was connected to the PC via a local area network and the data logged within a second VI. The data was measured in 20 s bursts where the sensors were scanned every 5 s, with a

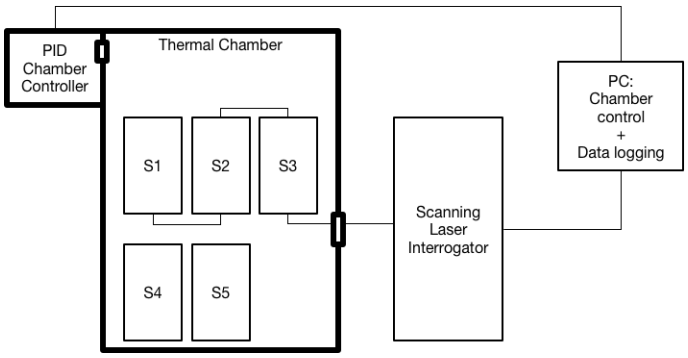

Figure 5.2: FBG testing experimental configuration, showing sensors S1-S5 located within a thermal chamber, measured by an interrogator. A PC was used for chamber control and data logging.

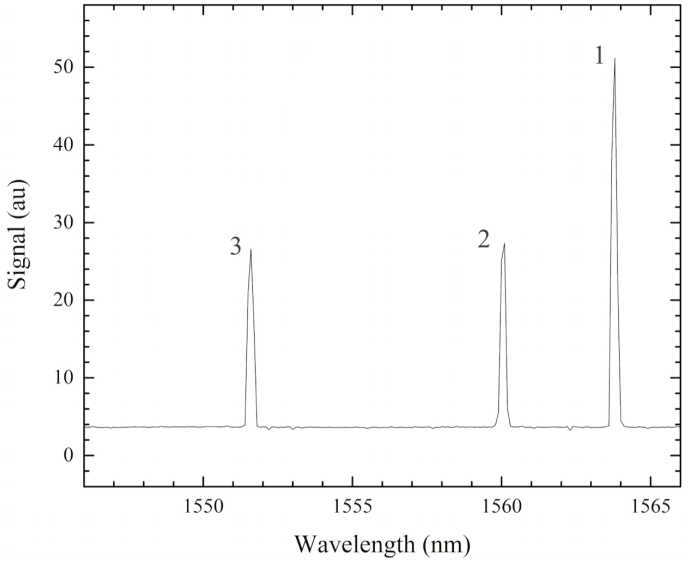

Figure 5.3: FBG experiment example spectra showing the measured reflection peaks from the three FBG temperature sensors. They are ordered 1 to 3, in decreasing wavelength (right to left).

burst every $10\,\text{min}$. This measurement scheme was used to ensure any high-frequency variations in temperature caused by the chamber would be recorded. The interrogator has a stated wavelength accuracy of $5\,\text{pm}$ [20] such that when used to measure a typical FBG temperature sensor, a temperature accuracy of $\leq 0.5\,^{\circ}\text{C}$ was achieved. The uncertainty in the experiment measurements, attributed to the interrogator, was therefore less than the sensing accuracy requirement, so the instrument was considered suitable for assessing whether the FBGs were still operating.

Results

The experiment ran over the period of one year with the sensors experiencing 180 full temperature cycles ranging from $-40\,^{\circ}\text{C}$ to $100\,^{\circ}\text{C}$. The experiment was halted a number of times during the year due to computer issues, chamber calibration, and facility

maintenance periods. The experiment finally concluded following a failure of the thermal chamber.

The environmental chamber's temperature regulation was investigated, using the data logged from the chamber controller. The temporal stability was assessed by analysing the deviations between the set-point and measured temperatures, and is represented in figure 5.4.

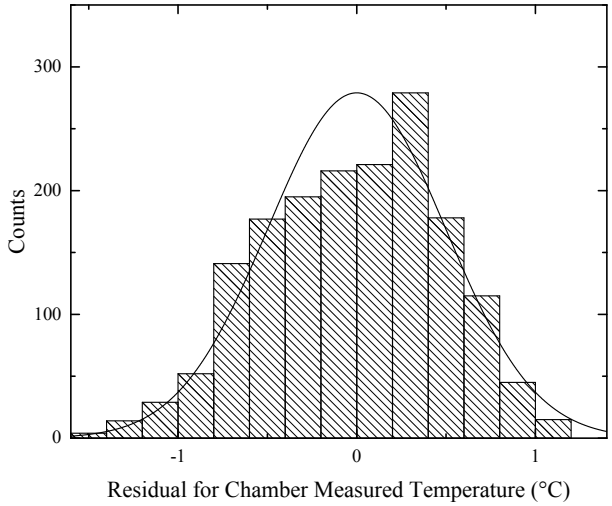

Figure 5.4: Temperature experiment thermal chamber temperature residual analysis.

Data captured while the chamber was transitioning between temperatures was discarded in this analysis, since only the quasi-isothermal periods were of interest. The chamber was assessed using the residual data to maintain a static temperature over $95\,\%$ of the time with a stability of $\pm 0.8\,°\mathrm{C}$. The chamber PID settings were optimised for transitioning between temperatures quickly, rather than maintaining stability at a static temperature, so no changes were made to improve the stability. This temporal uncertainty combined with the chamber's specified spatial uncertainty ($\pm 0.3\,°\mathrm{C}$) suggest a combined chamber temperature uncertainty of $\pm 0.9\,°\mathrm{C}$ for the experiment.

Analysis of the sensor data was achieved by performing a linear fit on each of the 180 temperature cycles for each sensor. The averages of the linear fit parameters are noted in table 5.2.

Sensor	Fit Gradient, pm °C^{-1}	Fit Offset, nm	SSE, nm^2
1 (os4100)	27.4 ± 0.1	1566.862 ± 0.009	1.0 ± 0.3
2 (os4100)	27.7 ± 0.1	1563.904 ± 0.009	2.5 ± 0.2
3 (os4200)	9.6 ± 0.1	1552.38 ± 0.01	0.7 ± 0.2

Table 5.2: FBG temperature evaluation results for the long-term stability. Results are calculated against a linear regression for each sensor. The SSEs were calculated for the measurements in each cycle, typically 500 measurements.

An example of the linear fit is shown in figure 5.5 for sensor 1 showing data from the full 180 cycles, supporting the choice of a linear fit for the analysis.

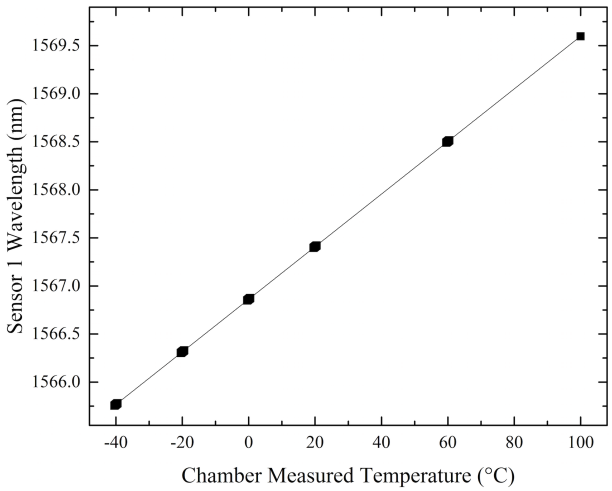

Figure 5.5: Linear fit applied to the FBG sensor 1 data from all 180 temperature cycles.

The fit gradient represented the responsivity of each sensor, and the fit offset represented the wavelength for which the sensor reports $0\,°\text{C}$. A significant difference in responsivity between the os4100 type sensors and the os4200 type was detected, as expected from their datasheets [19, 22]. It was probable the os4100 FBG experienced an additional strain response caused by the thermal expansion of its stainless steel housing, where as the os4200 was strain-isolated. The CTEs for fused silica and stainless steel 304 are $0.55 \times 10^{-6}\,\text{K}^{-1}$ [243] and $15.8 \times 10^{-6}\,\text{K}^{-1}$ [244] respectively, suggesting only partial strain coupling within the os4100. The variations noted in the gradients and offsets were considered small, but also uninformative, so the parameters for each cycle were plotted, as shown in figure 5.6, for the fit gradient, offset and SSE from the linear fitting.

A systematic increase in sensitivity and decrease in wavelength offset was noted for all three sensors, but the total drift observed corresponded to a maximum temperature measurement offset of $0.8\,°\text{C}$, which was within the chamber temperature uncertainty of $\pm 0.9\,°\text{C}$. Therefore the drift could have been attributed to the chamber temperature sensor and/or PID controller which reported the measurement to the PC for data logging.

The daily linear fit analysis suggested the sensors were performing within the experimental uncertainty throughout the 180 cycles. To further support this conclusion, a linear fit was calculated on all the data collected for each sensor, to ensure features were not averaged out by the previous analysis. Histograms of the residuals of the full-data fits are shown in figure 5.7. The majority of data points for sensor 1 and 2 occurred within $\pm 0.15\,\text{nm}$ of the linear fit. Sensor 3 operated within $\pm 0.10\,\text{nm}$ of the fit, likely due to its

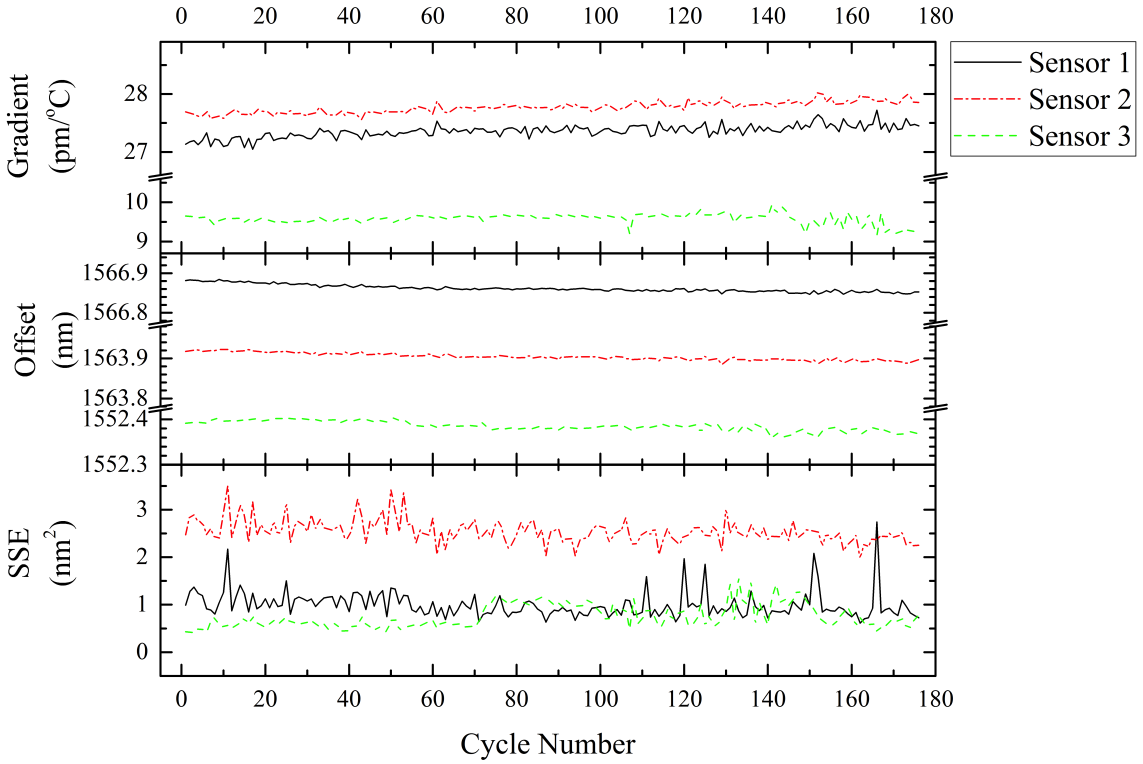

Figure 5.6: Linear fitting parameters for the FBG sensor response for each temperature cycle.

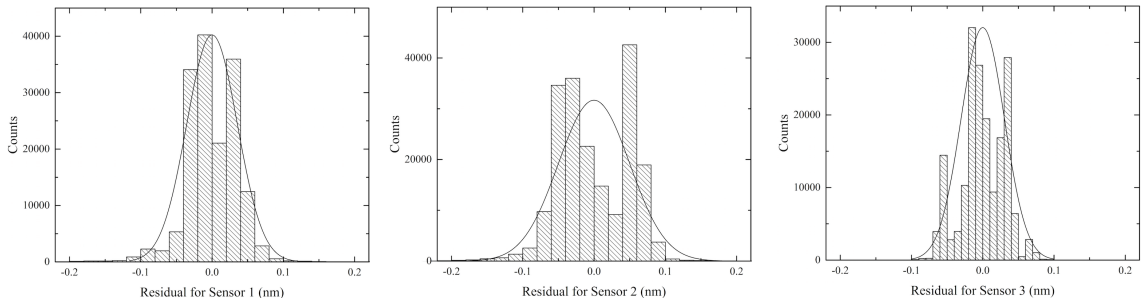

(a) Sensor 1. **(b)** Sensor 2. **(c)** Sensor 3.

Figure 5.7: Temperature FBG sensor residual analysis for all data collected during the experiment.

lower sensitivity. The standard deviations for the sensors were calculated from analysis of the residuals, and are displayed in table 5.3, both in terms of λ_B wavelength shift, and converted to temperature variation using the sensors' responsivity values. The standard deviations for the sensor variations, when calculated over the full 180 cycles, were larger than the experimental uncertainty.

The per-cycle fit data, as detailed in table 5.2 and figure 5.6, suggested the sensor performance was not degrading during the experiment. But the 180-cycle fit data indicated the sensors were not performing within the project temperature accuracy requirements of $\pm 1\,^{\circ}\mathrm{C}$. Since the variations in SSE were small, as shown in figure 5.6, it was concluded the sensor performance was likely consistently outside the required accuracy level. Based on previous work at AWE evaluating these types of sensors, it was

Sensor	Standard Deviation, nm	Standard Deviation, °C
1 (os4100)	0.036	1.5
2 (os4100)	0.050	1.8
3 (os4200)	0.031	3.1

Table 5.3: FBG temperature evaluation standard deviations from a linear regression formed from all captured data.

thought possible the experimental temperature was less stable than calculated, potentially due to use of a forced-air chamber causing the surface temperature of the sensor flange to oscillate more significantly than the chamber temperature.

5.3 Conclusions

Measuring temperature is an important technique during experiments where chemical processes are dominant, or where absorption spectroscopy is used, such as in materials ageing experiments. Previous work had identified FBGs as a potentially suitable optical temperature sensing technique, but their use within a long-term experiment had not been evaluated.

Three commercially available FBG temperature sensors were temperature cycled 180 times over a 1 year period. The sensors were cycled over their specified operational range, which was larger than the sensing range required in this project. No discernible changes in sensor performance, in terms of sensitivity variation of baseline, were detected. All three sensors were still considered fully operational at the end of the experimental period, but their performance was found to be outside the project temperature accuracy requirements over the extended temperature range of $-40\,°C$ to $100\,°C$. The sensors remained detectable by the interrogator throughout the experiment suggesting no significant changes in FBG structure occurred. Since none of the sensors failed a lifetime prediction cannot be extrapolated [245], but their successful operation across a wider temperature range than would be expected within experimental use, suggests operational lifetimes of at least one year, since this work evaluated them over that duration.

The sensor evaluation experiment was conducted until the thermal chamber experienced a mechanical breakdown. It took some time for the chamber to be repaired and re-calibrated, and at that time it was decided to not restart the FBG evaluation. Instead it was considered more valuable to use the chamber to test electronic temperature sensors (Chapter 4) and sub-system operation across a range of temperatures (Chapter 8 and 9).

Future assessments would benefit from monitoring a larger number of sensors in

order to increase the likelihood of observing a failure. Conducting the experiment with a higher temperature stability would enable further investigation of the drift characteristic identified within this work, and better assess the FBG sensor ability to satisfy the accuracy requirements. Higher stability could be achieved by adjusting the chamber PID settings, using a smaller chamber, or using a water or oil bath. Testing the sensors within the mechanical housings they would be deployed within an experiment (such as the one developed in Chapter 9) would also be worthwhile, to ensure the entire sensor system is correctly evaluated.

This work systematically cycled FBG temperature sensors in a novel study aiming to evaluate their long-term performance. The experiment lasted one year, in which time no sensor failures were detected, preventing lifetime estimation to be formed [245], but providing confidence in the short-term stability of the technique. Future studies aiming to provide a lifetime predication could evaluate a larger batch of sensors and run the experiment for a longer duration, increasing the chance of detecting a failure.

Chapter 6: Barometric Pressure Sensing

In a materials ageing experiment that features a sealed environment, monitoring the internal gas pressure can provide important data. In simple experiments without gas speciation sensing, a rise in pressure can indicate the evolution of gas-phase chemicals. When deployed alongside gas sensing techniques in more complex experiments, a pressure measurement can be required by some techniques to calculate the chemical species concentration. The availability of suitable barometric pressure sensors therefore enables the maximum flexibility in the design of material ageing experiments.

Optical fibre pressure monitoring techniques have been demonstrated in a number of forms [56, 87], but previous work at AWE [237] has investigated commercially available FFP based barometric pressure sensors [90]. The sensors were found to function within the range and accuracy required by this project, but their long-term reliability had not been evaluated [237].

This work investigated the endurance of FFP based barometric pressure sensors to aid assessment of their suitability for use within a materials ageing experiment. An accelerated testing approach was used to repeatedly cycle the sensors across their measurement range. The analysis of sensor failures would be used to provide information useful in forming a sensor operational life assessment.

The project required pressure measurements throughout the experimental duration able to measure from 0 mbar to 1200 mbar with an accuracy of ± 2 mbar. This pressure range was to ensure compatibility of the diagnostics with chemical experiments which require operation under vacuum and under known atmospheric conditions.

6.1 Predicted Failure Modes

The sensors were considered able to fail in multiple ways, such as those described below. The experiment was required to be able to detect complete failure of the sensor, or response changes such as baseline drift and sensitivity variation, in order to determine if this type of optical sensor would meet the project requirements over an extended period.

It was predicted the most likely failure mode for the sensor configuration would be loss of the pressure differential across the diaphragm. This could be caused by either a rupture in the metallic diaphragm or by a failure in the adhesive. Without the differential pressure the diaphragm would not respond to a change in barometric pressure and would result in complete sensor failure.

Baseline drift was thought possible due to fibre displacement within the tube, or due to a change in pressure within the evacuated cavity caused by gas permeation through the diaphragm or adhesive. Uncompensated baseline drift could be interpreted as a slow pressure change in an experiment.

Sensitivity change could have been possible through a change in diaphragm flexibility due to material work hardening over multiple cycles. A sensitivity change could cause misinterpretation of barometric pressure within an experiment, especially when the pressure is varying.

6.2 Long-Term Evaluation

An experiment was conducted to pressure cycle a number of COTS FFP sensors repeatedly, to aid in evaluating their suitability for long-term use.

Experimental Design

To investigate the predicted failure modes, six FFP sensors manufactured by Fiso (Canada) [90], were cycled over their specified range of 0 mbar to 1000 mbar. The aim was to simulate extensive use of sensors by incurring a number of pressure cycles significantly faster than would be seen in real-world experimental use, in a similar way as in the FBG evaluation experiment (Chapter 5). Figure 6.1 represents the pressure cycle pattern the sensors were subjected to. The cycle repeated weekly (168 hours) and started with a reference pattern which provided 200 mbar intervals for data analysis in support of the failure mode predictions. During the remaining six days the pressure was cycled between 1000 mbar and vacuum hourly resulting in 145 full-scale pressure cycles a week.

The experiment placed the six pressure sensors within a computer controlled pressure vessel as shown in figure 6.2, which was created for this work. The vessel hardware PID control system, MKS Instruments (USA) 250E, operated continuously, with PC software VI control updating and logging at 5 second intervals. The vessel pressure was measured using a calibrated Baratron capacitive transducer. The FFP sensors were supported within

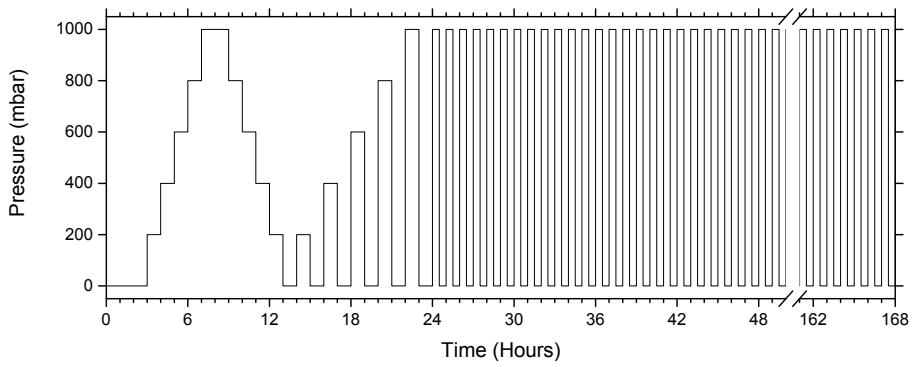

Figure 6.1: Weekly vacuum vessel pressure cycle pattern. The first day (0-24 hours) conducts a reference pattern. The remaining six days (24-168 hours) cycles the pressure between vacuum and 1000 mbar every hour.

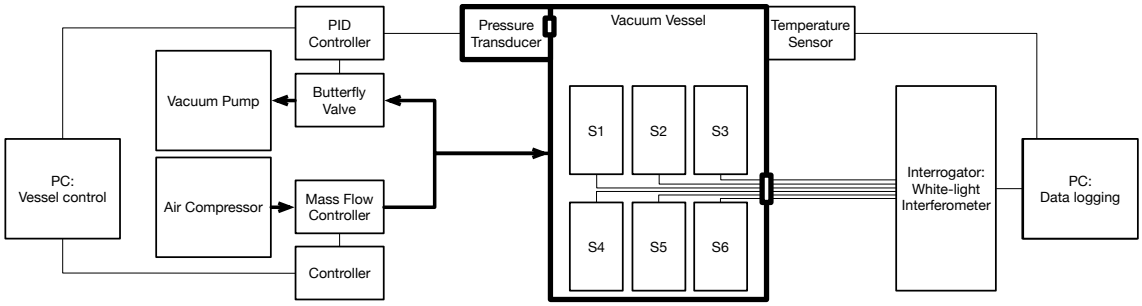

Figure 6.2: Schematic of experimental configuration. The vessel pressure is controlled using a vacuum pump and an air compressor. A calibrated pressure transducer provides the feedback for a PID control system. Six sensors (S1-S6) are connected via optical fibres from within the vessel to an interrogator through a custom-made vacuum feed-through.

the vessel on a rapid prototype (RP) frame, shown in figure 6.3, and were interrogated using a FieldSens white light polarisation interferometer from Opsens (Canada) [246]. This data along with vessel temperature were logged to a computer every 10 s. The experiment was not temperature controlled and operated at the ambient lab temperature. The vessel control and data logging VIs were written in LabVIEW and ran on a single PC (two are shown in figure 6.2 for diagrammatic clarity).

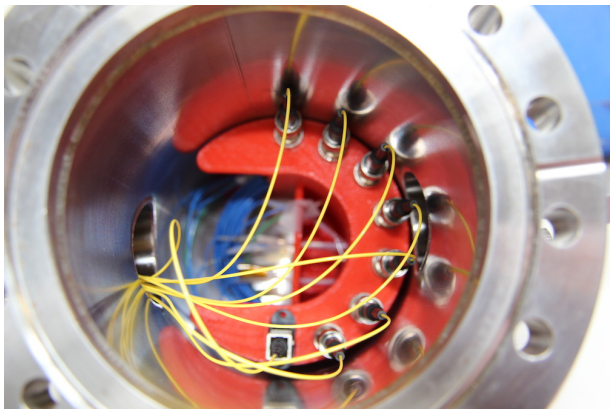

Figure 6.3: Photograph of the vessel interior of the long-term FFP sensor evaluation. The stainless steel vessel contained the six sensors supported within an orange RP support. The support contained 8 fibre couplers to manage the fibre connections (yellow) which entered the vessel.

Results

The experiment operated for a total of 51 weeks, after which the hardware PID controller malfunctioned resulting in unregulated vessel pressure. During the experiment each sensor received over 7300 full-scale cycles.

The pressure regulation of the vessel was investigated and shown in figure 6.4. The

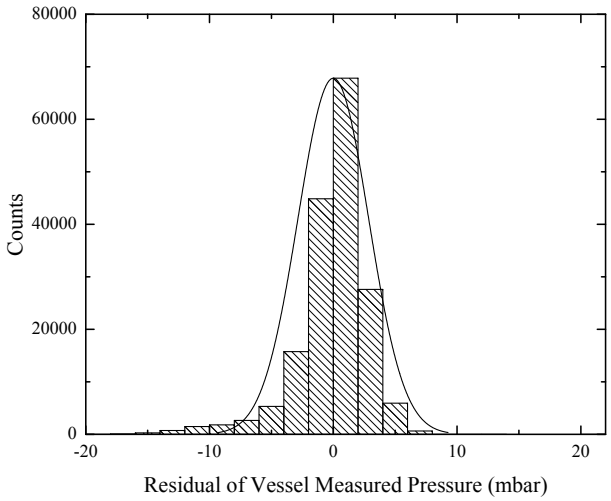

Figure 6.4: Pressure experiment measured vessel pressure residual analysis.

vessel pressure deviation from the set-point pressure was measured to be ± 4 mbar with a standard deviation of 2.8 mbar. The PID control loop gain settings had been set to enable the fast cycles shown in figure 6.1, at the expense of fine regulation during the quasi-isostatic periods. The vessel control system also contained uncertainties which contributed to the measured deviation. The vessel pressure readings had a stated accuracy of 0.2 % (of measured value), while the PID controller had a stated control accuracy of 0.25 % (of full-scale, $\approx$ 1340 mbar). At 1000 mbar these would suggest a combined

uncertainty of ± 4.1 mbar. As such, a measured vessel pressure stability of ± 4 mbar was considered reasonable.

The reference pattern data was extracted from the data (5600 measurements for each sensor per week) and the sensor cavity length was analysed relative to the measured vessel pressure. Figure 6.5 shows the sensor responses from the start of the experiment. A linear

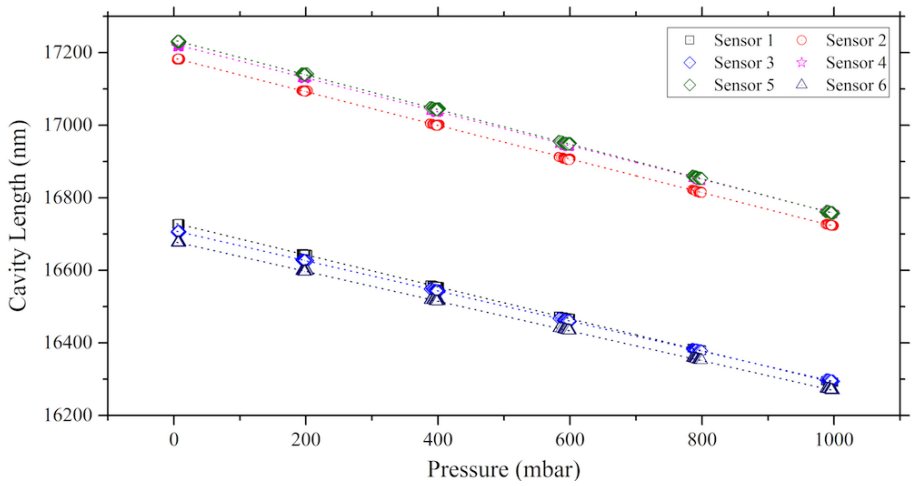

Figure 6.5: First weekly reference pattern response for the six FFP pressure sensors. Each sensor response is linearly fitted. Two distinct batches of sensors are apparent with different mean cavity lengths.

fit has been applied to each sensor's data to determine the sensitivity and offset.

Two batches of sensors were suggested by the pronounced difference in cavity lengths for sensors 1, 3 and 6 compared to sensors 2, 4 and 5. Further, the gradient for each sensor was different, suggesting a variation in sensitivities. These differences were attributed to variations in manufacture, and highlighted a requirement to characterise each sensor individually prior to use in an experiment. From each of the weekly reference patturns, a linear fit was performed for each sensor. The average gradients, offsets and SSEs for each sensor from these linear fits, over the entire experiment duration, are shown in table 6.1. The gradient was a measure of the sensor cavity length sensitivity to pressure, and the offset related to the zero-pressure cavity length. The SSE represented a measure of spread in the data of which an increase could be attributed to effects such as hysteresis.

The results suggested that the largest deviations between the FFP sensors and reference transducer measurements corresponded to a pressure measurement variation of 2.8 mbar, which matched the standard deviation of the vessel's pressure stability. Therefore the sensors were considered to have functioned as designed for the duration of the experiment without any sensor failures or discernible changes in sensitivity or offset. To further assist in this assessment, the weekly reference pattern data were plotted as a

Sensor	Gradient (nm mbar^{-1})	Offset (nm)	SSE (nm^2)
1	-0.4390 ± 0.0006	$16\,727 \pm 1$	3000 ± 1000
2	-0.4642 ± 0.0009	$17\,184 \pm 3$	7000 ± 4000
3	-0.4148 ± 0.0005	$16\,707.0 \pm 0.9$	2800 ± 600
4	-0.470 ± 0.001	$17\,228 \pm 3$	$10\,000 \pm 6000$
5	-0.4797 ± 0.0008	$17\,237 \pm 3$	9000 ± 6000
6	-0.4086 ± 0.0006	$16\,677.0 \pm 0.7$	6000 ± 3000

Table 6.1: Linear fit gradient, offset and SSE for each sensor over the experimental duration.

function of time, as in figure 6.6, showing the gradient, offset and SSE from the linear fitting. The vessel temperature is also shown in the graph as an indication of shifts in the experimental environment.

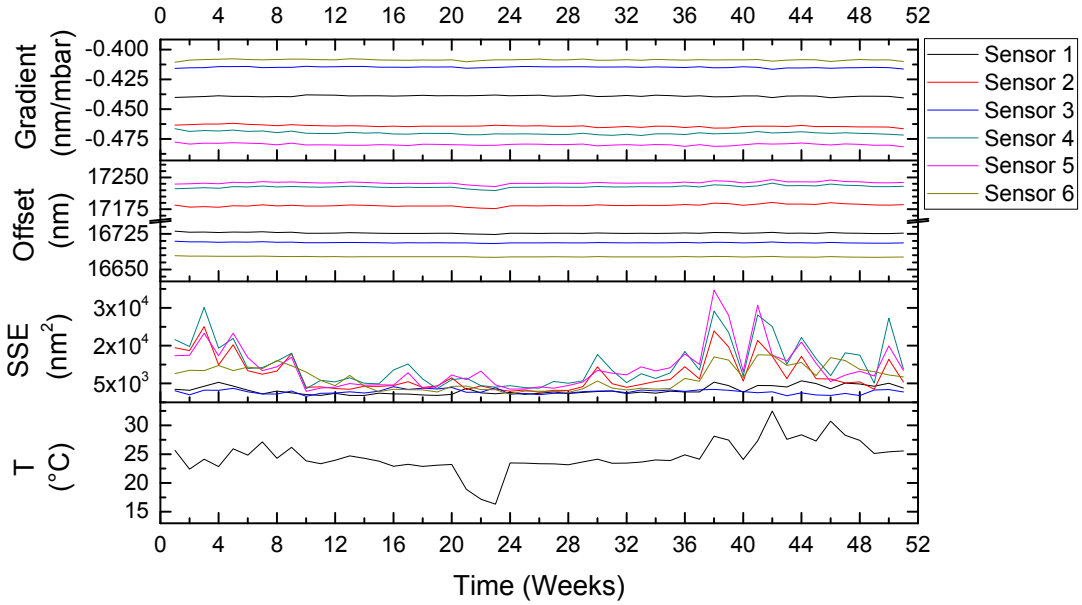

Figure 6.6: Linear fit coefficients for the weekly reference patterns with the sum of the squared errors (SSEs) for each fit and the weekly averaged vessel temperature during the reference pattern collection.

No large deviations were discernible, supporting the suggestion that all six sensors were still operational at the end of the experiment. The largest variations were in the linear fit offset values, but these can be attributed to changes in ambient temperature, suggesting a sensor cross-sensitivity to temperature, shown in figure 6.7. The variations in SSE values are more pronounced during times of higher temperature, and could be attributed primarily to temperature changes during the 24 hours period required for the reference pattern. The largest source of uncertainty in the experiment was from the vessel pressure regulation, ± 4 mbar, which suggested a minimum expected SSE of $5000\,\text{nm}^2$.

To evaluate the FFP sensor response at the end of the experiment, the final week's data for each sensor were correlated to their fitted linear regression, and the deviation presented

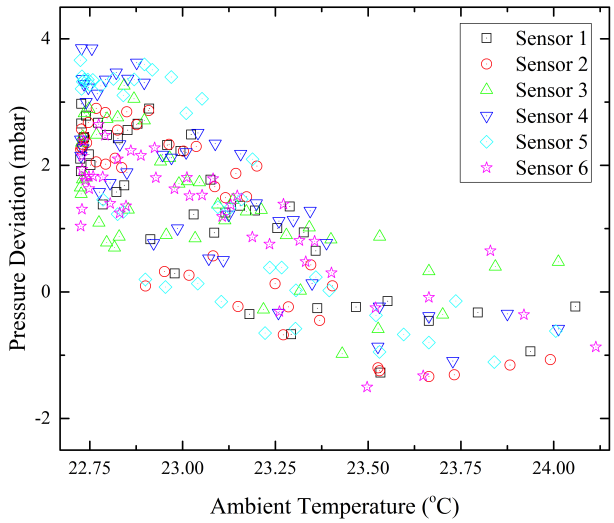

Figure 6.7: FFP sensor pressure value deviations from measured vessel pressure as a function of ambient temperature.

as histograms, as shown in figure 6.8. The histograms suggested the sensors were all operating simillarly to their initial measurements in week one, with some histograms indicating lower measurement deviations were observed in week 52, as supported by the corresponding reduction in SSE for some sensors between week 1 and week 52, as shown in figure 6.6.

Using the fitting gradients to convert from the cavity length (in nm) to barometric pressure (in mbar), the standard deviations from the histograms, shown in table 6.2, suggested all six FFP sensors were operating satisfactorily within the vessel pressure stability of ± 4 mbar, even after the 7300 pressure cycles. Sensors 5 and 6 were evaluted with deviations in excess of 2 mbar (the project requirements). Since this experiment focused on long-term performance not absolute accuracy, the vessel stability was ± 4 mbar, therefore further work would be required to confirm these deviations.

Sensor	Standard Deviation, nm	Standard Deviation, mbar
1	0.66	1.50
2	0.91	1.96
3	0.63	1.52
4	0.76	1.62
5	1.05	2.19
6	0.87	2.13

Table 6.2: FFP pressure evaluation from linear regressions from the final week (week 51) data.

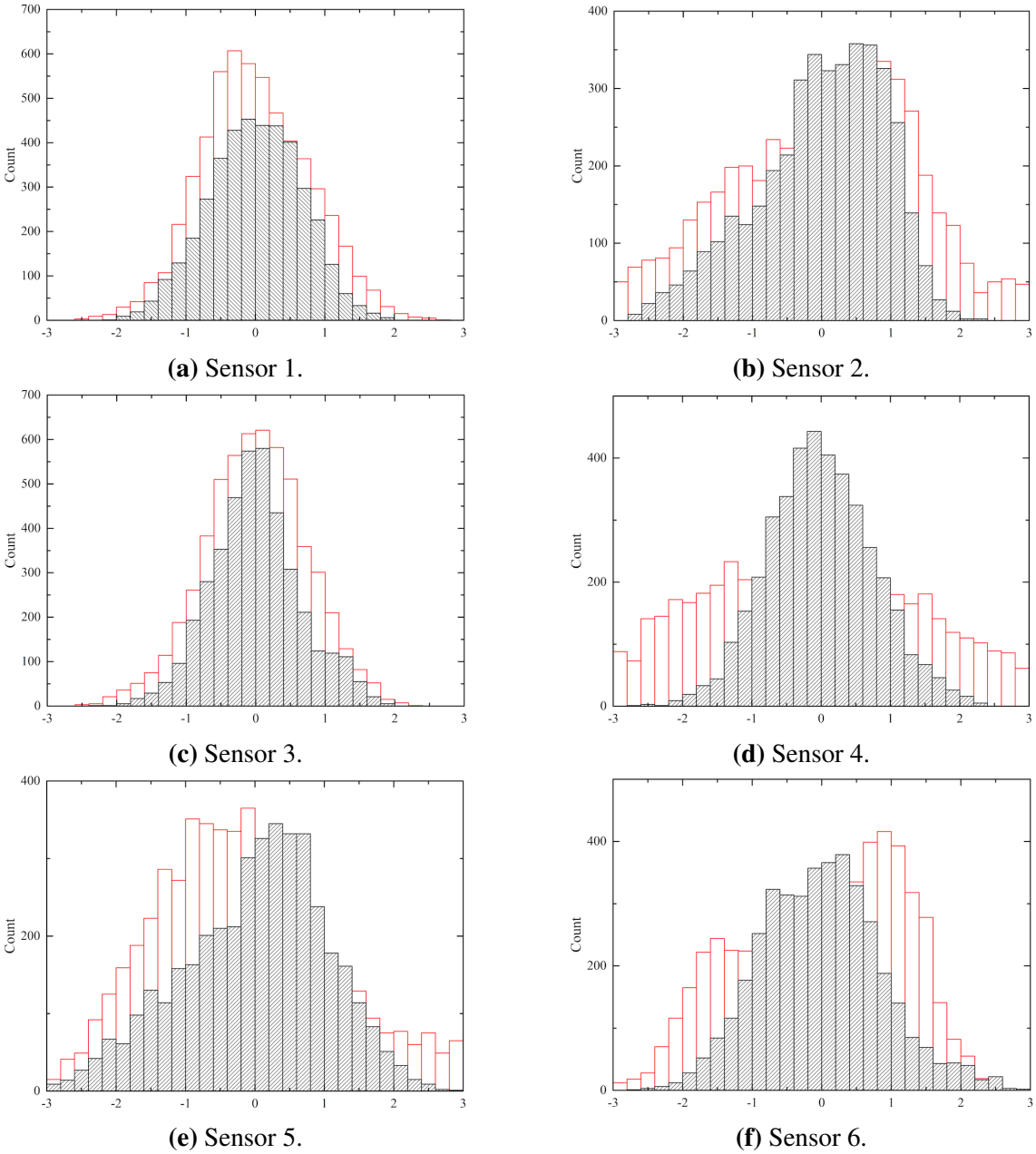

(a) Sensor 1.

(b) Sensor 2.

(c) Sensor 3.

(d) Sensor 4.

(e) Sensor 5.

(f) Sensor 6.

Figure 6.8: FFP sensor pressure experiment histogram analysis showing deviations in sensor cavity length (nm). In black, final week (week 51) measurements. In red, initial week (week 1).

6.3 Conclusions

The measurement of barometric pressure within a material ageing experiment is essential for enabling quantitative gas speciation measurements. Previous work had identified a potentially suitable sensor technique, but it's performance over a long time period, such as in a materials ageing experiment, needed evaluation.

Six FFP pressure sensors were cycled in excess of 7300 times over their specified pressure range and no discernible change in sensitivity or baseline was detected. These results support the use of such sensors within long-duration experiments and increase the confidence in the data they would provide. Since none of the six sensors experienced a failure a conclusion on the failure mode predictions cannot be made, nor can the data be extrapolated to predict sensor lifetime [245]. The data does however suggest confidence in operating these sensors at ambient conditions over the duration of one year, as was conducted in this thesis.

The experiment was halted by the failure of equipment required to control the vessel pressure. At the time of the failure the experiment had generated a significant amount of data, having operated for almost one year. As a result the experiment was not restarted once the equipment was replaced, instead choosing to use the system to evaluate electronic pressure sensors, such as those used in Chapter 4 and Chapter 8.

Further work could continue to cycle these sensors until failures are detected, and potentially adding additional sensors to increase the chance of failure. Analysis of these failure modes could potentially be used to form a sensor life prediction. To assist in identifying sensor failure modes, testing the sensors up to their maximum specified operating pressures could be investigated, as could operating the sensors at higher temperatures. Temperature cross-sensitivity of the sensors was identified within this experiment, and therefore deployment of these sensors would require a co-located temperature sensor to enable the accurate pressure to be resolved. Further in the future, use of alternative optical techniques for measuring barometric pressure may become advantageous, so regular review of the sector is recommended.

Chapter 7: Gaseous Chemical Detection

This chapter details work conducted on gaseous chemical detection. The feasibility of using absorption spectroscopy in the NIR was assessed and a bespoke multi-pass spectroscopic gas cell was developed to support measurement of H_2O. The cell was designed, manufactured, and assembled for evaluation. An alternative technique was required to satisfy the project sensing requirements for the detection of O_2. A specification analysis of a COTS fluorescence based sensor satisfied the project requirements, apart from confidence in its long-term performance. A long-term stability study of the sensor was therefore performed.

Within a materials ageing experiment, where single or multiple materials are within a sealed volume, analysing the chemical species within the head-space is a powerful tool for providing clues as to what chemical processes are occurring within the materials. Measuring the head-space composition, *in situ* and without modifying the chemistry of the system, could enable continuous and quantitative monitoring of the experiment.

The two techniques investigated in this work were both optically based and interrogated via optical fibres. The spectroscopic gas cell was intended for detecting H_2O, and the fluorescence based sensor was marketed for detecting O_2. Both systems were evaluated against the project requirements for both gas detection and for integration into the experimental scenario.

Requirements

The development and evaluation work were driven by the project requirements, to ensure the resulting suitability of techniques for potential use at AWE. The project requirements for gas detection were:

- To provide an *in situ* gas analysis capability within the head-space of the experimental configuration, enabling gas detection of:
  - H_2O from 40 ppm (by volume) to $100\,000$ ppm with a resolution of 40 ppm, [1]

[1] At 300 K these relate to minimum concentrations equivalent to -54 °C dew point, and 0.1 %RH. The maximum concentration is approximately equivalent to saturation up to 44 °C.

and
- O_2 from $0\,\%$ to $25\,\%$ with a resolution of $0.1\,\%$,

when measured at $300\,\mathrm{K}$ and $1000\,\mathrm{mbar}$.

Due to the gas sensing being located within the sealed volume of the experimental system, the developed system was also constrained by the following integration requirements:

- To provide high-confidence measurements throughout the experimental time-frame,
- To minimise impact to the experiment (e.g. chemically compatible),
- To be compact and able to fit within the experimental volume and shape,
- To be interfaced via compatible optical fibres to those used in the modular interrogation system (Chapter 3).

These requirements were used to direct down-selection of potential techniques and for the evaluation of the work conducted.

7.1 Detection Techniques Theory

Techniques for detecting gaseous chemicals are numerous, and have been developed for industrial, domestic, regulatory, defence, and scientific use [99,247]. This project focused its search on optical techniques which could provide quantifiable gas concentration measurements, chemical identification, and low interaction with the gas. From the survey conducted in Chapter 2, molecular absorption spectroscopy was chosen for further investigation. It was considered to be compatible with the project requirements and have the potential to provide quantifiable measurements, chemical identification, and no consumption of gas. Previous work at AWE [105,124] also ensured support was available.

Absorption spectroscopy

Absorption spectroscopy passes light through a gas and monitors the received light intensity as a function of wavelength. Individual gaseous chemical species exhibit unique *fingerprints* of wavelength-specific absorptions which can be detected optically. Identification of the gas can be achieved by measuring the absorption wavelengths, and the gas concentration can be related to the absorbance magnitude.

The absorbance magnitude is described by the Beer–Lambert law [248]:

$$\alpha(\lambda) = -\ln\left(\frac{I(\lambda)}{I_0(\lambda)}\right), \tag{7.1}$$

where I denotes the transmitted optical intensity through the gas, and I_0 is the initial signal intensity, at wavelength λ. The absorbance, α, is also defined in terms of gas properties [248]:

$$\alpha(\lambda) = L \sum_j S_j n \chi \psi_j(\lambda), \tag{7.2}$$

where L is the optical to gas interaction length, S is the (temperature dependant) linestrength of transition j, n is the number density of the gas of interest, χ is the mole fraction of the gas, and ψ is the (temperature, pressure, wavelength, and concentration dependant) lineshape function.

Using equations (7.1) and (7.2), a relationship for measured intensity can be formed:

$$I(\lambda) = I_0(\lambda) e^{-Lk(j,\lambda)}, \tag{7.3}$$

where k is chosen to contain the gas-specific functions in equation (7.2). In an experiment, I_0 and L can be varied in the design, but the other values would be constrained by the experimental design and gas species. Equation (7.3) shows the optical to gas interaction length (optical path length, L) is more critical than initial intensity in impacting the concentration measurement. Estimations of required optical path lengths were made to enable an evaluation of technique feasibility, but first operating wavelengths needed to be selected in order to find typical gas linestrength values.

The project required spectroscopy to be performed at wavelengths supported by NIR optical fibres. A search was conducted to find absorption wavelengths for H_2O, and O_2. It was important the wavelengths selected had suitable lasers and detectors available, and that the spectral region was specific to one of the chemicals, to enable identification. Absorptions close to 1352 nm have been previously demonstrated for H_2O detection (absorption lines shown in figure 7.1) [101, 105, 124]. Measuring O_2 using absorption spectroscopy is typically achieved at 761 nm (absorption lines shown in figure 7.2) [251] and commercial instruments are available based on this technique at this wavelength [125]. In both cases, the absorption regions are free from absorption features from the other chemical of interest. H_2O vapour is more commonly measured at 1396 nm [99], but the wavelengths chosen were based on AWE availability of DFB lasers and to ensure potential parasitic absorptions from materials within an ageing experiment were avoided [15].

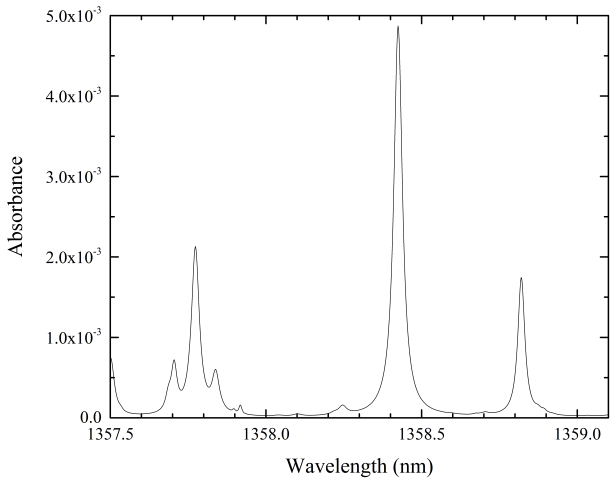

Figure 7.1: HITRAN [249, 250] H_2O simulation at $1358\,\text{nm}$ over a $0.1\,\text{m}$ path length, at $1000\,\text{mbar}$ and at $300\,\text{K}$, for a $0.1\,\%$ concentration of H_2O by volume.

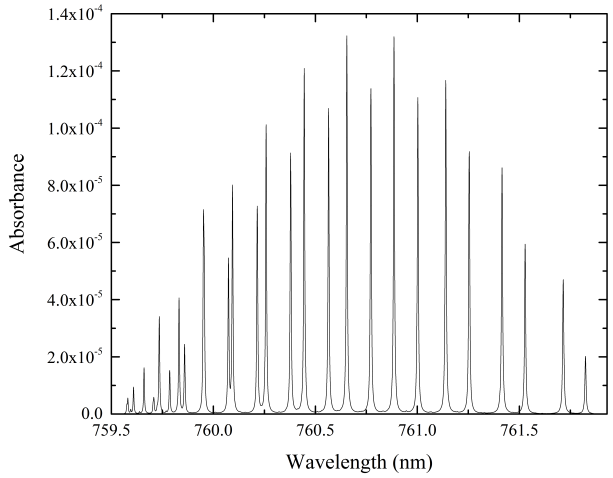

Figure 7.2: HITRAN [249, 250] O_2 simulation at $761\,\text{nm}$ over a $0.1\,\text{m}$ path length, at $1000\,\text{mbar}$ and at $300\,\text{K}$, for a $0.1\,\%$ concentration of O_2 by volume.

For the purpose of evaluating the potential for measuring the required chemicals using absorption spectroscopy, the high resolution transmission (HITRAN) database [248–250] was used to provide the chemical absorption database for simulations of spectroscopic configurations. From prior AWE experience, absorbance values between 0.01 to 3 (absorption: $\frac{I}{I_0} = 99\,\%$ to $5\,\%$), with a noise equivalent absorption (NEA) of $1 \times 10^{-3}\,\text{Hz}^{-1/2}$, were considered achievable using laboratory equipment to assemble a TDLAS system [15]. These values were considered optimistic based on a number of interrogation technique improvements demonstrated in literature, with minimum absorptions repeatedly demonstrated down to 1×10^{-9} [99,101,247] (compared to 0.01), but the values chosen by AWE were used to inform the development and evaluation of sensing techniques in this thesis. This project was focused on the identification and evaluation of gas detection techniques, rather than providing a fully optimised TDLAS

interrogation solution.

Through iterating HITRAN-based simulations and using the absorbance minimum threshold of 0.01, a search for the optical path length (L) required to satisfy the project requirements was conducted. The H_2O resolution requirement of 40 ppm was found to require an optical path length in the order of 6 m, when using the absorption at 1352.48 nm, at 300 K, and 1000 mbar. At this path length the detection system would be likely to saturate at the maximum required concentration of $100\,000$ ppm, since the simulation peaked at an absorbance of 24, which is significantly above 3. A number of other H_2O absorptions are located within the wavelength tuning range of a typical DFB laser of ≈ 0.8 nm, as shown in figure 7.1. For instance, by measuring the H_2O absorption at 1352.00 nm, in addition to the one at 1352.48 nm, could enable the maximum required concentration to be measured with an absorbance of 1.6 (when simulated at maximum concentration and at 317.15 °C) within the 6 m path length. Therefore a single cell could provide the full range of H_2O concentration values required using a single DFB laser.

Detection of O_2 with a resolution of 0.1 % was predicted to require an optical path length in the order of 90 m, when detecting at 760.89 nm, at 300 K, and 1000 mbar. The maximum required concentration is 25 %; this measurement would not saturate based on our system estimation. This optical path length estimation yielded a significantly longer length than that required for H_2O and CO_2, and was considered impractical. Alternative techniques were therefore investigated for the detection of O_2.

Detection of H_2O within the project requirements using TDLAS was considered achievable based on these calculations. It was considered ideal to measure both gases within a single spectroscopic gas cell, by using different wavelength lasers in the interrogation system. However, the required 6 m of optical path length was too long to fit into an experimental system. Multiple geometries have been previously demonstrated that enable the path to be folded between mirrors to enable the creation of compact gas cells with long optical lengths [99, 106, 108, 109, 124, 251–261].

Resonant techniques, such as those used in cavity-enhanced systems or cavity ring-down spectroscopy [108, 109], were discounted from further review due their wavelength-specific design. Such restrictions make the design of a multi-gas cell complex due to the multiple wavelength operation required. For non-resonant multi-pass gas cells with typical path lengths starting from multiple meters, those originated by White and Herriott are often demonstrated in literature [99, 259, 262, 263]. A multi-pass cell named after its geometry, the circular multi-reflection (CMR) cell has also been demonstrated [99, 105,

124,252]. Figure 7.3 provides an overview of these three common multi-pass cell designs. Many other geometries have been shown and each has a unique set of advantages and

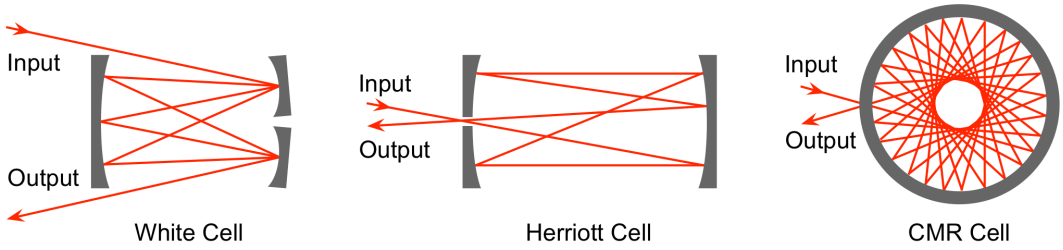

Figure 7.3: Diagrammatic overviews of three multi-pass gas cell designs: the White cell, the Herriott cell, and the circular multi-reflection (CMR) cell. In each case the input and output beams are identified.

disadvantages [99], but typically the simpler configurations see the most use. The key advantage typically associated with the White cell design is its ability to accept a high numerical aperture (NA) optical input [99], which could reduce collimation requirements in a fibre-coupled configuration. The Herriott cell is known to have high optomechanical stability [99, 257], which could be advantageous for long-term experimental use. The Chernin cell, which is physically similar to the White Cell (figure 7.3) but with additional small mirrors arranged in a 2-dimensional matrix, also accepts high NA inputs and has been demonstrated for path lengths in excess of 1 km [99, 261], which is far in excess of path lengths required for this work.

From the review of multi-pass gas cells conducted, the Herriott cell geometry was selected as the most suitable for this project due to its high optomechanical stability and demonstrated multi-gas use [99, 257]. A review of COTS Herriott cells was conducted with the requirements of fibre coupling, compact size, and optical path length of approximately 6 m. No commercially available options were found meeting the fibre coupled and compact size requirements, and cell designs included within literature were also not sufficiently compact or suitable for fibre-coupling. Therefore the decision was made to develop a bespoke cell for use within this work.

Fluorometry

An alternative gas sensing technique, that doesn't require optical path lengths, is fluorometry. Fluorometry is the general name given to sensing techniques which use variations in fluorescence lifetime or intensity to indicate a change in a sensing parameter of interest [65, 264–266].

Fluorescence is the optical process where higher energy photons are absorbed by

a material and then lower energy photons are emitted. The absorbed photons excite electrons from their ground state to some excited state. The electrons subsequently de-excite back to the ground state, but via multiple possible routes, some containing an optically radiative transition and one or more non-radiative transitions. The result is a broad range of emitted wavelengths from the material, at longer (lower energy) wavelengths than those used for the excitation [66, 67]. The process was first described by Stokes in 1852 [267]. In biology and chemistry, molecules used for their fluorescent properties are often called *fluorophores* where they are used as markers or tracers [67].

The intensity, I, of the light emitted from a *fluorophore* can be expressed as [67]:

$$I = I_0 k \Phi A_M, \tag{7.4}$$

where I_0 is the intensity of the illuminating light, k is a constant relating to the light coupling efficiency of the experiment, Φ is the quantum yield, and A_M is the molar absorptivity. In chemical or biological processes where the *fluorophore* is consumed or created, the intensity of fluorescence can be used as a measure of concentration [67].

An alternative technique is to monitor the fluorescence lifetime [268]. The lifetime can be modified by the presence of another chemical, through a quenching process, called intramolecular deactivation. The measured lifetime, τ, can be used to infer the concentration of a quenching chemical, [Q]. The Stern-Volmer relation provides the conversion between τ and [Q] [268, 269]:

$$\tau = \frac{\tau_0}{1 + \tau_0 k_q [\mathrm{Q}]}, \tag{7.5}$$

$$\therefore [\mathrm{Q}] = \frac{1}{\tau k_q} - \frac{1}{\tau_0 k_q}, \tag{7.6}$$

where τ_0 is the emission lifetime under quencher-free conditions and k_q is the bimolecular quenching rate constant. An example of the fluorescence lifetime variation due to changes in quencher concentration, formed from equation (7.6), is shown in figure 7.4, which indicates the sensitivity of this technique is greater at lower concentrations.

Molecular oxygen sensing has been previously demonstrated using this fluorescence quenching technique [270–272], and commercially produced sensors are also available [273, 274]. Baleiza *et al* use a dual *fluorophore* technique to simultaneously measure temperature, using a (ruthenium tris-1,10-phenanthroline) dye, and O_2 concentration, using fullerene C_{70} contained within a polymer [270]. The technique was

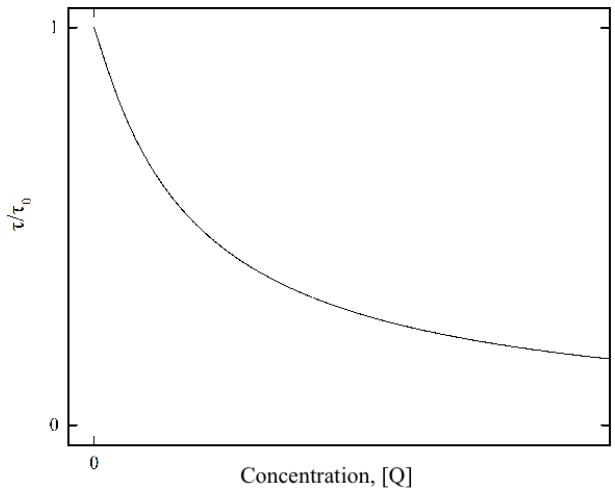

Figure 7.4: Fluorescence lifetime dependence on quencher concentration.

not demonstrated with an optical fibre based configuration, as is required for this thesis, but demonstrated a detection limit (DL) below 530 ppb, which is far below that required for this project (of 1000 ppm). Concentrations are only demonstrated up to 50 ppm, so performance at higher levels would need to be evaluated, before fibre integration was considered. Fresnadillo *et al* use ruthenium(II) tris-chelate complexes within polymer for creation of an O_2 sensor [272]. The temperature sensitivity of the fluorescence technique used is noted as significant and the sensor is not optical fibre integrated, so not suitable for use in this thesis. The evaluation is presented for concentrations from $0\,\%$ to $100\,\%$, in approximately $15\,\%$ increments.

Fluorescence-based sensors are typically interrogated using phase-fluorometers [273], since the decay time typically varies in the range of 10 ns to 10 µs and is therefore non-trivial to measure. The phase-fluorometer modulates the intensity, I_0, of the optical stimulation at a frequency, ω, while monitoring the return intensity, I, of the fluorescence signal. The phase difference between the stimulation and return signals, ϕ, can be related to decay time, τ, where [266]:

$$\tau = \frac{\tan(\phi)}{\omega}, \tag{7.7}$$

when a sinusoidal modulation scheme is used. The modulation frequency can be varied to maximise the sensitivity of the measurement and mitigate the phase-degeneracy introduced by the tangent function.

The COTS PSt7 sensor from PreSens (Germany) has a stated resolution of $\pm 0.05\,\%$ and an operating concentration range from $0\,\%$ to $100\,\%$ [274], suggesting compatibility with the project requirements. At low concentrations ($1\,\%$) the resolution is stated to

improve to $\pm 0.01\,\%$ [274], supporting the relationship shown in figure 7.4. The PSt7 is an optical fibre-based device and seemed likely to satisfy the project integration requirements, but experimental investigation to provide confidence in its long-term performance was recommended.

Conclusions

Using absorption spectroscopy to detect and measure H_2O to the project requirements was considered achievable, if a $6\,\mathrm{m}$ optical path length was achieved. The Herriott geometry was chosen for the basis of a bespoke compact gas cell design.

Detection and measurement of O_2 was not considered feasible via absorption spectroscopy due to an exceedingly long path length estimation to meet the project requirements. Instead, a fluorescence based sensor was considered likely to meet the project requirements based on a COTS sensor specification, but its operating performance over a long experimental time-frame was unknown. A long-term experiment was therefore required to provide confidence in the sensor and confirm if it could meet the project requirements. Since no extended study of such sensors has been reported, a novel experiment was conducted to repeatedly interrogate a fluorescence based sensor over a protracted time-frame and evaluate its performance.

7.2 Spectroscopic Gas Cell

A multi-pass spectroscopic gas cell was developed to enable H_2O measurements within the project's experimental system. The key design requirements for the cell were: the need for a compact size, integration with NIR optical fibres, chemical compatibility, and long-term robustness.

It was identified that an optical path length in the order of $6\,\mathrm{m}$ was required and that the Herriott cell geometry would be utilised.

Herriott multi-pass geometry

The Herriott cell geometry was chosen for use within the bespoke gas cell due to its optomechanical robustness and multi-pass topology. The physical shape of cells based on the Herriott geometry is typically cylindrical which was considered a suitable configuration to fit within many typical experimental systems. Multi-pass topology was considered advantageous compared to alternative resonant techniques, since one cell was

desired for the detection of multiple chemical species. A cell designed on the Herriott geometry is not wavelength dependant, so the range of wavelengths supported is only limited by the launch and collection optics.

In 1964 Herriott demonstrated a technique for reflecting a laser beam multiple times between two mirrors [262]. The design is non-resonant and can be used to create an 'open path', meaning the light does not re-travel the same path on its multiple reflection route within the cell. The geometry was contained between the two mirrors, where light enters the system at one mirror, typically through a hole, and then reflects many times between the two mirrors in a defined pattern, before exiting, typically through the entry hole, as shown in figure 7.3. In the Herriott configuration each trip through the cell has a unique reflection position on each mirror. The technique is shown for both spherically curved and for astigmatic curved mirrors [263], the latter enabling a wider coverage of reflections on the mirrors, at the expense of higher alignment tolerance requirements [99].

The Herriott geometry was modelled in this thesis using the ray transfer matrix method, which is a technique commonly used for optical systems [45, 46, 218–224]. For this project, a Herriott cell geometry with two spherical mirrors was chosen due to lower alignment tolerances. It was considered that future work could investigate the potential for creating an astigmatic cell design either to enable more compact cell designs or longer optical path lengths. Spherical mirror cell designs can result in a number of beam profiles on the mirrors, but one typically targeted is the tri-lobed design, which features a significant 120° rotational symmetry [257], and was used within this design.

The transfer matrix form used took the beam position in x and y and the beam angle, θ_x and θ_y, and represented them in a matrix form:

$$\mathbf{M} = \begin{pmatrix} x \\ \theta_x \\ y \\ \theta_y \end{pmatrix}. \tag{7.8}$$

One round trip through the gas cell, starting at the front face of the entry mirror, consists of: a translation along the cell, a reflection from the far mirror, a second translation along the cell, and a reflection from the entry mirror. The transformation

matrix for translation along the cell, $\mathbf{T}$, can be constructed:

$$\mathbf{T} = \begin{pmatrix} 1 & d & 0 & 0 \\ 0 & 1 & 0 & 0 \\ 0 & 0 & 1 & d \\ 0 & 0 & 0 & 1 \end{pmatrix}, \tag{7.9}$$

where d is the distance between the mirrors in meters. The two similar mirrors were spherically curved and placed perpendicular to the optical axis. The transformation matrix for a mirror reflection, $\mathbf{R}$, can therefore be constructed:

$$\mathbf{R} = \begin{pmatrix} 1 & 0 & 0 & 0 \\ -\frac{2}{R} & 1 & 0 & 0 \\ 0 & 0 & 1 & 0 \\ 0 & 0 & -\frac{2}{R} & 1 \end{pmatrix}, \tag{7.10}$$

where R is the mirror radius of curvature in meters.

A round trip transformation matrix for the cell, $\mathbf{C}$, can be constructed using $\mathbf{T}$ and $\mathbf{R}$:

$$\mathbf{C} = \mathbf{RTRT} \tag{7.11}$$

$$\mathbf{C} = \begin{pmatrix} 1 & 0 & 0 & 0 \\ -\frac{2}{R} & 1 & 0 & 0 \\ 0 & 0 & 1 & 0 \\ 0 & 0 & -\frac{2}{R} & 1 \end{pmatrix} \begin{pmatrix} 1 & d & 0 & 0 \\ 0 & 1 & 0 & 0 \\ 0 & 0 & 1 & d \\ 0 & 0 & 0 & 1 \end{pmatrix} \begin{pmatrix} 1 & 0 & 0 & 0 \\ -\frac{2}{R} & 1 & 0 & 0 \\ 0 & 0 & 1 & 0 \\ 0 & 0 & -\frac{2}{R} & 1 \end{pmatrix} \begin{pmatrix} 1 & d & 0 & 0 \\ 0 & 1 & 0 & 0 \\ 0 & 0 & 1 & d \\ 0 & 0 & 0 & 1 \end{pmatrix} \tag{7.12}$$

$$= \begin{pmatrix} 1 & 0 & 0 & 0 \\ -\frac{2}{R} & 1 & 0 & 0 \\ 0 & 0 & 1 & 0 \\ 0 & 0 & -\frac{2}{R} & 1 \end{pmatrix} \begin{pmatrix} 1 & d & 0 & 0 \\ 0 & 1 & 0 & 0 \\ 0 & 0 & 1 & d \\ 0 & 0 & 0 & 1 \end{pmatrix} \begin{pmatrix} 1 & d & 0 & 0 \\ -\frac{2}{R} & 1-\frac{2d}{R} & 0 & 0 \\ 0 & 0 & 1 & d \\ 0 & 0 & -\frac{2}{R} & 1-\frac{2d}{R} \end{pmatrix} \tag{7.13}$$

$$= \begin{pmatrix} 1 & 0 & 0 & 0 \\ -\frac{2}{R} & 1 & 0 & 0 \\ 0 & 0 & 1 & 0 \\ 0 & 0 & -\frac{2}{R} & 1 \end{pmatrix} \begin{pmatrix} 1-\frac{2d}{R} & d(2-\frac{2d}{R}) & 0 & 0 \\ -\frac{2}{R} & 1-\frac{2d}{R} & 0 & 0 \\ 0 & 0 & 1-\frac{2d}{R} & d(2-\frac{2d}{R}) \\ 0 & 0 & -\frac{2}{R} & 1-\frac{2d}{R} \end{pmatrix} \tag{7.14}$$

$$\mathbf{C} = \begin{pmatrix} 1-\frac{2d}{R} & \frac{2d(R-d)}{R} & 0 & 0 \\ \frac{4(d-R)}{R^2} & \frac{4d^2-6dR+R^2}{R^2} & 0 & 0 \\ 0 & 0 & 1-\frac{2d}{R} & \frac{2d(R-d)}{R} \\ 0 & 0 & \frac{4(d-R)}{R^2} & \frac{4d^2-6dR+R^2}{R^2} \end{pmatrix}. \tag{7.15}$$

Using this transformation matrix, the beam position could be calculated after its reflection on the entry mirror after any number of round-trips through the cell, n, given a known starting beam position and angle, using:

$$\mathbf{M_n} = \mathbf{C^n}\,\mathbf{M_0}. \tag{7.16}$$

The method was used by choosing initial starting beam properties containing a desired

position and arbitrary small angles:

$$\mathbf{M_0} = \begin{pmatrix} 0 \\ -0.01 \\ 0.004 \\ -0.01 \end{pmatrix}. \tag{7.17}$$

Microsoft (USA) Excel was then used to numerically calculate the final beam position after 37 round-trips through the cell with mirrors of focal length $100\,\text{mm}$ and mirror separation of $95.2\,\text{mm}$. The input beam angles were adjusted until the $\mathbf{M_{37}}$ x and y position matched the initial position to within $0.1\,\text{mm}$. The adjustment to the angles were made using Excel's in-built *Solver* goal-seeking feature. In a typical Herriott cell arrangement the resulting input and output angles could then be used to assist in experimental alignment. The aim of this work was to create a cell with the required angles engineered into the mechanical structure to provide mechanical robustness and long-term alignment stability. The model was used used to calculate the mechanical tolerances required for alignment, as described further below.

Because the input and output angle difference is small, to assist in fibre coupling to the system, the cell was designed to enable collection of the beam from trip 36 (as opposed to trip 37, which would be the typical configuration) through a second hole in the entry mirror. The second hole would be approximately 120° from the first around the axis of the cell, providing sufficient space to fit both optical fibre collimators side-by-side behind the entry mirror. The output beam properties were calculated using equation (7.16) for $\mathbf{M_{36}}$. This method modelled the position where the beam would hit the mirror, but the angles were incorrect since they included a mirror reflection which would not occur. Equation (7.16) was modified to provide the desired position and angle:

$$\mathbf{M_n} = \mathbf{TRT}\ \ \mathbf{C^{n-1}}\,\mathbf{M_0}. \tag{7.18}$$

Using this method, 70 mirror positions, (entry, exit, and 36 round trips) were modelled and provided both the input and output beams positions and angles, which were used to inform the design of a bespoke spectroscopic gas cell. The position of each reflection on the entry mirror was calculated and is shown in figure 7.5. The numbering denotes the starting position of each full pass through the cell (not the resulting position), thus the first

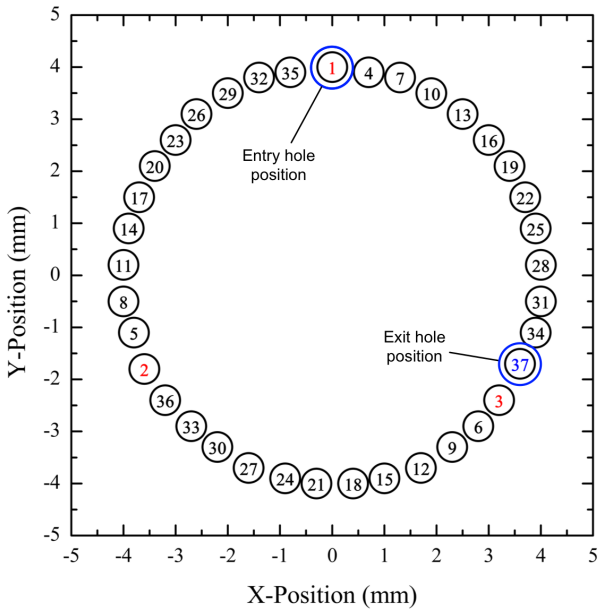

Figure 7.5: Modelled Herriott geometry beam positions on the entry mirror. Beam positions are numbered to indicate the order of beam reflection.

beam at position (0 mm, 4 mm) is marked 1 not 0. The first three positions are marked in red to highlight the tri-lobed pattern of the geometry. Position 37, marked in blue, is the exit location of the beam.

The matrix model was experimentally verified by placing the mirrors within laboratory breadboard optics mounts and launching light from a collimator along the calculated path. Since the experimental configuration was assembled from COTS components, the mirror separation and beam path desired were not exactly matched. The achieved configuration was examined and the matrix model was updated with the new values. A photograph of the entry mirror when the cell was illuminated from a fibre-coupled 632 nm red laser diode, overlaid with the matrix model reflection locations, is shown in figure 7.6. Good agreement was demonstrated between experimental and theoretical results. Minor deviations were expected from parallax errors in the photograph due to the angle from which it was taken; the rear mirror blocked access for a perpendicular image. The entry hole (top) and exit hole (mid-left) are also visible and were rear-illuminated by a white LED.

This breadboard demonstration provided confidence in both the technique and validity of the matrix transfer method employed. The model was therefore used to generate a cell geometry to achieve an estimated 6.85 m of optical path length, which was intended to enable gas sensing of H_2O meeting the project requirements.

By varying parameters within the model, including collimator angle, collimator

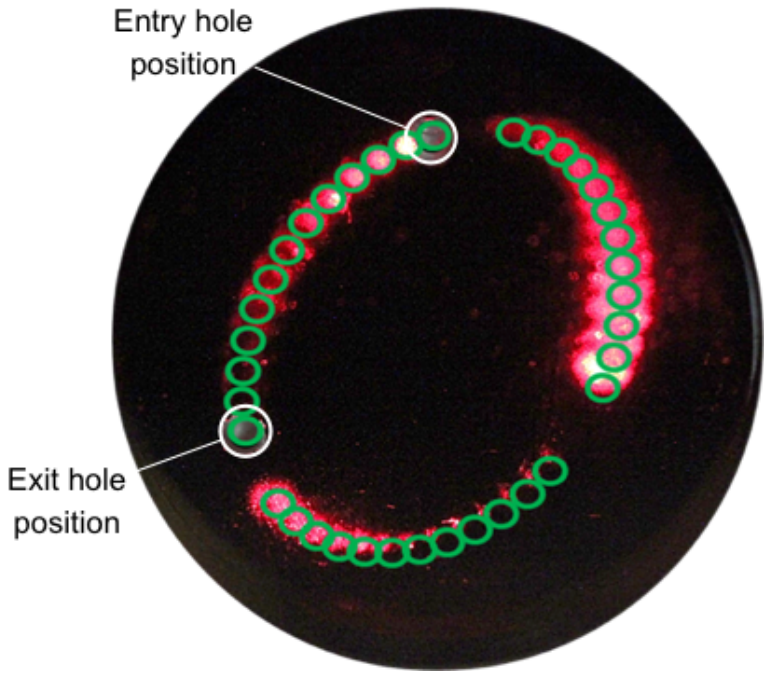

Figure 7.6: Photograph of Herriott geometry model verification on the launch mirror with overlaid theoretical locations. Photograph was taken at an angle so parallax errors are present in the image.

position, mirror separation distance, and mirror radius of curvature, the sensitivity to mechanical perturbations were evaluated. The collimator angle was required to be maintained within $\pm 0.5°$, the collimator positions were required to be within ± 0.2 mm, the distance between the mirrors was required to be within ± 0.1 mm, and the mirror radius of curvature was required to be within ± 0.5 mm. These tolerances were considered to be within manufacturing limits, and once assembled only the mirror separation distance would be likely to vary. This distance could be affected by changes in temperature which would cause thermal expansion or contraction of the cell. If manufactured from stainless steel 316, the ± 0.1 mm mirror separation tolerance would equate to a temperature variation of ± 10 °C.

Spectroscopic gas cell mechanical design

Using the modelled geometry, a spectroscopic gas cell was designed to achieve the 36 round trip, 6.85 m path length design. The model provided the specification for mirror separation, mirror curvature, hole positions on the entry mirror, and optical fibre collimator angles. Key aims were fibre coupling, small size, long term robustness, and chemical compatibility. The engineering sketch of the entry mirror designed is shown in figure 7.7. The alignment notch was included to provide a rotational constraint during assembly. The rear mirror was identical to the entry mirror, but without the two 0.6 mm

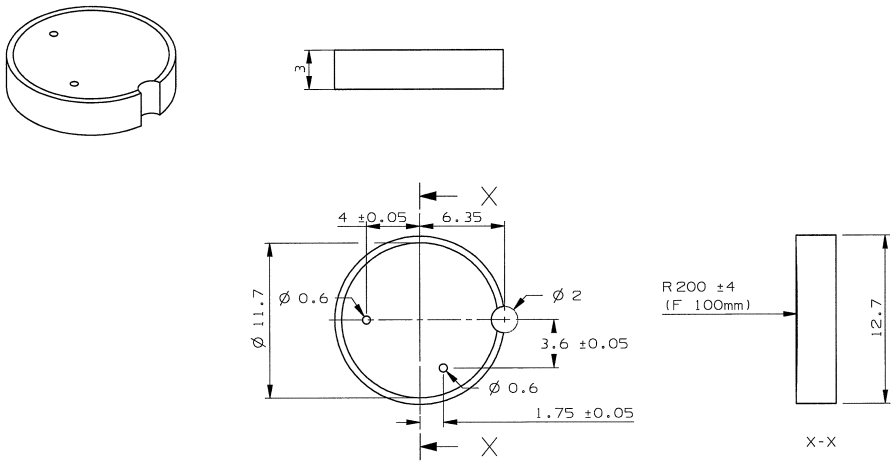

Figure 7.7: Entry mirror sketch for Herriott cell design. The design features two holes and an alignment notch.

holes. The collimated beam diameter $(1/e^2)$ was designed to be 0.4 mm, which ensured that within the mirror hole size, physical tolerances, and beam angle, the beam and mirror would not interfere.

The cell was required to constrain the two mirrors in parallel and at a specific separation, while also holding two optical fibre collimators at the correct position and angle. The cell design contained holes to enable free diffusion of gas to ensure the gas detected within the cell was an accurate representation of the experimental environment. Multiple cell mounting options were also included to aid evaluation and experimental design. A schematic diagram of the cell construction is shown in figure 7.8. The mirrors

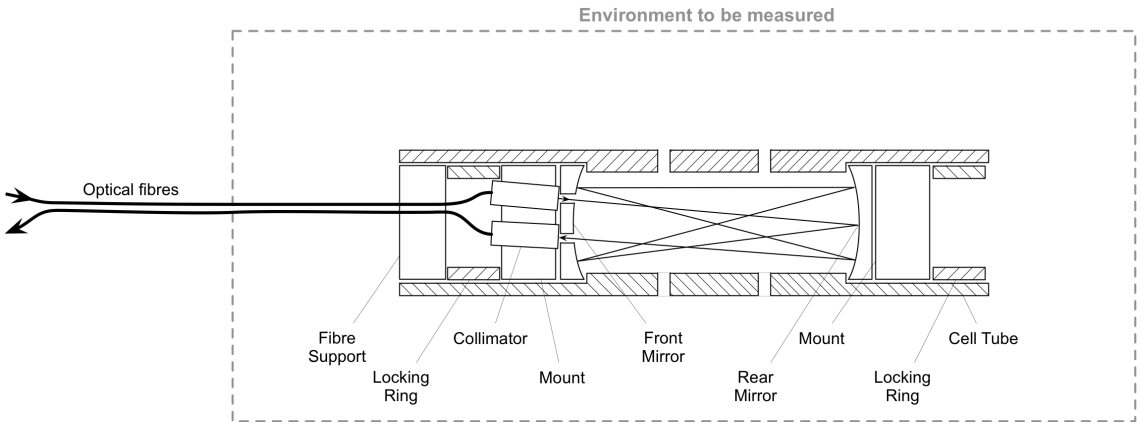

Figure 7.8: Diagram of bespoke Herriott cell design construction. Beam paths shown are illustrative only.

are located within the cell tube, positioned on an internal lip. The mirrors are kept in position by a mount and a threaded locking ring which provides pressure locating the mirror robustly on the internal lip. The mount has angled holes at the correct positions to align two collimators with the mirror holes and geometric modelling. There are

no alignment features included within the design, such as collimator angle or mirror separation adjustments, to aid with long-term robustness, since there are no adjustments to become miss-aligned over time.

A 3D representation of the design, including beam paths based on the matrix model, is shown in figure 7.9.

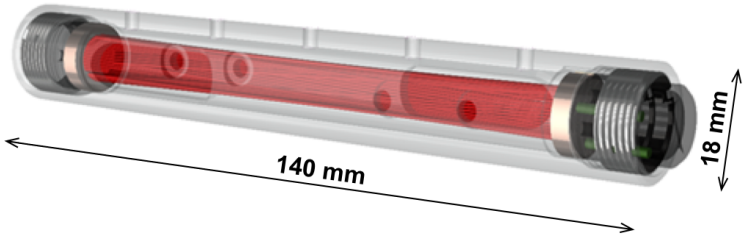

Figure 7.9: CAD image of designed multi-pass Herriott cell. The cell tube is shown translucent, and the (red) optical path is shown following the simulated geometry.

The cell design had an outer diameter of 18 mm and a total length of 140 mm with two optical fibres exiting from one end. The design was intended to be sufficiently defined and toleranced to negate the need for alignment during assembly, both simplifying the assembly procedure and removing sources of drift during an experiment.

Spectroscopic gas cell manufacture

Manufacture of the cell required the purchase of custom gold coated mirrors and pigtailed optical fibre graded index collimators, the drilling of holes within the entry mirrors, and the machining of three metal parts.

Mechanical drilling of the holes was achieved by Mr Mark Leonard, a technician with the School of Engineering and Physical Sciences at Heriot-Watt University. A photograph of one of the drilled holes is shown in figure 7.10. The hole was drilled to a diameter of 0.8 mm and localised damage to the gold coating was noted.

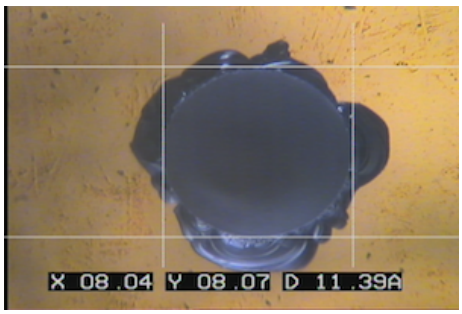

Figure 7.10: Photograph of drilled mirror hole for the bespoke Herriott cell. The cursors are indicating a finished hole size of approximately 0.8 mm.

The damage was sufficiently close to the hole to not cause significant impact on the operation of the cell, since only the entry and exit beams pass close to the holes.

The three metal components (cell tube, mount, and locking ring) were manufactured in-house at AWE with support from the tooling drawing office and the conventional materials manufacturing facilities. A photograph of the cell tube is shown in figure 7.11. A photograph of the mount is shown in figure 7.12. These three parts were manufactured

Figure 7.11: Photograph of manufactured bespoke multi-pass Herriott cell tube.

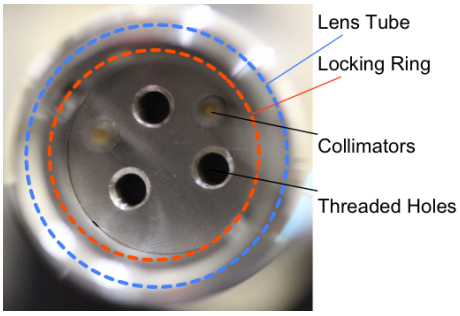

Figure 7.12: Photograph of mount within the lens tube and with locking ring in place, with two fibre collimators visible, and three threaded holes for grub screw adjustment (not used).

from stainless steel 316. The material choice was made for its chemical compatibility within a large range of experiments and its low thermal expansion, which was estimated to enable the cell to function within a $\pm 10\,^{\circ}\mathrm{C}$ temperature range. Whilst this range was too small for all experimental configurations, such as thermally accelerated ageing experiments, it was thought sufficient to enable laboratory cell evaluation. Re-manufacturing in a near-zero thermal expansion material such as Invar (FeNi36) was considered possible in the future.

The purchase of the gold coated mirrors was processed as a custom order due to the non-standard combination of $12.7\,\mathrm{mm}$ diameter and focal length of $100\,\mathrm{mm}$ ($R = 200\,\mathrm{mm}$). The drilling of the holes within the front mirror was one of the more complex processes required. The Heriot-Watt University team tried a number of techniques including laser drilling, but the final mirrors were created by mechanically drilling under a layer of water. The final mirrors featured holes larger than originally specified but it was considered acceptable for the beam spot size and mirror reflection density of the design. The pigtailed graded refractive index (GRIN) fibre collimators were standard catalogue

items, but they were not produced to the angular tolerances required. Upon enquiry it was indicated the angular tolerance required could be achieved, but no quotation was forthcoming from the manufacturer at the low quantities the project desired. In the future, a larger order should be able to yield a higher level of supplier engagement, but this work continued using the collimators procured. The manufacture of the metal components at AWE was achieved, once it was accepted the tight tolerances were a requirement.

Upon full assembly the components fitted together as expected. The full assembly consisted of $1\times$ cell tube, $1\times$ front mirror, $1\times$ rear mirror, $2\times$ mount, $2\times$ locking ring, $2\times$ pigtailed fibre collimator. Alignment was evaluated using a $632\,\text{nm}$ fibre-coupled laser diode after assembly. Since the collimators did not meet the required specification for coaxial beam output, the cell did not function as intended. The collimators required adjusting to achieve alignment, which consisted of rotating the collimators within their holes in the mount until a secondary Herriott geometry solution was found. With the support of the computational model, this was found to be achievable using a 34-pass solution, which was confirmed when light was detected in the collection fibre.

Spectroscopic gas cell experimental evaluation

A TDLAS experimental configuration was assembled from bench-top equipment to enable evaluation of the manufactured gas cell. The equipment was connected as shown in figure 7.13. A signal generator was used to provide a saw-tooth modulation source, a

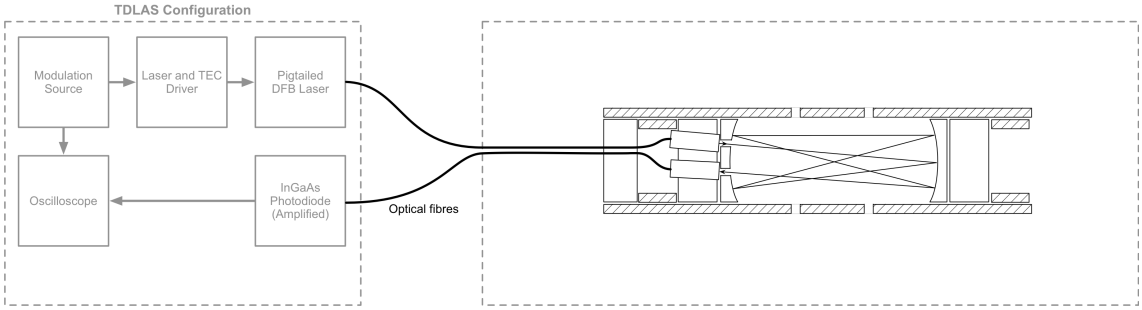

Figure 7.13: TDLAS evaluation experimental configuration.

NanoPlus (Germany) $1352\,\text{nm}$ DFB pigtailed diode laser was driven from a Thorlabs (USA) Pro8000 laser and TEC driver. An InGaAs amplified photodiode with fibre coupling was used to measure the returned optical signal from the cell, and an oscilloscope was used to capture the data.

The laser driver used the modulation input from the signal generator to vary the drive current to the diode laser. The TEC driver maintained the laser package at a constant

34 °C. As the drive current was varied, the wavelength of the laser also changed. The wavelength change was sufficient to cause the laser to scan over four absorption lines of H_2O. The laser was modulated at 500 Hz. The relationship between modulation voltage and wavelength was evaluated to enable the creation of a conversion fit, shown in figure 7.14. The relationship was measured using three wavelength references within the

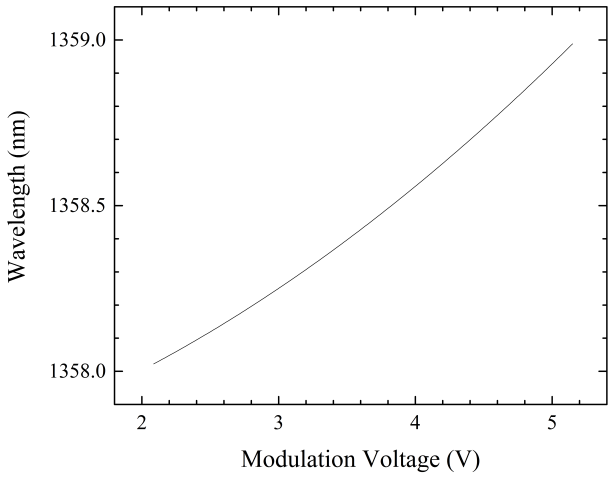

Figure 7.14: Modulation voltage to wavelength relation for the assembled TDLAS system using a 1352 nm DFB laser.

scan window and numerically fitting a 2nd order polynomial. The signal generator was noted to introduce noise to the system in the form of a non-linear sweep. Figure 7.15 shows the residual of the linear modulation sweep as a function of laser wavelength. The ± 0.01 V deviations of the modulation signal would cause a corresponding deviation in laser wavelength. This experimental configuration was considered non-ideal but sufficient to perform an experimental evaluation of the gas cell to inform future development. To partially mitigate the modulation deviations, the oscilloscope performed a 256 rolling average during data acquisition.

The TDLAS system was initially used to evaluate the cell test configuration which was assembled to perform the ray matrix transfer model validation. The experiment was conducted in the open laboratory environment with the aim of detecting the ambient H_2O. The local temperature and relative humidity were separately monitored. The measured optical power as a function of time was recorded, along with the modulation voltage as a function of time. The optical power as a function of modulation voltage was then calculated and converted using the fit in figure 7.14 to reveal the optical power as a function of wavelength. The detector baseline signal level (signal with the laser off) was then subtracted. To this signal a linear baseline was fitted to account for the increasing laser power output which accompanied the increasing drive current and wavelength shift.

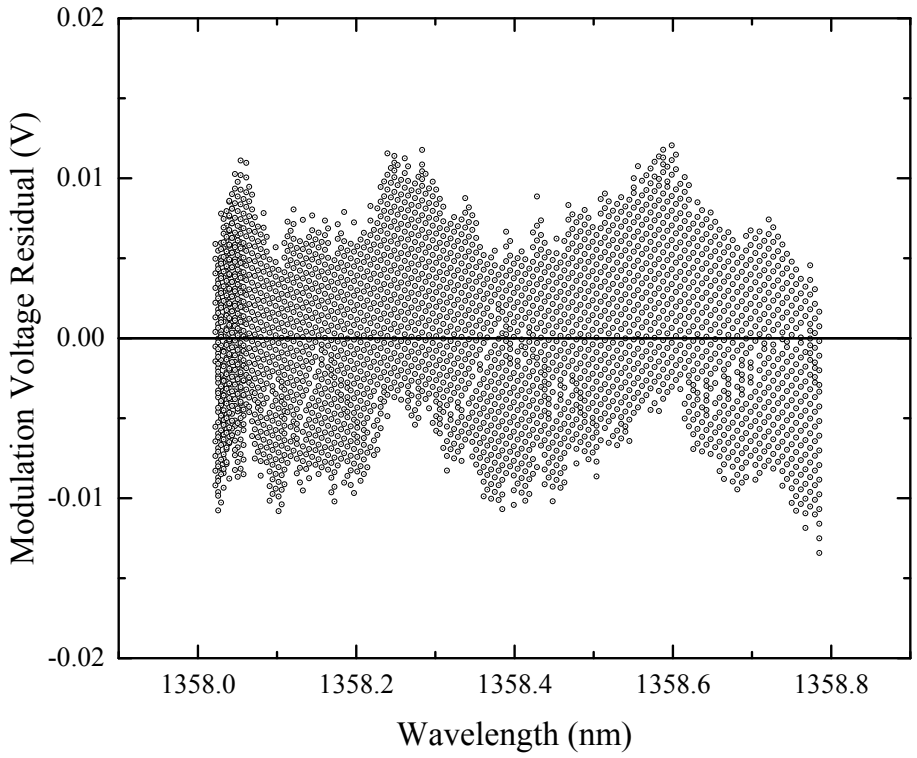

Figure 7.15: The residual of 2nd order polynomial fitting of the TDLAS modulation voltage, showing deviations from a linear voltage increase.

The signal was then divided by the calculated baseline to give absorption as a function of wavelength. Finally the absorbance was calculated from the absorption data by taking the negative of the natural logarithm. The calculation steps can be summarised as:

$$\text{Take measurement:} \quad \text{Signal}(t), \text{Modulation}(t) \tag{7.19}$$

$$\text{Adjust to wavelength:} \quad \Rightarrow \text{Signal(Modulation)} \quad \Rightarrow \text{Signal}(\lambda) \tag{7.20}$$

$$\text{Detector adjustment:} \quad \text{Signal}(\lambda) - \text{Detector baseline} \quad = \text{Signal}^*(\lambda) \tag{7.21}$$

$$\text{Calculate baseline:} \quad \text{Linear fit } \left[\text{Signal}^*(\lambda)\right] \quad \Rightarrow \text{Baseline}(\lambda) \tag{7.22}$$

$$\text{Calculate absorption:} \quad \frac{\text{Signal}^*(\lambda)}{\text{Baseline}(\lambda)} \quad = A(\lambda) \tag{7.23}$$

$$\text{Calculate absorbance:} \quad -\ln A(\lambda) \quad = \alpha(\lambda) \tag{7.24}$$

The resulting absorbance as a function of wavelength is shown in figure 7.16, along with the superimposed HITRAN simulated data in equivalent conditions. Strong agreement was noted between the measured signal and the simulated HITRAN values, suggesting the test configuration was working as expected. Only two H_2O peaks were detected within the laser scan range, and the geometry was estimated to achieve an optical path length of (6.47 ± 0.05) m.

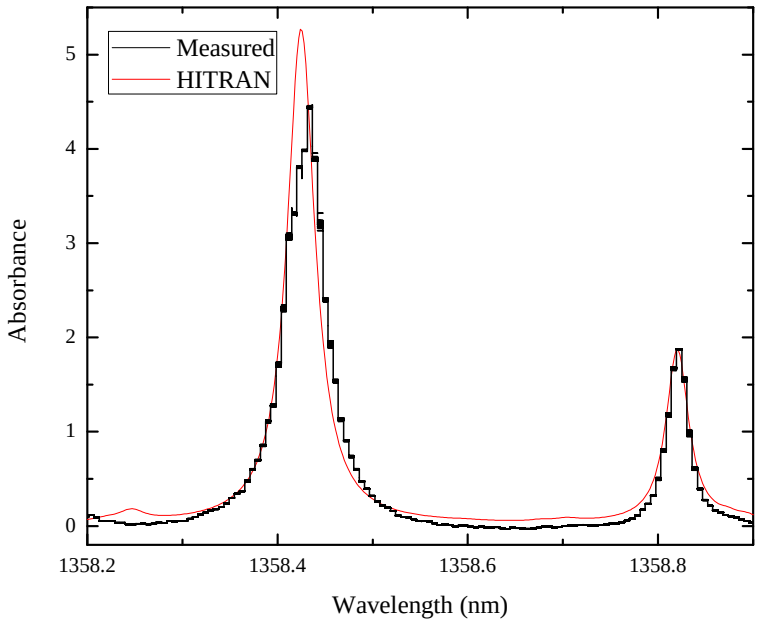

Figure 7.16: TDLAS experimental evaluation of breadboarded gas cell geometry while detecting ambient H_2O. HITRAN simulated spectra are also shown for comparison.

The TDLAS system was then used to measure the assembled gas cell that was designed and manufactured as part of this project. The system was used to measure the ambient laboratory H_2O level as before. The measured absorbance and corresponding HITRAN simulation are shown in figure 7.17. Good correlation was noted between the measured signal and the HITRAN simulation. The absorption near $1358.4\,\text{nm}$ had saturated the TDLAS system so data shown with absorbance above ≈ 2.8 was considered indicative rather than quantitative. The absorption near $1358.8\,\text{nm}$ was measured to be smaller than expected. Operation at the design geometry would require a new batch of collimators, assembled within the required tolerance, but the path length achieved of $(6.47 \pm 0.05)\,\text{m}$, was considered to be close to the target length of $6.85\,\text{m}$. Using HITRAN simulations and the results from the manufactured gas cell, the maximum detection resolution of the cell was evaluated, using the reference absorbance 0.01, and taking account of uncertainties in path-length, measured humidity, and the cell alignment, the detection limit was determined to be $(38 \pm 12)\,\text{ppm}$ of H_2O, which met the project's requirement of $40\,\text{ppm}$.

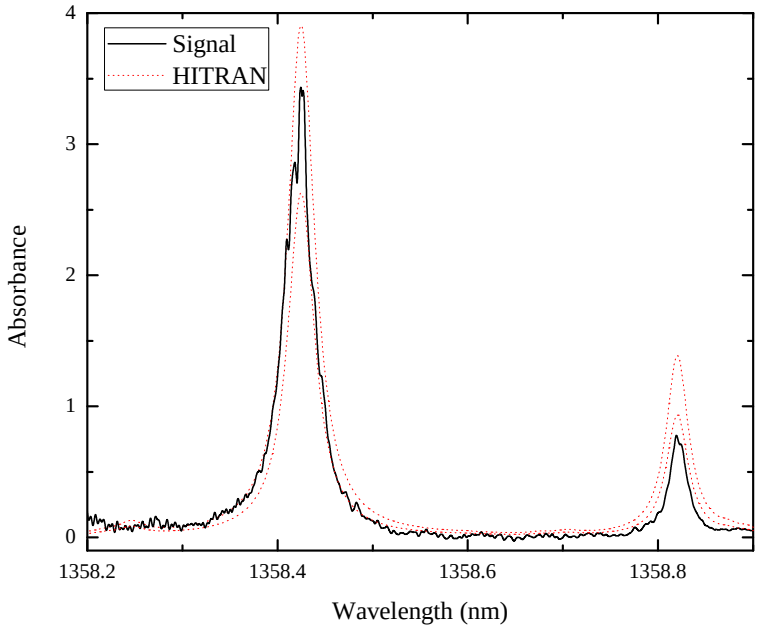

Figure 7.17: TDLAS experimental evaluation of manufactured gas cell while detecting ambient H_2O. HITRAN simulated spectra are also shown with an upper and lower prediction band based on the ambient humidity measurement uncertainty.

Spectroscopic gas cell conclusions

Absorption spectroscopy in the NIR was selected for detection of H_2O and CO_2. A non-resonant multi-path optical arrangement was chosen to enable multiple chemicals to be detected by one gas cell while enabling a physically compact arrangement. The Herriott geometry was chosen requiring two spherical mirrors. A mathematical model was developed to calculate the mechanical cell parameters following which the cell was designed and manufactured. The manufactured cell was experimentally evaluated using a TDLAS system to measure ambient H_2O. The results indicated the cell was functional, but suggest the path length achieved was below the designed length. The cause was identified as the optical fibre collimators, which were found to have poor coaxial alignment resulting in a Herriott geometry different to that designed. In the future the issue could be rectified by purchasing to a higher specification, or assembling the collimators in-house. The size of the cell and fibre coupling was considered suitable for integration into a likely experimental configuration. The stainless steel cell tube would need to be manufactured from a different material, such as Invar, for thermal stability, but the system was considered chemically compatible. Fibres and collimators, in future, likely require metal coating or encapsulation in a suitable material (see chapter 9). Fibre coupling was achieved and the fibre used, SMF-28, was compatible with the interrogation system fibre routing. The estimated detection resolution of H_2O using this cell was

(38 ± 12) ppm which met the project requirements.

Future improvements to the TDLAS technique used in this work would be able to decrease the noise in the measurement and increase the sensitivity. Ideally in the future a module for the modular interrogation system discussed in chapter 3 would be designed to achieve TDLAS. Multiple modules, each operating at a different wavelength, could be used to target a number of gaseous chemicals of interest.

The cell could be suitable for CO_2 and CH_4 sensing without modification using DFB lasers at approximately $2004\,\text{nm}$ and $1654\,\text{nm}$ respectively. Based on the performance for detecting H_2O and the shorter optical path length estimation, an expected resolution possible was estimated for CO_2 to be (120 ± 5) ppm, and for CH_4 to be (45 ± 2) ppm.

7.3 Fluorescence Oxygen Sensing

Commercially available O_2 optical fibre sensors based on the fluorescence quenching have previously been evaluated at AWE [237]. The sensor performance was found to meet the O_2 sensing requirements of this project, but the long-term performance was not assessed. The sensors were IMP-PSt7 sensors, manufactured by PreSens Precision Sensing (Germany). The *fluorophore* material was not stated for the sensor, but it was thought to be constructed from platinum porphyrine or ruthenium(II) complexes [271]. A diagram of the sensor construction is shown in figure 7.18.

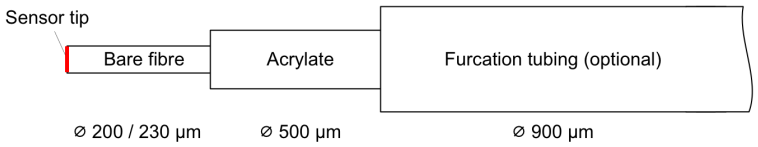

Figure 7.18: Schematic of the PreSens IMP-PSt7 sensor.

The manufacturer makes no claim for long-term stability, in fact their instruction manual states [275] that:

> *It is recommended to calibrate the oxygen microsensor prior to each measurement. Especially after longer measurements (more than* $18\,000$ *measuring points or* $8\,\text{h}$ *continuous sensor illumination) the sensor should be re-calibrated.*

The statement specifically suggests the sensor does not have long-term stability, and the measurement process of the sensor causes sensor drift. Further, the sensor storage stability was also stated as [274]:

> *5 years provided the sensor material is stored at room temperature in dry conditions and in the dark.*

5 years is shorter than the experimental duration of interest in this project, and if used within a thermally accelerated ageing experiment, these conditions would not be met even when the sensor is not being measured.

Neither the specified operating or storage times were within the project requirements. This work investigates the significance of the change in sensor performance from repeated measurements and from storage periods.

Long-term oxygen sensor experimental design

The IMP-PSt7 sensors, from PreSens Precision Sensing (Germany), were measured using the manufacturer's Microx TX3 interrogator [276], logging data to a bespoke LabVIEW VI via a RS232 connection. The interrogator provided the reported phase and intensity from each sensor measurement, the PT1000 temperature value, along with a calculated temperature-compensated O_2 concentration value. The ambient temperature and ambient barometric pressure were also monitored.

The experiment was configured as shown in figure 7.19. The experimental

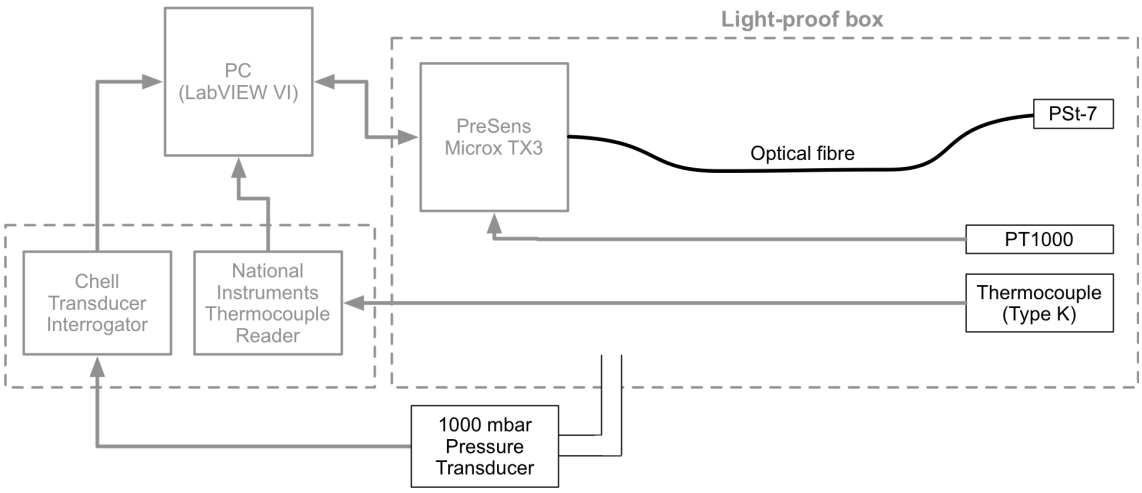

Figure 7.19: Diagram of the oxygen-sensor long-term testing experimental configuration.

configuration was assembled and tested. The environmental conditions of the experiment were not controlled but were monitored. A photograph of the experiment is shown in figure 7.20. The PSt7 was calibrated following the manufacturer's process [276] prior to commencing the experiment.

Figure 7.20: Photograph of the long-term oxygen sensor experimental configuration. The experiment was housed in a light-proof box.

Long-term oxygen sensor results and discussion

The experiment operated during a 21 week period starting in August 2016 consisting of a four week interrogation period, 16 weeks at ambient conditions, followed by a further two weeks of interrogation. During each interrogation period five measurements were taken per minute, resulting in approximately $50\,000$ measurements per week, and over $250\,000$ measurements of the sensor in total. The results are shown in figure 7.21. The oxygen reading was found to have an increasing trend throughout the interrogation period, even during the time at ambient conditions. The ambient temperature measurement showed smaller variations following the interrogation break, attributed to the activation of the building heating system during the interrogation break. The PT1000 reported temperature values agreed with the ambient thermocouple measurements within their respective uncertainties. The fluorescence intensity and phase readings showed strong correlation with temperature, shown in figure 7.22. Both phase and intensity showed a negative dependence on temperature. This explains the need of the Microx TX3 interrogator to measure the ambient temperature using its PT1000 sensor in order to generate a $\%O_2$ reading. In an all-optical sensor deployment, the PT1000 would need

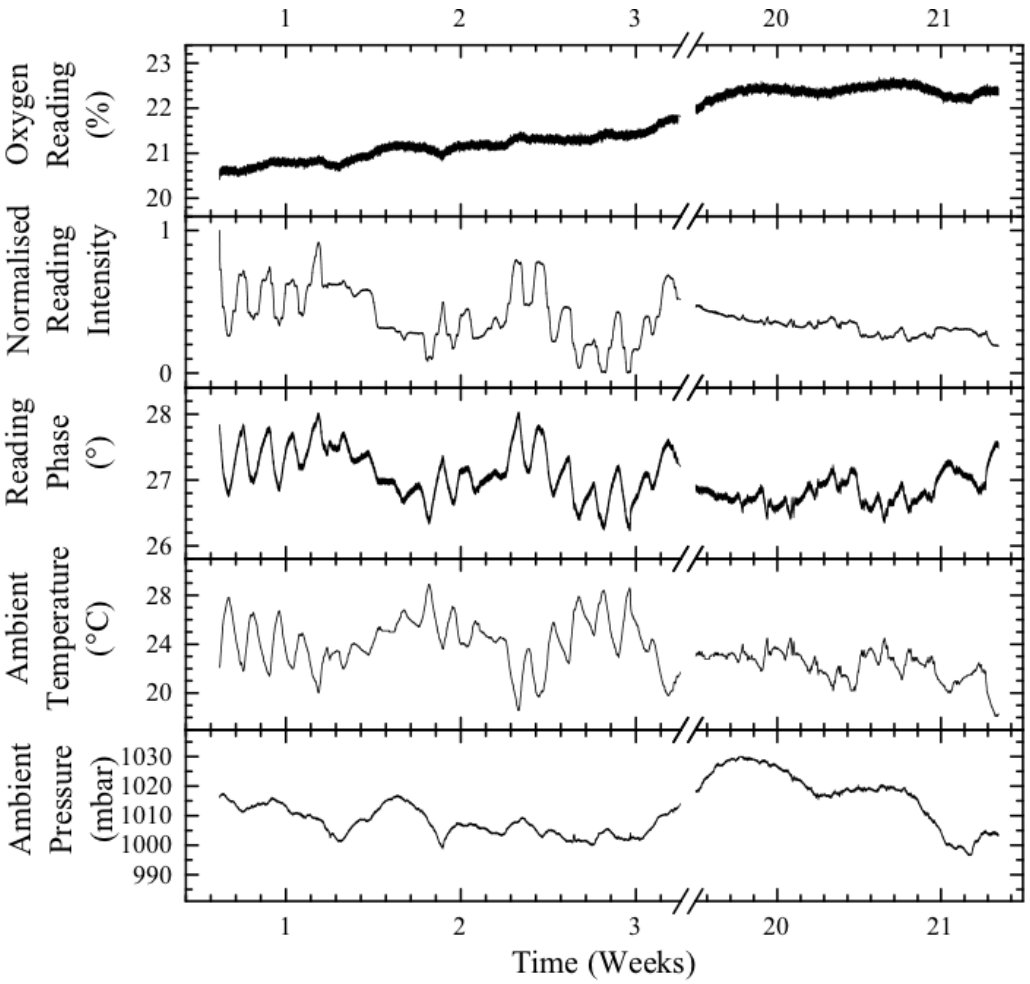

Figure 7.21: Oxygen sensor long-term testing results showing the Microx TX3 oxygen reading, intensity, phase and temperature. The experiment's ambient pressure is also displayed.

to be replaced with an optical temperature sensor, such as an FBG.

The oxygen reading was observed to contain short-term measurement noise. Figure 7.23 shows a histogram of the deviations from a 3 h moving average of the measured oxygen reading. The histogram shows that over a short time period of 3 h, the sensor measurement noise was within the project's ± 0.1 % resolution requirement, however it exceeded the manufacturer's specification for sensor performance.

During the experiment the ambient barometric pressure was not constant. The measured pressure was used to convert the optical oxygen values into volume fraction values. The resulting data is shown in figure 7.24. The measured oxygen reading was found to continuously increase throughout the experiment. While being interrogated, the drift was approximately an increase in partial volume of 0.001 per 10 000 measurements. While the sensor was not interrogated, but left at ambient conditions, the increase was approximately 0.004 every 10 days. If the drift was constant, over the course of an experiment, the sensor measurement would potentially read over 100 % without any

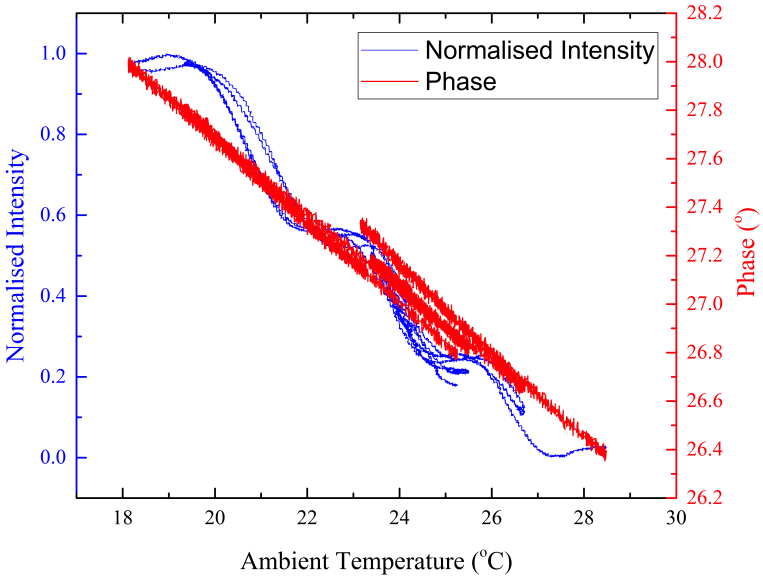

Figure 7.22: Oxygen sensor's intensity and phase measurements correlation to temperature analysis, for measurements captured at an ambient pressure of (1010.40 ± 0.05) mbar.

increase in actual oxygen concentration within the experiment.

The cause of the measurement drift could have been due to a number of processes. The process was likely located within the tip of the sensor, directly affecting the *fluorophores*. Effects such as photobleaching are well known within fluorometry, especially in environments containing oxygen [269], and results in a reduction of active *fluorophore* numbers. The cause is typically associated to reactions between a *fluorophore* and a surrounding molecule while the *fluorophore* is in an optically excited state (and hence more reactive) [269, 277]. Therefore photobleaching occurs predominantly while the *fluorophores* are excited (illuminated), and the number of interrogations would directly impact the sensor performance. This is supported by the manufacturer's statement to recalibrate the sensor after $18\,000$ measurements. The sensor drift observed during the interrogation break in the experiment, suggests such a mechanism also occurs, at a slower rate, even when not excited. The increase in measured oxygen concentration suggests that photobleached *fluorophores*, which have bonded with a molecule such as oxygen, act as additional quenchers to the still active *fluorophores*, reducing the lifetime τ.

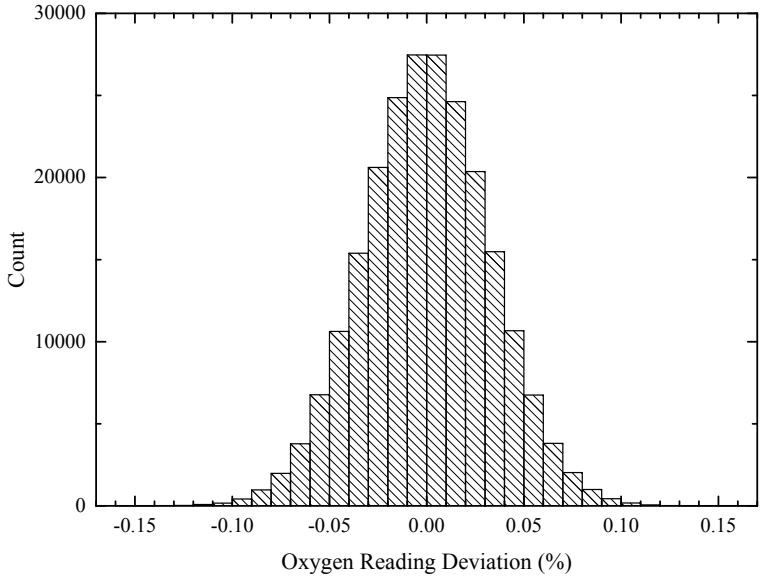

Figure 7.23: Oxygen sensor long-term oxygen value deviation histogram compared to a 3 hourly average.

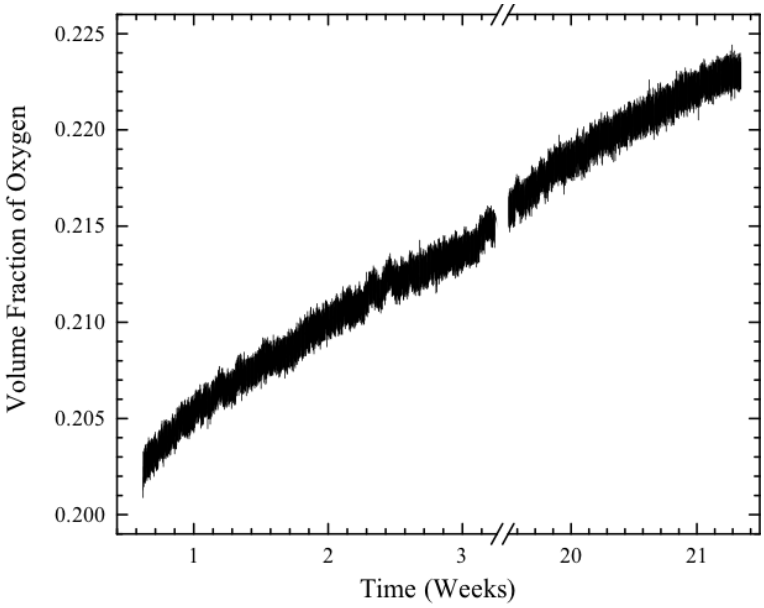

Figure 7.24: Oxygen sensor long-term measurement drift analysis shown for volume fraction of O_2 against experiment time.

Long-term oxygen sensor conclusions

The optical oxygen sensor readings were found to increase throughout the long-term experiment, attributed to measurement instability of the *fluorophores* used. The drift was faster during times where the sensor was regularly interrogated, suggesting a light-stimulated degradation to the sensor, such as photobleaching, was occurring. While the sensor was not interrogated measurement drift was still found, indicating that even an infrequently-interrogated sensor would not perform as required by this project.

The optical oxygen sensor was not chosen for further development, but it was noted the form factor was suitable for use within an experimental configuration. Future development of highly stable fluorescent materials could result in a suitable sensing technique, such as C_70 fullerene *fluorophores* demonstrated by Baleiza *et al* [270], which demonstrate a DL below 530 ppb.

7.4 Gas Detection Conclusions

Development and investigation of gas sensing techniques were conducted, resulting in the development of a multi-reflection multi-gas cell suitable for NIR absorption spectroscopy, and the long-term analysis of a fluorescence based optical fibre oxygen sensor.

A gas cell was designed based on the Herriott multi-reflection geometry, and manufactured to achieve (6.47 ± 0.05) m of gas interaction path-length. The cell was manufactured and experimentally evaluated for H_2O, but was also considered suitable for CO_2 and CH_4 measurement. The physical size of the cell was considered appropriate for inclusion within an experimental configuration. The cell was fibre-coupled and was intended to be long-term stable. The cell was interrogated using a TDLAS system. The modular interrogation system (Chapter 3) was designed to be able to support TDLAS, following future module development. This would enable the developed gas cell to be integrated with the diagnostic system developed within this thesis.

The optical fibre fluorescence based oxygen sensor was a commercially available sensor in a small form factor. The experiment found the sensor experienced drift both when being frequently measured and also during periods without interrogation. It was concluded the sensor was not suitable for use within the experimental configuration.

Further work

Within the next 3 years further development of the NIR absorption spectroscopy technique could be achieved. Further design iteration and evaluation of the gas cell developed and improving the collimator coaxial tolerances, together with creating a TDLAS interrogation module, would greatly improve the ability to deploy gas detection techniques within material ageing experiments. Investigation of chemicals of interest which could be measured within an SMF-28 fibre coupled system could also be completed, potentially in conjunction with collimator improvements, to maximise the use of the gas cell once located within an experiment.

The project requirements have necessitated the experiment to remain electrically isolated. Work reported later, in chapter 8, challenges the all-optical approach which has been the focus in this chapter. Further development of that work has the potential to enable electronic gas sensors to be used within the experiments without breaching the electrical isolation. Further, optical techniques such as non-dispersive infrared (NDIR) sensing could be deployed locally within the experiment, leveraging MIR techniques without requiring optical fibres operating at those wavelengths. Moving gas sensing to the MIR decreases the absorption overlaps between differing gaseous species as experienced in the NIR, potentially improving the confidence in the diagnostic measurements.

In 3-6 years time, it could be possible to include wavelength modulation spectroscopy techniques within an interrogation module, in order to improve the system sensitivity. This improvement could enable the use of shorter path-length gas cells offering a reduction in volume required within the experiment, while also removing the saturation concerns at high concentrations.

Previously demonstrated photonic crystal techniques for refractive index and bio-sensing utilising slow-light photonic effects and slotted waveguides [278–283] could in the future, enable miniature gas cells to be created that in only a few centimetres are able to achieve multiple meters of gas/optical interaction length.

Further in the future, the use of MIR spectroscopy techniques *in situ* may become viable. At the time of this project the MIR optical fibres commercially available were lacking in flexibility, reliability, and compatible optical components. If MIR fibre and optical techniques become as developed as those in the NIR then *in situ* spectroscopy within the MIR would offer many advantages. The number of gaseous species which could be detected would be much larger, and their differentiation would also be improved.

Hollow core gas sensing techniques previously demonstrated [99, 141, 284, 285] can create shape-conforming gas cells with many meters of path length. The practical deployment of the technique has been limited due to the necessity of the gas to diffuse into the fibre core, either from the fibre ends, or through laser-drilled side holes. If further development of this technique can increase the diffusion into the core, reducing the likelihood of creating local-environments while improving the response time, the technique may be able to meet the requirements of this project. The use of long path-length gas cells could enable the detection of O_2 using absorption spectroscopy.

Chapter 8: Optically Isolated Electronic Sensors

This chapter details work that investigated the use of electronic sensors within an electrically isolated experiment (OIES), by powering and communicating with them entirely over optical fibres. The aim was to examine the feasibility of using mature electronic sensing technologies while maintaining strict electrical and radio frequency (RF) isolation.

Requirements

The system was required to operate over single-mode NIR optical fibre, compatible with Corning (USA) SMF-28. All components used in the design were required to be readily available for purchase, with multiple sources or compatible parts being preferable. Electronic sensor measurements were required to occur periodically and pre-processing of data was acceptable. A battery was not permitted in the remote sensing node due to the protracted operating time-scale of all technology required within this research project. Minimising the stored amount of energy within the sensing node was also preferable. A 2018 internal AWE report reviewed the potential safety implications of deploying an optically powered electronic system design within an electrically excluded experiment and the approach was considered to have potential.

It was desirable that no significant laser safety precautions would be required, even in the case of fibre disconnection or fibre damage, so the system was required to be Class 2M or lower. If the operating wavelength was outside the range $400\,\text{nm}$ to $700\,\text{nm}$, then the limiting class would be 1M [179], due to the light's invisible nature.

8.1 System Design

The focus of the initial development was to demonstrate a functioning remote sensing system in a short time-scale. As a result, minimal prototyping was conducted before circuit design, PCB layout, enclosure design, and demonstrator production.

As discussed, the requirement for NIR fibre (SMF-28) operation rapidly directed

the system design towards operation at either $1310\,\text{nm}$ or $1550\,\text{nm}$. As common telecommunications wavelengths, devices such as lasers, photodiodes, couplers and optical circulators were readily available.

To satisfy the laser safety requirement, a laser operating at $1310\,\text{nm}$ would require its optical output power to remain below $500\,\text{mW}$ (for Class 1M, $1250\,\text{nm}$ to $1400\,\text{nm}$ [179]). However, a laser operating at $1550\,\text{nm}$ would be required to remain below $10\,\text{mW}$ (Class 1M, $1400\,\text{nm}$ to $4000\,\text{nm}$ [179]). Therefore operation at $1310\,\text{nm}$ was preferable, and fibre-coupled laser diodes (Fabry-Pérot cavity types) with optical outputs of $50\,\text{mW}$ and $200\,\text{mW}$ were procured from Thorlabs (USA) and Laser Components (UK) respectively.

At this wavelength InGaAs photodiodes were the obvious choice for receiving the optical power. At $1310\,\text{nm}$ their small-signal responsivity is typically greater than $0.9\,\text{A}\,\text{W}^{-1}$ [286–288] which suggested high conversion efficiencies were possible. The open-circuit voltage was estimated by subtracting the typical InGaAs intrinsic diode voltage from the photon energy, calculated using the Planck-Einstein relation:

$$E = \frac{hc}{\lambda}, \tag{8.1}$$

where E represents the photon energy in electron-volts, h is Planck's constant in eV s, c the speed of light, and λ the wavelength of the photon. For photons at a wavelength of $1310\,\text{nm}$, equation (8.1) reveals an energy of $E = 0.946\,\text{eV}$. Due to the nature of the electron volt, the energy value calculated is equal to the EMF (voltage) generated. This value, subtracting the InGaAs diode voltage (≈ 0.46), results in an expected open-circuit voltage in the region of $0.47\,\text{V}$. Under load it was anticipated that this voltage would drop [289, 290], but at this stage of development the operating voltage was unknown.

The system design consisted of an interrogation module and a remote sensor node, linked by a single optical fibre. The interrogation module contained a laser, a photodiode, and a micro-controller, and was discussed in Chapter 3. The laser provided the optical power for the remote sensor node, and the photodiode received the sensor data for the electronics to demodulate. The remote sensor node contained components to convert the energy from optical to electrical and to control the electrical energy, as well as electronic sensors, and the EOM. Dual parallel photodiodes performed the optical to electrical conversion; the voltage is subsequently boosted and the energy stored within capacitors. Electronic sensor data is captured on a micro-controller and transmitted optically using the EOM. The single optical fibre was designed to be a single-mode $8/125\,\mu\text{m}$ silica fibre,

such as SMF-28 or similar, operating at 1310 nm.

A block diagram of the system design is shown in figure 8.1. The electrical circuit

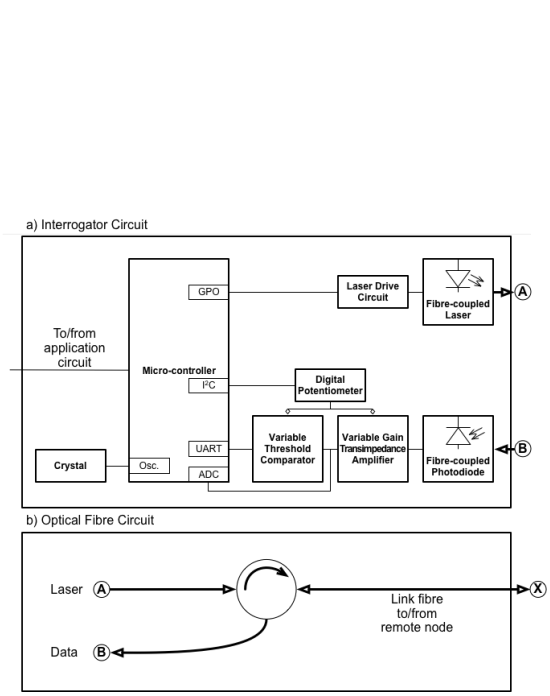

(a) Block diagram for the optically powered sensor interrogator.

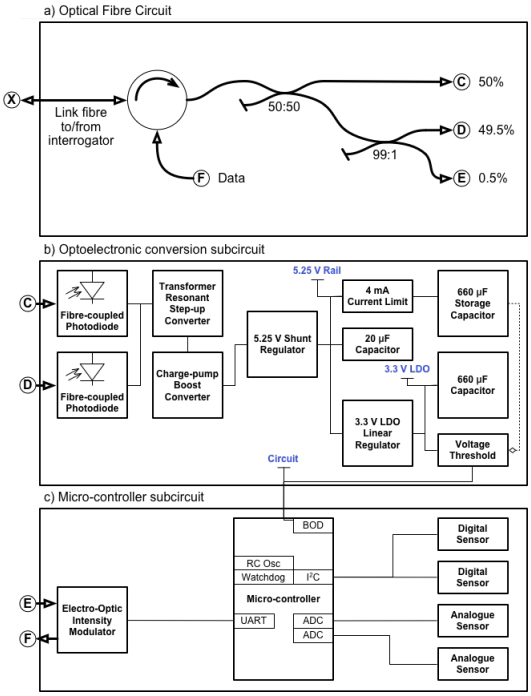

(b) Block diagram for the optically powered sensor node.

Figure 8.1: Block diagram for the optically powered sensor system.

(8.1a, a) contained a micro-controller and a single-mode 1310 nm 50 mW fibre-coupled Fabry-Pérot type laser diode (Thorlabs LPSC-1310-FC). The laser was driven from a constant current laser drive circuit controlled by the micro-controller using a general purpose output (GPO). Laser monitoring circuitry is not shown for clarity. Wavelength monitoring was not included since strict wavelength stability was not required for this system.

An FC fibre bulkhead-coupled InGaAs photodiode (Thorlabs FGA01FC) was connected to a variable-gain transimpedance amplifier circuit and a variable-threshold comparator circuit. The digital output from the comparator was compatible with the micro-controller universal asynchronous receiver-transmitter (UART) hardware. The micro-controller could vary the signal gain and threshold to enable optical return intensity tracking using a digital potentiometer controlled using the I^2C protocol. The circuit shown used a 16 MHz crystal for oscillator timing.

The optical circuit (8.1a, b) contained a circulator designed for operation at 1310 nm (Thorlabs CIR1310). The circulator enabled single-fibre operation by routing the laser down the link fibre, Ⓐ, and routing the return signal to the photodiode, Ⓑ.

The sensor node optical circuit (8.1b, a) contained a corresponding optical circulator (CIR1310) to route the input light to a 50:50 $1310\,\mathrm{nm}$ directional coupler (Thorlabs TN1310R5A1). One output of the coupler, Ⓒ, connected to one of the two photodiodes. The photodiodes were of the same type as those in the interrogator. The second output from the coupler connected to a 99:1 directional coupler (Thorlabs TN1310R1A1). The $99\,\%$ output, Ⓓ, connected to the second photodiode. The $1\,\%$ output, Ⓔ, connected to the input of the intensity EOM. The output of the EOM, Ⓕ, returned the modulated signal to the circulator, where it was directed back along the link fibre to the interrogation module.

The optoelectronic conversion subcircuit (8.1b, b) used the two photodiodes in photovoltaic operation for the optical to electrical conversion. The photodiodes were wired in parallel and the generated voltage was increased by a transformer resonant step-up DC:DC converter within the LTC3108. The voltage was increased above the minimum start-up threshold of the second DC:DC converter, a charge-pump boost converter, that increased the voltage further. A shunt regulator limited the maximum output voltage to $5.25\,\mathrm{V}$.

Wiring the photodiodes in series, as opposed to parallel, would have doubled the open-circuit voltage available and would have negated the need for two DC:DC conversion stages. Parallel operation was chosen to limit the current flowing through each photodiode's bond wires, which were specified for $20\,\mathrm{mA}$. Parallel operation also provided a level of redundancy, enabling power conversion to continue even if one photodiode failed open-circuit.

The shunt-regulated output formed the $5.25\,\mathrm{V}$ rail. The rail connected to a storage capacitor ($660\,\mu\mathrm{F}$ aluminium solid polymer electrolytic, Panasonic OS-CON SEPF series) via a current limiter ($4\,\mathrm{mA}$), $20\,\mu\mathrm{F}$ bulk decoupling ceramic capacitors, and a $3.3\,\mathrm{V}$ low drop-out (LDO) linear voltage regulator. A second $660\,\mu\mathrm{F}$ capacitor (SEPF) was connected to the $3.3\,\mathrm{V}$ LDO regulator output, as was a voltage threshold circuit that incorporated a high-side metal-oxide-semiconductor field-effect transistor (MOSFET) switch. The threshold circuit monitored the voltage in the storage capacitor and when it reached $(2.8 \pm 0.2)\,\mathrm{V}$ activated power to the micro-controller subcircuit. The current limiter ensured predictable initial capacitor charging sequencing and therefore correct operation of the threshold switch. The threshold switch was required to ensure the micro-controller would have sufficient power to complete its start-up routines and enter sleep mode in a controlled manner. Once active the threshold circuit remained latched until the

micro-controller circuit voltage dropped below $(1.4 \pm 0.4)\,\mathrm{V}$ and the micro-controller's internal brown-out detection threshold was set to $1.8\,\mathrm{V}$, to ensure predictable start-up conditions. The Linear Technology LTC3108 DC:DC converter is separated into its functional elements for clarity, and contains the transformer resonant step-up converter, charge-pump boost converter, $5.25\,\mathrm{V}$ shunt regulator, $4\,\mathrm{mA}$ current limit, $3.3\,\mathrm{V}$ LDO linear regulator, and the voltage threshold switch.

The micro-controller subcircuit (8.1b, c) consisted of a micro-controller (Atmel (USA) ATmega644PV) operating using an internal resistor-capacitor (RC) derived, calibrated, and subdivided $1\,\mathrm{MHz}$ oscillator. Multiple digital sensors were interfaced using the $\mathrm{I^2C}$ protocol hardware within the micro-controller. Analogue sensors were supported using the micro-controller's 10-bit ADC hardware. The intensity EOM (Thorlabs LN82S) was driven directly by the micro-controller UART hardware at $240\,\mathrm{kHz}$ baud. The EOM was modulated significantly below its $10\,\mathrm{GHz}$ designed operation, so the UART signal was connected to the *DC bias* input, rather than the main input that incorporated a high-pass filter [291]. The voltage required to cause a π phase shift, V_π, was $\approx 4\,\mathrm{V}$ [292], so the UART was able to generate high modulation depth operating at $0.3\,\mathrm{V}$ to $3.0\,\mathrm{V}$. The EOM controlled the optical intensity by use of an internal Mach-Zehnder interferometer and a lithium niobate ($\mathrm{LiNbO_3}$) crystal, whose refractive index varied as a function of electric field. The field was controlled by the application of a potential difference, which enabled this technique to be very low power, since the *DC bias* input was purely capacitive featuring no measurable DC resistance. Therefore the power consumption of the data transfer was dictated by the input's AC reactance, which could be varied by adjustment of the data transmission baud rate. The current required, I_{RMS}, for data transmission in this way was predicted from first principles:

$$I_{\mathrm{RMS}} = \frac{V_{\mathrm{RMS}}}{X_{\mathrm{C}}} = V_{\mathrm{RMS}} \cdot 2\pi C f, \tag{8.2}$$

where V_{RMS} denotes the root mean square (RMS) of the modulation voltage, X_{C} the reactance of the EOM's capacitive input, C the capacitance value, and f the data modulation frequency.

From the block diagram a circuit was designed and the power conversion circuit was successfully verified on breadboard, leading to the design and production of the circuits on PCBs. A photograph of the PCB and assembly (without enclosure lid) is shown in figure 8.2. The design featured a circular shape to enable integration into a

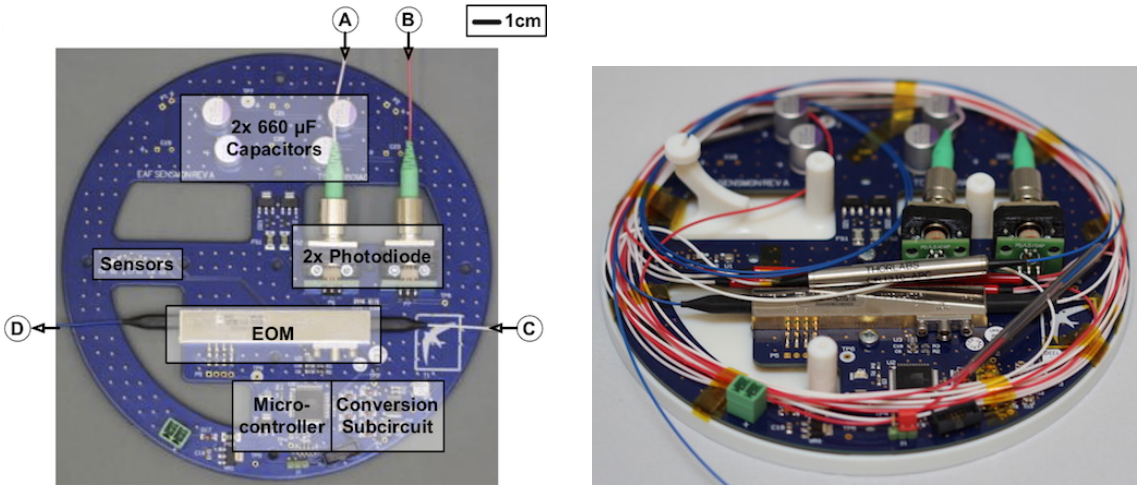

(a) Annotated PCB photograph.

(b) Sensor node assembled without enclosure lid.

Figure 8.2: Photographs of the optically powered sensor system remote node.

material ageing experiment based largely on a cylindrical vessel design. The location of the storage capacitors, photodiodes, sensors, EOM, micro-controller, and optoelectronic conversion subcircuit are highlighted. The fibre labelling corresponds to that within figure 8.1. The sensors are located on the PCB to minimise localised heating effects from other components, and near cut-outs in the board to ensure measurements are of the experimental environment. The sensors included within this design can measure temperature, humidity, and barometric pressure, and are similar to those evaluated in Chapter 4.

The system was programmed in C (AVR-GCC) following the flow diagram shown in figure 8.3. Both the interrogator and sensor node would repeat their operation until powered down, providing periodic sensor measurements indefinitely. A number of systems were manufactured and assembled to enable experimental evaluation.

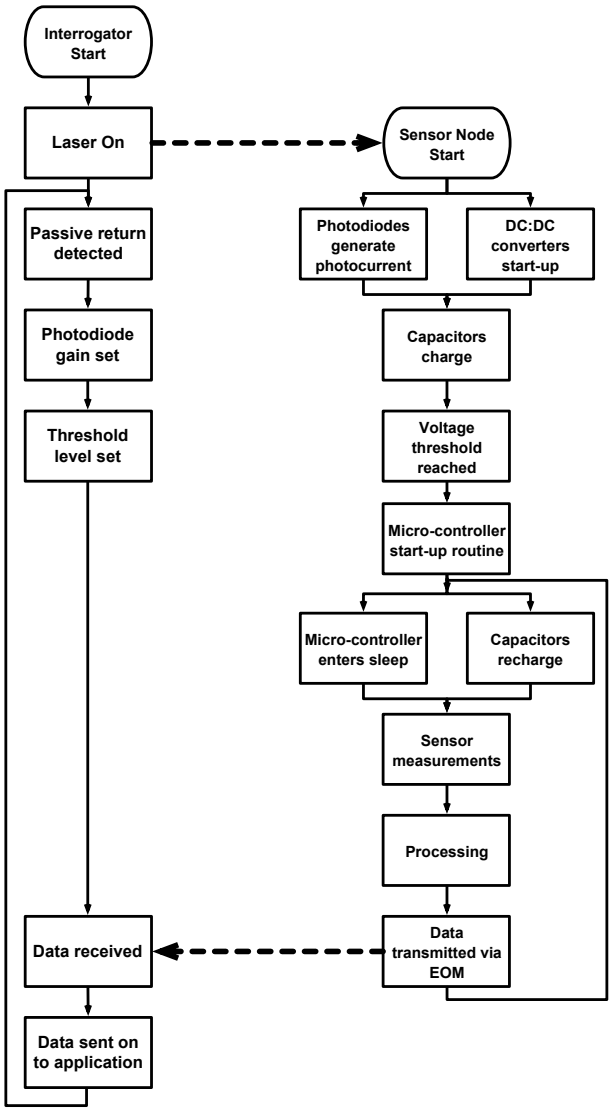

Figure 8.3: Program flow diagram for the optically powered sensor system.

8.2 System Evaluation

The first evaluation conducted on the circuit was to measure the output current and voltage. Figure 8.4 shows the measured Current (I) against Voltage (V) (IV) available from the optical to electrical conversion. The measurement shows voltage regulation at 3.28 V and that a continuous current draw of up to 200 µA was achievable from the system without significant voltage decrease. Higher current draws resulted in output voltage decreases, until the voltage threshold circuit deactivated at 1.0 V.

The sensor node circuit, consisting primarily of the micro-controller, sensors, and an EOM, was measured to require (1.3 ± 0.1) mA for (500 ± 10) ms during operation, and (5.2 ± 0.2) µA during sleep. The node operated in a store-then-burst operation, enabling energy to be stored within capacitors while the circuit was in sleep, then wake to perform sensor measurements, process the data, and transmit via the EOM, before returning to

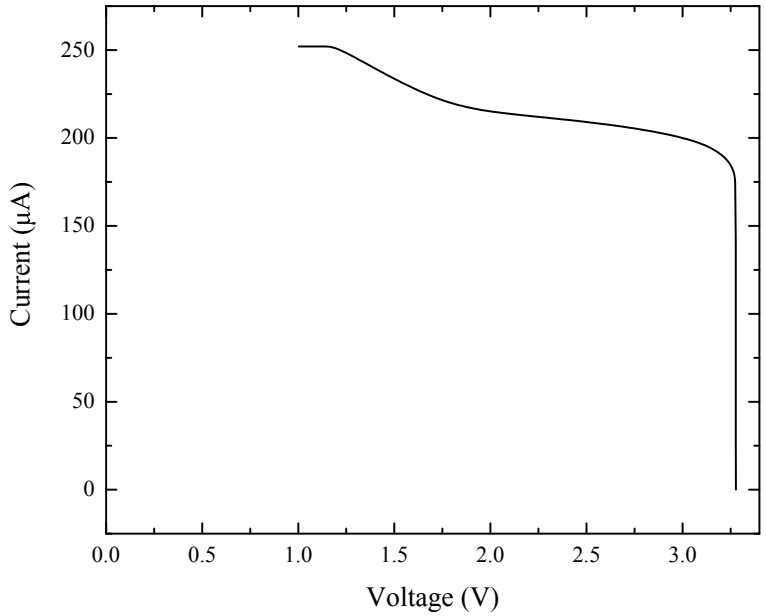

Figure 8.4: IV measurement for the optically powered sensor system. The voltage is regulated at $\approx 3.3\,\mathrm{V}$ at low currents, and the voltage threshold circuit disconnects when the voltage drops below $1.0\,\mathrm{V}$.

sleep. The circuit operation was tested and found to function reliably across a temperature range of $-10\,°\mathrm{C}$ to $40\,°\mathrm{C}$. An example of the received data by the interrogation module is shown in figure 8.5. Good modulation depth was evident in the analogue response and good digitisation by the comparator. The micro-controller UART peripheral was sufficient to decode the $240\,\mathrm{kHz}$ baud data.

The calculated optical to electrical conversion efficiency of the sensor node was $1.9\,\%$, which was within the range of reviewed systems (table 2.6), but was still considered low. To evaluate the cause of the low efficiency, the LTC3108 based conversion circuit was evaluated in isolation. The power efficiency as a function of input voltage was measured as shown in figure 8.6. The peak efficiency measured was $(2.34 \pm 0.09)\,\%$, which was far below the $80\,\%$ expected [180]. The low efficiency was attributed to losses within the transformer resonant step-up converter which was the first stage of the LTC3108 DC:DC conversion [293].

The optical to electrical conversion efficiency of the system was low, at $1.9\,\%$, but the system did function and successfully measure and report sensor data from the remote node via a single optical fibre. The system concept demonstrator satisfied the requirements: it used SMF-28, did not require batteries within the remote node, and was within the laser Class 1M; the work was therefore considered successful. The material suitability of the sensor node was not evaluated within this work, but it was noted the large PCB size presented a significant amount of fibreglass within the experimental volume. Work to

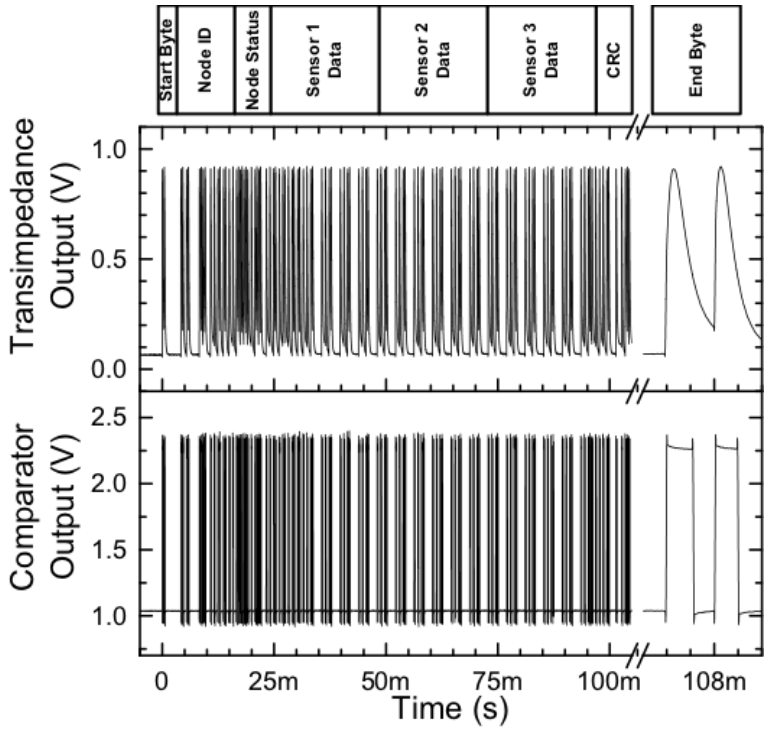

Figure 8.5: Data reception example from the optically powered node, as received by the interrogator. Both the analogue transimpedance amplifier output and digital comparator output are shown.

investigate the potential impact of such fibreglass was conducted by colleagues within AWE, but was not concluded at the time of writing.

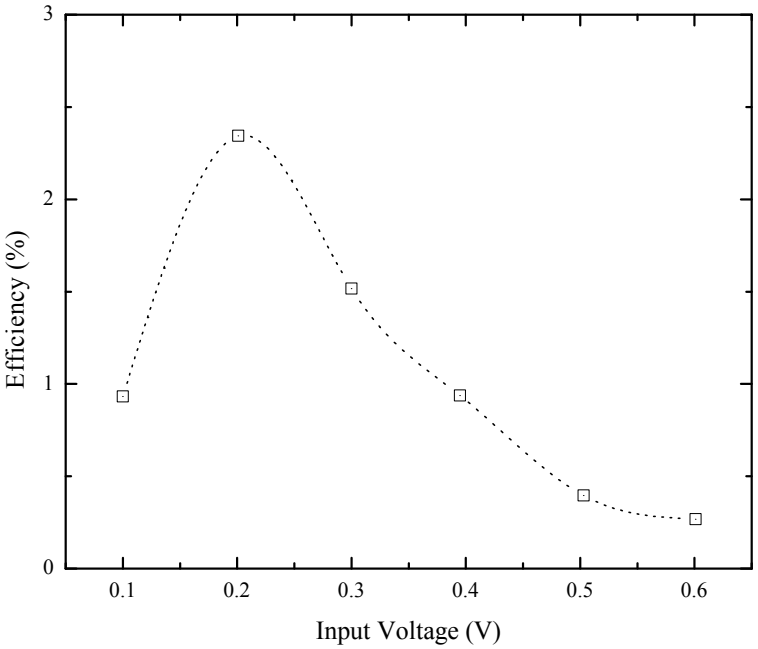

Figure 8.6: Input-voltage efficiency measurement for the LTC3108-based DC:DC conversion solution. A peak efficiency of $(2.34 \pm 0.09)\,\%$ was measured at an input voltage of $(0.201 \pm 0.001)\,\mathrm{V}$. The data points denote the measurements; the line dotted is only for diagrammatic clarity.

8.3 Further Research

Due to the successful demonstration of the initial sensing system, the decision to conduct further development was taken. Where the focus of the initial system was to demonstrate a functioning sensing system, the focus of this further development work was to increase the optical to electrical conversion efficiency in order to support future increases in sensing techniques used. The aim was to create demonstrator system hardware providing higher efficiency, with a secondary aim to reduce the amount of energy stored within capacitors on the remote node, and use different techniques to the initial system to increase the diversity of components and methods investigated. Reducing the remote sensor node PCB area was considered beneficial.

The work started with an analysis of the behaviour of InGaAs photodiodes in order to understand the optical and electrical parameters which may lead to maximum conversion efficiency. Then the efficiency of DC:DC boost converters was experimentally investigated to decide which commercial device to use in the revised system. Lastly the pairing of photodiode configurations with DC:DC converters was evaluated.

The definition of DC:DC efficiency equated the input and output electrical power, as noted in equation (8.3). The optical to electrical efficiency was quantified using the same

method, shown in equation (8.4).

$$\eta_{\text{EE}} \left(V_{\text{IN}} \cdot I_{\text{IN}} \right) = V_{\text{OUT}} \cdot I_{\text{OUT}}, \tag{8.3}$$

$$\eta_{\text{OE}} \cdot P_{\text{IN}} = V_{\text{OUT}} \cdot I_{\text{OUT}}, \tag{8.4}$$

where η represents the conversion efficiency (EE for electrical to electrical [1], and OE for optical to electrical), V_{IN} and V_{OUT} the input and output voltage respectively, P_{IN} the optical input power, and I_{IN} and I_{OUT} the input and output currents.

Photodiode analysis

Fibre-coupled InGaAs photodiodes were evaluated to investigate the parameters important for high efficiency operation, in terms of optical input power, output load, and output voltage.

Three photodiode models were selected for analysis: the Thorlabs (USA)FGA01FC used in the initial design, the Fermionics (USA) FD300FC, and the Thorlabs FDGA05. The FGA01FC is a FC fibre-coupled device with an internal ball-lens and an active area of $0.011\,\text{mm}^2$ ($\varnothing 120\,\mu\text{m}$) [286]. The FD300FC is also a FC fibre-coupled device with an active area of $0.071\,\text{mm}^2$ ($\varnothing 300\,\mu\text{m}$) [288]. The FDGA05 is not a fibre-coupled device, so a custom housing was designed and made using a RP technique to facilitate coupling to a FC fibre connector. The device has a $0.193\,\text{mm}^2$ ($\varnothing 500\,\mu\text{m}$) active area [287].

To measure the most efficient optical power to operate the photodiodes at, the output short-circuit current (SCC) was measured as a function of input optical power. A $200\,\text{mW}$ $1310\,\text{nm}$ fibre-coupled laser diode was used as the variable-power input source. The laser was controlled from a constant-current power supply, and the optical output was monitored using a calibrated $0.9\,\%$ optical fibre tap and Thorlabs PM20 optical power meter. The SCC was measured using a calibrated Fluke (USA) 87V multimeter on its mA range which has a nominal shunt resistance of $1.8\,\Omega$ [294]. The resulting measurement for the three photodiode models is shown in figure 8.7. The FDA01FC and FD300FC photodiodes were both found to saturate within the optical power range tested, but the FDGA05 photodiode did not reach saturation within the $193\,\text{mW}$ tested. The FDA01FC achieved the highest responsivity of the photodiodes tested, but the FDGA05 achieved the highest SCC. All three photodiodes were operating below their specified

[1] The electrical to electrical efficiency was always measured for the DC:DC conversion circuit only, and does not take into account the electrical to optical laser efficiency. It is not the *wall-plug* efficiency.

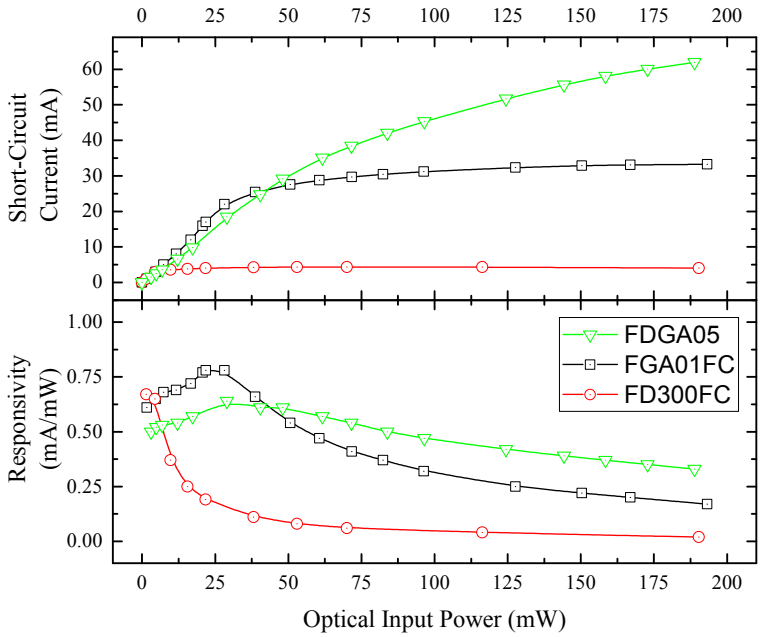

Figure 8.7: Photodiode short-circuit current and responsivity as a function of optical input power. The data points denote the measurements; the line dotted is only for diagrammatic clarity. Responses from models of photodiode are shown: The FGA01FC has a peak responsivity of $0.78\,\text{mA}\,\text{mW}^{-1}$ at $28.19\,\text{mW}$ generating $22.04\,\text{mA}$ of SCC. The FD300FC has a peak responsivity of $0.67\,\text{mA}\,\text{mW}^{-1}$ at $1.43\,\text{mW}$ generating $0.96\,\text{mA}$ of SCC. The FDGA05 has a peak responsivity of $0.64\,\text{mA}\,\text{mW}^{-1}$ at $28.96\,\text{mW}$ generating $18.46\,\text{mA}$ of SCC.

responsivities, which was likely due to the SCC measurement technique. An increased measurement impedance may have increased the measured responsivity, but for the purposes of comparing the three photodiode models and evaluating their peak optical power efficiency point, the technique used was considered appropriate.

The FD300FC photodiode had the lowest SCC and responsivity at the higher optical powers than the other two types tested. As the energy over fibre system will likely operate in excess of $10\,\text{mW}$, it was decided that the FD300FC would not be evaluated further, since the other two photodiode options were more likely to result in a higher-efficiency system.

The FDA01FC and FDGA05 photodiodes were evaluated using a constant optical input power and a varying resistive load to generate an IV relationship. IV plots for the two photodiodes in three configurations are shown in figure 8.8. The dual and quad experiments were conducted with the photodiodes in a series string arrangement. For all the measurements the laser diode was operating at $180\,\text{mW}$ which was split equally between the number of photodiodes being measured. In general as the number of photodiodes increased, the open-circuit voltage increased and the SCC decreased, but it was difficult to determine more significant trends. As a result, figure 8.9 plots the IV responses on a common x-axis scaled to each measurement's open-circuit voltage. This

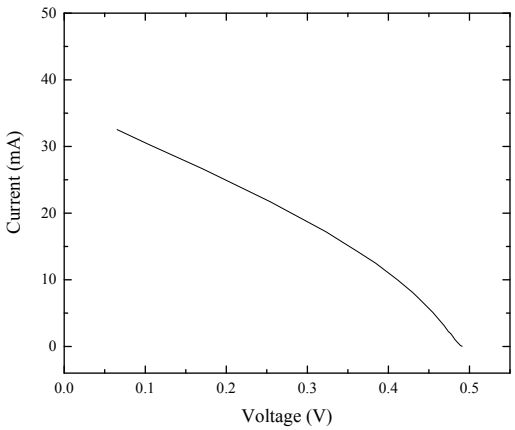

(a) Single FGA01FC.

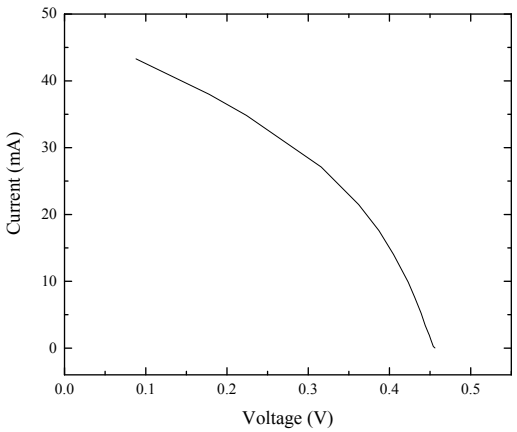

(b) Single FDGA05.

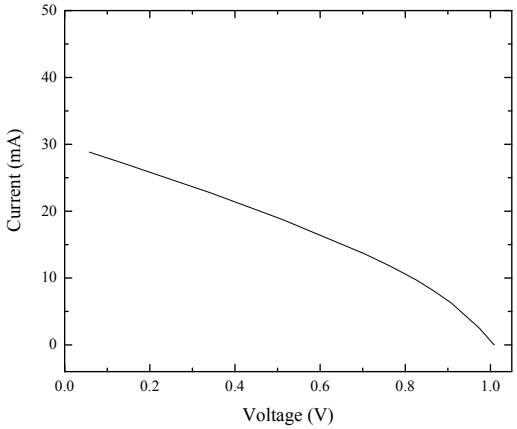

(c) Dual series FGA01FC.

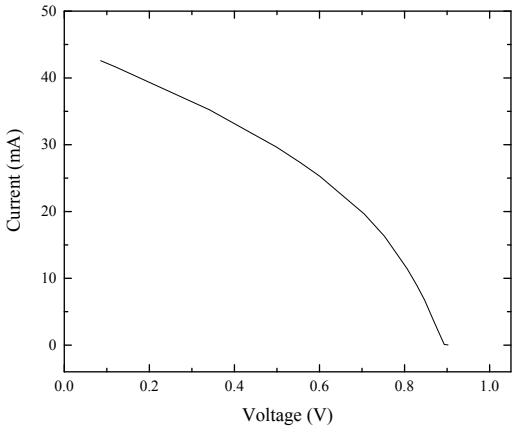

(d) Dual series FDGA05.

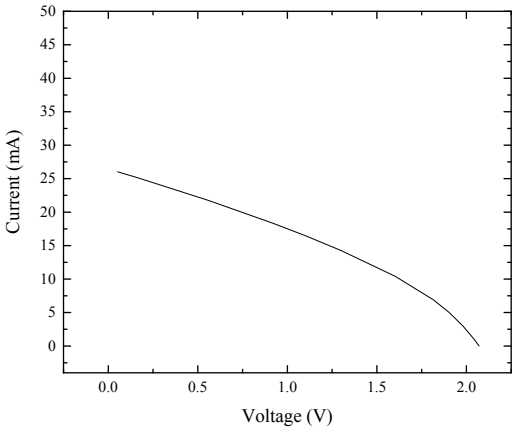

(e) Quad series FGA01FC.

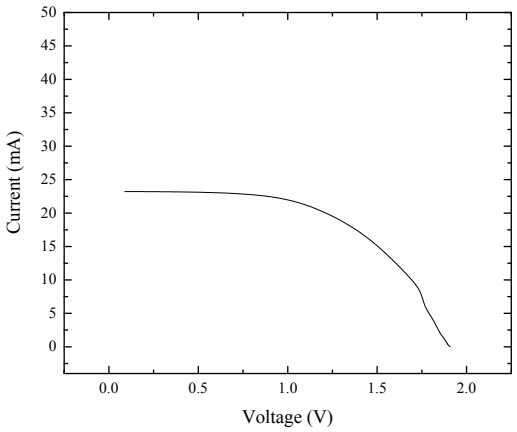

(f) Quad series FDGA05.

Figure 8.8: IV measurements of photodiodes illuminated with 1310 nm at 180 mW (sum of power incident during each measurement).

enabled a direct comparison between the configurations. The power generated by each photodiode configuration is also shown.

The single FDGA05 photodiode generated the highest output current of the configuration tested, but the dual and quad photodiode configurations converted more power. The significant increase in power converted was likely due to the reduction in optical power incident on each photodiode in the series string, and therefore operating

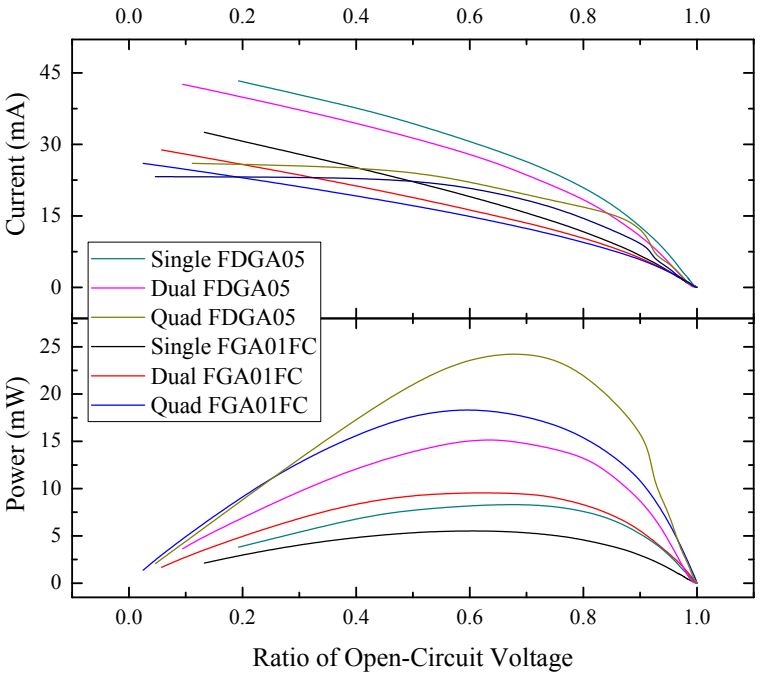

Figure 8.9: Comparison of IV and output power for single and dual series photodiodes scaled to their peak open-circuit voltage. Photodiodes were illuminated by a fibre-coupled 1310 nm laser at 180 mW (sum of power incident during each measurement).

closer to the photodiode's peak optical efficiency point (see figure 8.7). The FDGA05 photodiodes, with custom fibre-coupling solution, converted more power than the FGA01FC photodiodes due to the high optical powers tested and difference in saturation levels. Increasing the number of photodiodes in a series configuration significantly increased the converted power. The maximum power point for MPPT was found consistently to be between 60 % to 70 % of open-circuit voltage.

From the analysis of photodiodes, further work is recommended using four series FDGA05 photodiodes, ideally operating at approximately 70 % of their open-circuit voltage.

DC:DC converter analysis

Previous work had identified a number of DC:DC converter options potentially suitable for use within an energy over fibre system, which were summarised in table 2.6. The LTC3108 was used in the initial design and upon evaluation was found to operate at low efficiencies (below 2.5 %) even when tested with a low-impedance power supply. The remaining three converter options: the Linear Technology (USA) LTC3525D-3.3, Texas Instruments (USA) BQ25504, and Texas Instruments BQ25570, were evaluated for electrical to electrical efficiency as defined in equation (8.3).

For each a test configuration was created featuring a variable voltage low-impedance

power supply, calibrated voltage and current meters for both the input and output connections from the converter, and a variable load in the form of a multi-turn $10\,\mathrm{k}\Omega$ potentiometer. The input voltage was varied from $0\,\mathrm{V}$ to $V_{\mathrm{IN}}^{\mathrm{MAX}}$ for each converter, while the potentiometer was used to load the converter's output just below the regulation set-point to ensure no pulse-skipping algorithms were running. For each input voltage tested, the input and output voltages and currents were logged. A schematic of the configuration is shown in figure 8.10.

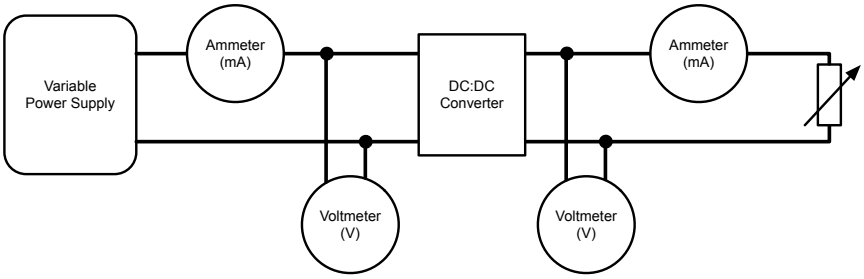

Figure 8.10: DC:DC input voltage dependence on power efficiency test configuration schematic.

The LTC3525D-3.3 was initially tested and was found to poorly regulate the output under light loads, with the output voltage increasing up to $6\,\mathrm{V}$. Since the sleep current of the previous energy over fibre system was low, this lack of regulation was of concern. As a result further evaluation of the LTC3525D-3.3 was not conducted.

The BQ25504 was evaluated as described, and the results are shown in figure 8.11. The peak efficiency measured was $(88 \pm 3)\,\%$ at an input voltage of $(1.263 \pm 0.002)\,\mathrm{V}$.

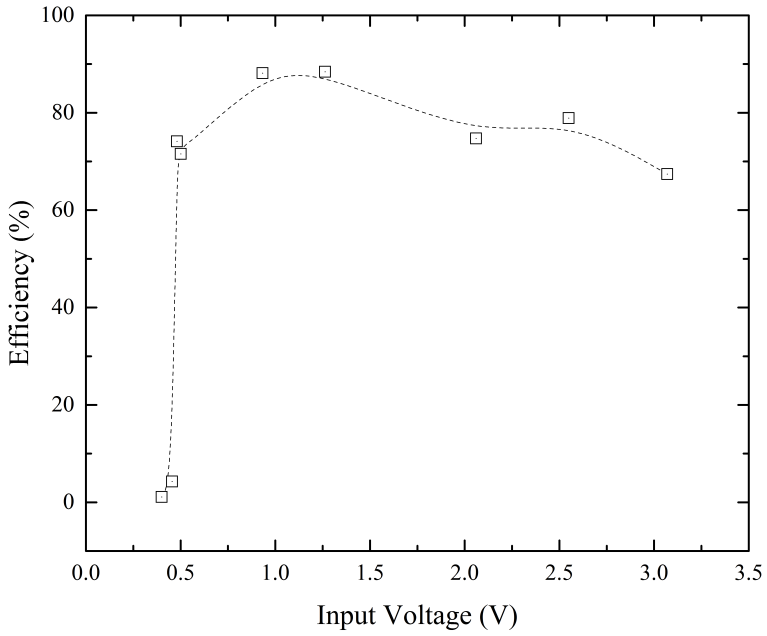

Figure 8.11: Input-voltage efficiency measurement for the BQ25504-based DC:DC conversion solution. The data points denote the measurements; the line dotted is only for diagrammatic clarity.

For the experiment the BQ25504 circuit was configured to disable MPPT and regulate the output to $3.12\,\mathrm{V}$. MPPT was disabled due to the periodic V_{IN} sampling technique used by the BQ25504, which caused measurement inconsistencies and loss of output regulation during photodiode operation. The MPPT sampling is specified to occur every $16\,\mathrm{s}$ and disconnects the input from the circuit for $256\,\mathrm{ms}$ in order to sample the open-circuit input voltage. This voltage is then used to regulate V_{IN} to the resistor-specified maximum power-point [182]. During both circuit testing and for photodiode operation, the nominal $256\,\mathrm{ms}$ sampling disconnection time was found to cause a significant drop in output voltage, likely due to the minimal storage and output capacitance in the test circuit ($104.8\,\mu\mathrm{F}$).

The BQ25570 was evaluated using the same method, and the results are shown in figure 8.12. The peak efficiency measured was $(74.8 \pm 0.8)\,\%$ at an input voltage of

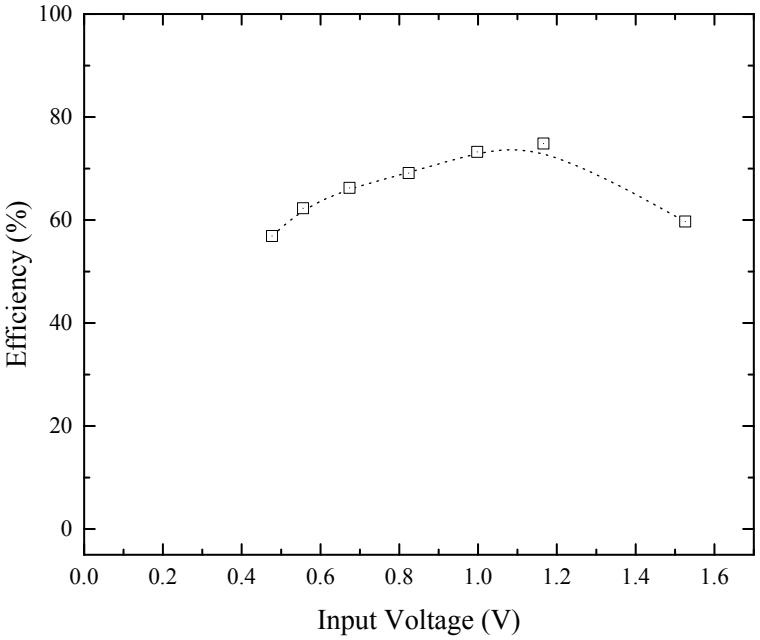

Figure 8.12: Input-voltage efficiency measurement for the BQ25570-based DC:DC conversion solution. The data points denote the measurements; the line dotted is only for diagrammatic clarity.

$(1.166 \pm 0.002)\,\mathrm{V}$. For the experiment the BQ25504 circuit was also configured to disable MPPT and regulate the output to $1.8\,\mathrm{V}$, and energy storage ($100\,\mu\mathrm{F}$) at $4.2\,\mathrm{V}$.

The BQ25570 was measured to operate at a lower peak efficiency than the BQ25504, and the ability of increased energy storage density was of low interest, since a secondary aim of the further research was to reduce the quantity of stored energy in the sensor node. Therefore, from the selected devices in table 2.6, the BQ25504 showed the highest efficiency and closest match to the research aims, so was selected for all further evaluation and development.

Photodiodes coupled with BQ25504

The BQ25504-based DC:DC conversion circuit, configured with MPPT disabled and to regulate to 3.12 V, was powered by Thorlabs FGA01FC photodiodes. Each photodiode was powered from (30.0 ± 0.3) mW of optical power at 1310 nm. The circuit was tested in four configurations: a single photodiode, two in series, four in series, and four in a paired series-parallel. The measured IV response for each is shown in figure 8.13. The

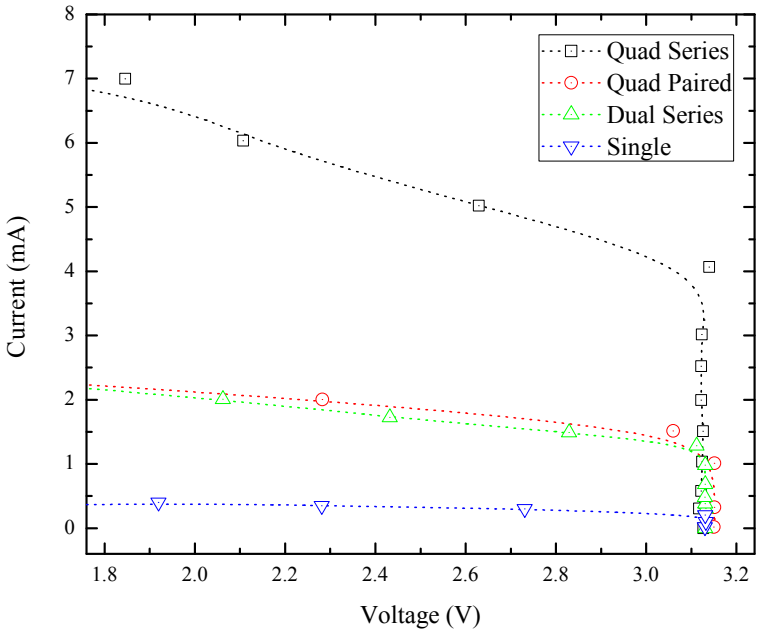

Figure 8.13: Output IV measurements for the BQ25504 converter with Thorlabs FGA01 InGaAs photodiodes, illuminated at 1310 nm with 30 mW per photodiode. The data points denote the measurements; the line dotted is only for diagrammatic clarity.

four photodiodes in series configuration achieved the consistently highest output current across the voltage range tested. The peak-power output measured was (13.20 ± 0.04) mW at (2.629 ± 0.002) V and (5.02 ± 0.01) mA. The optical to electrical efficiency was calculated to be (11.0 ± 0.2) %, and the BQ25504 operated at (86.3 ± 0.6) % electrical to electrical efficiency with a photodiode input voltage of (1.587 ± 0.002) V. The optical conversion efficiency was a significant improvement on the initial system developed, and the BQ25504 was operating at close to its peak efficiency.

The BQ25504-based circuit was evaluated using the same method for the Thorlabs FDGA05 photodiodes, fibre-coupled using custom-designed housings. The resulting IV measurements are shown in figure 8.14, for both four series and three series arrangements of the photodiodes. As before, the four photodiodes in series configuration achieved the highest output current, with a peak-power output of (17.25 ± 0.05) mW at (3.071 ± 0.003) V and (5.63 ± 0.02) mA. The optical to electrical efficiency was

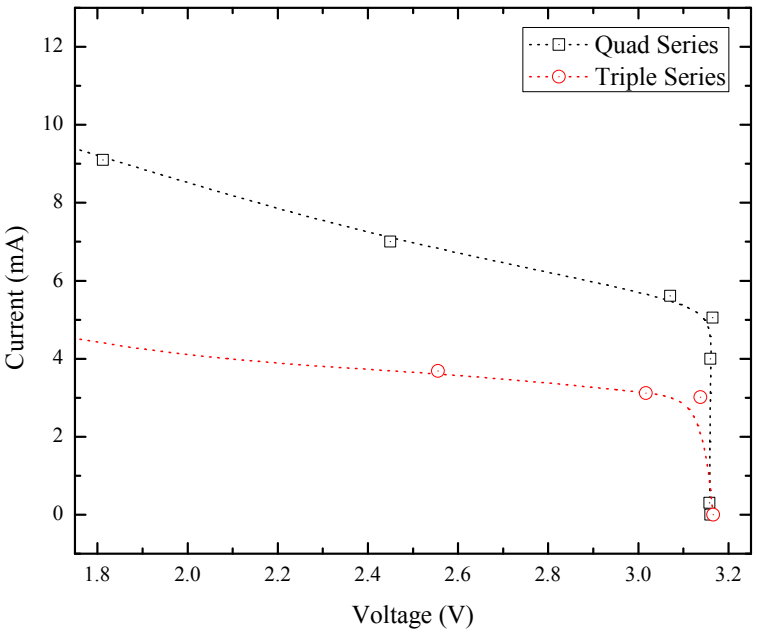

Figure 8.14: Output IV measurements for the BQ25504 converter with Thorlabs FDGA05 InGaAs photodiodes, illuminated at 1310 nm with (50 ± 2) mW per photodiode. The data points denote the measurements; the line dotted is only for diagrammatic clarity.

calculated to be (8.54 ± 0.09) % and the BQ25504 operated with an electrical to electrical power efficiency of (89.9 ± 0.5) %. The optical conversion efficiency was lower than expected, but the BQ25504 efficiency was the highest so far measured.

To investigate the lower optical conversion efficiency, the quad-series FDGA05 photodiode arrangement was measured while varing the 1310 nm optical input between 0 mW and (200 ± 3) mW, with the aim to find the highest efficiency operating optical power. The electrical output was resistively loaded, using a variable resistor, to maintain an output voltage of (2.3 ± 0.1) V to provide consistency between results. Figure 8.15 shows the measured optical to electrical efficiency and the output electrical power for the circuit as described. The highest optical to electrical power efficiency measured was (17.6 ± 0.6) % at a total combined optical input power of (32 ± 1) mW. The BQ25504 operated at an electrical to electrical power efficiency of (92 ± 2) %. The optical conversion efficiency measured was significantly higher than the previous highest measurement, of (11.0 ± 0.2) % and that of the previous system demonstrated (1.9 %). The use of FDGA05 photodiodes, fibre-coupled in custom housings, connecting to a BQ25504-based DC:DC circuit was selected to form the basis of the next hardware demonstrator.

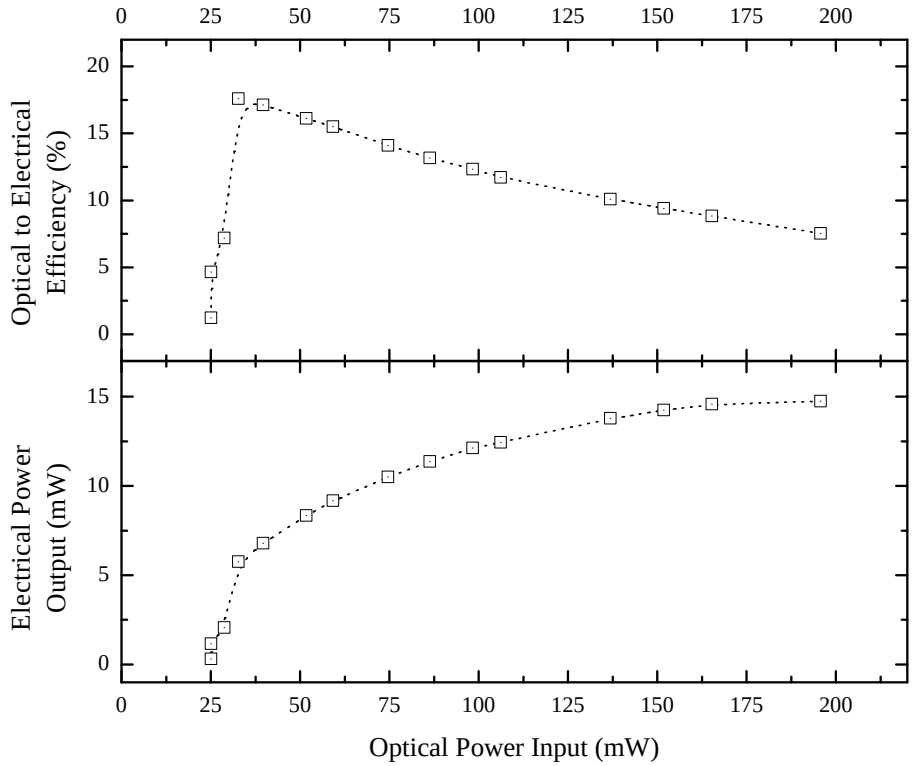

Figure 8.15: Electrical and optical efficiency measurements for the BQ25504-based DC:DC conversion solution using four Thorlabs InGaAs FDGA05 photodiodes in series and using self-aligned fibre coupling enclosures. The data points denote the measurements; the line dotted is only for diagrammatic clarity.

Technique confirmation

The technique used in both the initial demonstration hardware and the further research was based around generating a low voltage from photodiodes, and boosting via a DC:DC converter to the circuit operating voltage. It was conceivable to remove the DC:DC converter step by increasing the number of photodiodes in series, such that their operating voltage equals the circuit operating voltage. This is similar to the technique used within specialised photovoltaic converters, which are able to reach high efficiencies [295].

A test was performed using eight Thorlabs (USA) FGA01FC photodiodes in series with a combined optical input of $180\,\mathrm{mW}$ at $1310\,\mathrm{nm}$. The measured IV performance and converted power are shown in figure 8.16. If a shunt regulator was added to limit the voltage output to $3.3\,\mathrm{V}$ for light loads, the technique appeared suitable for providing power to a micro-controller based circuit.

The efficiency achieved of $(17.0 \pm 0.2)\,\%$ was similar to that of the FDGA05 and BQ25504 coupled system. This eight photodiode technique would constrain the number of photodiodes the circuit requires, reducing the flexibility of the system design, and resulting in potentially higher costs due to the additional lasers or optical fibre splitters

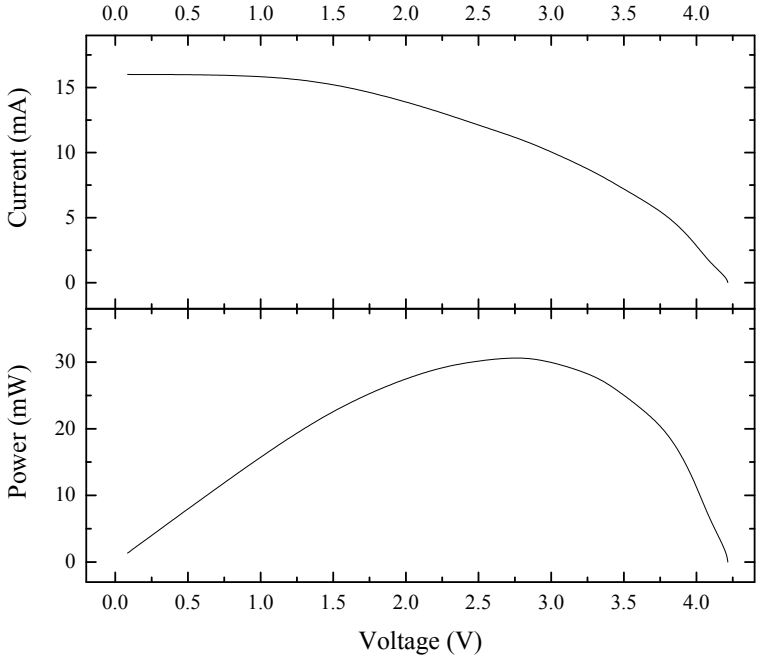

Figure 8.16: SCC IV measurement for eight series FGA01FC photodiodes. The calculated power converted is also shown.

required.

This test therefore confirmed the validity of the technique chosen for development, which utilised one to four photodiodes and DC:DC converter to boost the voltage as required.

Analysis summary

Investigations on photodiodes and DC:DC converters yielded an updated set of components for inclusion in a redesigned remote sensor node. Changing the photodiodes from the Thorlabs (USA) FD01FC to the FDGA05 had the potential to increase the conversion efficiency, especially at higher optical powers. Operating the photodiodes in a quad series configuration would also be beneficial, especially compared to the inefficient dual parallel mode used in the initial system, but at the expense of redundancy. The LTC3108 DC:DC converter was also recommended to be changed for the BQ25504 converter which was expected to provide significantly higher efficiency operation, especially when paired with the quad-series photodiode configuration.

The use of FDGA05 photodiodes in custom housings (to provide fibre-coupling), and use of the BQ25504 DC:DC converter was recommended for the second generation demonstrator. Increasing the optical power output from the interrogator from $50\,\mathrm{mW}$ to $200\,\mathrm{mW}$ was also recommended.

8.4 Revised System Design

The revised energy over fibre system was designed to incorporate the recommendations from the further research analysis, but also offer a reduced footprint and additional sensors. A block diagram of the revised sensor node is shown in figure 8.17. The

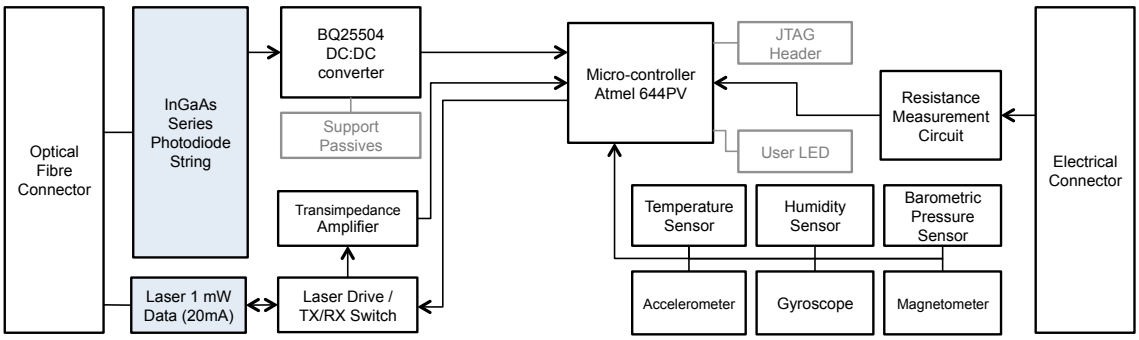

Figure 8.17: Functional block diagram for the revised energy over fibre sensor node.

node was designed to operate from a number of FDGA05 InGaAs photodiodes in a series string. These would connect to a BQ25504 DC:DC boost converter which would provide a regulated 3.4 V circuit supply. A 1 mW fibre-coupled laser diode operating at either 1310 nm or 1550 nm (Laser Components (UK) PL13/15 FP Series [296]) was designed for data communications. Bi-directional data transfer was achieved using the single laser diode by employing a half-duplex communication scheme. The band-gap junction within the laser itself was used for data reception, operating similarly to a photodiode. Care was taken within this design to ensure inter-cavity intensity would not be exceeded when receiving light from the interrogator. The circuit configuration to achieve bi-directionality is represented in figure 8.18. Due to the increased conversion efficiency expected from the

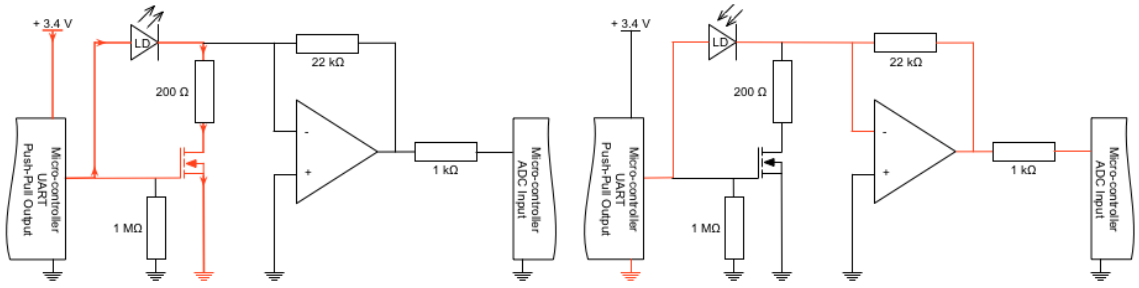

(a) Data transmission. **(b)** Data reception.

Figure 8.18: Schematic for half-duplex data using a single laser diode, showing the significant current path during data transmission and during reception.

revised design, it was possible to provide sufficient current to drive the laser diode. It was considered advantageous to include the laser diode, despite its high power requirements, due to the ability for bi-directional data transfer with minimal additional components. It

also provided an additional technique for evaluation, compared to the EOM used in the initial system design.

The same Atmel micro-processor was used, along with the same temperature, humidity, and barometric pressure sensors. A three-axis accelerometer, gyroscope, and a magnetometer were added. Some analogue sensors for measuring parameters such as temperature or gas concentration are interrogated by measuring their resistance. A four-wire compatible resistance circuit was therefore added to enable future demonstration of a range of sensing parameters.

A circuit diagram was constructed from this block diagram and subsequently a PCB was designed. Photographs of the PCB are shown in figure 8.19. The PCB measured

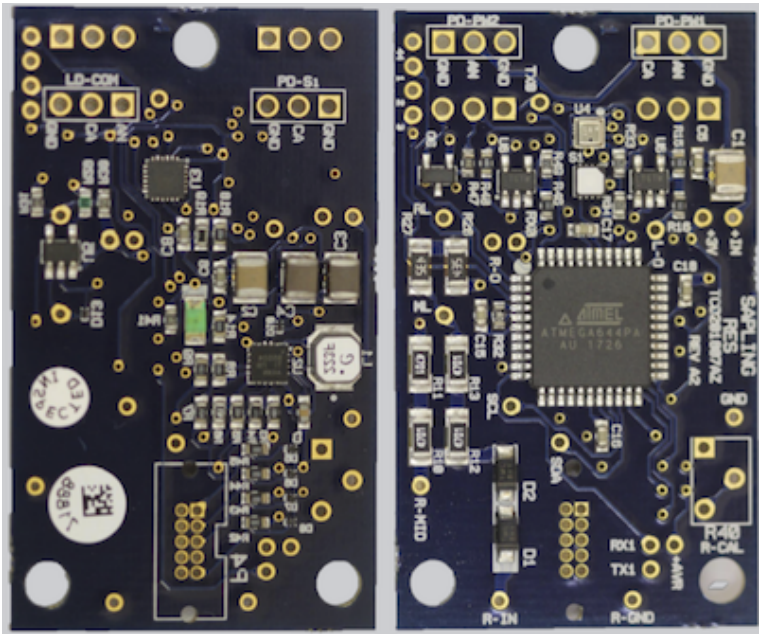

Figure 8.19: Photograph of revised optically powered electronics PCB. Left photograph shows the PCB underside and is flipped to provide alignment with the right photograph, the PCB top.

50.8 mm by 30 mm representing a board area reduction of 91 % from the initial design.

The system used custom-mounted photodiodes supported in pairs, as shown in figure 8.20. The figure shows the reverse side detailing the phododiodes, the front side featured two FC/PC bulkhead fittings to enable simple and robust fibre connection. The photodiodes were aligned while illuminated and their short-circuit current was monitored. Once a maximum was found which provided a greater than 28 mA short-circuit current, epoxy resin was applied to the rear face to secure the photodiode in place. The process was repeated for the second device and the assembly was then placed into a 60 °C incubator for a minimum of 12 h to cure the resin.

The redesigned remote sensor node used the FDGA05 photodiodes, which were

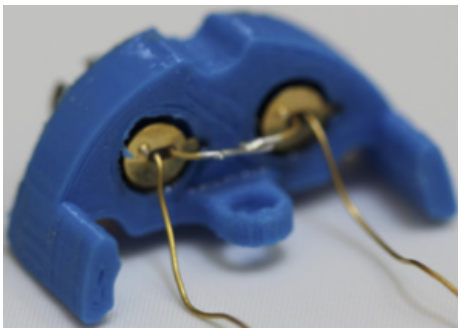

Figure 8.20: Custom rapid prototyped photodiode mount.

different to those used in the initial design. It also used the BQ25504 DC:DC converter, which was again different to that used in the initial design. Additional sensors were added to the node along with the ability to measure resistance. A laser diode was included to provide half-duplex data communication, a change from the low power EOM used in the initial design.

The revised node was manufactured and assembled for evaluation. The initial system interrogator design was reused with a $200\,\text{mW}$ laser diode. Data communication was tested using a breadboarded circuit, pending a redesign of the interrogator to support the bi-directional data configuration.

8.5 Revised System Evaluation

The revised system hardware was evaluated for correct operation, and for optical to electrical conversion efficiency. The system was assembled with four FDGA05 photodiodes in series and a $1310\,\text{nm}$ laser diode for data.

The module was programmed to perform periodic sensor measurements in a similar way to the initial system, but since the revised design did not feature storage capacitors, no charging time was required. The temperature, humidity, and barometric pressure sensors were measured and operated as expected. The accelerometer, gyroscope, and magnetometer, were not measured during the evaluation, instead left for future testing. The resistance measurement circuit was tested and evaluated for resistances between $5\,\Omega$ and $200\,\Omega$. Data transmission and reception were demonstrated using the laser diode at $1310\,\text{nm}$ and $960\,\text{kHz}$ baud rate. The baud rate was increased from the initial system since the power consumption was now proportional to transmission time, so inversely proportional to baud rate. Ideally faster baud rates would have been used, but due to a design oversight, no crystal oscillator was added to the remote node. As a result the UART timing was derived from a RC oscillator with inherently lower accuracy. The timing

variations could have been overcome in the interrogator software, but that development work was not deemed necessary at the time. Instead the node operated at a baud rate balanced between reducing power consumption and maintaining timing accuracy.

The assembled system's optical to electrical conversion was evaluated in two experiments using the test configuration shown in figure 8.21. The first experiment

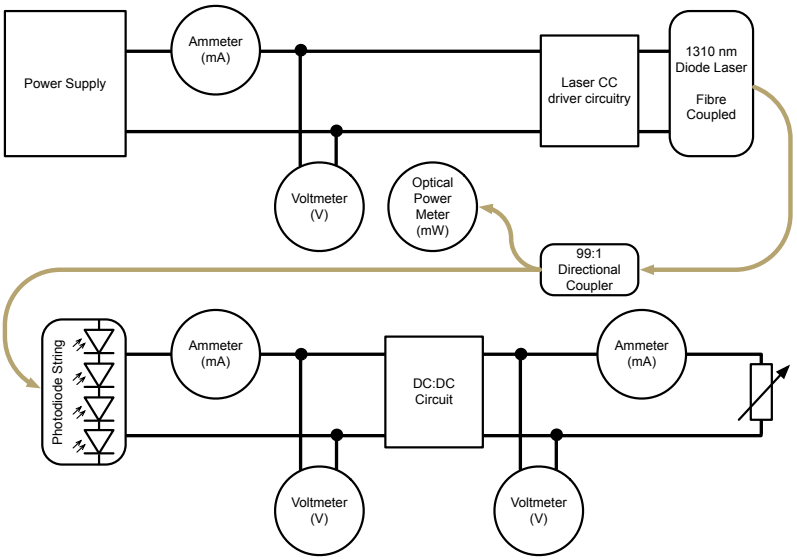

Figure 8.21: Diagram of experimental evaluation configuration.

operated the system at a fixed optical input power to measure the output IV and related characteristics. The second experiment varied the optical input power to find the system's peak efficiency.

The IV measurement experiment was conducted with an optical input power of (194 ± 1) mW from a 1310 nm fibre-coupled laser diode; the results are shown in figure 8.22. The photodiode voltage was measured across the four-diode series string during circuit operation. While load was being drawn from the circuit the photodiode voltage dropped to (1.149 ± 0.003) V from the open-circuit voltage of (1.183 ± 0.003) V, suggesting a photodiode operating point of $61\,\%$. This was in the range suggested by figure 8.9 for the photodiode maximum power point. Therefore power extraction from the photodiodes was indicated to be highly efficient, even without MPPT activated within the BQ25504.

The conversion efficiency was measured across optical input powers ranging from (12.4 ± 0.2) mW to (202.8 ± 0.2) mW, as shown in figure 8.23. Peak total conversion efficiency (optical to electrical output) was measured to be $(24.0 \pm 0.2)\,\%$ at a total combined optical input power of (25.0 ± 0.2) mW.

The *wallplug* efficiency represents the electrical input power to electrical output

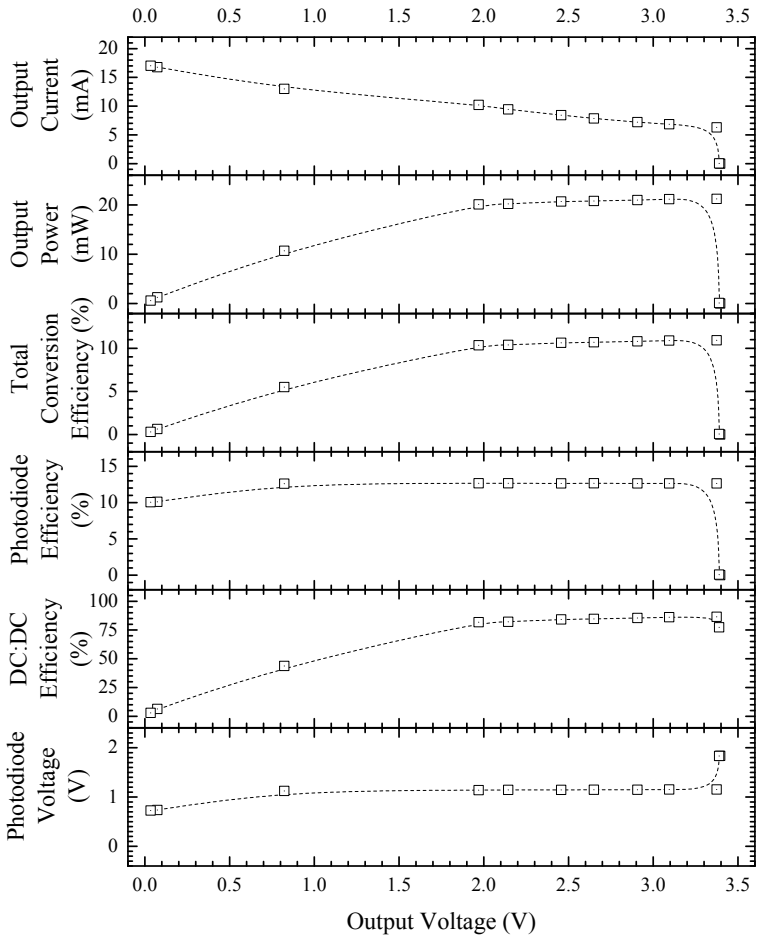

Figure 8.22: Revised optically powered electronics system performance evaluation with a constant optical input power of (194 ± 1) mW. The data points denote the measurements; the line dotted is only for diagrammatic clarity.

power efficiency, so incorporates the laser driving circuitry and laser electrical to optical efficiency. The efficiency for the laser drive and laser was measured to peak at (8.5 ± 0.2) % while generating (87.4 ± 0.2) mW from the optical fibre. The laser used in these experiments was not highly efficient but was chosen due to its output power capability at the wavelength desired. The 50 mW laser diode used in the earlier system operated at a higher efficiency, measured up to 15 %. The *wallplug* efficiency peaked at (1.58 ± 0.05) % with an optical input power of (38 ± 2) mW. As the optical input power increased the electrical output power also increased within the range tested. Therefore even though the highest efficiency operation was possible at optical input powers less than 100 mW, there are practical uses at higher optical powers due to the increase in output power. The majority of the optical power transmitted to the OIES node was not converted to electrical power, and likely resulted in localised heating within the experimental volume. Consideration of sensor and photodiode placement within an experiment will be required to ensure sensors measurements are representative and minimise impact to

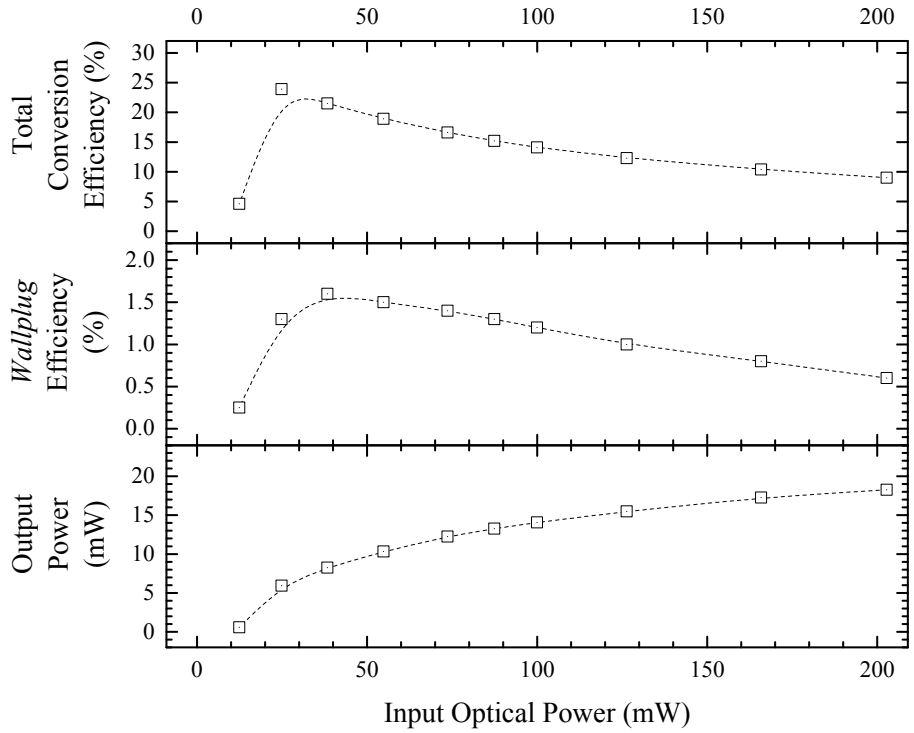

Figure 8.23: Revised optically powered electronics system performance evaluation with a varying optical input power. The data points denote the measurements; the line dotted is only for diagrammatic clarity.

the chemical evolution within the experiment.

The module was successfully programmed and demonstrated measuring on-board sensors, resistance, and transmitting and receiving digital data. The optical to electrical conversion efficiency was measured to reach $(24.0 \pm 0.2)\,\%$, which was more than 12 times greater than that achieved by the initial design.

8.6 Conclusions

Optically powering electronic sensors was considered as a potential technique for providing electronic sensor measurements within an electrically isolated experiment. Commercial solutions were searched and open literature reviewed, and subsequently two hardware systems were designed, manufactured, and evaluated.

Both systems operated from $1310\,\text{nm}$ lasers using SMF-28 optical fibre, remaining within the 1M laser classification (less that $500\,\text{mW}$ at $1310\,\text{nm}$ [179]). The first system developed used two photodiodes in parallel and a dual-stage DC:DC conversion topology. An EOM was used for data transmission from the temperature, humidity, and barometric pressure sensors. The system included the design and production of an interrogator module to power and receive data from the remote node. The evaluation of the system

was successful and an optical to electrical conversion efficiency of $1.9\,\%$ was measured.

The second system developed aimed to improve upon the first system in terms of conversion efficiency and by reducing size. Four photodiodes were used in series connected to a single-stage DC:DC converter, and a laser diode was used for bi-directional data communication. The evaluation of the system revealed an optical to electrical conversion efficiency of $(24.0 \pm 0.2)\,\%$, and a *wallplug* efficiency of $(1.58 \pm 0.05)\,\%$. This conversion efficiency was significantly improved from the first design and the size was greatly reduced.

The project requirements were satisfied: both systems used SMF-28; all components used were readily available, and through the development of two designs typically two components were evaluated for each function; periodic measurements and pre-processing were supported in both designs; no batteries were required in the sensor node, and in the second design no stored energy was required; both systems used Class 1M lasers. A 2018 internal AWE technical memorandum reviewed the component diversity achieved with the two designs and confidence was achieved that such a system would be supportable in the future even if specific parts used became obsolete.

The work demonstrated a potentially useful technique which could enable the use of high maturity electronic sensors within areas typically excluded from electrical connections. The use of telecommunications wavelengths was advantageous since components such as lasers, photodiodes, circulators, and optical couplers, were all readily available. The electronic components required were also readily available given the current rise in low-power IoT targeted devices.

From a research project perspective the work reported in this chapter was complete, having delivered its requirements and two sets of concept demonstrator hardware. Future development in the short-term could design an interrogator for the second system which would support the bi-directional data transfer provisioned within the sensor node. In the medium-term a future system could be developed from a combination of the two demonstrated here, customising the solution to satisfy the requirements of a specific application. Also a review of the newly available Broadcom (USA) PV arrays could be conducted, but their operating wavelength range of $800\,\text{nm}$ to $850\,\text{nm}$ [161] would likely result in use of a Class 3B or 4 laser [179]. In the longer-term, further improvements to the conversion efficiency, or the inclusion of energy storage capacitors within the second system topology, could enable the use of relatively high-power sensing techniques such as metal oxide chemical and NDIR gas sensors. For example, the Sensirion (Germany)

SCD30 NDIR CO_2 sensor module requires 250 mW [297] during a measurement, which would either require an increase of over 10 times in electrical output power, or use of energy storage capacitors. Use of such sensors could provide a valuable technique to measure gaseous species otherwise difficult to measure by absorption spectroscopy via NIR optical fibres.

Part IV

Fibre Integration and Conclusions

Chapter 9: Optical Fibre Infrastructure Components

The project work discussed so far has included the design of interrogation hardware, long-term stability assessments of temperature and pressure sensors, development and evaluation of gas sensing options, and design of optically powered electronic sensor systems. Maturing these technologies is vital to provide options for future diagnostic capabilities, but to be deployed within an experiment, additional infrastructure components are required. These components must be matured to a similar level or else there could be the situation where a sensor is considered ready for use, but there is no way to connect fibres to it within the experiment.

The work in this chapter investigated techniques to enable integration of diagnostics with a materials ageing experiment. These techniques included optical fibre hermetic seals, a fibre connector suitable for use inside an experiment, practical techniques for optical fibre feed-throughs, rugged sensor packaging, optical fibre encapsulation, and an optical fibre umbilical connector.

Together these approaches could provide the ability to connect optical fibres from the interrogation system to the experimental system, enable the fibres to enter the hermetically sealed experimental volume, and interface with sensors while remaining chemically compatible with the experiment. Techniques to simplify the assembly of an experiment containing diagnostics, and increase the ruggedness of the sensors and fibres, are also of interest.

Requirements

This chapter discusses a number of techniques, each with a similar set of requirements. A matrix mapping the requirements to the techniques is included in table 9.1.

Chemical compatibility required the diagnostics and support components to not interfere with the chemistry of the experimental system. This was to ensure the diagnostics measure the correct chemical evolution, not that of a system perturbed by the presence of diagnostics. The specific chemical compatibility requirements would

Requirement	Hermetic seals	Internal connections	Feed-through	Sensor packaging	Fibre encapsulation	Umbilical connector
Chemically compatible	✓	✓	✓	✓	✓	
Long-term stable	✓	✓	✓	✓	✓	
Physically small	✓	✓	(✓)	✓	✓	
Physically robust	(✓)	✓	(✓)	✓	✓	✓
User friendly		✓				✓
Hermetic seal	✓		✓			
Environment seal						✓

Table 9.1: Project requirements mapping to optical fibre ruggedisation techniques. Brackets denote desirable features.

depend on the experiment being performed, but in general metals such as stainless steel were considered suitable, whereas organic materials, such as plastics, were considered unsuitable. Techniques were required to exhibit long-term stability if they were to be located within the experimental system, and therefore would be unable to be accessed throughout the duration of the experiment. Confidence in continued operation without intervention was required. Techniques were also required to be physically small (mm to cm scale) to fit within an experimental configuration. Physical robustness was required to ensure that during the assembly process the diagnostics and accessories would not be broken. Typically optical fibres and components are fragile, especially when compared to typical engineering assemblies. Both the internal fibre connector and the umbilical connector were desired to be user friendly. The internal connector would need to be mated during the experiment assembly, possibly in confined locations. The umbilical connector may be connected and disconnected many times over the experimental duration. Hermetic sealing within this project was defined as achieving below a 1×10^{-9} mbar l min^{-1} helium leak rate, to ensure the fibre seals performed to the same specification as commercial research-grade gas fittings [195], but this was an order of magnitude lower than typically specified in commercial optical fibre products [184, 298]. The fibre umbilical connector required environmental sealing, to reduce the chance of water or other contaminants entering and depositing on the fibre end faces. Hermetic sealing was not required since the umbilical would only be used outside of the experimental volume. The umbilical was

also required to connect a minimum of 30 optical fibres, and it was advantageous if the type of optical fibre used (such as SM and MM) could be varied during development.

These design requirements were used to evaluate commercially available options, and inform the development of suitable techniques and their subsequent evaluations.

9.1 Hermetic Fibre Seals

A technique for creating compact and long-term stable hermetic seals was desired in order to enable optical fibres to pass into the sealed environment of the experiment. The seal was required to provide hermeticity to a leak-rate of 1×10^{-9} mbar l min^{-1}, be chemically compatible with the experiment, and be physically compact to fit within the experimental design. A technique which was able to adapt to different experimental configurations and geometries was considered advantageous.

Use of polymeric and adhesive seals were discounted due to a lack of long-term confidence and potential incompatibility with the experimental chemistry. A technique using COTS electronics Tin-Silver-Copper (SnAgCu) solder was devised, utilising commercially purchased metal-coated optical fibres, to develop an all metal hermetic seal. Silver-solder seals have been reported [188–191] including applications such as telecommunications under-sea seals, suggesting the method could satisfy the project requirements.

The manufacturing technique devised consisted of placing one or more copper coated optical fibres within a short section 3 mm stainless steel Swagelok tube. The tube was heated at the centre of its length with an hot air gun set to $400\,^{\circ}$C. Commercial electronics SnAgCu solder wire, with embedded flux, was fed into the tube from one end, alongside the optical fibre. The heat was slowly moved towards the solder feeding end while the solder was continuously applied. Once the heat reached the open end of the tube, the solder application ceased and the heat was withdrawn. The tube assembly was then allowed to cool to room temperature. The solder used consisted of $0.5\,\%$ copper, $3\,\%$ silver, and $96.5\,\%$ tin, with rosin-based flux.

The technique was found to be easily achievable within the laboratory environment. Swagelok tubing was utilised to aid with seal evaluation, but it was thought possible to adapt to other geometries in the future if the technique was successful. The inclusion of flux within the solder was considered necessary to assist in providing wetting to the fibre coatings and to the stainless steel tube, but the potential for trapped flux gasses within the

tube was undesirable. Over the protracted time-scale of an experiment, the gasses could migrate into the experimental volume and impact on the experimental chemistry.

The manufactured seals were evaluated using a vacuum helium leak-tester. Once optical continuity through the fibre had been confirmed, the optical fibre was terminated short at one end of the tube, and a Swagelok tube fitting was used to connect to the leak-tester. The optical fibre feed-through created is shown in figure 9.1. Under test,

Figure 9.1: Photograph of solder seal optical fibre feed-through with Swagelok (USA) adaptor fitted for leak-testing.

with helium gas flowed around the rear surface of the seal, the measured leak rate was $3.5 \times 10^{-10}\,\mathrm{mbar\,l\,min^{-1}}$, which was at the sensitivity limit of the leak-tester, but satisfied the requirement of $1 \times 10^{-9}\,\mathrm{mbar\,l\,min^{-1}}$. The seal was temperature cycled between $-40\,°\mathrm{C}$ to $100\,°\mathrm{C}$ daily for a two week period and then re-tested at ambient conditions resulting in the same leak-rate measurement as before. The temperature cycling suggested the seal created was stable with minimal amounts of solder creep within the tube, suggesting a good bond was made between the fibre coating and the solder, and between the solder and the stainless steel tube. Longer durations of thermal cycling would increase confidence in the stability of the seal. This feed-through was not considered sufficiently robust for experimental integration, since the fibre entry into the seal was vulnerable to damage. A concept for integrating this sealing technique into an experiment is detailed in section 9.4.

To further assess the bonding achieved with the solder seal, the tube was sectioned using a hand saw and polished using silicon carbide polishing film, using grit sizes from $30\,\mu\mathrm{m}$ to $5\,\mu\mathrm{m}$, under distilled water. The total polishing depth, from the cut point, was less than 1 mm resulting in cut damage remaining visible after the polishing was complete. Deeper polishing depths were not feasible due to the maximum grit size available of $30\,\mu\mathrm{m}$.

The polished feed-through section was placed within a scanning electron microscope (SEM). The sample was imaged and chemically mapped using energy-dispersive X-ray (EDX), as shown in Figures 9.2a and 9.2b. Significant deformation to the solder and

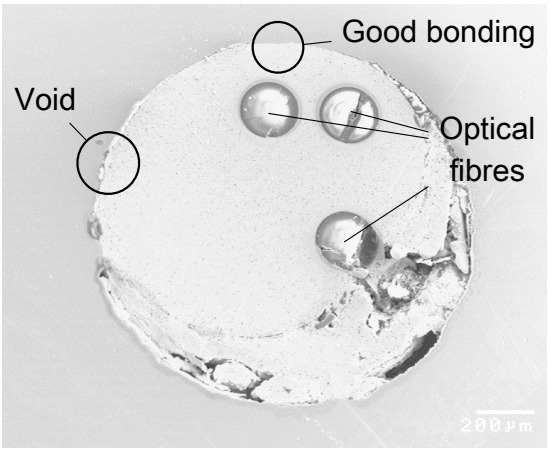

(a) SEM image at 100× magnification. Significant cut damage is visible across the lower portion of the solder seal.

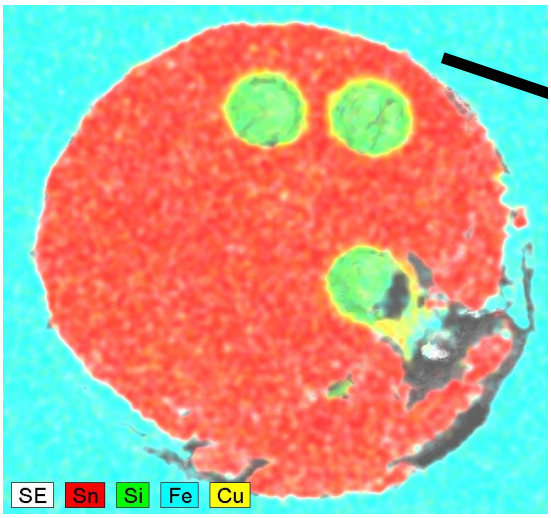

(b) EDX mapping overlaid on SEM image analysed for tin (Sn) within the solder, silicon (Si) within the silica optical fibres, iron (Fe) within the stainless steel tube, and copper (Cu) coating the optical fibres.

Figure 9.2: Analysis of solder seal feed-through test section.

fibre on the lower portion of the seal was attributed to cut damage, due to the shallow polish depth. Around the interface between the solder and the stainless steel tube shows areas of good bonding and a well-defined interface. Other areas, however, appear as voids suggesting an inhomogeneous sealing along the tube. From the analysis, the bond between the solder and the copper-coated optical fibres was considered good.

The inclusion of voids within the seal suggests the low leak-rate performance measured was due to the seal's physical length within the tube. Each cross-section taken of the seal revealed variations in fibre location and solder voids. These randomly placed voids meant no gas path existed through the seal, as each void was sealed further along the tube. Therefore shorter seals may not perform as well. Another concern is that the voids may contain flux gases which over time could permeate into the sealed volume and affect the chemistry of the system. A technique incorporating an annealing stage within a vacuum furnace to remove any trapped gases could mitigate these concerns and potentially improve bonding consistency within the tube. Evaluation would be required to ensure damage to the optical fibres was not sustained during the annealing process.

Initial proof of principal work was conducted and the manufactured seals were evaluated. The concept achieved the required leak rate and was considered potentially viable. Further work would be required to investigate the consistency of the solder seal along the tube length, develop techniques for the removal of the flux chemicals or negate

their use, develop techniques for alternative seal geometries, and evaluate the long-term stability. The use of copper coated fibres, and copper within the solder, was not ideal, since a chemical reaction with oxygen would be expected over time. Evaluation of alternative coatings, such as nickel or gold, should be conducted.

9.2 Internal Fibre Connections

Incorporating optical diagnostics within an experimental design required consideration of internal optical fibre connections. In an ideal case there would be no fibre connections within the experiment, ensuring the highest confidence in the stability of the optical signal throughout the experimental duration. However, the practicalities of assembling a complex experiment would likely necessitate the ability to incrementally insert diagnostics throughout the assembly process.

An optical fibre connector was therefore required to provide the means for connecting fibres that was compatible for use within the sealed environment of the experiment. The connector was required to be chemically compatible with the experiment, physically small, simple to connect in confined spaces, and be able to maintain a consistent connection for the duration of the experiment. The connector was not required to be removable or re-usable, but for development such features were advantageous.

No specific requirement was stated for the number of fibres the connector should support, but given the range of optical diagnostic techniques being investigated, a multi-fibre solution was deemed beneficial. A scheme using the commercially available MPO/MTP connector ferrule [202, 203, 299] was developed. The MPO/MTP ferrules are available from a number of manufacturers, able to support between 8 and 72 optical fibres, while maintaining the same outer dimensions. This work used the 24 fibre variant, which was considered a sufficiently high number for the project, while remaining practical to hand assemble in the laboratory. The MPO/MTP ferrules align using high-precision pins which locate in holes within the ferules themselves. The pins provide the sub-micron alignment required for effective single-mode fibre connection. The connector system developed was required to hold the ferrules with sufficient rigidity to maintain face contact and avoid applying bending forces to the pins. Commercially available ferrules are constructed from organic polymers, such as polyphenylene sulfide resin [299], which as discussed previously was not ideal for use within a long-term experiment. It was considered likely that either ferrules could be custom made from a metal or ceramic in the

future, or metal coating the ferrule sides and rear would be deemed sufficient for isolation with the experimental environment.

A connector system was devised which consisted of two parts: a ferrule support, and an interconnection spar. This initial design connected by the use of four M2 machine screws, which enabled the connector to be re-used. A diagram of the connection system, shown mating two MPO/MTP ferrules, can be seen in figure 9.3. A future version was

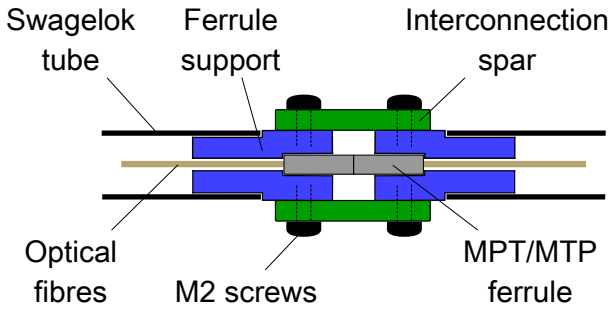

Figure 9.3: Diagram of the developed MPO/MTP ferrule-based connector system. The two ferrule support components are shown in blue, and the two interconnection spars are shown in green. Diagram is representative; not to scale.

intended to remove the need for screws, opting for a self-latching single-use design. This future version was not designed within this project, but would potentially enable connection of fibres in highly confined spaces.

The ferrule support component was designed to be as compact as possible, opting for a largely cylindrical shape not much larger than the MPO/MTP ferrule, as shown in figure 9.4. The ferrule is located within a U-shaped notch and protruded by $1\,\text{mm}$. The

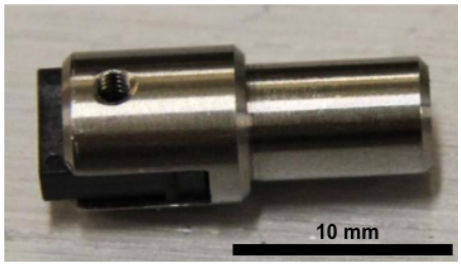

Figure 9.4: Photograph of MPO/MTP ferrule-based connector: ferrule support component with ferrule in place.

diameter of the main section of the connector was $(7.9 \pm 0.1)\,\text{mm}$ which stepped down to $(5.8 \pm 0.1)\,\text{mm}$ at the rear. The narrower section was hollow to enable the optical fibres to pass through, and was sized to enable an $8\,\text{mm}$ Swagelok tube to locate over. This enabled the connector to be used in a system where the fibre is contained within Swagelok tubing, isolating it from the experimental environment. Two tapped holes were included in the

forward section of the support, one on each side of the U-notch, to facilitate connector mating.

The interconnection spar was designed to mate two ferrule support components. The spar featured an internal radius to match the outer of the ferrule support and provide lateral constraint to the connected assembly, shown in figure 9.5. Two M2 machine screws

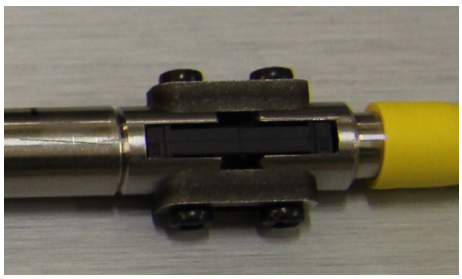

Figure 9.5: Photograph of an MPO/MTP ferrule-based connector assembly with two ferrules mated, two ferrule supports, and two interconnection spars. The plastic yellow connector boot on the right was fitted for laboratory evaluation only.

attached each spar to the ferrule supports. Connection of the fibres was achieved by inserting the alignment pins from one ferrule in to the other, and attaching two spars with four screws. As the screws were tightened slight pressure was applied to keep the ferrule faces touching.

The ferrule support and interconnection spars were manufactured in-house at AWE in stainless steel 316. The ferrules purchased were the 24F MM MT from USConec (USA). The connector parts were physically assembled with SMF-28e fibre installed within the ferrules. A custom adaptor was produced to enable polishing of the ferrule within an automated polisher, while located within the ferrule support. For long-term use, a thread-locking technique would be required for the M2 screws.

The connector was optically evaluated using a $1310\,\text{nm}$ laser and an optical power of $0.8\,\text{mW}$ using SMF-28e single-mode optical fibres. For fibre channels in the centre of the ferrule, the attenuation was measured to be $0.2\,\text{dB}$, but for fibres at the outside of the ferrule, the attenuation was measured to be $0.4\,\text{dB}$. No significant difference in loss was noted between the rows of the MPO/MTP ferrule, but the attenuation was found to increase the further from the centre of the ferrule the fibre was located. This suggested a slight curve was present across the face of the ferrule, which was a known phenomenon of the ferrule polishing process used. The attenuation measured was considered acceptable when compared to typical commercial optical connector specifications of between $0.2\,\text{dB}$ and $1\,\text{dB}$ [201].

The connector system was considered successfully demonstrated and provided a

simple and robust option for future use. Further work would investigate developing a push-fit single-use variant of the connector, and evaluating the connection for long-term stability and across a range of environmental conditions.

9.3 Fibre Feed-Through

The solder-based hermetic seal technique discussed in section 9.1 demonstrated the ability to enable optical fibres to enter a sealed environment. The technique on its own was not well suited to deployment in an experimental system, since it required passing the fibre through a hole in a experimental vessel, sealing of the fibre within the hole, then terminating the fibre. The process would require significant modification to a vessel to achieve, and result in a delicate feature within the vessel which would require additional care during assembly of the experiment.

This work aimed to provide a solution where the hermetic fibre seal could be achieved separately, and only mated with the experimental vessel during assembly. The technique would require a small modification to the vessel, but could reduce the risk of damaging the seal during experiment assembly.

Since the feed-through was intended to be inserted during assembly, the optical fibres would also need connecting to the sensors during assembly. The connector scheme discussed in section 9.2 was therefore utilised, to provide a 24 fibre feed-through solution (expandable to 72 fibres). The MPO/MTP ferrule support of the *internal connector* design had a maximum diameter of 8 mm and was designed to locate within a 8 mm diameter Swagelok tube.

A short length of Swagelok tube was assembled with a bespoke *internal connector* located at each end, as shown in figure 9.6. The solder seal would be achieved within the

Figure 9.6: Photograph of fibre feed-through concept based around 8 mm Swagelok tubing and the bespoke *internal connector* design. Shown coupled onto a test breakout protected by a yellow plastic boot and furcation tubing.

Swagelok tubing and the ferrule supports could be welded or crimped to the tube. The resulting tube can be passed through a 8 mm hole, or used in conjunction with a Swagelok tube fitting.

Use of this feed-through concept could include attaching a 12 mm Swagelok tube

(1.0 mm or 1.5 mm wall thickness) to the experimental vessel. This modification was considered minor, simple to achieve, and would not significantly affect the vessel's robustness. A Swagelok 12 mm to 8 mm coupler, with fully bored centre, could then be attached to the installed tube. During assembly the optical fibre sealed 8 mm tube could be inserted into the fitting and secured. A diagram overlay of a demonstration assembly is shown in figure 9.7. The hermetic seal is provided by the solder seal within the optical

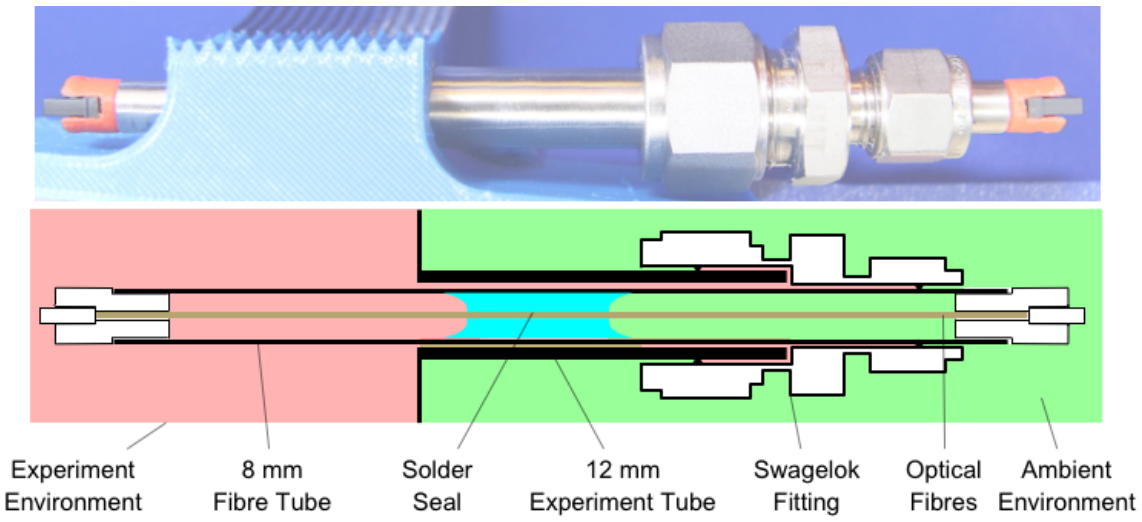

Figure 9.7: Photograph and diagram of feed-through assembly of a demonstration assembly. The feed-through is shown separating the (red) experimental environment and the (green) ambient environment. An 8 mm fibre tube is fitted with two ferrule supports and ferrules, connected by optical fibre. A solder seal is shown in the centre of the tube. A 12 mm tube is attached to the experiment vessel wall, and a Swagelok fitting connects the two tubes.

fibre tube, and the two Swagelok ferrule connections within the fitting. The long-term integrity of the Swagelok fitting technique was not evaluated within this work.

This work demonstrated a practical application of the solder-seal technique discussed in section 9.1. A technique was devised utilising Swagelok tubing and fittings to enable the separation of the optical fibre hermetic seal and the experiment vessel until final experimental assembly. This would potentially reduce the chance of damaging the optical fibres or hermetic seal. The *internal connector* system devised for this project was used.

The feed-through concept was assembled and presented internally at AWE. It was considered a potential technique for future use following further development. It was noted the technique had the potential to significantly reduce the number of concurrent fibres present during experiment assembly, since it used a multi-fibre connector, and the feed-through can be added when required. Further development was not conducted within this project to enable the potential applications for this connector system to be understood, before creating an updated requirements set for future development.

9.4 Sensor Packaging

Integrating sensors within an experimental design requires careful consideration to ensure the sensor measures the expected parameter, the sensor response is not influenced by unexpected or changing factors, and the sensor is sufficiently robust to survive the experiment assembly process. In some cases sensors could be integrated within materials, which may offer some mechanical protection. In other cases, where the ambient conditions require monitoring, the sensors may wish to be in their own housing. This work investigates the creation of a robust sensor package to provide an option for the deployment of FBG temperature sensors and FFP barometric pressure sensors.

The diagnostics element of this project investigated temperature, barometric pressure, and gas sensing techniques. FBG based temperature sensors were evaluated for long-term stability with promising results (Chapter 5), but the commercial housings used were physically large. FFP based barometric pressure sensors were also evaluated and were also promising (Chapter 6), but the sensors were physically fragile. The gas spectroscopy cell developed within Chapter 7 was designed to be compact and robust, so did not receive further attention.

A sensor package was designed that could house one FBG sensor for measuring temperature, and one FFP sensor for barometric pressure monitoring. A secondary package was also designed that housed two of the FBG temperature sensors to provide an increased confidence dual temperature sensing option.

It was decided to base the sensor packaging on the MPO/MTP ferrule and ferrule support which was under development as an *internal connector* solution. The sensor package would need to connect to a fibre within the experimental configuration, so it was logical to use the connector designed to be used within that environment. A support housing was designed to hold the sensors in place and locate them to selected fibre channels within the MPO/MTP 24 way connector, which can be seen in figure 9.8.

To ensure the FBG only reported temperature effects, it was strain-isolated within a glass capillary tube which had an internal diameter of $128\,\mu$m, which prevented fibre bending that could have been erroneously interpreted as a change in temperature. The FBG was purchased from Micron Optics (USA), written into SMF-28 fibre.

The FBG position was located in the fibre by sweeping a localised heat source along the length of the fibre while actively monitoring the FBG reflection wavelength. Once the location was known to within a few millimetres the fibre was fractured to one side

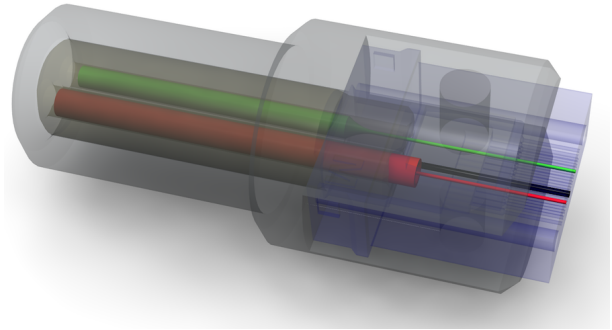

Figure 9.8: CAD rendering of sensor housing within an MPO/MTP ferrule and ferrule support component. Also shown in red a strain-isolated FBG sensor and in green a FFP pressure sensor.

of the FBG. The fibre coating was removed and the sensor was inserted into the glass capillary. The fibre was secured to the capillary by epoxy once it was located within the sensor housing and MPO/MTP ferrule. The epoxy was intended to only contact the outside of the capillary, leaving the FBG itself uncoated. The volume of epoxy used was small (< 0.2 ml), but its use was still undesirable within this project. In the future, the use of a metal solder would be advantageous.

The FFP sensor was designed to be of the same type used in Chapter 6 and would have its fibre cut to the correct length, coating stripped, and be inserted into the sensor housing and ferrule. Due to a limited number of FFP sensors purchased and at the time the ongoing nature of the long-term evaluation, only the dual temperature variant of the sensor package was assembled.

For evaluation the sensor housings were manufactured in-house at AWE on a Stratasys (USA) J750 UV-cured acrylic resin 3D printer. For long-term use, the housings would be required to be manufactured from stainless steel or similar, since plastic was not suitable for introduction into the experiment. The processing of the FBG sensors proceeded as described, but the mating of the sensor housing and the MPO/MTP ferrule required care. Aligning the two uncoated FBG fibres between the capillary tubes and the ferrule was a highly delicate procedure; achieved using a steady hand and a microscope. Figure 9.9 shows an assembled sensor package.

The assembled sensor packages were connected to a Micron Optics (USA) SM125 FBG interrogator using the *internal connector* system developed. All FBGs were able to be measured, but it was noted that they had consistently experienced a wavelength shift, compared to their pre-assembled response, equating to approximately a $6\,^{\circ}$C offset. Their temperature sensitivity was evaluated and was found to be consistent with their initial performance.

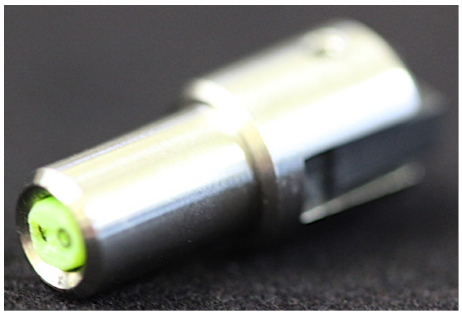

Figure 9.9: Photograph of assembled sensor package with the green sensor housing supporting two glass capillary tubes visible.

A rugged optical fibre sensor package was designed, manufactured, assembled, and evaluated. The package was designed to enable both temperature and barometric pressure measurements, but only all-temperature packages were assembled. Handling uncoated optical fibres required practice and delicate treatment, especially when manoeuvring them into ferrules. The strain-isolated FBGs were evaluated within the assembled packages and were found to be functional, but had experienced a base-line shift during the assembly.

The sensor packaging provided a robust sensor housing option which could enable the deployment of sensors into an experiment, confident they would be unlikely to experience physical damage. The shift in wavelength experienced by the FBG sensors suggested they were under strain within the assembly, most likely caused by epoxy wicking within the capillary tube. This process, if occurring, was considered undesirable since any change in epoxy properties during the experiment duration could be misinterpreted as variations in temperature. The wavelength shift demonstrated the requirement to re-calibrate sensors once they are within their final assemblies, and not relying on initial evaluations.

Further work would demonstrate the inclusion of a FFP pressure sensor within the package as designed, and confirm the cause of the FBG wavelength offset. The inclusion of further sensors, or combining the temperature and pressure sensors within the spectroscopic gas cell would also be avenues for further development.

9.5 Optical Fibre Encapsulation

Techniques have been presented here to enable optical fibres to enter the experimental vessel while maintaining hermeticity, and to package sensors to make them sufficiently robust for use within a complex experiment. Connecting the feed-throughs to the sensors and gas cells would require optical fibre links. The fibre links were required to be chemically compatible with the experiment chemistry, easy to handle, and physically

robust to prevent damage during experiment assembly.

Fibres are commercially available with coatings such as acrylate, polyaimide, ORMOCER® [300, 301], and a variety of metals. Due to the wide range of coatings available, it is likely that depending on the experiment at least one coating would be chemically compatible. However, some coatings are more complex to remove for fibre termination, and single fibres are typically delicate and bend unpredictably when handled.

This work looks at a technique to encapsulate a number of fibres so that the fibre coating is isolated from the experiment, and to increase the mechanical robustness and ease of handling.

Polyimide (Kapton® [302]) was chosen as an encapsulation material to form a flat fibre assembly, similar to an electrical ribbon cable. Kapton® is a thin, mechanically robust, and typically chemically compatible material. The fibre coating chosen for development was acrylate due to its high commercial availability and simple mechanical stripping compatibility.

Multiple fibres were assembled in parallel on top of a length of self-adhesive Kapton® film. A second layer of film was then applied on top, resulting in a ribbon-like assembly. The ribbon was simple to manage since it could only bend in one axis, therefore as it was handled it would bend in predicable directions. The Kapton® provided additional mechanical protection to the optical fibres, but the additional protection was not considered robust. If the encapsulation was performed optimally, it would serve to isolate the acrylate from the experiment chemistry. The self-adhesive film used was not ideal for long-term use, but a heat-sealable variant of Kapton® is available [302] which could produce a stable assembly. Using the self-adhesive film also introduced the potential to create small pockets of trapped gas which could migrate into the system over time. The use of the heat-sealable variant, and assembly within a vacuum oven, could remove this potential issue.

The optical fibre encapsulation technique was demonstrated and successfully produced a 1×24 fibre MPO/MTP to 3×8 fibre MPO/MTP fan-out assembly, shown in figure 9.10. The fibre was well contained within the Kapton® encapsulant and was provided significant mechanical support. The flat ribbon structure constrained the fibre assembly to one axis of bending providing a higher level of predictability and control when routing the fibres within an experiment. The mechanical robustness was not tested, but was considered an improvement over non-encapsulated fibres and would only improve as the encapsulation technique was developed. Chemical compatibility of the resulting

Figure 9.10: Photograph of encapsulated ribbonised optical fibre fitted with *internal connectors* and forming a 1 to 3 fibre fan-out.

assembly was not assessed, also pending development of the technique.

Further work would investigate improved techniques for producing encapsulated optical fibres and fibre assemblies, and evaluate their robustness and chemical compatibility. No further work was conducted within this project beyond that presented. The technique demonstrated was considered a potential direction, but considerable resources would have been required to continue. Further resourcing was not allocated due to the low technology readiness level (TRL) of 2 (Appendix A) attributed to the work demonstrated. It was decided to delay further resource allocation until the sensing and feed-through techniques were more mature, and the requirements for routing fibres within an experiment were better constrained.

9.6 Fibre Umbilical Connector

Connecting multiple optical fibres between the interrogation system (Chapter 3) and the material ageing experiment required careful consideration. The method was required to be simple to use, support over 30 fibres, robust, and flexible. The quantity and type of optical fibres required for an experiment was not known at the time of this work, so a solution was required which could be adapted over time as the requirements were revisited.

Commercial options were reviewed but none simultaneously met the requirement for fibre count and adaptability. High fibre count connectors were available, but only as full assemblies created from standard fibre bundles. Therefore an adaptable approach or a customisable selection of fibre types would not be possible without significant expense. As a result a bespoke connector and umbilical system was developed.

A connector utilising the MPO/MTP ferrules was designed. Three ferrules would enable an umbilical of up to 72 fibres using 24-fibre ferrules, but expandable to 216

fibres if 72-fibre ferrules were used. Since MPO/MTP ferrules are available as loose components, the connector could be loaded with any type of fibre in any location. An advantage of using multi-fibre ferrules within the larger connector was that only three polishing operations were required, as opposed to one per fibre.

To maximise the room for polishing the ferrules, the connector was designed so it could be assembled around the pre-terminated and polished fibres and ferrules, as shown in figure 9.11. The design was formed of two connectors, one panel-mounting and the

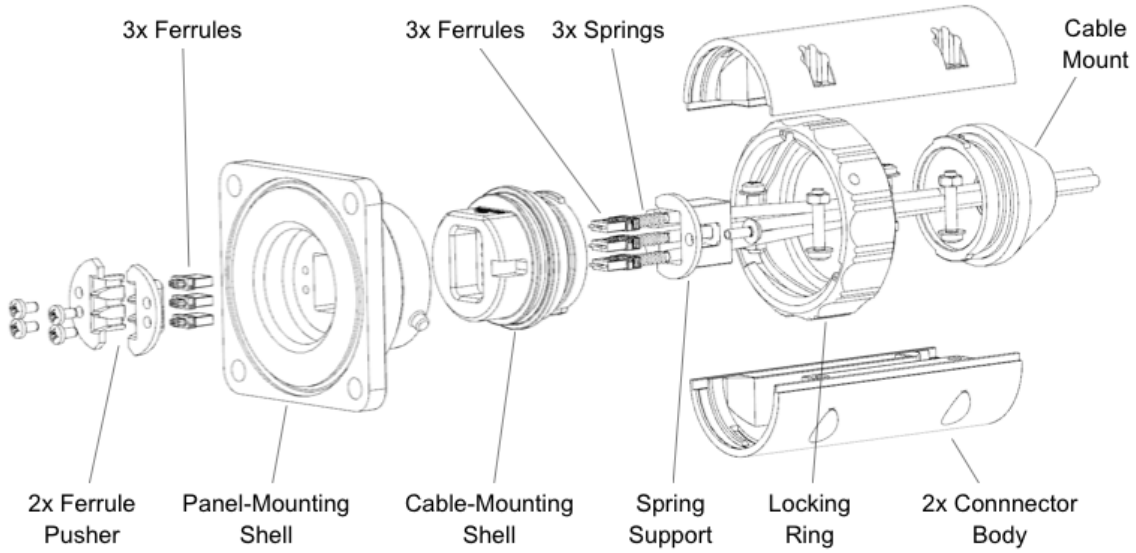

Figure 9.11: Expanded CAD view rendering of the bespoke umbilical connector showing both the panel-mounting and corresponding cable-mounting connector parts in an 'exploded' arrangement.

other cable-mounting. The panel-mounting connector consisted of a shell and a ferrule pusher. Assembly required one shell and two ferrule pushers, which were assembled around three pre-terminated MPO/MTP ferrules, and four M2 machine screws. The design supported MPO/MTP ferrules which were parallel-flat polished or angle polished, but it was only evaluated using flat polished ferrules. A flat polish is generally more widely supported by mechanical polishing equipment, but an angle polish could be preferable in systems where back-reflections need to be minimised. The cable-mounting connector consisted of a shell, spring support, locking ring, connector body, and a cable mount. Assembly required one of each component and two connector bodies, three pre-terminated MPO/MTP ferrules, two M2 machine screws, and four M3 machine screws with nuts. The ferrules were fitted with alignment pins and springs which were standard MPO/MTP components. The cable mount supported attachment of a variety of protective sheath for the optical fibres, such as flexible electrical conduit or non-conductive rubber hosing.

In the panel-mounting connector the ferrules were held rigidly within the shell in tight-toleranced slots. The recess in the rear of the panel-mounting shell was designed to support adhesive potting materials, which together with an o-ring groove, could provide environmental sealing. In the cable-mounting connector the ferrules were individually spring-loaded. The alignment was achieved via tight-toleranced slots in the cable-mounting shell, and contract pressure between the ferrules in each connector was maintained by the individual springs, which were held in place by the spring support connector. The locking ring connected the two connectors with a quarter-turn operation for ease of use, once the two shells are fully engaged. The cable-mounting connector featured o-rings to provide environmental protection to the fibres, and once mated the ferrule faces are also environmentally sealed. Caps were designed for each connector to protect the ferrule ends while not mated. Ferrule faces were recessed within the two shell components to reduce the chance of accidental damage during use.

The connector parts were manufactured in-house at AWE on a Stratasys (USA) J750 UV-cured acrylic resin 3D printer, shown in figure 9.12. Metals parts were not

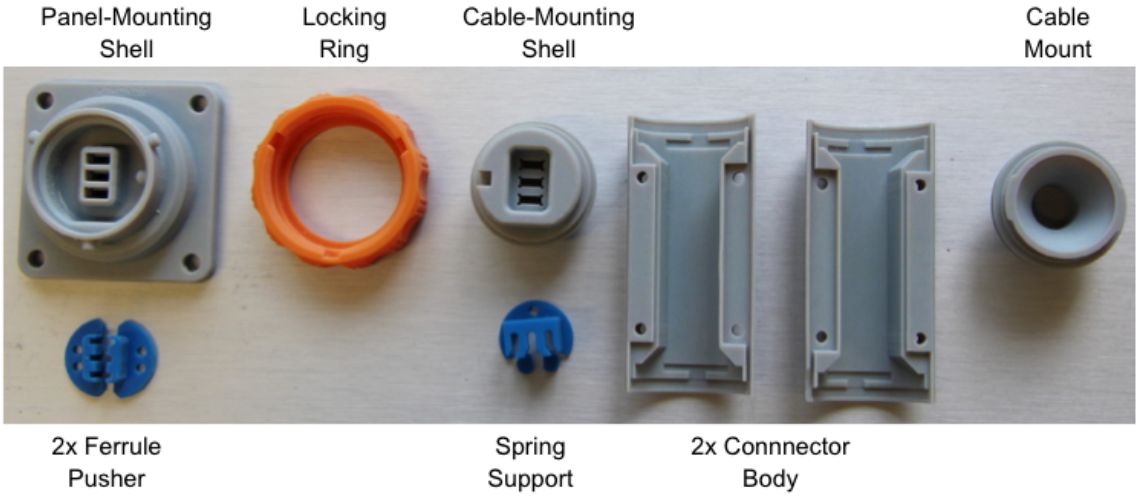

Figure 9.12: Photograph of umbilical connector parts which were 3D printed for evaluation.

manufactured for evaluation given the physical complexity of some of the components. Providing engineering drawings of such parts would have required considerable support from a drawing office draughtsman, which was not considered beneficial before the design had been verified. However, a final production version would be manufactured from metal.

The parts were initially assembled for mechanical evaluation; the cable-mounting connector is shown in figure 9.13. The connectors were tested to mate as expected, so a test umbilical was assembled using with SMF-28e fibre. Assembly was achieved

as described with all components mating as expected. Good access was provided for polishing the MPO/MTP ferrules due to the connector design.

Figure 9.13: Photograph of cable-mounting umbilical connector assembled to verify mechanical operation.

The umbilical was found to align the ferrules sufficiently to enable the MPO/MTP pins to achieve final alignment. The spring pressure applied ensured ferrule face contact was maintained even if the umbilical was flexed. The locking ring enabled quick and user-friendly operation of the connector.

The umbilical was optically evaluated at a wavelength of 1310 nm and a power of 0.8 mW for an MPO/MTP connector ferrule in the central position of the connector loaded with 24 SMF-28e single-mode optical fibres. No significant difference in loss was noted depending on which row of the MPO/MTP ferrule the fibre was, but the attenuation was found to increase the further from the centre of the ferrule the fibre was located. In the centre the attenuation was measured to be 0.3 dB but at the outside the attenuation was measured to be 0.7 dB.

An optical fibre connector was designed which enabled user-friendly simultaneous mating of 72 fibres (expandable to 216). The design used industry standard MPO/MTP ferrules and components to simplify the umbilical build process. Assembly of the connector was possible after the ferrules were terminated and polished. The connector was found to function with low attenuation losses.

Due to the lack of availability of a connector suitable for this project which motivated the design of the presented work, the optical fibre connector was reviewed by an independent panel at AWE. The design was considered novel, with significant market potential, and subsequently the design was passed to the Ministry of Defence (MOD) for further review and their decision was to pursue a patent. The patent was drafted and filed on the 11th December 2018 with application number: GB1820122.8 [3].

Further work would see the umbilical connector manufactured from a metal such as aluminium, to enable its robustness to be evaluated. Environmental testing would be required of the connector once manufactured from metal. No further development or evaluation of the connector design was conducted since a functioning umbilical demonstrator had been achieved. Focus was therefore aligned to the remaining streams of the project.

9.7 Conclusions

Techniques were developed to aid in the practical deployment of long-term material ageing experiments. The techniques included optical fibre hermetic sealing, fibre *internal connector*, fibre feed-throughs, sensor packaging, fibre encapsulation, and a fibre umbilical connector. These were seen as enabling technologies which were required to ensure optical diagnostics were a practical option for future use.

The hermetic seal technique utilised silver-based solder to create a non-organic solution for passing optical fibres into a sealed experimental vessel. The technique was used to create highly performing seals, but long-term robustness was not evaluated.

A connector suitable for use within a material ageing experiment was designed, manufactured, and evaluated. The connector used the industry standard MPO/MTP ferrule allowing up to 72 fibres to be mated at once. The *internal connector* was compact and manufactured from stainless steel. A single-use variant was planned but not developed.

A feed-through technique was developed which utilised the solder-seal method and *internal connector* design. The aim was to enable the delicate optical fibre part of a feed-through to be constructed separately from the experimental vessel and only mated during experiment assembly. The physical concept was demonstrated but the method was not experimentally evaluated.

A packaging option for optical temperature and pressure sensors was developed. A housing which located within an *internal connector* was designed, and a dual-temperature module was assembled for evaluation. The technique provided a robust package which could enable inclusion of optical sensors in locations where physical robustness was required.

Optical fibres were encapsulated within Kapton® film to form a ribbon-like assembly. The film added a layer of physical robustness to the fibres and restricted their movement

such that their handling resulted in predicable results. The Kapton® had the potential to isolate the experimental chemistry from the fibre coating, but further work was required to enable evaluation.

A multi-fibre umbilical connector system was designed which could support up to 72 fibres (and expandable to 216 fibres) within one housing. The connector was prototyped and evaluated to function as a fibre connector. Further work would manufacture the connector design to enable the robustness of the design to be evaluated.

These enabling techniques together support the deployment of optical diagnostics within an experimental system, as shown in figure 9.14.

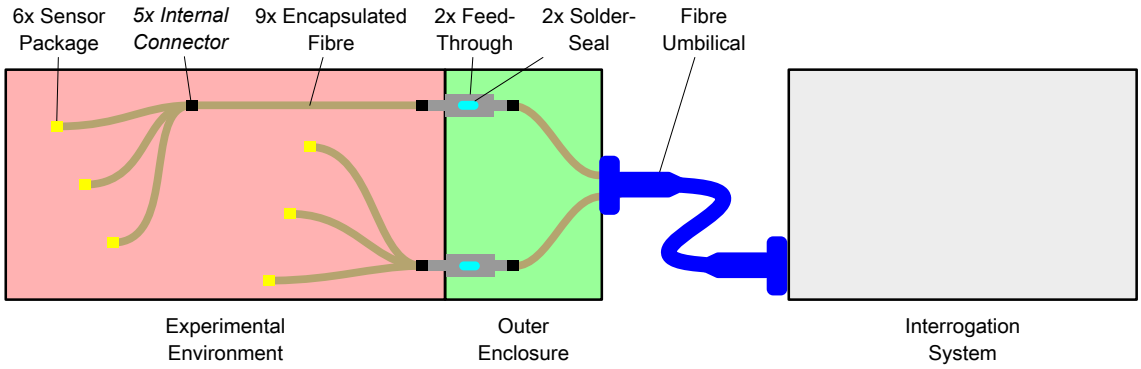

Figure 9.14: Diagram of enabled experimental configuration demonstrating (yellow) sensor packages, (black) *internal connector*, (gold) encapsulated fibre, (grey) feed-though containing (cyan) solder seal, and (blue) fibre umbilical.

Further work

Future development of the solder seal would improve the technique to ensure consistency of the seal and removal of trapped flux chemicals. The long-term reliability of the seal would also be conducted.

Further work on the *internal connector* would develop the single-use push-fit variant which would enable its use within confined spaces. Additionally removing the polymer-based ferrule in preference to a ceramic or metallic solution would be beneficial. Long-term reliability of the connector would require evaluation.

The feed-through technique would require experimental evaluation and potentially development to reduce the size and complexity of the design. Due to the removable nature of the fibre tube from the feed-through, commercial production of the solder-seal within the tube could be investigated.

The sensor packaging technique would benefit from the experimental assembly of a combined temperature and pressure node for evaluation. Miniaturisation of the housing

would be a potential avenue for further development, or integration into the spectroscopic gas cell.

Further evaluation of the fibre encapsulation technique would require heat-sealing of Kapton® film around the optical fibres. A full evaluation of the chemical compatibility of the technique could then be experimentally assessed. Alternative options such as metal coatings of fibres should also be investigated.

The umbilical connector required evaluation after manufacture in metal. The optical performance, mechanical robustness, operation across a range of environments, and long-term use would be evaluated.

Chapter 10: Discussion and Conclusions

This research project developed diagnostic options for *in situ* use within future materials ageing experiments. The techniques included: optical fibre, and electronic, sensor evaluation and integration; a bespoke modular interrogation system; and novel fibre routing and connector solutions.

In this chapter the results of the work are discussed, explained within the context of a proposed experimental scenario, and concluded. Potential avenues for further development are presented.

10.1 Discussion

This research project aimed to produce technologies and techniques as options for potential future use within long-term materials ageing experiments at the Atomic Weapons Establishment (AWE). The work utilised optically interrogated sensors and techniques, to ensure the experiment could be electrically isolated, if required. A focus of the work was to produce concept demonstrating hardware to enable laboratory evaluation of the developed technologies. The scope of the project covered the hardware required for delivering a long-duration experiment, including diagnostic sensor packages, interrogation hardware, and hardware required for integration into an experimental system. The project objectives and requirements were satisfied, and AWE was provided with numerous technology options for further development towards a diagnostic system suitable for future long-term materials ageing experiments. A discussion of the work detailed in this thesis is presented below.

Chapter 1 described the motivation of this research project, and presented the aim, objectives, and requirements. As noted, these targets were considered satisfied, providing AWE with a conceptual diagnostic system with the ability, following further maturation and development, to support future materials ageing experiments. A discussion of the project objectives is noted below, and within each chapter the techniques are evaluated against their specific project requirements.

Chapter 2 detailed a survey which was conducted to search for previously presented and commercially available interrogation systems, and for optical fibre-based: temperature sensing, barometric pressure sensing, gas phase chemical speciation techniques. Interrogation systems able to measure multiple types of sensors with the long-term confidence required by the project were not identified within the review, motivating the development of a bespoke solution, as documented in Chapter 3. A large number of fibre Bragg grating (FBG) interrogators were commercially available, with suitable performance specifications, but their lack of integration and long-term support hindered their use within this thesis. Temperature sensing using FBGs was recommended and a novel experimental long-term investigation was performed, as discussed in Chapter 5. Other techniques, such as fibre Fabry-Pérot (FFP) sensors, luminescence, and distributed sensing were reviewed, but FBGs were considered suitable to satisfy the project requirements while being a well matured technique. Barometric pressure sensing using FFP cavities was considered likely to satisfy the project requirements, and the technique was further investigated in Chapter 6. The use of a FBG pressure sensing configuration was considered, but the smaller size and commercial availability of the FFP sensors was considered advantageous. Gas sensing techniques were considered, with absorption spectroscopy being the technique of interest. Cavity ring-down (CRD) spectroscopy and tunable diode-laser absorption spectroscopy (TDLAS) were reviewed, with TDLAS being the recommended technique, and forming the basis of the work reported in Chapter 7. The typical use of high-finesse gas cells in the CRD technique was considered a potential source of error within a long-term experiment, since changes of finesse would be difficult to detect remotely, a feature TDLAS did not require.

Chapter 3 discusses the modular interrogation system, which was designed to be a standalone system suitable for interrogating all deployed diagnostics within the ageing experiment. The system was based on replaceable modules to provide long-term serviceability, and full AWE intellectual property (IP) ownership ensured a supply of replacement modules was achievable. The interrogation system infrastructure was fully designed and assembled within this project, and supported demonstration of the modules operating *in situ*. Two smaller system enclosures were also developed to provide secondary uses for the modules, potentially supporting shorter-term experiments. System modules, such as those for power, cooling, and controlling the system were produced and integrated. Interrogation modules for measuring FBG temperature sensors were developed, opting to pursue two measurement techniques to provide both module and

design diversity and redundancy. The developed swept laser module was demonstrated measuring a FBG temperature sensor successfully, and the developed optical spectrum analyser (OSA) module was successfully evaluated. The optically isolated electronic sensors (OIES) interrogation module was demonstrated providing power to a bespoke OIES sensor node, and receiving the returning digital sensor data. Modules for optical fibre routing were vital for operation as an integrated diagnostic system. Such modules were developed, manufactured, and evaluated. A novel study was also performed to evaluate the performance of the optical fibre switches used within this work for repeated use, concluding that multi-year operation was predicted.

Chapter 4 detailed the selection and performance evaluation of electronic sensors that were integrated throughout the modular interrogation system. The sensors were included on each of the modules to enable module-level environmental conditions to be monitored, and the data used to support system maintenance over the multi-decade duration of an experiment. A review of electronic sensing techniques was conducted and commercial sensors were selected which featured digital data interfaces, inter-integrated circuit protocol (I^2C), which simplified their integration onto the interrogation modules. Four electronic sensors were chosen for experimental evaluation and were integrated into a bespoke test-bed system. The sensors were evaluated for measuring temperature, barometric pressure, and humidity. All the sensors evaluated performed within the measurement requirements, and two were selected for integration into the interrogation system, between which the three environmental parameters could be monitored. The selected sensors were subsequently integrated into all of the interrogation system modules developed.

Optical fibre temperature measurement using FBGs was considered likely to satisfy the project requirements, but no systematic study of long-term performance or failure modes was found. Chapter 5 details a novel experiment where three commercial off-the-shelf (COTS) FBG temperature sensors were cycled 180 times over a range of $-40\,°C$ to $100\,°C$ during the period of one year. No sensor failures were identified during the experiment, providing confidence in their use, but since no failures occurred, a sensor lifetime prediction was not formed. Further evaluation would be required to gain the confidence needed to deploy such sensors into a long-term experiment, due to the inability to calibrate the sensors once the experiment has commenced.

A similar experiment was conducted in Chapter 6 on FFP-based barometric pressure sensors. Six COTS sensors were pressure cycled in excess of 7300 times from vacuum

to (1000 ± 4) mbar, with no sensor failures discovered, over the period of one year. As with the temperature sensors, no sensor lifetime prediction was able to be concluded, but additional confidence in the technique was gained. Further evaluation of these sensors was also recommended.

Chapter 7 detailed the development of a bespoke fibre-coupled multi-pass gas cell, and the evaluation of an optical fibre fluorescence based oxygen sensor. The gas cell was designed, manufactured, and evaluated for detecting water vapour (H_2O). The design was supported by mathematical beam-path modelling which predicted the beam position throughout its multiple reflections in the cell. The design utilised the Herriott cell geometry, and had an optical path-length in excess of 6 m within an enclosure 140 mm long. The design was considered mechanically robust, and featured a novel two-hole mirror arrangement to aid in fibre-coupling of the cell. The oxygen sensor was measured in excess of $250\,000$ times and was not found to be long-term stable, requiring frequent re-calibrations to provide accurate data. The oxygen sensor was therefore not recommended for use within a long-term materials ageing experiment. Further development of the gas cell was recommended and it was considered possible to measure multiple gaseous species within the single cell, such as H_2O, CO_2 and CH_4.

Following the experimental evaluation of both electronic and optical sensors, as described, a technique to power electronic sensors over an optical fibre was pursued. The technique developed, OIES, discussed in Chapter 8, used light sent down a fibre, converted to electrical power at the remote node, to enable electronic sensor measurements and optical data transmission of the results back along the fibre. This potentially enabled electronic sensors to be used without compromising the electrical isolation of the experiment. The technique was demonstrated successfully, using a bespoke arrangement of readily available commercial components, and achieving an optical to electrical conversion efficiency of $1.9\,\%$. Following the success of the hardware demonstration, further development was conducted and a revised version of the node was designed and manufactured, improving the conversion efficiency to $(24.0 \pm 0.2)\,\%$. The increase in efficiency provided higher continuous power in the node, which potentially enabled an increase in measurement frequency, and broadened the range of electronic sensing techniques that could be supported in the future.

Chapter 9 described development work of optical fibre infrastructure components, that provided options to aid in the practical deployment of a long-term experiment. The project had investigated diagnostic sensor options and interrogation hardware, but

integrating the sensors and optical fibres into the experimental system also required consideration. The techniques developed included: optical fibre hermetic sealing, fibre *internal connector*, fibre feed-throughs, sensor packaging, fibre encapsulation, and a fibre umbilical connector. Together these techniques were seen to form enabling technologies which would be required if optical diagnostics were to be considered a practical option for future use. Of the six techniques developed, the sensor packaging, fibre *internal connector*, and fibre umbilical connector were the most mature; offering practical solutions for fibre interconnections and robust sensor housing. The fibre feed-through technique, and optical fibre encapsulation, would require the most further development and maturation before use within a materials ageing experiment.

The project objectives were assessed against the work conducted. The objective to *investigate sensor interrogation hardware solutions* was completed by the creation of the bespoke modular interrogation system. The objective to *develop optical diagnostic techniques*, was considered completed due to the long-term evaluation conducted on FBG and FFP sensors, and the development of a sensor packaging technique. The gas phase speciation development consisted of the design, manufacture, and evaluation of a bespoke multi-pass gas cell, and the evaluation of a commercial oxygen sensor. The objective to *develop optical fibre integration technologies* was completed by development of the optical fibre support components. Each technology was evaluated as satisfying its specific requirements, as noted throughout the chapters.

10.2 Experimental Scenario

From the work described, a future materials ageing experiment incorporating the diagnostics discussed could be assembled as shown in figure 10.1. The schematic includes the modular interrogation system and modules discussed in Chapter 3, the electronic sensors investigated in Chapter 4, FBG temperature sensors evaluated in Chapter 5, FFP barometric pressure sensors evaluated in Chapter 6, multi-pass gas cell detailed in Chapter 7, the OIES node discussed in Chapter 8, and the optical fibre support components discussed in Chapter 9.

Together these techniques provided concepts for possible technology solutions for delivering a complete experimental system that incorporated comprehensive optical diagnostics.

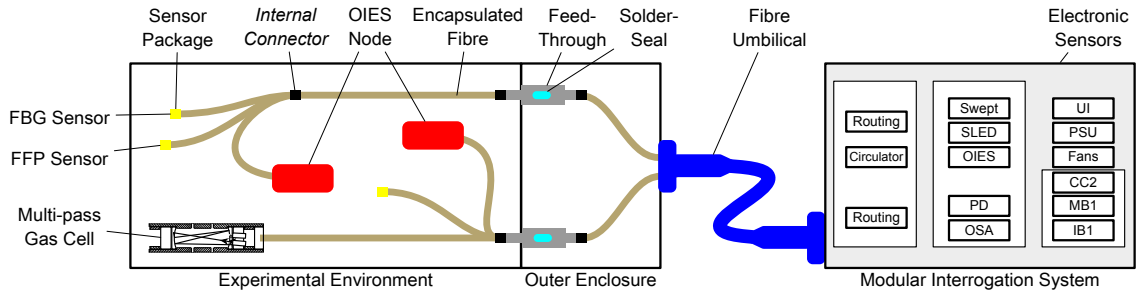

Figure 10.1: Schematic concept of a future materials ageing experiment incorporating the diagnostic techniques developed.

10.3 TRL Assessment

A range of technologies were developed throughout this project. Each was assessed against their requirements, as described in the relevant sections of this work, but they were not often assessed for *readiness*. Table 10.1 summarises the technologies developed and details the appropriate equivalent technology readiness level (TRL), following the guide shown in Appendix A.

To visualise the overall *readiness* of the technologies discussed, the assignments from the table are shown in histgram form in figure 10.2. The majority of the hardware was assessed as TRL 5/6, but a significant amount of work would be required to elevate the technologies to TRL 8/9, which would be necessary before use within a materials ageing experiment.

Chapter	Technique/Technology	TRL
Modular Interrogation System	Module system, frame, and UI	5
	Control Card 2 (CC2)	6
	Interface Buffer (IB1)	6
	Module Buffer (MB1)	6
	Routing (OR) Module	6
	SLED Module	6
	Photodiode (PD) Module	6
	Spectrometer (OSA) Module	6
	Swept Laser Module	6
	OIES Interrogation Module	6
	SUBCACE Enclosure	5
	MINICACE Enclosure	5
Electronic Sensor Integration	Sensor test-bed	6
Gaseous Chemical Detection	Multi-pass multi-gas cell	5
Optical Isolated Electronic Sensors	Initial Sensor Node	5
	Revised Sensor Node	5
Optical Fibre Infrastructure	Hermetic Solder Seals	3
	Internal Fibre Connector	6
	Fibre Feed-through Technique	2
	Sensor Packaging	6
	Optical Fibre Encapsulation	2
	Fibre Umbilical Connector	4

Table 10.1: Technology readiness level assessment for the techniques and technologies developed within this project.

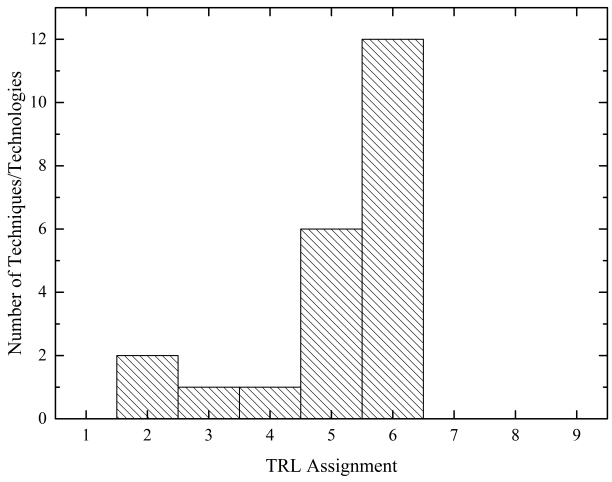

Figure 10.2: Histogram of TRL assignments.

10.4 Conclusions

This research project aimed to produce technologies and techniques as options for potential future use within long-term materials ageing experiments at AWE. The work utilised optically interrogated sensors and techniques, to ensure the experiment could be electrically isolated, if required. The project objectives were satisfied, and AWE was provided with numerous technology options for further development towards a diagnostic system suitable for future long-term materials ageing experiments.

The modular interrogation system discussed in Chapter 3 was based on replaceable modules to provide long-term serviceability satisfying requirement 1g. The design provided full AWE IP ownership ensured a supply of replacement modules was achievable over a multi-decade experimental duration, satisfying requirement 1b. The interrogation system infrastructure was designed and assembled, and supported demonstration of the modules operating *in situ*, satisfying requirement 1a. Two smaller system enclosures were also developed to provide secondary uses for the modules, potentially supporting short-term experiments. System modules, such as those for power, cooling, and controlling the system were produced. Interrogation modules for measuring FBG temperature sensors were developed, opting to pursue two measurement techniques to provide diversity and redundancy. The swept laser module was demonstrated measuring a FBG temperature sensor successfully, and the OSA module was successfully evaluated operating in the $1550\,\text{nm}$ region with a bandwidth of $150\,\text{nm}$ and a resolution of $(140 \pm 10)\,\text{pm}$, satisfying requirement 1c and 1d. The OIES interrogation module was demonstrated providing power to a OIES sensor node, and receiving sensor data, satisfying requirement 1e. Modules for optical fibre routing were vital for the system operation, and such modules were created and evaluated. The framework demonstrated through the creation of these modules was considered to satisfy requirement 1f.

Chapter 4 detailed the selection and performance evaluation of electronic sensors that were integrated throughout the modular interrogation system, satisfying requirement 1h. The sensors were included to enable module-level environmental conditions to be monitored and the data used to support system maintenance over the multi-decade duration of an experiment. All the sensors evaluated performed within the measurement requirements 1i, 1j, and 1k of: $-10\,^{\circ}\text{C}$ to $40\,^{\circ}\text{C}$ with an accuracy of $\pm 1\,^{\circ}\text{C}$; $10\,\%\text{RH}$ to $90\,\%\text{RH}$ with an accuracy of $\pm 5\,\%\text{RH}$; and $900\,\text{mbar}$ to $1100\,\text{mbar}$ with an accuracy of $\pm 5\,\text{mbar}$. Two were selected for integration into the interrogation system, between which

the three environmental parameters could be monitored.

Optical fibre temperature measurement was required using FBGs to satisfy requirement 2g, but no systematic study of long-term performance or failure modes was found. Chapter 5 details a novel experiment where three COTS FBG temperature sensors were cycled 180 times over a range of $-40\,°C$ to $100\,°C$in a 1 year period. No sensor failures were suggested during the experiment, providing confidence in their use, but a sensor lifetime prediction was not possible. This work provides evidence in support of requirement 2d for long-term stability. The technique was based on a mature technology, was chemically compatible not requiring the use of organics, and was inherently integrated with optical fibres, satisfying requirements 2a, 2b, 2c, and 2e. With the custom housings developed within Chapter 9 strain-isolated FBG sensors were possible in a length shorter than $20\,mm$, satisfying requirement 2f. Previous work reviewed in Chapter 2 provided confidence the measurement range and accuracy of $-20\,°C$ to $70\,°C$ / $\pm 1\,°C$ would satisfy requirement 2h.

A similar experiment was conducted in Chapter 6 on FFP-based barometric pressure sensors to satisfy requirement 2i. Six COTS sensors were pressure cycled in excess of 7300 times in a 1 year period, with no sensor failures discovered. As with the temperature sensors, no sensor lifetime prediction was concluded, but additional confidence in the technique was gained. As with the FBG evaluation, this work supported requirement 2d and satisfied requirements 2a, 2b, 2c, 2e, and 2f. The measurement requirement, 2j, of $0\,mbar$ to $1200\,mbar$ with an accuracy of $\pm 2\,mbar$ was considered achievable based on the literature review within Chapter 2.

Chapter 7 detailed the development of a bespoke fibre-coupled multi-pass gas cell to provide H_2O sensing capability in support of requirement 2k, and the evaluation of an optical fibre fluorescence based oxygen sensor to support requirement 2m. The gas cell was designed, manufactured, and evaluated. The design had an optical path-length of $(6.47 \pm 0.05)\,m$ and achieved a detection resolution of $(38 \pm 12)\,ppm$ with a design capability of measuring from $40\,ppm$ to $100\,000\,ppm$, satisfying requirement 2l. The design was $140\,mm$ long, was considered mechanically robust, chemically compatible, and featured a novel two-hole mirror arrangement to aid in fibre-coupling of the cell, satisfying requirements 2f, 2d, 2b, 2c, and 2e. The oxygen sensor (requirement 2n) was measured in excess of $250\,000$ times and was not found to be long-term stable, requiring frequent re-calibrations to provide accurate data. It was therefore not recommended for use within a long-term materials ageing experiment, therefore a technique to satisfy

requirement 2m was not found within this thesis. The specification of the sensor was however suitable to satisfy requirement 2n.

A technique to power electronic sensors over an optical fibre was developed, OIES, discussed in Chapter 8. The technique was demonstrated successfully using a bespoke arrangement of readily available commercial components, achieving an optical to electrical conversion efficiency of $1.9\,\%$ and satisfying requirement 2o. Further development was conducted and a revised version of the node was designed and manufactured, improving the conversion efficiency to $(24.0 \pm 0.2)\,\%$. The increase in efficiency provided higher continuous power in the node, which potentially enabled an increase in measurement frequency, and broadened the range of electronic sensing techniques that could be supported. The technique utilised SMF-28 optical fibre satisfying requirement 2p, and used a Class 1M $200\,\text{mW}$ $1310\,\text{nm}$ laser satisfying requirement 2q.

Chapter 9 described development work of optical fibre infrastructure components, that provided options to aid in the practical deployment of a long-term experiment. The techniques developed included: optical fibre hermetic sealing, fibre *internal connector*, fibre feed-throughs, sensor packaging, fibre encapsulation, and a fibre umbilical connector, to satisfy requirements 3e, 3f, 3g, 3h, and 3i. Together these techniques were seen to form enabling technologies which would be required if optical diagnostics were to be considered a practical option for future use. The techniques were designed to satisfy the project size requirement (3d) and were all below the threshold length of $160\,\text{mm}$. The umbilical connector was designed to incorporate environmental sealing and was evaluated to be user-friendly to use, satisfying requirement 2j.

All the requirements were considered satisfied, but the following were highlighted as the focus for future development:

2b Concepts that are chemically compatible with materials ageing experiments.

2c General chemical compatibility within this thesis focuses on minimal inclusion of organics and metals which may interact with oxygen and water (e.g. copper).

2m A technique to measure gaseous oxygen (O_2) concentration.

3a Concepts that are chemically compatible with materials ageing experiments.

3b General chemical compatibility within this thesis focuses on minimal inclusion of organics and metals which may interact with oxygen and water (e.g. copper).

3c Concepts with the potential to be long-term stable over multiple decades.

Requirements 2b, 2c, 3a, and 3b were not fully satisfied due to the inclusion of small quantities of organics in the FFP sensor design (adhesive) and *internal connector* multiple-fibre push-on-pull-off/mechanical transfer polished (MPO/MTP) ferrule (plastic). A technique for requirement 2m was identified, but after evaluation the specific design chosen was found not to be sufficiently long-term stable. Requirement 3c was not experimentally evaluated due to the low maturity of the Chapter 9 components, but the aim of long-term stability was included within the design of the concepts.

10.5 Future Work

This research project was intended to provide technology concepts for future development towards potential deployment. As such, potentially advantageous routes of further development are presented for each topic investigated.

The development of further interrogation modules for the modular interrogation system could expand the interrogation system beyond FBG sensing and the OIES system, to incorporate techniques such as TDLAS and/or fluorescence sensing. The modular interrogation system infrastructure could also be developed into additional module count configurations, further supporting small and medium-scale experiments.

The electronic sensors, which were embedded within the interrogation system, could benefit from an investigation of their long-term performance, to further support their use in long-term condition monitoring. It could also be advantageous to periodically investigate newer models of similar sensors that may offer performance improvements. Such sensors could be incorporated into the design as existing modules are revised, or as future modules are designed.

Further assessments of FBG and FFP sensors would benefit from monitoring a larger number of sensors in order to increase the likelihood of observing a failure. Conducting the experiments with greater environmental stability would be beneficial, to assist in the data analysis. Testing the sensors within the mechanical housings they would be deployed within, in an experiment (such as the one developed in Chapter 9), would also be worthwhile, to ensure the entire sensor system is correctly evaluated.

Further development of the near infrared (NIR) absorption spectroscopy technique could be achieved by improving the optical fibre collimator coaxial tolerances, which together with creating a TDLAS interrogation module, could improve the performance of

the technique. Investigation of chemicals of interest which could be measured within an SMF-28 fibre coupled system could also be completed to maximise the use of the gas cell once located within an experiment.

The OIES technique presented underwent a significant design revision within this project, but further improvements to the conversion efficiency are likely possible. The inclusion of energy storage capacitors within the revised system topology, could potentially enable the use of higher-power sensing techniques such as metal oxide chemical and non-dispersive infrared (NDIR) gas sensors. Use of such sensors could provide a valuable technique to measure gaseous species otherwise difficult to measure by absorption spectroscopy via NIR optical fibres.

Future development of the solder seal technique could improve consistency of the seal and ensure removal of potentially trapped flux chemicals. The long-term reliability of the seal could also be further assessed. Further work on the *internal connector* could develop a single-use push-fit variant that could enable use within confined spaces. The feed-through technique could be experimentally evaluated and potentially further developed to reduce the size of the design. Due to the removable nature of the fibre tube from the feed-through, commercial production of the solder-seal within the tube could also be investigated. The sensor packaging technique could benefit from the experimental assembly of a combined temperature and pressure node for evaluation. Miniaturisation of the housing would be a potential avenue for further development, as would investigating integration into the spectroscopic gas cell. Further evaluation of the fibre encapsulation technique could benefit from heat-sealing the Kapton film around the optical fibres. A full evaluation of the chemical compatibility of the technique could then be experimentally assessed. Alternative options such as metal coatings of fibres could also be investigated. The umbilical connector could be experimentally evaluated if it were manufactured in metal. The optical performance, mechanical robustness, operation across a range of environments, and long- term use could be evaluated.

From this thesis multiple avenues for further development have been identified, and would be required before a mature diagnostic system is available to AWE. At the time of writing, many of the techniques have started further investigation though two part-AWE funded PhD projects based at Heriot-Watt University, which are focusing on optical fibre infrastructure components and optical sensors.

Part V

Appendices

Appendix A: Technology Readiness Levels

The Ministry of Defence (MOD) definition of TRLs from their framework agreement for technical support (FATS) [303, 304] are provided in table A.1 for reference. These definitions were used when assigning the appropriate TRL of the hardware concepts developed and evaluated within this project.

TRLs are typically used as a measure of technical risk, but the risk would only be realised if the proposed technology were introduced operationally at that time.

TRLs relate to individual technologies, and do not suggest the individual technologies could be integrated and work together.

The TRL does not indicate that the technology is right for the job or that application of the technology will result in successful development of the system [305].

	Title	Description
1	Basic principles observed and reported	Lowest level of technology readiness. Scientific research begins to be evaluated for military applications. Examples might include paper studies of a technology's basic properties
2	Technology concept and/or application formulated	Invention begins. Once basic principles are observed, practical applications can be postulated. The application is speculative and there is no proof or detailed analysis to support the assumptions. Examples are still limited to paper studies
3	Analytical and experimental critical function and/or characteristic proof-of-concept	Analytical studies and laboratory studies to physically validate analytical predictions of separate elements of the technology are undertaken. Examples include components that are not yet integrated or representative
4	Technology component and/or basic technology sub-system validation in laboratory environment	Basic technology components are integrated. This is relatively "low fidelity" compared to the eventual system. Examples include integration of "ad hoc" hardware in a laboratory
5	Technology component and/or basic sub-system validation in relevant environment	Fidelity of sub-system representation increases significantly. The basic technological components are integrated with realistic supporting elements so that the technology can be tested in a simulated environment. Examples include "high fidelity" laboratory integration of components
6	Technology system/subsystem model or prototype demonstration in a relevant environment	Representative model or prototype system, which is well beyond the representation tested for TRL 5, is tested in a relevant environment. Represents a major step up in a technology's demonstrated readiness. Examples include testing a prototype in a high fidelity laboratory environment or in simulated operational environment
7	Technology system prototype demonstration in an operational environment	Prototype near or at planned operational system. Represents a major step up from TRL 6, requiring the demonstration of an actual system prototype in an operational environment, such as in an aircraft or vehicle. Information to allow supportability assessments is obtained. Examples include testing the prototype in a test bed aircraft
8	Actual technology system completed and qualified through test and demonstration	Technology has been proven to work in its final form and under expected conditions. In almost all cases, this TRL represents the end of Demonstration. Examples include test and evaluation of the system in its intended weapon system to determine if it meets design specifications, including those relating to supportability
9	Actual technology system qualified through reliability and maintainability demonstration in service	Application of the technology in its final form and under mission conditions, such as those encountered in operational test and evaluation and reliability trials. Examples include using the system under operational mission conditions

Table A.1: Technology readiness level definitions used within the evaluation of hardware within this project.

Bibliography

[1] A. A. Milne, *Winnie-the-Pooh* (Methuen & Company, Ltd., London, 1926).

[2] W. M. Haynes, D. Lide, and T. Bruno, eds., *Handbook of Chemistry and Physics* (CRC Press, Boca Raton, FL, 2015), 96th ed.

[3] T. C. Dyer, W. N. MacPherson, and S. J. Brooks, *Optical Fibre Connector* (UK Patent Application: GB1820122, 2018).

[4] T. C. Dyer, W. N. MacPherson, S. J. Brooks, and S. McCulloch, "Accelerated Through-Life Performance Evaluation of Fibre Fabry-Pérot Pressure Sensors," in "26th International Conference on Optical Fiber Sensors," (OSA, 2018), p. TuE33. Available: dx.doi.org/10.1364/OFS.2018.TuE33.

[5] K. O'Nions, R. Pitman, and C. Marsh, "Science of nuclear warheads," Nature **415**, 853–857 (2002). Available: dx.doi.org/10.1038/415853a.

[6] B. T. Goodwin and G. Mara, "Stewarding a Reduced Stockpile," Tech. rep., Lawrence Livermore National Laboratory, https://www.lanl.gov/conferences/sw/2009/docs/stewarding_reduced_stockpile.pdf (2008).

[7] S. McCulloch, G. Burnell, T. Boon, R. R. J. Maier, J. Barton, P. Harrison, E. Rigg, and J. Jones, "Long-term reliability requirements of fiber optic systems for remote sensing applications," in "Proc. SPIE 5465, Reliability of Optical Fibre Components, Devices, Systems, and Networks II," , H. G. Limberger and M. J. Matthewson, eds. (2004), pp. 84–91. Available: dx.doi.org/10.1117/12.546010.

[8] P. Horowitz, W. Hill, and T. C. Hayes, *The art of electronics* (Cambridge University Press, New York, NY, 2015), 3rd ed.

[9] P. R. N. Childs, J. R. Greenwood, and C. A. Long, "Review of temperature measurement," Review of Scientific Instruments **71**, 2959–2978 (2000). Available: dx.doi.org/10.1063/1.1305516.

[10] Z. Zhang, P. Sun, T. Pang, H. Xia, X. Cui, Z. Li, L. Han, B. Wu, Y. Wang, M. W. Sigrist, and F. Dong, "Reconstruction of combustion temperature and gas concentration distributions using line-of-sight tunable diode laser absorption spectroscopy," Optical Engineering **55**, 076107 (2016). Available: dx.doi.org/10.1117/1.OE.55.7.076107.

[11] C. S. Goldenstein, C. L. Strand, I. A. Schultz, K. Sun, J. B. Jeffries, and R. K. Hanson, "Fitting of calibration-free scanned-wavelength-modulation spectroscopy spectra for determination of gas properties and absorption lineshapes," Applied Optics **53**, 356 (2014). Available: dx.doi.org/10.1364/AO.53.000356.

[12] C. S. Goldenstein, R. Spearrin, J. B. Jeffries, and R. K. Hanson, "Infrared laser-absorption sensing for combustion gases," Progress in Energy and Combustion Science **60**, 132–176 (2017). Available: dx.doi.org/10.1016/j.pecs.2016.12.002.

[13] Y. Rao, "In-fibre Bragg grating sensors," Measurement Science and Technology **8**, 355–375 (1997). Available: dx.doi.org/10.1088/0957-0233/8/4/002.

[14] F. M. Haran, J. K. Rew, and P. D. Foote, "A strain-isolated fibre Bragg grating sensor for temperature compensation of fibre Bragg grating strain sensors," Measurement Science and Technology **9**, 1163–1166 (1998). Available: dx.doi.org/10.1088/0957-0233/9/8/004.

[15] AWE, "Private communication," (2016).

[16] J. M. López-Higuera, ed., *Handbook of optical fibre sensing technology* (John Wiley & Sons, 2002).

[17] E. Shafir, G. Berkovic, Y. Sadi, S. Rotter, and S. Gali, "Practical strain isolation in embedded fiber Bragg gratings," Smart Materials and Structures **14**, N26–N28 (2005). Available: dx.doi.org/10.1088/0964-1726/14/4/N04.

[18] Smart Fibres (UK), *SmartTemp FBG Temperature Sensors* (Technical Datasheet, 2016).

[19] Micron Optics (USA), *Temperature Probe os4200* (Technical Datasheet, 2018).

[20] Smart Fibres (UK), *SmartScan Interrogator* (Technical Datasheet, 2018).

[21] Micron Optics (USA), *Static Optical Sensing Interrogator - sm125* (Technical Datasheet, 2015).

[22] Micron Optics (USA), *Temperature Compensation Sensor os4100* (Technical Datasheet, 2018).

[23] G. M. H. Flockhart, R. R. J. Maier, J. S. Barton, W. N. MacPherson, J. D. C. Jones, K. E. Chisholm, L. Zhang, I. Bennion, I. Read, and P. D. Foote, "Quadratic behavior of fiber Bragg grating temperature coefficients," Applied Optics **43**, 2744 (2004). Available: dx.doi.org/10.1364/AO.43.002744.

[24] S. J. Mihailov, "Fiber Bragg Grating Sensors for Harsh Environments," Sensors **12**, 1898–1918 (2012). Available: dx.doi.org/10.3390/s120201898.

[25] K. Grattan and T. Sun, "Fiber optic sensor technology: an overview," Sensors and Actuators A: Physical **82**, 40–61 (2000). Available: dx.doi.org/10.1016/S0924-4247(99)00368-4.

[26] A.D. Kersey, M. Davis, H. J. Patrick, M. LeBlanc, K. P. Koo, C. G. Askins, M. Putnam, E. J. Friebele, A. Kersey, M. Davis, H. J. Patrick, M. LeBlanc, K. P. Koo, C. G. Askins, M. Putnam, and E. J. Friebele, "Fiber grating sensors," Journal of Lightwave Technology **15**, 1442–1463 (1997). Available: dx.doi.org/10.1109/50.618377.

[27] F. M. Araújo, L. A. Ferreira, J. L. Santos, and F. Farahi, "Temperature and strain insensitive bending measurements with D-type fibre Bragg gratings," Measurement Science and Technology **12**, 829–833 (2001). Available: dx.doi.org/10.1088/0957-0233/12/7/314.

[28] H.-N. Li, D.-S. Li, and G.-B. Song, "Recent applications of fiber optic sensors to health monitoring in civil engineering," Engineering Structures **26**, 1647–1657 (2004). Available: dx.doi.org/10.1016/j.engstruct.2004.05.018.

[29] J.-S. Heo, J.-H. Chung, and J.-J. Lee, "Tactile sensor arrays using fiber Bragg grating sensors," Sensors and Actuators A: Physical **126**, 312–327 (2006). Available: dx.doi.org/10.1016/j.sna.2005.10.048.

[30] M. Prabhugoud and K. J. Peters, "Efficient interpretation algorithm for embedded Bragg gratings for damage detection in composites," in "Proceedings Volume 5050, Smart Structures and Materials 2003: Smart Sensor Technology and Measurement Systems," , vol. 5050, D. Inaudi and E. Udd, eds. (2003), p. 159. Available: dx.doi.org/10.1117/12.484223.

[31] S. T. Kreger, D. K. Gifford, M. E. Froggatt, B. J. Soller, and M. S. Wolfe, "High Resolution Distributed Strain or Temperature Measurements in Single- and Multi-Mode Fiber Using Swept-Wavelength Interferometry," in "Optical Fiber Sensors," (OSA, 2006), p. ThE42. Available: dx.doi.org/10.1364/OFS.2006.ThE42.

[32] K. Kim and C. Chung, "Fiber Bragg Grating Sensor System for Dynamic Strain Measurement without Optical Filters," in "Proc. SPIE 5050, Smart Structures and Materials 2003: Smart Sensor Technology and Measurement Systems," (2003), pp. 152–158.

[33] W. R. Habel, K. Krebber, and W. Daum, "Standardization in fiber-optic sensing for structural safety: activities in the ISHMII and IEC," in "Proc. SPIE 9436: Smart Sensor Phenomena, Technology, Networks, and Systems Integration," , vol. 9436, K. J. Peters, ed. (2015), p. 94360S. Available: dx.doi.org/10.1117/12.2185602.

[34] D. Sporea, A. Stăncalie, D. Neguţ, G. Pilorget, S. Delepine-Lesoille, and L. Lablonde, "Comparative study of long period and fiber Bragg gratings under gamma irradiation," Sensors and Actuators A: Physical **233**, 295–301 (2015). Available: dx.doi.org/10.1016/j.sna.2015.07.007.

[35] A. Othonos, K. Kalli, D. Pureur, and A. Mugnier, *Wavelength Filters in Fibre Optics*, vol. 123 of *Springer Series in Optical Sciences* (Springer Berlin Heidelberg, 2006). Available: dx.doi.org/10.1007/3-540-31770-8.

[36] G. a. Cranch, G. M. H. Flockhart, and C. K. Kirkendall, "Efficient large-scale multiplexing of fiber Bragg grating and fiber Fabry-Perot sensors for structural health monitoring applications," in "Proc. SPIE 6179," , N. Meyendorf, G. Y. Baaklini, and B. Michel, eds. (2006), p. 61790P. Available: dx.doi.org/10.1117/12.657416.

[37] A. D. Kersey, W. W. Morey, and T. A. Berkoff, "Fiber-optic Bragg grating strain sensor with drift-compensated high-resolution interferometric wavelength-shift detection," Optics Letters **18**, 72 (1993). Available: dx.doi.org/10.1364/OL.18.000072.

[38] B. Moslehi, R. J. Black, J. M. Costa, E. H. Edwards, F. Faridian, and V. Sotoudeh, "Fast fiber Bragg grating interrogation system with scalability to support monitoring of large structures in harsh environments," in "Proc. SPIE 9062, Smart Sensor Phenomena, Technology, Networks, and Systems Integration,"

, W. Ecke, K. J. Peters, N. G. Meyendorf, and T. E. Matikas, eds. (2014), p. 906215. Available: dx.doi.org/10.1117/12.2058221.

[39] A. Hongo, K. Fukuchi, S. Kojima, and N. Takeda, "Embedded small-diameter fiber Bragg grating sensors and high speed wavelength detection," Proc. SPIE 5050, Smart Structures and Materials 2003: Smart Sensor Technology and Measurement Systems pp. 144–151 (2003). Available: dx.doi.org/10.1117/12.484249.

[40] Y. Yoon, S. Chung, M. Kim, W. Il, and B. Lee, "Vibration detection for a composite smart structure embedded with a fiber grating sensor," in "Proceedings Volume 5050, Smart Structures and Materials 2003: Smart Sensor Technology and Measurement Systems," , vol. 5050 (2003), pp. 350–357.

[41] R. J. Black, J. M. Costa, B. Moslehi, L. Zarnescu, D. Hackney, and K. Peters, "Fiber optic temperature profiling for thermal protection heat shields," in "Proceedings Volume 9062, Smart Sensor Phenomena, Technology, Networks, and Systems Integration," , vol. 9062 (2014), p. 906204. Available: dx.doi.org/10.1117/12.2057942.

[42] T. Chan, L. Yu, H. Tam, Y. Ni, S. Liu, W. Chung, and L. Cheng, "Fiber Bragg grating sensors for structural health monitoring of Tsing Ma bridge: Background and experimental observation," Engineering Structures **28**, 648–659 (2006). Available: dx.doi.org/10.1016/j.engstruct.2005.09.018.

[43] J. Grant, R. Kaul, S. Taylor, G. Myer, K. Jackson, A. Osei, and A. Sharma, "Distributed Sensing of Carbon-Epoxy Composites and Filament Wound Pressure Vessels Using Fiber-Bragg Gratings," Proc. SPIE 5050, Smart Structures and Materials 2003: Smart Sensor Technology and Measurement Systems pp. 187–196 (2003). Available: dx.doi.org/10.1117/12.484236.

[44] M. Majumder, T. K. Gangopadhyay, A. K. Chakraborty, K. Dasgupta, and D. Bhattacharya, "Fibre Bragg gratings in structural health monitoring—Present status and applications," Sensors and Actuators A: Physical **147**, 150–164 (2008). Available: dx.doi.org/10.1016/j.sna.2008.04.008.

[45] G. A. Cranch and G. M. Flockhart, "Tools for synthesising and characterising Bragg grating structures in optical fibres and waveguides," Journal of Modern Optics **59**, 493–526 (2012). Available: dx.doi.org/10.1080/09500340.2011.646332.

[46] K. Wang, B. Wang, B. Yan, X. Sang, J. Yuan, and G. D. Peng, "Simultaneous measurement of absolute strain and differential strain based on fiber Bragg grating Fabry-Perot sensor," Optics Communications **307**, 101–105 (2013). Available: dx.doi.org/10.1016/j.optcom.2013.06.015.

[47] D. Kinet, P. Mégret, K. Goossen, L. Qiu, D. Heider, and C. Caucheteur, "Fiber Bragg Grating Sensors toward Structural Health Monitoring in Composite Materials: Challenges and Solutions," Sensors **14**, 7394–7419 (2014). Available: dx.doi.org/10.3390/s140407394.

[48] D. Havermann, J. Mathew, W. N. MacPherson, R. R. J. Maier, and D. P. Hand, "In-situ measurements with fibre Bragg gratings embedded in stainless steel," in "Proc. SPIE 9157, 23rd International Conference on Optical Fiber Sensors," , J. M.

López-Higuera, J. D. C. Jones, M. López-Amo, and J. L. Santos, eds. (2014), p. 9157A1. Available: dx.doi.org/10.1117/12.2059587.

[49] B. Lee, "Review of the present status of optical fiber sensors," Optical Fiber Technology **9**, 57–79 (2003). Available: dx.doi.org/10.1016/S1068-5200(02)00527-8.

[50] D. Havermann, J. Mathew, W. N. MacPherson, R. R. J. Maier, and D. P. Hand, "Temperature and Strain Measurements With Fiber Bragg Gratings Embedded in Stainless Steel 316," Journal of Lightwave Technology **33**, 2474–2479 (2015). Available: dx.doi.org/10.1109/JLT.2014.2366835.

[51] A. Barrias, J. Casas, and S. Villalba, "A Review of Distributed Optical Fiber Sensors for Civil Engineering Applications," Sensors **16**, 748 (2016). Available: dx.doi.org/10.3390/s16050748.

[52] M. Jinesh, W. N. MacPherson, D. P. Hand, and R. R. J. Maier, "Stainless steel component with compressed fiber Bragg grating for high temperature sensing applications," in "Proceedings Volume 9916, Sixth European Workshop on Optical Fibre Sensors," , vol. 9916 (2016), p. 99160J. Available: dx.doi.org/10.1117/12.2236499.

[53] G. Cranch, G. Flockhart, and C. Kirkendall, "Efficient fiber Bragg grating and fiber fabry-Perot sensor multiplexing scheme using a broadband pulsed mode-locked laser," Journal of Lightwave Technology **23**, 3798–3807 (2005). Available: dx.doi.org/10.1109/JLT.2005.857735.

[54] W. N. MacPherson, S. R. Kidd, J. S. Barton, and J. D. C. Jones, "Phase demodulation on optical fibre Fabry-Perot sensors with inexact phase steps," IEE Proc. Optoelectron. **144**, 130–133 (1997).

[55] M. Gander, W. MacPherson, J. Barton, R. Reuben, J. Jones, R. Stevens, K. Chana, S. Anderson, and T. Jones, "Embedded micromachined fiber-optic fabry-perot pressure sensors in aerodynamics applications," IEEE Sensors Journal **3**, 102–107 (2003). Available: dx.doi.org/10.1109/JSEN.2003.810099.

[56] W. N. MacPherson, J. M. Kilpatrick, J. S. Barton, and J. D. C. Jones, "Miniature fiber optic pressure sensor for turbomachinery applications," Review of Scientific Instruments **70**, 1868 (1999). Available: dx.doi.org/10.1063/1.1149682.

[57] J. M. Kilpatrick, W. N. MacPherson, J. S. Barton, J. D. C. Jones, D. R. Buttsworth, T. V. Jones, K. S. Chana, and S. J. Anderson, "Measurement of unsteady gas temperature with optical fibre Fabry-Perot microsensors," Measurement Science and Technology **13**, 706–712 (2002). Available: dx.doi.org/10.1088/0957-0233/13/5/308.

[58] É. Pinet, "Fabry-Pérot Fiber-Optic Sensors for Physical Parameters Measurement in Challenging Conditions," Journal of Sensors **2009**, 1–9 (2009). Available: dx.doi.org/10.1155/2009/720980.

[59] A. Wang, H. Xiao, J. Wang, Z. Wang, W. Zhao, and R. May, "Self-calibrated interferometric-intensity-based optical fiber sensors," Journal of Lightwave Technology **19**, 1495–1501 (2001). Available: dx.doi.org/10.1109/50.956136.

[60] O. Schneller, J. Mathew, W. N. MacPherson, and R. R. J. Maier, "High temperature sensor based on an in-fibre Fabry-Perot cavity," in "Proc. SPIE 9157, 23rd International Conference on Optical Fibre Sensors," , J. M. López-Higuera, J. D. C. Jones, M. López-Amo, and J. L. Santos, eds. (2014), p. 91578L. Available: dx.doi.org/10.1117/12.2059651.

[61] H. Bae, D. Yun, H. Liu, D. A. Olson, and M. Yu, "Hybrid miniature fabry-perot sensor with dual optical cavities for simultaneous pressure and temperature measurements," Journal of Lightwave Technology **32**, 1585–1593 (2014). Available: dx.doi.org/10.1109/JLT.2014.2308060.

[62] D. Polyzos, M. Jinesh, W. N. MacPherson, and R. R. J. Maier, "Long-term stability testing of optical fibre Fabry-Perot temperature sensors," in "Proceedings of SPIE - The International Society for Optical Engineering," , vol. 9852, E. Udd, G. Pickrell, and H. H. Du, eds. (2016), p. 985218. Available: dx.doi.org/10.1117/12.2223889.

[63] FISO (Canada), *Nortech TPT - 62* (Technical Datasheet, 2019).

[64] Opsens (Canada), *Fiber optic temperature sensor OTP-A* (Technical Datasheet, 2019).

[65] X. Wang, O. S. Wolfbeis, and R. J. Meier, "Luminescent probes and sensors for temperature." Chemical Society reviews **42**, 7834–69 (2013). Available: dx.doi.org/10.1039/c3cs60102a.

[66] K. S. Krane, *Modern Physics* (John Wiley & Sons, Oxford, 1983).

[67] W. Godbey, "Fluorescence," in "An Introduction to Biotechnology," (Elsevier, Cambridge, 2014), pp. 173–186. Available: dx.doi.org/10.1016/B978-1-907568-28-2.00008-3.

[68] F. Vetrone, R. Naccache, A. Zamarron, A. Juarranz de la Fuente, F. Sanz-Rodriguez, L. Martinez Maestro, E. Martin Rodriguez, D. Jaque, J. Garcia Sole, and J. A. Capobianco, "Temperature Sensing Using Fluorescent Nanothermometers," ACS Nano **4**, 3254–3258 (2010). Available: dx.doi.org/10.1021/nn100244a.

[69] P. Kolodner and J. A. Tyson, "Remote thermal imaging with 0.7-μm spatial resolution using temperature-dependent fluorescent thin flims," Applied Physics Letters **42**, 117–119 (1983).

[70] F. Venturini, R. Bürgi, S. Borisov, and I. Klimant, "Optical temperature sensing using a new thermographic phosphor," Sensors and Actuators A: Physical **233**, 324–329 (2015). Available: dx.doi.org/10.1016/j.sna.2015.07.009.

[71] Z. Ding, C. Wang, K. Liu, J. Jiang, D. Yang, G. Pan, Z. Pu, and T. Liu, "Distributed Optical Fiber Sensors Based on Optical Frequency Domain Reflectometry: A review," Sensors **18**, 1072 (2018). Available: dx.doi.org/10.3390/s18041072.

[72] R. R. J. Maier, W. N. MacPherson, J. S. Barton, S. McCulloch, and B. J. S. Jones, "Distributed sensing using Rayleigh scatter in polarization-maintaining fibres for transverse load sensing," Measurement Science and Technology **21**, 094019 (2010). Available: dx.doi.org/10.1088/0957-0233/21/9/094019.

[73] M. Froggatt and J. Moore, "High-spatial-resolution distributed strain measurement in optical fiber with Rayleigh scatter," Applied Optics **37**, 1735 (1998). Available: dx.doi.org/10.1364/AO.37.001735.

[74] J. Song, W. Li, P. Lu, Y. Xu, L. Chen, and X. Bao, "Long-Range High Spatial Resolution Distributed Temperature and Strain Sensing Based on Optical Frequency-Domain Reflectometry," IEEE Photonics Journal **6** (2014). Available: dx.doi.org/10.1109/JPHOT.2014.2320742.

[75] Y. Koyamada, M. Imahama, K. Kubota, and K. Hogari, "Fiber-Optic Distributed Strain and Temperature Sensing With Very High Measurand Resolution Over Long Range Using Coherent OTDR," Journal of Lightwave Technology **27**, 1142–1146 (2009). Available: dx.doi.org/10.1109/JLT.2008.928957.

[76] E. Li, "Rayleigh scattering based distributed optical fiber sensing," in "AOPC 2017: Fiber Optic Sensing and Optical Communications," , L. Wei, W. Zhang, D. Jiang, W. Wang, K. T. Grattan, Y. Liao, and Z.-S. Zhao, eds. (SPIE, 2017), p. 97. Available: dx.doi.org/10.1117/12.2285293.

[77] X. Bao and L. Chen, "Recent Progress in Distributed Fiber Optic Sensors," Sensors **12**, 8601–8639 (2012). Available: dx.doi.org/10.3390/s120708601.

[78] D. Zhou, W. Li, L. Chen, and X. Bao, "Distributed Temperature and Strain Discrimination with Stimulated Brillouin Scattering and Rayleigh Backscatter in an Optical Fiber," Sensors **13**, 1836–1845 (2013). Available: dx.doi.org/10.3390/s130201836.

[79] R. Regier and N. Hoult, "Distributed strain monitoring for bridges: temperature effects," in "Proc. SPIE 9061, Sensors and Smart Structures Technologies for Civil, Mechanical, and Aerospace Systems," , vol. 9061, J. P. Lynch, K.-W. Wang, and H. Sohn, eds. (2014), p. 906131. Available: dx.doi.org/10.1117/12.2045428.

[80] Z. Ding, D. Yang, Y. Du, K. Liu, Y. Zhou, R. Zhang, Z. Xu, J. Jiang, and T. Liu, "Distributed Strain and Temperature Discrimination Using Two Types of Fiber in OFDR," IEEE Photonics Journal **8**, 1–8 (2016). Available: dx.doi.org/10.1109/JPHOT.2016.2605011.

[81] X. Bao, W. Li, Z. Qin, and L. Chen, "OTDR and OFDR for distributed multi-parameter sensing," in "Proc. SPIE 9062, Smart Sensor Phenomena, Technology, Networks, and Systems Integration," , vol. 9062, W. Ecke, K. J. Peters, N. G. Meyendorf, and T. E. Matikas, eds. (2014), p. 906202. Available: dx.doi.org/10.1117/12.2045807.

[82] A. J. Rogers, "Distributed optical-fibre sensors," Journal of Physics D: Applied Physics **19**, 2237–2255 (1986). Available: dx.doi.org/10.1088/0022-3727/19/12/004.

[83] D. Zhou, Z. Qin, W. Li, L. Chen, and X. Bao, "Distributed vibration sensing with time-resolved optical frequency-domain reflectometry," Optics Express **20**, 13138 (2012). Available: dx.doi.org/10.1364/OE.20.013138.

[84] S. Rizzolo, A. Boukenter, E. Marin, M. Cannas, J. Perisse, S. Bauer, J.-R. Mace, Y. Ouerdane, and S. Girard, "Vulnerability of OFDR-based distributed sensors to high γ-ray doses," Optics Express **23**, 18997 (2015). Available: dx.doi.org/10.1364/OE.23.018997.

[85] Luna (USA), *ODiSI 6000 Series* (Technical Datasheet, 2019).

[86] FBGS (Germany), *Temperature Probe TP-01* (Technical Datasheet, 2018).

[87] É. Pinet, "Pressure measurement with fiber-optic sensors: commercial technologies and applications," in "21st International Conference on Optical Fiber Sensors," , vol. 7753, W. J. Bock, J. Albert, and X. Bao, eds. (2011), p. 775304. Available: dx.doi.org/10.1117/12.895536.

[88] L. C. Philippe and R. K. Hanson, "Laser diode wavelength-modulation spectroscopy for simultaneous measurement of temperature, pressure, and velocity in shock-heated oxygen flows," Applied Optics **32**, 6090 (1993). Available: dx.doi.org/10.1364/AO.32.006090.

[89] C. S. Goldenstein, R. M. Spearrin, J. B. Jeffries, and R. K. Hanson, "Infrared laser absorption sensors for multiple performance parameters in a detonation combustor," Proceedings of the Combustion Institute **35**, 3739–3747 (2015). Available: dx.doi.org/10.1016/j.proci.2014.05.027.

[90] FISO (Canada), *FOP-M Pressure Sensor* (Technical Datasheet, 2006).

[91] Opsens (Canada), *Fibre Optic Pressure Sensor OPP-B* (Technical Datasheet, 2019).

[92] S. Watson, W. N. MacPherson, J. S. Barton, J. D. C. Jones, A. Tyas, A. V. Pichugin, A. Hindle, W. Parkes, C. Dunare, and T. Stevenson, "Investigation of shock waves in explosive blasts using fibre optic pressure sensors," Journal of Physics: Conference Series **15**, 226–231 (2005). Available: dx.doi.org/10.1088/1742-6596/15/1/038.

[93] J. Wang, M. Wang, J. Xu, L. Peng, M. Yang, M. Xia, and D. Jiang, "Underwater blast wave pressure sensor based on polymer film fiber Fabry–Perot cavity," Applied Optics **53**, 6494 (2014). Available: dx.doi.org/10.1364/AO.53.006494.

[94] M. Chavko, W. A. Koller, W. K. Prusaczyk, and R. M. McCarron, "Measurement of blast wave by a miniature fiber optic pressure transducer in the rat brain," Journal of Neuroscience Methods **159**, 277–281 (2007). Available: dx.doi.org/10.1016/j.jneumeth.2006.07.018.

[95] W. Parkes, V. Djakov, J. S. Barton, S. Watson, W. N. MacPherson, J. T. M. Stevenson, and C. C. Dunare, "Design and fabrication of dielectric diaphragm pressure sensors for applications to shock wave measurement in air," Journal of Micromechanics and Microengineering **17**, 1334–1342 (2007). Available: dx.doi.org/10.1088/0960-1317/17/7/016.

[96] E. Cibula, S. Pevec, B. Lenardic, E. Pinet, and D. Donlagic, "Miniature all-glass robust pressure sensor," Optics Express **17**, 5098 (2009). Available: dx.doi.org/10.1364/OE.17.005098.

[97] H.-Y. Ling, K.-T. Lau, and L. Cheng, "Determination of dynamic strain profile and delamination detection of composite structures using embedded multiplexed fibre-optic sensors," Composite Structures **66**, 317–326 (2004). Available: dx.doi.org/10.1016/j.compstruct.2004.04.054.

[98] R. R. J. Maier, J. S. Barton, J. D. C. Jones, S. McCulloch, and G. Burnell, "Dual-fibre Bragg grating sensor for barometric pressure measurement," Measurement Science and Technology **14**, 2015–2020 (2003). Available: dx.doi.org/10.1088/0957-0233/14/11/021.

[99] J. Hodgkinson and R. P. Tatam, "Optical gas sensing: a review," Measurement Science and Technology **24**, 012004 (2013). Available: dx.doi.org/10.1088/0957-0233/24/1/012004.

[100] AWE, "Private communication," (2017).

[101] R. Sur, K. Sun, J. B. Jeffries, R. K. Hanson, R. J. Pummill, T. Waind, D. R. Wagner, and K. J. Whitty, "TDLAS-based sensors for in situ measurement of syngas composition in a pressurized, oxygen-blown, entrained flow coal gasifier," Applied Physics B **116**, 33–42 (2014). Available: dx.doi.org/10.1007/s00340-013-5644-6.

[102] A. Chighine, E. Fisher, D. Wilson, M. Lengden, W. Johnstone, and H. McCann, "An FPGA-based lock-in detection system to enable Chemical Species Tomography using TDLAS," in "2015 IEEE International Conference on Imaging Systems and Techniques (IST)," (IEEE, 2015), pp. 1–5. Available: dx.doi.org/10.1109/IST.2015.7294460.

[103] B. Li, C. Zheng, H. Liu, Q. He, W. Ye, Y. Zhang, J. Pan, and Y. Wang, "Development and measurement of a near-infrared CH4 detection system using 1.654μm wavelength-modulated diode laser and open reflective gas sensing probe," Sensors and Actuators B: Chemical **225**, 188–198 (2016). Available: dx.doi.org/10.1016/j.snb.2015.11.037.

[104] A. Seidel, S. Wagner, A. Dreizler, and V. Ebert, "Robust, spatially scanning, open-path TDLAS hygrometer using retro-reflective foils for fast tomographic 2-D water vapor concentration field measurements," Atmospheric Measurement Techniques **8**, 2061–2068 (2015). Available: dx.doi.org/10.5194/amt-8-2061-2015.

[105] D. A. Knox, A. K. King, E. D. McNaghten, S. J. Brooks, P. A. Martin, and S. M. Pimblott, "Novel utilisation of a circular multi-reflection cell applied to materials ageing experiments," Applied Physics B **119**, 55–64 (2015). Available: dx.doi.org/10.1007/s00340-015-6008-1.

[106] A. Pogány, S. Wagner, O. Werhahn, and V. Ebert, "Development and metrological characterization of a tunable diode laser absorption spectroscopy (TDLAS) spectrometer for simultaneous absolute measurement of carbon dioxide and water vapor," Applied Spectroscopy **69**, 257–268 (2015). Available: dx.doi.org/10.1366/14-07575.

[107] J. Chen, A. Hangauer, R. Strzoda, and M.-C. Amann, "Laser spectroscopic oxygen sensor using diffuse reflector based optical cell and advanced signal processing," Applied Physics B **100**, 417–425 (2010). Available: dx.doi.org/10.1007/s00340-010-3956-3.

[108] A. O'Keefe and D. A. G. Deacon, "Cavity ring-down optical spectrometer for absorption measurements using pulsed laser sources," Review of Scientific Instruments **59**, 2544 (1988). Available: dx.doi.org/10.1063/1.1139895.

[109] I. G. E. Gore, N. Branch, T. Roman, E. Orange, K. Wayne, and R. A. Gore, *Ring-Down Cavity Spectroscopy Cell Using Continious Wave Excitation For Trace Species Detection* (US Patent: US005485919A, 1998).

[110] P. Zalicki and R. N. Zare, "Cavity ring-down spectroscopy for quantitative absorption measurements," The Journal of Chemical Physics **102**, 2708 (1995). Available: dx.doi.org/10.1063/1.468647.

[111] G. Berden, R. Peeters, and G. Meijer, "Cavity ring-down spectroscopy: Experimental schemes and applications," International Reviews in Physical Chemistry **19**, 565–607 (2000). Available: dx.doi.org/10.1080/014423500750040627.

[112] M. Levenson, B. Paldus, T. Spence, C. Harb, J. Harris Jr, and R. Zare, "Optical heterodyne detection in cavity ring-down spectroscopy," Chemical Physics Letters **290**, 335–340 (1998). Available: dx.doi.org/10.1016/S0009-2614(98)00500-4.

[113] E. Crosson, "A cavity ring-down analyzer for measuring atmospheric levels of methane, carbon dioxide, and water vapor," Applied Physics B **92**, 403–408 (2008). Available: dx.doi.org/10.1007/s00340-008-3135-y.

[114] P. B. Tarsa, P. Rabinowitz, and K. K. Lehmann, "Evanescent field absorption in a passive optical fiber resonator using continuous-wave cavity ring-down spectroscopy," Chemical Physics Letters **383**, 297–303 (2004). Available: dx.doi.org/10.1016/j.cplett.2003.11.043.

[115] M. C. Farries, A. M. Shaw, J. Fisk, and L. Garvey, "Detection of low chemical concentrations by cavity ring-down in an evanescently coupled fused optical fibre taper," in "Proc. SPIE 5617, Optically Based Biological and Chemical Sensing for Defence," , J. C. Carrano and A. Zukauskas, eds. (2004), p. 334. Available: dx.doi.org/10.1117/12.578549.

[116] Thorlabs (USA), *PRO8000* (Instruction Manual, 2017).

[117] Ibsen Photonics (Denmark), *I-MON High Speed Interrogation Monitors for FBG Sensor Systems* (Technical Datasheet, 2019).

[118] Prime Photonics (USA), *VectorLight 300* (Technical Datasheet, 2016).

[119] Smart Fibres (UK), *W4 WDM Laser Interrogator* (Technical Datasheet, 1994).

[120] Micron Optics (USA), *HYPERION Optical Sensing Instrument* (Technical Datasheet, 2016).

[121] Smart Fibres (UK), *SmartScope Interrogator* (Technical Datasheet, 1994).

[122] Y. Bao, D. Daugherty, K. Hsu, T. Q. Y. Li, C. M. Miller, and J. W. Miller, *Calibrated swept-wavelength laser and interrogator system for testing wavelength-division multiplexing system* (US Patent: US006449047B1, 2002).

[123] Y. Dai, G. Deng, J. Leng, and A. Asundi, "Time division multiplexing of FBG sensor system," in "Proc. SPIE 7375, International Conference on Experimental Mechanics," , X. He, H. Xie, and Y. Kang, eds. (2008), p. 73754J. Available: dx.doi.org/10.1117/12.839309.

[124] D. A. Knox, "High Resolution Gas Phase Spectroscopy At Solid / Solid Interfacial Regions," Phd, Manchester University (2015).

[125] Mettler-Toledo (USA), *GPro 500 TDL Series Compact Spectrometer with Versatile Process Adaptions* (Technical Datasheet, 2018).

[126] A. Brillant, *Digital and Analog Fiber Optic Communications for CATV and FTTx Applications* (SPIE, Bellingham, 2008). Available: dx.doi.org/10.1117/3.732502.

[127] J. Liu, Y. Li, and H. Zhao, "A Temperature Measurement System Based on PT100," International Conference on Electrical and Control Engineering pp. 296–298 (2010). Available: dx.doi.org/10.1109/iCECE.2010.79.

[128] RS (UK), *10KR NTC Thermister, 10s* (Technical Datasheet, 2016).

[129] F. Lacy, "Developing a theoretical relationship between electrical resistivity, temperature, and film thickness for conductors," Nanoscale Research Letters **6**, 636 (2011). Available: dx.doi.org/10.1186/1556-276X-6-636.

[130] Pico Technology (UK), *PT100 platinum resistance thermometers* (Technical Datasheet, 2016).

[131] Isotech (UK), *True Temperature Indicator TT* (Technical Datasheet, 2018).

[132] National Instruments (USA), *NI 9216* (Technical Datasheet, 2017).

[133] A. W. V. Herwaarden and P. M. Sarro, "Thermal Sensors Based on the Seebeck Effect," Sensors and Actuators **10**, 321–346 (1986).

[134] British Standards Institution, "BS EN 60584-1:2013 Thermocouples, EMF specifications and tolerances," (2013).

[135] National Instruments (USA), *NI 9205* (Technical Datasheet, 2015).

[136] National Instruments (USA), *USB-TC01* (Technical Specification, 2017).

[137] Texas Instruments (USA), *Semiconductor temperature sensors challenge precision RTDs and thermistors in building automation* (Application Report, 2015).

[138] Y. Deval, S. Ducouret, and J. Dom, "Ratiometric temperature stable current reference," Electronics Letters **29**, 1284 (1993). Available: dx.doi.org/10.1049/el:19930857.

[139] Texas Instruments (USA), *LMT70, LMT70A* (Technical Datasheet, 2015).

[140] Sensirion (Germany), *Datasheet STS21* (Technical Datasheet, 2011).

[141] S. Sikarwar and B. Yadav, "Opto-electronic humidity sensor: A review," Sensors and Actuators A: Physical **233**, 54–70 (2015). Available: dx.doi.org/10.1016/j.sna.2015.05.007.

[142] X. Yu, X. Chen, X. Ding, and X. Zhao, "A High-Stability Quartz Crystal Resonator Humidity Sensor Based on Tuning Capacitor," IEEE Transactions on Instrumentation and Measurement **67**, 1–7 (2018). Available: dx.doi.org/10.1109/TIM.2017.2784082.

[143] H. Farahani, R. Wagiran, and M. Hamidon, "Humidity Sensors Principle, Mechanism, and Fabrication Technologies: A Comprehensive Review," Sensors **14**, 7881–7939 (2014). Available: dx.doi.org/10.3390/s140507881.

[144] Texas Instruments (USA), *FDC2x1x EMI-Resistant 28-Bit , 12-Bit Capacitance-to-Digital Converter* (Technical Datasheet, 2015).

[145] P. Schubert and J. Nevin, "A polyimide-based capacitive humidity sensor," IEEE Transactions on Electron Devices **32**, 1220–1223 (1985). Available: dx.doi.org/10.1109/T-ED.1985.22104.

[146] S. Bera and S. Chattopadhyay, "A modified Schering bridge for measurement of the dielectric parameters of a material and the capacitance of a capacitive transducer," Measurement **33**, 3–7 (2003). Available: dx.doi.org/10.1016/S0263-2241(02)00040-4.

[147] Michell Instruments (UK), *Easidew Online Dew-Point Hygrometer* (Technical Datasheet, 2017).

[148] Sensirion (Germany), *Datasheet SHT21* (Technical Datasheet, 2010).

[149] F. Mayer and M. Lechner, "USOO6690569B1: Capacitive Sensor," (2004).

[150] Sensirion (Germany), *Sensor Specification Statement How to Understand Specification of Relative Humidity Sensors* (White Paper, 2018).

[151] Bosch Sensortec (Germany), *BME280: Combined humidity and pressure sensor* (Technical Datasheet, 2015).

[152] R. Lammel, S. Waffenchmidt, A. Feyh, G. O'Brien, and Andrew Graham, *Combined Pressure and Humidity Sensor* (US Patent: US20140116122A1, 2014).

[153] Keller (Germany), *Piezoresistive Pressure Transducers - Series 11* (Technical Datasheet, Datasheet, 2005).

[154] Keller (Germany), *Capacitive pressure transmitter - S41 X* (Technical Datasheet, 2010).

[155] TE Connectivity (Switzerland), *Barometric Pressure Sensor - MS5611-01BA03* (Technical Datasheet, 2017).

[156] Bosch Sensortec (Germany), *Digital pressure sensor BMP280* (Technical Datasheet, 2015).

[157] M. Mende, D. Knierim, and R. Booman, *Electro-optic sensor system* (European Patent Application: EP3252481A1, 2017).

[158] Tektronix (UK), *Isolated Measurement Systems TIVM1* (Technical Datasheet, 2018).

[159] M. Mende and R. Booman, *Measurement system including accessory with internal calibration signal* (US Patent: US009476960B2, 2016).

[160] M. Schumann, *Oscilloscope probe with fiber optic sensor for measuring floating electrical signals* (US Patent: US6603891B2, 2003).

[161] Broadcom (USA), *AFBR-POCxxxL Optical Power Converter* (Technical Datasheet, 2018).

[162] MH GoPower (Taiwan), *PoF Platform PoFP Series* (Technical Datasheet, 2018).

[163] D. R. Patriquin, *Optically Powered Sensor System* (US Patent: US4820916, 1989). Available: dx.doi.org/US005485919A.

[164] A. R. P. Spillman Jr, William B, *Optically Powered Sensor System With Improved Signal Conditioning* (US Patent: US4963729, 1990).

[165] JDSU (USA), *PPC-6E - 6V Photovoltaic Power Converter* (Technical Datasheet, 2006).

[166] J. Werthen, "Powering Next Generation Networks by Laser Light over Fiber," in "OFC/NFOEC 2008 - 2008 Conference on Optical Fiber Communication/National Fiber Optic Engineers Conference," (IEEE, 2008). Available: dx.doi.org/10.1109/OFC.2008.4528749.

[167] C. Budelmann, "Opto-Electronic Sensor Network Powered Over Fiber for Harsh Industrial Applications," IEEE Transactions on Industrial Electronics **65**, 1170–1177 (2018). Available: dx.doi.org/10.1109/TIE.2017.2733479.

[168] J. B. Rosolem and C. Floridia, "Power control and temperature sensing for fiber-powered active sensors." Applied Optics **47**, 6207–11 (2008). Available: dx.doi.org/0003-6935/08/336207-05.

[169] R. Heinzelmann, A. Stohr, M. Groz, D. Kalinowski, T. Alder, M. Schmidt, and D. Idger, "Optically powered remote optical field sensor system using an electroabsorption-modulator," in "IEEE MTT-S International Microwave Symposium Digest," , vol. 3 (IEEE, 1998), pp. 1225–1228. Available: dx.doi.org/10.1109/MWSYM.1998.700595.

[170] B. Beaumont, J. Guillaume, M. Vilela, A. Saletes, and C. Verie, "High efficiency conversion of laser energy and its application to optical power transmission," in "The Conference Record of the Twenty-Second IEEE Photovoltaic Specialists Conference," (IEEE, 1991), pp. 1503–1507. Available: dx.doi.org/10.1109/PVSC.1991.169454.

[171] J. Werthen, A. Andersson, S. Weiss, and H. Bjorklund, "Current measurements using optical power," in "Proceedings of the Transmission and Distribution Conference and Exposition," (IEEE, 1996), pp. 213–218. Available: dx.doi.org/10.1109/TDC.1996.545937.

[172] R. Peña, C. Algora, I. R. Matías, and M. López-Amo, "Fiber-based 205-mW (27% efficiency) power-delivery system for an all-fiber network with optoelectronic sensor units," Applied Optics **38**, 2463 (1999). Available: dx.doi.org/10.1364/AO.38.002463.

[173] A. Takahashi, M. Kinoshita, K. Kashiwagi, Y. Tanaka, and T. Kurokawa, "Fiber Sensor Network with Optical Power Supply," in "Conference on Lasers and Electro-Optics," (Optical Society of America, 2009), p. WH3_3. Available: dx.doi.org/10.1117/12.885968.

[174] Y. Tanaka, T. Shioda, T. Kurokawa, J. Oka, K. Ueta, and T. Fukuoka, "Power line monitoring system using fiber optic power supply," Optical Review **16**, 257–261 (2009). Available: dx.doi.org/10.1007/s10043-009-0048-x.

[175] C. Budelmann and B. Krieg-Brückner, "From sensorial to smart materials: Intelligent optical sensor network for embedded applications," Journal of Intelligent Material Systems and Structures **24**, 2183–2188 (2013). Available: dx.doi.org/10.1177/1045389X12462647.

[176] G. Böttger, M. Dreschmann, C. Klamouris, M. Hübner, M. Roger, A. W. Bett, T. Kueng, J. Becker, W. Freude, and J. Leuthold, "An optically powered video camera link," IEEE Photonics Technology Letters **20**, 39–41 (2008). Available: dx.doi.org/10.1109/LPT.2007.912695.

[177] M. Roger, W. Freude, G. Boettger, M. Dreschmann, M. Huebner, C. Klamouris, A. Bett, J. Becker, and J. Leuthold, "Optically powered fiber networks," Optics Express **16**, 21821 (2008). Available: dx.doi.org/10.1364/OE.16.021821.

[178] Y. Tanaka and T. Kurokawa, "A fiber sensor network using fiber optic power supply," in "22nd International Conference on Optical Fiber Sensor," , Y. Liao, W. Jin, D. D. Sampson, R. Yamauchi, Y. Chung, K. Nakamura, and Y. Rao, eds. (2012), p. 84211M. Available: dx.doi.org/10.1117/12.981524.

[179] BSI Standards Publication, "IEC 60825-1 - Safety of laser products," (2014).

[180] Linear Technology (USA), *LTC3108 Ultralow Voltage Step-Up Converter and Power Manager* (Technical Datasheet, 2010).

[181] Linear Technology Datasheet, *LTC3525 - 400mA Micropower Synchronous Step-Up DC/DC Converter with Output Disconnect* (Technical Datasheet, 2005).

[182] Texas Instruments (USA), *BQ25504 - Ultra Low-Power Boost Converter With Battery Management for Energy Harvester Applications* (Technical Datasheet, 2015).

[183] Texas Instruments (USA), *BQ25570 - Nano Power Boost Charger and Buck Converter for Energy Harvester Powered Applications* (Technical Datasheet, 2016).

[184] Pave Technology Company (USA), *Single-fibre 6.20mm piston o-ring: SP4S-E-150-1-SMF28ULTRA-39FC/APC-35* (Technical Drawing, 2018).

[185] Sinclair Manufacturing (USA), *Package Construction Common Materials Matrix* (Datasheet, 2011).

[186] A. Wasserman and L. Kerek, *Hermetic Optical Fiber Feedthrough Arrangement* (US Patent: US005155795A, 1992).

[187] M. W. Holt, F. P. Gehrke, and G. W. Walker, *Hermetic Seal on Metallized Fiber Optics* (US Patent: US007430357B2, 2008).

[188] W. W. Benson, I. Camlibel, D. R. Mackenzie, and T. C. Rich, *Optical Fiber-To-Metal Hermetic Seal* (US Patent: US4252457, 1981).

[189] T. F. Kovats, *Optical Fiber Hermetic Seal* (US Patent: US4413881, 1983).

[190] R. W. Filas, R. S. Moyer, and G. G. Smith, *In-Line Solder Seal for Optical Fiber* (US Patent: US006088504A, 2000).

[191] Q. Yu and J.-P. Noel, *Hermetic Seal for Optical Waveguide Ribbon Feed Through* (US Patent: US006763173B2, 2004).

[192] G. Bubel, J. Krause, B. Bickta, and R. Ku, "Mechanical reliability of metallized optical fiber for hermetic terminations," Journal of Lightwave Technology **7**, 1488–1493 (1989). Available: dx.doi.org/10.1109/50.39086.

[193] R. L. Dietz, "Optical fiber sealing with solder glass: design guidelines," (2004). Available: dx.doi.org/10.1117/12.567851.

[194] M. Shaw, R. Galeotti, and G. Coppo, "Method of fixing an optical fibre in a laser package," in "51st Electronic Components and Technology Conference," (IEEE, 2001), pp. 1441–1446. Available: dx.doi.org/10.1109/ECTC.2001.928025.

[195] Swagelok (USA), *VCR Metal Gasket Face Seal Fittings* (Catalogue, 2018).

[196] Fiberguide (USA), *Aluminum Coated Fiber* (Technical Datasheet, 2012).

[197] Fibercore (UK), *Fiber In Metal Tube* (www.fibercore.com/product/fiber-in-metal-tube, 2018).

[198] Thorlabs (USA), *FT023SS* (Specification, 2018).

[199] K. E. Lu, G. S. Glaesemann, M. T. Lee, D. R. Powers, and J. S. Abbott, "Mechanical and hydrogen characteristics of hermetically coated optical fibre," Optical and Quantum Electronics **22**, 227–237 (1990). Available: dx.doi.org/10.1007/BF02189429.

[200] Fibercore (UK), "Private communication," (2016).

[201] H. J. R. Dutton, *Understanding Optical Communications* (IBM Redbooks, 1998).

[202] USCONEC (USA), *SM MT Elite Drawing C7593: Assy, Ferrule & Boot* (Technical Drawing, 2004).

[203] M. Ott, P. Friedberg, and N. Gsfc, "Characterization of the Twelve Channel 100 / 140 Micron Optical Fiber , Ribbon Cable and MTP Array Connector Assembly for Space Flight Environments ." in "Proc. SPIE 4732: Photonic and Quantum Technologies for Aerospace Applications IV," , E. Donkor, M. J. Hayduk, A. R. Pirich, and E. W. Taylor, eds. (2002), pp. 79–88. Available: dx.doi.org/10.1117/12.477419.

[204] Amphenol Fiber Systems International (USA), *Optron Hybrid Fiber Optic/Electric Connectors* (Technical Datasheet, 2013).

[205] Amphenol Fiber Systems International (USA), "Private Communication," (2016).

[206] Molex (USA), *Circular MT Optical Cable Assemblies Circular MT Optical Cable Assemblies* (Marketing Brochure, 2010).

[207] Molex Incorporated, "Private Communication," (2016).

[208] Ibsen Photonics (Denmark), *I-MON USB* (Technical Datasheet, 2018).

[209] Oplink (USA), *OFMS SM Series Fiber-optic Switch* (Technical Datasheet, 2014).

[210] Laser Components (UK), *Optical Switch Singlemode 1x2, 1x4, 2x2* (Technical Datasheet, 2016).

[211] T. S. El-Bawab, *Optical Switching* (Springer, New York, 2006). Available: dx.doi.org/10.1007/0-387-29159-8.

[212] J. Watson, *Fundamentals of photonics* (John Wiley & Sons, 1992). Available: dx.doi.org/10.1016/0030-3992(92)90141-N.

[213] M. D. Todd, G. A. Johnson, and B. L. Althouse, "A novel Bragg grating sensor interrogation system utilizing a scanning filter, a Mach-Zehnder interferometer and a 3x3 coupler," Measurement Science and Technology **12**, 771–777 (2001). Available: dx.doi.org/10.1088/0957-0233/12/7/303.

[214] H. Park and M. Song, "Linear FBG Temperature Sensor Interrogation with Fabry-Perot ITU Multi-wavelength Reference," Sensors **8**, 6769–6776 (2008). Available: dx.doi.org/10.3390/s8106769.

[215] Y. Ma, C. Wang, Y. Yang, S. Yan, and J. Li, "High resolution and wide scale fiber Bragg grating sensor interrogation system," Optics & Laser Technology **50**, 107–111 (2013). Available: dx.doi.org/10.1016/j.optlastec.2013.02.018.

[216] P. Tsai, F. Sun, G. Xiao, Z. Zhang, S. Rahimi, and D. Ban, "A New Fiber-Bragg-Grating Sensor Interrogation System Deploying Free-Spectral-Range-Matching Scheme With High Precision and Fast Detection Rate," IEEE Photonics Technology Letters **20**, 300–302 (2008). Available: dx.doi.org/10.1109/LPT.2007.915638.

[217] Micron Optics (USA), *Fiber Fabry-Perot Tunable Filter, FFP-TF* (Technical Datasheet, 2015).

[218] U. Sharma and X. Wei, *Fiber Optic Sensing and Imaging* (Springer, New York, 2013). Available: dx.doi.org/10.1007/978-1-4614-7482-1.

[219] Q. Wang, X. Feng, Y. Zhao, J. Li, and H. Hu, "Research on fiber loop coupled resonator slow light and displacement sensing technology," Sensors and Actuators A: Physical **233**, 472–479 (2015). Available: dx.doi.org/10.1016/j.sna.2015.08.004.

[220] J. D. Joannopoulos, S. Johnson, J. N. J. Winn, and R. R. D. Meade, *Photonic crystals: molding the flow of light* (Princeton University Press, 2008), 2nd ed.. Available: dx.doi.org/10.1063/1.1586781.

[221] X. Wang, G. Hu, Y. Li, and J. Yao, "Numerical analysis of beam parameters and stability regions in a folded or ring cavity," Journal of the Optical Society of America A **11**, 2265 (1994). Available: dx.doi.org/10.1364/JOSAA.11.002265.

[222] R. Bandyopadhyay and R. Chakraborty, "Design of tunable transmission filter using one-dimensional defective photonic crystal structure containing electro-optic material," Optical Engineering **54**, 117105 (2015). Available: dx.doi.org/10.1117/1.OE.54.11.117105.

[223] J. Chen, H. Jiang, T. Liu, and X. Fu, "Wavelength detection in FBG sensor networks using least squares support vector regression," Journal of Optics **16**, 045402 (2014). Available: dx.doi.org/10.1088/2040-8978/16/4/045402.

[224] C. Perrotton, N. Javahiraly, M. Slaman, B. Dam, and P. Meyrueis, "Fiber optic Surface Plasmon Resonance sensor based on wavelength modulation for hydrogen sensing," Optics Express **19**, A1175 (2011). Available: dx.doi.org/10.1364/OE.19.0A1175.

[225] Thorlabs (USA), *Optical Spectrum Analyzers, OSA203* (Instruction Manual, 2017).

[226] Micron Optics (USA), *Fiber Fabry-Perot Interferometer, FFP-I* (Technical Datasheet, 2018).

[227] P. B. Harrison, R. R. J. Maier, J. S. Barton, J. D. C. Jones, S. McCulloch, and G. Burnell, "Fibre optic broadband interferometry for absolute distance measurements through optically dense media," in "Proc. SPIE 5855, 17th International Conference on Optical Fibre Sensors," , M. Voet, R. Willsch, W. Ecke, J. Jones, and B. Culshaw, eds. (2005), pp. 683–686. Available: dx.doi.org/10.1117/12.623395.

[228] P. B. Harrison, R. R. J. Maier, J. S. Barton, J. D. C. Jones, S. McCulloch, and G. Burnell, "Component position measurement through polymer material by broadband absolute distance interferometry," Measurement Science and Technology **16**, 2066–2071 (2005). Available: dx.doi.org/10.1088/0957-0233/16/10/023.

[229] S. Yang, D. Xiang, A. Bryant, P. Mawby, L. Ran, and P. Tavner, "Condition Monitoring for Device Reliability in Power Electronic Converters: A Review," IEEE Transactions on Power Electronics **25**, 2734–2752 (2010). Available: dx.doi.org/10.1109/TPEL.2010.2049377.

[230] L. Chen and C. Chen, "Uncertainly Analysis of Two Types of Humidity Sensors by a Humidity Generator with a Divided-Flow System," Sensors **18**, 637 (2018). Available: dx.doi.org/10.3390/s18020637.

[231] AWE, "Private communication," (2018).

[232] W. Wagner and A. Pruß, "The IAPWS Formulation 1995 for the Thermodynamic Properties of Ordinary Water Substance for General and Scientific Use," Journal of Physical and Chemical Reference Data **31**, 387–535 (2002). Available: dx.doi.org/10.1063/1.1461829.

[233] Vaisala Oyj (Finland), *Humidity Conversion Formulas - Calculation formulas for humidity* (White Paper, 2013).

[234] Sensirion (Germany), *Humidity at a Glance - Most Relevant Equations with Sample Code* (White Paper, 2008).

[235] British Standards Institution, "BS 1339-1:2002 Humidity," (2002).

[236] J. I. Steinfeld, J. S. Francisco, and W. L. Hase, *Chemical Kinetics and Dynamics* (Prentice Hall, 1989).

[237] AWE, "Private communication," (2015).

[238] C. S. Goldenstein and R. K. Hanson, "Diode-laser measurements of linestrength and temperature-dependent lineshape parameters for H2O transitions near 1.4μm using Voigt, Rautian, Galatry, and speed-dependent Voigt profiles," Journal of Quantitative Spectroscopy and Radiative Transfer **152** (2015). Available: dx.doi.org/10.1016/j.jqsrt.2014.11.008.

[239] M. Bolshov, Y. Kuritsyn, and Y. Romanovskii, "Tunable diode laser spectroscopy as a technique for combustion diagnostics," Spectrochimica Acta Part B: Atomic Spectroscopy **106**, 45–66 (2015). Available: dx.doi.org/10.1016/j.sab.2015.01.010.

[240] D. K. W. Lam and B. K. Garside, "Characterization of single-mode optical fiber filters," Applied Optics **20**, 440 (1981). Available: dx.doi.org/10.1364/AO.20.000440.

[241] D. Polyzos, J. Mathew, W. N. MacPherson, and R. R. J. Maier, "Effect of Dopant Diffusion on the Long-Term Stability of Fabry–Pérot Optical Fiber Sensors," Journal of Lightwave Technology **35**, 5317–5323 (2017). Available: dx.doi.org/10.1109/JLT.2017.2773501.

[242] Temperature Applied Sciences Datasheet, *Series 3 Specification* (Technical Datasheet, 2015).

[243] X. Feng, C. Sun, X. Zhang, and F. Ansari, "Determination of the coefficient of thermal expansion with embedded long-gauge fiber optic sensors," Measurement Science and Technology **21**, 065302 (2010). Available: dx.doi.org/10.1088/0957-0233/21/6/065302.

[244] Bal Seal Engineering (USA), *Coefficient of Thermal Expansion for Various Materials*, vol. 18 (White Paper, 2004).

[245] M. Pecht and F. Nash, "Predicting the reliability of electronic equipment," Proceedings of the IEEE **82**, 992–1004 (1994). Available: dx.doi.org/10.1109/5.293157.

[246] Opsens (Canada), *Signal conditioner FieldSens IMP0007* (Technical Datasheet, 2014).

[247] J. R. P. Bain, "Near Infrared Tunable Diode Laser Spectroscopy for Aero Engine Related Applications," Ph.D. thesis, University of Strathclyde (2012).

[248] C. S. Goldenstein, V. A. Miller, R. Mitchell Spearrin, and C. L. Strand, "SpectraPlot.com: Integrated spectroscopic modeling of atomic and molecular gases," Journal of Quantitative Spectroscopy and Radiative Transfer **200**, 249–257 (2017). Available: dx.doi.org/10.1016/j.jqsrt.2017.06.007.

[249] L. Rothman, I. Gordon, Y. Babikov, A. Barbe, D. Chris Benner, P. Bernath, M. Birk, L. Bizzocchi, V. Boudon, L. Brown, A. Campargue, K. Chance, E. Cohen, L. Coudert, V. Devi, B. Drouin, A. Fayt, J.-M. Flaud, R. Gamache, J. Harrison, J.-M. Hartmann, C. Hill, J. Hodges, D. Jacquemart, A. Jolly, J. Lamouroux, R. Le Roy, G. Li, D. Long, O. Lyulin, C. Mackie, S. Massie, S. Mikhailenko, H. Müller, O. Naumenko, A. Nikitin, J. Orphal, V. Perevalov, A. Perrin, E. Polovtseva, C. Richard, M. Smith, E. Starikova, K. Sung, S. Tashkun, J. Tennyson, G. Toon, V. Tyuterev, and G. Wagner, "The HITRAN2012 molecular spectroscopic database," Journal of Quantitative Spectroscopy and Radiative Transfer **130**, 4–50 (2013). Available: dx.doi.org/10.1016/j.jqsrt.2013.07.002.

[250] L. Rothman, C. Rinsland, A. Goldman, S. Massie, D. Edwards, J.-m. Flaud, A. Perrin, C. Camy-peyret, V. Dana, J.-y. Mandin, J. Schroeder, A. Mccann, R. Gamache, R. Wattson, K. Yoshino, K. Chance, K. Jucks, L. Brown, V. Nemtchinov, and P. Varanasi, "The hitran molecular spectroscopic database and hawks (hitran atmospheric workstation): 1996 edition," Journal of Quantitative Spectroscopy and Radiative Transfer **60**, 665–710 (1998). Available: dx.doi.org/10.1016/S0022-4073(98)00078-8.

[251] Mettler-Toledo (USA), *Tunable Diode Laser Spectroscopy - Theory and Background* (White Paper, 2012).

[252] M. Mangold, B. Tuzson, M. Hundt, J. Jágerská, H. Looser, and L. Emmenegger, "Circular paraboloid reflection cell for laser spectroscopic trace gas analysis," Journal of the Optical Society of America A **33**, 913 (2016). Available: dx.doi.org/10.1364/JOSAA.33.000913.

[253] R. Ghorbani and F. M. Schmidt, "ICL-based TDLAS sensor for real-time breath gas analysis of carbon monoxide isotopes," Optics Express **25**, 12743 (2017). Available: dx.doi.org/10.1364/OE.25.012743.

[254] A. Pogány, S. Wagner, O. Werhahn, and V. Ebert, "Development and Metrological Characterization of a Tunable Diode Laser Absorption Spectroscopy (TDLAS) Spectrometer for Simultaneous Absolute Measurement of Carbon Dioxide and Water Vapor," Applied Spectroscopy **69**, 257–268 (2015). Available: dx.doi.org/10.1366/14-07575.

[255] K. Liu, L. Wang, T. Tan, G. Wang, W. Zhang, W. Chen, and X. Gao, "Highly sensitive detection of methane by near-infrared laser absorption spectroscopy using a compact dense-pattern multipass cell," Sensors and Actuators B: Chemical **220**, 1000–1005 (2015). Available: dx.doi.org/10.1016/j.snb.2015.05.136.

[256] S. Kong, F. Application, and P. Data, "Absorption Spectroscopy Instrument With Off-Axis Light Insertion Into Cavity," (2004). Available: dx.doi.org/10.1016/j.(73).

[257] C. G. Tarsitano and C. R. Webster, "Multilaser Herriott cell for planetary tunable laser spectrometers," Applied Optics **46**, 6923 (2007). Available: dx.doi.org/10.1364/AO.46.006923.

[258] G. Kychakoff, R. D. Howe, and R. K. Hanson, "Spatially resolved combustion measurements using cross-beam saturated absorption spectroscopy," Applied Optics **23**, 1303 (1984). Available: dx.doi.org/10.1364/AO.23.001303.

[259] J. U. White, "Long Optical Paths of Large Aperture," Journal of the Optical Society of America **32**, 285 (1942). Available: dx.doi.org/10.1364/JOSA.32.000285.

[260] S. M. Chernin and E. G. Barskaya, "Optical multipass matrix systems," Applied Optics **30**, 51 (1991). Available: dx.doi.org/10.1364/AO.30.000051.

[261] D. W. Steyert, J. M. Sirota, M. E. Mickelson, and D. C. Reuter, "Two new long-pass cells for infrared and visible spectroscopy," Review of Scientific Instruments **72**, 4337–4343 (2001). Available: dx.doi.org/10.1063/1.1409565.

[262] D. Herriott, H. Kogelnik, and R. Kompfner, "Off-Axis Paths in Spherical Mirror Interferometers," Applied Optics **3**, 523 (1964). Available: dx.doi.org/10.1364/AO.3.000523.

[263] D. R. Herriott and H. J. Schulte, "Folded Optical Delay Lines," Applied Optics **4**, 883 (1965). Available: dx.doi.org/10.1364/AO.4.000883.

[264] O. S. Wolfbeis, "Materials for fluorescence-based optical chemical sensors," Journal of Materials Chemistry **15**, 2657 (2005). Available: dx.doi.org/10.1039/b501536g.

[265] Ocean Optics (USA), *Smart Oxygen Cuvette for Optical Monitoring of Dissolved Oxygen in Biological Blood Samples* (Application Note, 2010). Available: dx.doi.org/10.1117/1.3156837.

[266] F. W. J. Teale, *Phase and Modulation Fluorometry* (Springer, Boston, 1983), pp. 59–80.

[267] G. G. Stokes, "On the Change of Refrangibility of Light," Philosophical Transactions of the Royal Society of London **142**, 463–562 (1852). Available: dx.doi.org/10.1098/rstl.1852.0022.

[268] J. Demas, *Excited State Lifetime Measurements* (Elsevier, 1983). Available: dx.doi.org/10.1016/B978-0-12-208920-6.X5001-0.

[269] P. P. Mondal and A. Diaspro, *Fundamentals of Fluorescence Microscopy* (Springer Netherlands, Dordrecht, 2014). Available: dx.doi.org/10.1007/978-94-007-7545-9.

[270] C. Baleizao, S. Nagl, M. Schaferling, M. N. Berberan-Santos, and O. S. Wolfbeis, "Dual Fluorescence Sensor for Trace Oxygen and Temperature with Unmatched Range and Sensitivity," Analytical Chemistry **80**, 6449–6457 (2008). Available: dx.doi.org/10.1021/ac801034p.

[271] C. Stehning and G. A. Holst, "DSP-based measuring system for temperature-compensated fiber optical oxygen sensors," in "Proc. SPIE 4578: Fiber Optic Sensor Technology and Applications," , vol. 4578, M. A. Marcus and B. Culshaw, eds. (2002), pp. 259–270. Available: dx.doi.org/10.1117/12.456078.

[272] D. García-Fresnadillo, M. D. Marazuela, M. C. Moreno-Bondi, and G. Orellana, "Luminescent Nafion Membranes Dyed with Ruthenium(II) Complexes as Sensing Materials for Dissolved Oxygen," Langmuir **15**, 6451–6459 (1999). Available: dx.doi.org/10.1021/la981689c.

[273] Ocean Optics (USA), *Oxygen Sensing, NeoFox* (Quick Start Instructions, 2018). Available: dx.doi.org/10.1007/b111080.

[274] PreSens (Canada), *Optical Oxygen Sensors & Meters* (Technical Datasheet, 2001).

[275] PreSens (Canada), *Oxygen Microsensors* (Technical Datasheet, 2017).

[276] PreSens (Canada), *Microx TX3 Micro fiber optic oxygen transmitter* (Instruction Manual, 2016).

[277] L. Song, E. Hennink, I. Young, and H. Tanke, "Photobleaching kinetics of fluorescein in quantitative fluorescence microscopy," Biophysical Journal **68**, 2588–2600 (1995). Available: dx.doi.org/10.1016/S0006-3495(95)80442-X.

[278] Y. Zhao, Y.-n. Zhang, and Q. Wang, "Optimization of Slow Light in Slotted Photonic Crystal Waveguide With Liquid Infiltration," Journal of Lightwave Technology **31**, 2448–2454 (2013). Available: dx.doi.org/10.1109/JLT.2013.2267272.

[279] A. Di Falco, L. O'Faolain, and T. Krauss, "Photonic crystal slotted slab waveguides," Photonics and Nanostructures - Fundamentals and Applications **6**, 38–41 (2008). Available: dx.doi.org/10.1016/j.photonics.2007.08.001.

[280] M. Scullion, T. Krauss, and A. Di Falco, "Slotted Photonic Crystal Sensors," Sensors **13**, 3675–3710 (2013). Available: dx.doi.org/10.3390/s130303675.

[281] M. G. Scullion, A. Di Falco, and T. F. Krauss, "Contra-directional coupling into slotted photonic crystals for spectrometric applications," Optics Letters **39**, 4345 (2014). Available: dx.doi.org/10.1364/OL.39.004345.

[282] A. Di Falco, M. Massari, M. G. Scullion, S. A. Schulz, F. Romanato, and T. F. Krauss, "Propagation Losses of Slotted Photonic Crystal Waveguides," IEEE Photonics Journal **4**, 1536–1541 (2012). Available: dx.doi.org/10.1109/JPHOT.2012.2211342.

[283] M. Scullion, A. Di Falco, and T. Krauss, "Slotted photonic crystal cavities with integrated microfluidics for biosensing applications," Biosensors and Bioelectronics **27**, 101–105 (2011). Available: dx.doi.org/10.1016/j.bios.2011.06.023.

[284] J. P. Parry, B. C. Griffiths, N. Gayraud, E. D. McNaghten, A. M. Parkes, W. N. MacPherson, and D. P. Hand, "Towards practical gas sensing with micro-structured fibres," Measurement Science and Technology **20**, 075301 (2009). Available: dx.doi.org/10.1088/0957-0233/20/7/075301.

[285] B. Lee, S. Roh, and J. Park, "Current status of micro- and nano-structured optical fiber sensors," Optical Fiber Technology **15**, 209–221 (2009). Available: dx.doi.org/10.1016/j.yofte.2009.02.006.

[286] Thorlabs (USA), *FGA01FC - InGaAs Photodiode* (Technical Datasheet, 2017).

[287] Thorlabs (USA), *FDGA05 - InGaAs Photodiode* (Technical Datasheet, 2017).

[288] Fermionics (USA), *FD300 - InGaAs Photodiode* (Technical Datasheet, 2018).

[289] G. Allwood, G. Wild, and S. Hinckley, "A Comparison of InGaAs and Ge photonic power converters for long wavelength power over fibre," in "COMMAD 2012," (IEEE, 2012), pp. 15–16. Available: dx.doi.org/10.1109/COMMAD.2012.6472337.

[290] G. Allwood, G. Wild, and S. Hinckley, "Power over Fibre: Material Properties of Homojunction Photovoltaic Micro-Cells," in "2011 Sixth IEEE International Symposium on Electronic Design, Test and Application," (IEEE, 2011), pp. 78–82. Available: dx.doi.org/10.1109/DELTA.2011.66.

[291] Thorlabs (USA), "Private Communication," (2017).

[292] Thorlabs (USA), *LN82S-FC 10 GHz Lithium Niobate Intensity Modulator with Internal Photodetector* (Technical Datasheet, 2018).

[293] W. Pathirana and A. Muhtaroglu, "Low voltage DC-DC conversion without magnetic components for energy harvesting," in "2012 International Conference on Energy Aware Computing," (IEEE, 2012), pp. 1–6. Available: dx.doi.org/10.1109/ICEAC.2012.6471010.

[294] Fluke (USA), *83V and 87V Digital Multimeters - Detailed Specifications* (Datasheet, 2005).

[295] T. Shan and X. Qi, "Performance of series connected GaAs photovoltaic converters under multimode optical fiber illumination," Advances in OptoElectronics **2014**, 824181 (2014). Available: dx.doi.org/10.1155/2014/824181.

[296] Laser Components (UK), *PL13/15 FP Series Laser Diode Modules* (Technical Datasheet, 2016).

[297] Sensirion (Germany), *Sensirion SCD30 Sensor Module* (Datasheet, 2018).

[298] Laser Components (UK), *Hermetic Feedthroughs M12* (Datasheet, 2013).

[299] USCONEC (USA), *C12557 Ferrule 24F PPS MM MT Elite* (Technical Drawing, 2009).

[300] K.-H. Haas, S. Amberg-Schwab, K. Rose, and G. Schottner, "Functionalized coatings based on inorganic–organic polymers (ORMOCER®s) and their combination with vapor deposited inorganic thin films," Surface and Coatings Technology **111**, 72–79 (1999). Available: dx.doi.org/10.1016/S0257-8972(98)00711-7.

[301] K.-H. Haas and H. Wolter, "Synthesis, properties and applications of inorganic–organic copolymers (ORMOCER®s)," Current Opinion in Solid State and Materials Science **4**, 571–580 (1999). Available: dx.doi.org/10.1016/S1359-0286(00)00009-7.

[302] Dupont (USA), *DuPont Kapton* (www.dupont.com/content/dam/dupont/products-and-services/membranes-and-films/polyimde-films/documents/ DEC-Kapton-summary-of-properties.pdf, 2012).

[303] Ministry of Defence, *MOD technology readiness levels and their definitions* (Webarchive.nationalarchives.gov.uk/20121026065214/www.mod.uk/NR/rdonlyres/BB63DF2A-EEA7-4328-A685-5E1349AE2B62/0/20090331 FATS3_AnnexGtoSch1U.pdf, 2017).

[304] Ministry of Defence Guidance, "Acquisition System Guidance (ASG)," (2015).

[305] "Guide to Technology Readiness Levels for the NDA Estate and its Supply Chain," Tech. rep., Nuclear Decommissioning Authority (2014).